CRANFIELD UNIVERSITY

HAKIM OHEDA

ARTIFICIAL NEURAL NETWORK CONTROL STRATEGIES FOR FUEL CELL HYBRID SYSTEM

SCHOOL OF ENGINEERING
DEPARTMENT OF ENGINEERING PHYSICS

SUBMITTED FOR THE DEGREE OF PHD
Academic Year: 2012 - 2013

SUPERVISOR: DR. SAVVARIS, A.
May 2013

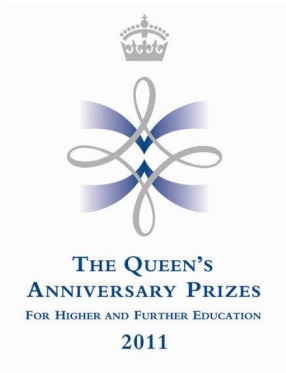

CRANFIELD UNIVERSITY

SCHOOL OF ENGINEERING
Department of Engineering Physics

SUBMITTED FOR THE DEGREE OF PHD

Academic Year 2012 - 2013

HAKIM OHEDA

ARTIFICIAL NEURAL NETWORK CONTROL STRATEGIES FOR FUEL CELL HYBRID SYSTEM

Supervisor: Dr. Savvaris, A.
May 2013

This thesis is submitted in partial fulfilment of the requirements for the degree of PhD

ABSTRACT

The greening of air transport is the driver for developing technologies to reduce the environmental impact of aviation with the aim of halving the amount of carbon dioxide (CO_2) emitted by air transport, cutting specific emissions of nitrogen oxides (NO_x) by 80% and halving perceived noise by the year 2020. Fuel Cells (FC) play an important role in the new power generation field as inherently clean, efficient and reliable source of power especially when comparing with the traditional fossil-fuel based technologies.

The project investigates the feasibility of using an electric hybrid system consisting of a fuel cell and battery to power a small model aircraft (PiperCub J3). In order to meet the desired power requirements at different phases of flight efficiently, a simulation model of the complete system was first developed, consisting of a Proton Exchange Membrane hybrid fuel cell system, 6DoF aircraft model and neural network based controller. The system was then integrated in one simulation environment to run in real-time and finally was also tested in hardware-in-the-loop with real-time control.

The control strategy developed is based on a neural network model identification technique; specifically Model Reference Control (MRC), since neural network is well suited to nonlinear systems. To meet the power demands at different phases of flight, the controller controls the battery current and rate of charging/discharging.

Three case studies were used to validate and assess the performance of the hybrid system: battery fully charged (high SOC), worst case scenario and taking into account the external factors such as wind speeds and wind direction. In addition, the performance of the Artificial Neural Network Controller was compared to that of a Fuzzy Logic controller. In all cases the fuel cell act as the main power source for the PiperCub J3 aircraft. The tests were carried-out in both simulation and hardware-in-the-loop.

Keywords:
PEM Fuel cell; Modelling and Simulation PEM; Dynamic performance; Transient response; Artificial Neural Network; Fuzzy Logic; Hybrid systems

ACKNOWLEDGEMENTS

This research was carried out in the Department of Engineering Physics at Cranfield University, UK from 2009 to 2013.

I thank God for the strength and faith given to me, which enabled the completion of this work. I want to take this opportunity to express my appreciation to all those people who have supported me during my Ph.D. program at Cranfield University.

First of all, I would like to express my deepest appreciation and sincere respect to my research advisor, Dr. Al Savvaris, for his patience, understanding and support in my research process. I appreciate people who, always took time out of their busy schedule to give help and offer valuable suggestions.

I have also to thank all the people that I have met during these years, whose friendship are among the most valuable assets gained during this period of my life, especially my departmental colleagues namely Kashif Iqbal, Guido Monterzino, Ramey Jamal, Mudassir Lone, Solange Baena, Paul Jemitola, Ken Lai, Peter Thomas, Henry Leonardo, Ting Ding, Francis Salama, Yosuke Shimada, Samer Aldhaher, Shirley Mao and Marco Melega whose memories in and out of the office are appreciated. Your friendship made life in Cranfield much more bearable.

Special thanks goes to Tareq Alawadi and Hamid Al-Turbah for their help and support in this work, also for all the good and the bad times that we shared together in and out of the office. It's been a real pleasure knowing both of you.

Finally, I would like to acknowledge all my family members, especially my parents and my wife - Mrs. Dalal Shneti, who stood by me during all the good and bad times; not forgetting my lovely daughter Amani and my naughty son Mohammed, you have been in my heart ever since I was blessed with you.

May 3, 2013

Hakim Oheda

Table of Contents

List of figures

List of Tables

SYMBOLS, INDICES AND ABBREVIATIONS

Symbol	Description	Unit(s)
k_{H2}	Hydrogen valve molar constant	$[kmol\ s^{-1}atm]$
k_{H2O}	Water valve molar constant	$[kmol\ s^{-1}atm]$
k_{O2}	Oxygen valve molar constant	$[kmol\ s^{-1}atm]$
q_{H2}	Molar flow of hydrogen	$[kmol\ s^{-1}]$
q_{H2O}	Molar flow of water	$[kmol\ s^{-1}]$
q_{O2}	Molar flow of oxygen	$[kmol\ s^{-1}]$
q_{H2}^{in}	Hydrogen input flow	$[kmol\ s^{-1}]$
q_{H2}^{out}	Hydrogen output flow	$[kmol\ s^{-1}]$
q_{H2}^{r}	Hydrogen flow that reacts	$[kmol\ s^{-1}]$
P_{H2}	Hydrogen partial pressure	$[atm]$
P_{H2O}	Water partial pressure	$[atm]$
P_{O2}	Oxygen partial pressure	$[atm]$
τ_{H2}	Hydrogen time constant	$[s]$
τ_{H2O}	Water time constant	$[s]$
τ_{O2}	Oxygen time constant	$[s]$
M_{H2}	Molar mass of hydrogen	$[kg\ mol\ s^{-1}]$
M_{H2O}	Molar mass of water	$[kg\ mol\ s^{-1}]$
τ_{a}	Fuel flow delay	$[s]$
τ_{c}	Oxidant flow delay	$[s]$
M_{O2}	Molar mass of oxygen	$[kg\ mol\ s^{-1}]$
Van	Volume of the anode channel	$[m^3]$
Vca	Volume of the cathode channel	$[m^3]$
R	Universal gas constant	$[\ J\ kmol\ s^{-1}]$
C_{O2}	Oxygen concentration (0.21%)	[%]
Tc	Temperature in degrees C^o	$[C^o]$
Tk	Temperature in k	$[k]$
T	Stack Temperature	$[k]$
i	Stack current	$[A/cm^2]$
I	Cell current density	$[A/cm^2]$
F	Faraday's constant	$[Coulombs]$
z	Number of electrons	$[-]$

kr	Modelling constant = No/4F	$[kmol\ s^{-1}A]$
$\mathcal{V}_{out}$	DC output voltage of FC stack	$[V]$
P_{out}	Power delivered by the stack	$[w]$
E	Nernst voltage	$[V]$
r	Stack internal resistance	$[\Omega]$
V_o	Open-circuit voltage of the power module	$[V]$
I_{fc}	Output current of the power module	$[A]$
E	Nernst voltage	$[V]$
$\mathcal{V}_{ohmic}$	Over potential due to ohmic loss	$[V]$
V_{act}	Activation over potential	$[V]$
V_{conc}	Concentration over potential	$[V]$
A	Area of cell	$[cm^2]$
io	Exchange Current Density	$[A/cm^2]$
iL	Limiting current density	$[A/cm^2]$
Gf	Gibbs function in liquid form	$[J\ kmol]$
η	Overvoltage	$[V], [mV]$
Δ_g	Specific Gibb's free enthalpy	$[J\ mol^{-1}]$
Δh	Specific reaction enthalpy	$[J\ mol^{-1}]$
U	Voltage	$[V]$
U_{cell}	Cell voltage	$[V]$
No	Number of cells in the stack	
b	Constant of Tafel	
s	*s* domain	
α	Transfer coefficient	
α1	Amplification constant	
k	Constant k used in mass transport	
η_{th}	Thermodynamic efficiency	
η_{volt}	Voltage efficiency	
U_{OCV}^{th}	Maximum thermodynamic value	
η_{Faradaic}	Faradaic efficiency	
v	Number of moles reacting per unit time	
γ_{fuel}	Un acted fuel that supplied	

1. Glossary

ANN	Artificial Neural Network Controller
PI	Proportional-plus-Integral
FLC	Fuzzy Logic Controller
CO_2	Carbon dioxide
NO_x	Nitrogen oxides
$ACARE$	Advisory Council for Aeronautical Research in Europe
PEM	Proton Exchange Membrane
FC	Fuel Cell
AFC	Alkaline Fuel Cell
KOH	Potassium hydroxide
APU	Auxiliary power
MRE	Mean relative error
DC	Direct Current
$MCFC$	Molten Carbonate Fuel Cell
$PAFC$	Phosphoric Acid Fuel Cell
$SOFC$	Solid Oxide Fuel Cell
SOC	State Of Charge
NRC	National research Council
$PTFE$	Polytetrafluoroethylene
GDL	Gas diffusion layer
MPL	Micro-porous layer
$BR\&TE$	Boeing Research and Technology Europe
FCV	Fuel cell vehicle
$ICEV$	Internal combustions engine vehicle
FCB	Fuel cells bus
HEV	Hybrid electrical vehicle
ESS	Energy Storage System
UC	Ultra-capacitors
CCM	Continuous Conduction Mode
DCM	Discontinuous Conduction Mode
SMPS	Switched-Mode Power supply
VLP	Voltage Loop

S	Switch
V	Voltage
V_L	Low voltage side
V_H	High voltage side
V_{in}	Input voltage
V_{out}	Output voltage
V_{ref}	Reference voltage
PWM	Pulse Width Modulation
D	Duty cycle
f	Frequency
t	Time
T_{on}	Switching signal On time
T_{off}	Switching signal Off time
T_s	Switching signal period
R	Resistance
C	Capacitance
L	Inductance
D_i	Diode
$MOSFET$	Metal–oxide–semiconductor field-effect transistor
VCM	Voltage control mode
CCM	Current control mode
$6DoF$	Six-degrees of freedom
SAS	Stability augmentation system
MLP	Multilayer Perceptron
DAQ	Data acquisition system
GUI	Graphical user interface
EoM	Equations of motion
$ECMS$	Equivalent consumption minimization strategy
BP	Back-Propagation

Aircraft variables

Symbol	Description
h	Height: Centre of gravity position on reference chord: Spanwise coordinate along wing sweep line
g	Acceleration due to gravity
I_x	Moment of inertia in roll
I_z	Moment of inertia in yaw
I_y	Moment of inertia in pitch
I_{xz}	Product of inertia about $ox\ and\ oy$ axes
k	General constant : spring stiffness coefficient
M	Mass
A	State matrix
B	Input matrix
M	‘’Mass’’ matrix
n	Total normal load factor
N	Yawing moment
p	Roll rate perturbation
q	Pitch rate perturbation
s	Wing semi-span; Laplace
r	Yaw rate perturbation
t	Time: Maximum aerofoil section
T	Time constant
u	Axial velocity perturbation
u	Input vector
U	Total axial velocity
U_e	axial components of steady equilibrium velocity
U_E	axial velocity components referred to datum-path earth axes
v	Lateral velocity perturbation
w	Normal velocity perturbation
W	Total normal perturbation
W_e	Normal component of steady equilibrium velocity
W_E	Normal velocity component referred to datum-path earth axes
x	State vector

x	Longitudinal coordinate in axis system
x_τ	Axial coordinate of engine thrust line
y	Lateral coordinate in axis system
z	Normal coordinate in axis system
z_τ	Normal coordinate of engine thrust line
Z	Normal force component
ε	Throttle lever angle: Downwash angle at tailplane: Closed loop
θ	Pitch angle perturbation: A general angle
ζ	Rudder angle perturbation
ϕ	Roll angle perturbation
ψ	Yaw angle perturbation
η	Elevator angle perturbation
ξ	Aileron angle perturbation
τ	Engine thrust perturbation: Time parameter

Subscripts

Symbol	Description
g	Gravitational
L	Lift
m	Pitching moment: manoeuvre
n	Neutral point: yawing moment
p	Power: roll rate; phugoid
q	Pitch rate
r	Yaw rate: Roll rate
R	Rudder
u	Axial velocity
v	Lateral velocity
w	Aeroplane wind stability axes: Wing or wing-body: Normal velocity
x	ox axis
y	oy axis
z	oz axis
ε	Throttle lever
θ	Pitch
ζ	Rudder
η	Elevator
ξ	Ailerons
τ	Thrust

Chapter 1

Introduction

1. INTRODUCTION

The greening of air transport is the driver for developing technologies to reduce the environmental impact of aviation with the aim of halving the amount of carbon dioxide (CO_2) emitted by air transport, cutting specific emissions of nitrogen oxides (NO_x) by 80% and halving perceived noise, by the year 2020. The targets reflect the Ultra Green High Level Target Concepts developed by the Advisory Council for Aeronautical Research in Europe (ACARE) in its strategic research agenda (also known as ACARE 2020 Vision) [1].

Fuel Cells (FCs) are among the enabling technologies under consideration. They are emission-free and quieter than hydrocarbon fuel-powered engines. Specifically, Proton Exchange Membrane (PEM) FC is the most likely option. PEM FCs can operate at relatively low temperatures (around $80C^o$), which allows them to start up quickly (no warming time). They could deliver high power density and the thinness of the membrane electrode assemblies gives them the advantages of low weight and volume [1].

1.1 Aim and Objectives

The aim of this research project is to investigate the feasibility of using an electric hybrid system consisting of a FC and battery pack to power a small aircraft and implement a ANN controller for the system. In order to achieve the desired power at different phases of flight, PEM FC will act as primary power plant for the electric motor in combination with the battery pack which will act as an auxiliary power unit.

This thesis will focus mainly on developing a fuel cell model, its validation and the implementation of the controller for the hybrid system. The simulation results obtained will be validated by a comparison with experimental results using hardware-in-the-loop from the experimental Nexa hybrid system.

The main objectives of the project are outlined as follows:

- Develop a simulation model of the PEM fuel cell
- Develop a simulation model of the complete hybrid system ($FC + Battery$) and integrate in one environment to run in real time including the 6DoF aircraft model and neural network based controller

- Develop a base controller for the system; then ANN and Fuzzy Logic controllers and compare the result

- Validate the results obtained from simulation for different flight test cases with the results obtained from the hardware-in-the-loop test and assess the performance of the ANN controller

- Consider external factors e.g. wind and assess the impact on power requirements

1.2 Contribution to Knowledge

The novelty of this work can be summarised into the following points:

- Development of an Intelligent Energy Management System to manage the power supply from the fuel cell and battery and to meet the power requirement for the different phases of flight and operating conditions

- The FC model's novelty in comparison with similar existing models is that it takes into account the Equivalent Internal Resistance of the fuel cell module

- Integration of the complete hybrid fuel cell system to run in real time together with the 6Dof aircraft model and the artificial neural network controller in one environment; and to test the system using hardware-in-the-loop with real time control for the specific application

- Take into account external factors namely wind speeds and wind direction

1.3 Outline of the Thesis

This thesis has the following structure:

- Following the introductory chapter, the content of chapter 2 presents the state–of–the–art in the field of fuel cell systems technology; the basic concepts regarding fuel cells (basic operations, types and applications). In particular, focusing on PEM FC and how to determine their energy; review of the loss mechanisms which determine the maximum cell performance and efficiency are also presented

- Chapter 3 gives an overview of the hardware setup and the complete fuel cell hybrid system and their types/configuration. The different types of energy storage system used to complement the slower power output of the fuel cell are also discussed. Including the battery model, electrical engine model and Piper Cub J3 aircraft model. Details of the experimental set-up are discussed and each component of the hybrid system individually described with its specification and interface between the hardware and the software. The chapter also discuss the two DC/DC converters that were used in this work, one to regulate the voltage and the other to charge/discharge the battery pack.

- Chapter 4 presents the experimental results and analysis of the dynamic performance of the Nexa PEM FC power module.

- Chapter 5 begins by introducing some of the current fuel cell models that were developed by various researchers; so also the fuel cell performance, characteristic, losses mechanism and their phenomena are discussed. One of the objectives of this research was to develop an improved dynamic fuel cell model. The developed dynamic electrochemical PEM FC model is presented in this chapter with the theoretical equations, assumptions, results and discussion. The improved model is then validated using experimental results.

- Chapter 6 describes the implementation of the control strategies for the FC hybrid system. The control strategies started with design and implementation of PI controller and then improved by adding an anti-windup loop to I-term using a saturation block with the same limits as the saturation in the real system. A more advanced controller artificial neural networks replacing the PI controller is also implemented and is presented here. This is followed by a discussion of the performance of each controller in the hardware loop and a comparison of their results.

- Chapter 7; several cases studies were used to validate and assess the performance of the hybrid system. A brief description of each case is given with its result and discussion. In addition, the desired aircraft power and fuel consumption for different phases of flight were provided including worst case scenario and taking into account external factors

- Finally, Chapter 8 concludes the thesis and the main contributions of this thesis are presented. Also, suggestions of some possible future lines of research are given.

Chapter 2

Review of Fuel Cell Technology

2. REVIEW OF FUEL CELL TECHNOLOGY

This chapter provides a general look at the field of fuel cell and covers some aspects of what other work that have been researched and carried-out in this area. A summary of the basics of Proton Exchange Membrane Fuel Cells PEM FCs technology is given, including the explanation of the working principle and the main construction elements. A review of the loss mechanisms which determine the maximal cell performance is also presented (detailed explanation is given in chapter 5). A summary of the different types of fuel cell, their advantages and disadvantages compared to other power techniques and their application is also presented in this chapter.

2.1 Introduction

Fuel cells are efficient electric energy sources that produce negligible pollutant emissions. For that reason called low emission power sources. A FC is a device that converts the chemical energy of a fuel (hydrogen, natural gas, methanol, gasoline, etc.) and an oxidant (air or oxygen) into electricity. In principle, a FC operates like a battery. Unlike a battery however, a FC does not run down or require recharging. It will produce electricity and heat as long as fuel and an oxidiser are supplied [2].

Both batteries and FCs are electrochemical devices. As such, both have a positively charged anode, a negatively charged cathode and an ion-conducting material called an electrolyte. FCs are classified by their electrolyte material. Electrochemical devices generate electricity without combustion of the fuel and oxidizer, as opposed to what occurs with traditional methods of electricity generation.

FC construction generally consists of a fuel electrode (anode) and an oxidant electrode (cathode) separated by an ion-conducting membrane. Oxygen passes over one electrode and hydrogen over the other, generating electricity, water and heat.

2.2 Advantage of Fuel Cell

FCs provide a range of significant benefits that no other single power technology can match. In fact, FCs combine many of the advantages of both engines and batteries. Since FCs

produce electricity directly from chemical energy, they are often far more efficient than combustion engines. Fuel cells can be 2 to 3 times more efficient than diesel or gasoline internal composition engines as they are not limited by temperature as is the heat engine [3]; and offer the advantages of low weight and volume, compared with other FCs. FC itself has no moving parts making it a quiet and reliable source of power. Also, undesirable products such as NO_x, SO_x, and particulate emissions are virtually zero.

Unlike batteries, FCs allow easy independent scaling between power (determined by the FC size) and capacity (determined by the fuel reservoir size). In batteries, power and capacity are often convoluted. FCs offer potentially higher densities than batteries and can be quickly recharged by refuelling, whereas batteries must be thrown away or plugged in for a time-consuming recharge [2,4].

As mentioned previously fuel cells are typically classified by their type of electrolyte used for ionic conduction. The different characteristics of other fuel cell types will not be discussed here, but for a fundamental difference which separates them from PEM fuel cell systems: majority of FC technologies require a relatively high operating temperature, although a benefit in terms of cooling system designs but a major disadvantage because of requiring a pre-heating of the cell before operation. However, the PEM fuel cell systems require no warm up time and power is generated immediately.

2.3 Basic Operation of PEM FC and Typical Cell Construction:

A fuel cell generates electrical power by continuously converting the chemical energy of a fuel into electrical energy by way of an electrochemical reaction. The FC itself has no moving parts, making it a quiet and reliable source of power. FCs typically utilize hydrogen as the fuel, usually stored in tanks and oxygen as the oxidant which can be stored in tanks or consumed directly from the air in the electrochemical reaction. The reaction results in electricity, and by-products of water vapour and heat. The electrochemical reaction equations are given by:

Anode reaction: $2H_2 \Rightarrow 4H^+ + 4e^-$ {2.1}

Cathode reaction: $O_2 + 4H^+ + 4e^- \Rightarrow 2H_2O$ {2.2}

The whole reaction ends up looking like this:

$$2H_2 + O_2 => 2H_2O + \text{heat} + \text{electricity} \qquad \{2.3\}$$

Where: {2.1} equation gives the amount of hydrogen required to be fed to the anode to meet a load; {2.2} equation gives amount of oxygen required to be fed to cathode to maintain reaction, while equation {2.3} gives the amount of water produced. Because the fuel is converted directly to electricity, a FC can operate at much higher efficiencies than internal combustion engines, extracting more electricity from the same amount of fuel.

When hydrogen gas is introduced into the system as shown in the typical construction of a PEM FC Figure 2.1, the catalyst surface of the membrane splits hydrogen gas molecules into protons and electrons. The protons (H^+) pass through the membrane to react with oxygen in the air (forming water). The electrons (e^+), which cannot pass through the membrane, must travel around it, thus creating the source of DC electricity. Individual FC can then be combined into a FC "stack". The number of FCs in the stack determines the total voltage, and the surface area of each cell determines the total current. Multiplying the voltage by the current yields the total electrical power generated [5].

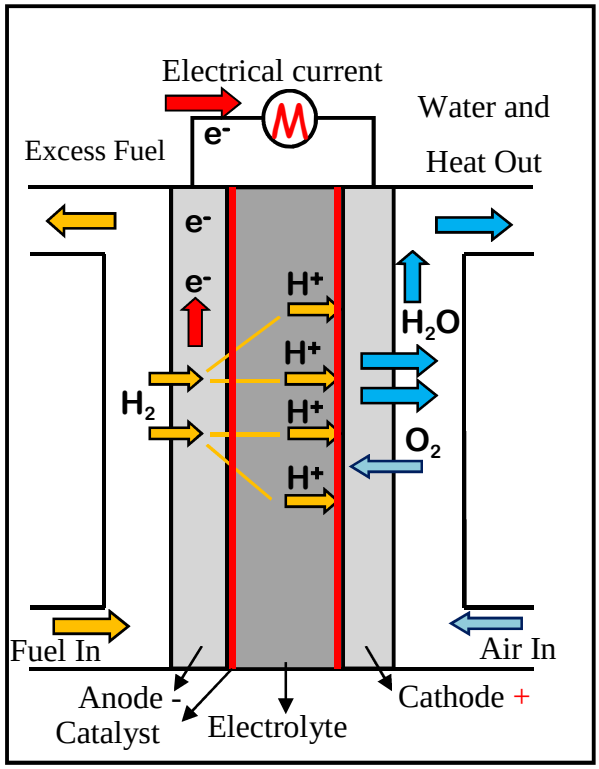

Figure 2.1 PEM Proton exchange membrane [5]

The power and energy is the same as that for any electrical system.

$$Power = VI \quad \text{and} \quad Energy = Power * t = VIt \qquad \{2.4\}$$

where V is the voltage, I is the current and t is the time.

2.3.1 Membrane

The membrane has to achieve three different functions: separation of the gaseous reactants, electrical insulation and proton conduction. It is a film made of solid polymer electrolyte. The most commonly used material for PEM FC membranes is Nafion® (DuPont), a sulfonated polymer based on a polytetrafluoroethylene (PTFE) backbone, originally developed as a Na^+ conductor for the Chloralkali electrolysis. Alternative materials include radiation grafted polymer electrolytes, which are produced by grafting side chains on commercially available polymer films ($e.g. FEP, ETFE$) and consequently sulfonating them [6].

A characteristic of the polymer electrolyte membrane is that their dimensions increase as they swell with water.

2.3.2 Catalyst Layer

The catalyst layer includes the catalyst particles themselves such as Platinum nanoparticles, which are typically supported on carbon particles. This carbon supported catalyst is mixed with a proton conducting ionomer – normally, the same polymer electrolyte as used for the membrane – in order for the protons to have access to the catalyst particles which are not in direct contact with the membrane. The presence of carbon particles in the catalyst layer makes it electrically conducting, and some porosity is present in order to bring access to the gaseous reactants.

2.3.3 Gas Diffusion Layer

The gas diffusion layer (GDL) is a porous layer made of carbon fibers, carbon binder particles, and optionally, hydrophobic material such as PTFE. Its occupations are to bring access to the gaseous reactant to the areas that are under the lands of the flow field, and to make electrical contact with the areas which are under the gas channels. The gas diffusion

layers are commonly compressible; furthermore they provide a damping of the mechanical changes induced by the swelling of the membrane.

State-of-the-art gas diffusion layers typically include a layer made of fine carbon particles mixed with hydrophobic PTFE particles, a micro-porous layer (MPL).

2.3.4 Flow Field Plates

The flow field plates have channels that ensure the circulated gases are distributed over the whole active area of the cell. The flow field plate also acts as a current collector. When a complete fuel cells stack is realized, the most common choice for technical devices, a single component could include the anode side flow field of the adjacent cell and the cathode side flow field of a cell. In this case, the flow field plates are referred to as separators or bipolar plates.

Flow field plates might be realized in metals such as aluminium, or stainless steel. Due to the higher corrosion resistance of graphite, it makes it the first option. However, metallic flow field plates have ease of manufacturing in addition to robustness but require the development of cost-effective corrosion-preventing coatings.

2.4 Thermodynamic, Reversible and Open Circuit Voltages

The thermodynamic voltage is determined based on the enthalpy of the hydrogen combustion reaction ($\Delta h_r = -285.8\ \mathrm{kJ/mol}$) and on the relation:

$$U_{th}^{0} = -\frac{\Delta h_r}{z\,F} \cong 1.48\ \mathrm{V} \qquad \{2.5\}$$

where *F* is the faraday constant ($96485\ \mathrm{A \cdot s \cdot mol^{-1}}$) and *z* is the number of electrons transferred in the reaction. This thermodynamic voltage can, according to the second law of thermodynamics, not be reached due to entropic losses. The reversible voltage is calculated in the same as the thermodynamic voltage, but based on the Gibbs free enthalpy (Δg_r)which corresponds to the enthalpy of the reaction (Δh_r) minus the losses (T) induced by the increase of entropy(Δs):

$$\Delta g_r = \Delta h_r - T \,.\, \Delta s \qquad \{2.6\}$$

For conditions related to PEM FC operation, the value of reversible voltage (U_{rev}) calculated is:

$$U_{rev} \cong 1.23\ V \qquad \{2.7\}$$

The open cell voltage, often called open circuit voltage (OCV) is the voltage that is measured when no external current is applied to the cell. The reversible voltage of $1.23\ V$ is not reached in practice, due to overvoltage losses. Typically, values from (0.95 to 1.1 V) are obtained.

2.5 Efficiency

The efficiency of a chemical process must be evaluated differently than the conventional heat engine. The theoretical efficiency of a fuel cell is only limited by entropic losses. The maximum possible efficiency of a PEM FC is therefore determined by the ratio between the standard Gibbs free energy and the reaction enthalpy.

$$\eta_{th} = \frac{\Delta G}{\Delta h_r} = \frac{-237kJ/mol}{-286kJ/mol} = 0.83 \qquad \{2.8\}$$

So the maximum thermodynamic efficiency of η_{th}= 83 %.

Due to the different overvoltage losses described in Section 5.2.2 on page 59, the efficiency will decrease significantly and the theoretical efficiency can only be achieved at small current densities. The efficiency value taking into account the influence of voltage losses is referred to as voltage efficiency η_{volt}. This value relates the actual cell voltage U_{cell} to the maximum thermodynamic value of $U_{OCV}^{th} = 1.23V$.

$$\eta_{volt} = \frac{U_{cell}}{U_{OCV}^{th}} \qquad \{2.9\}$$

Whereas η_{volt} calculates the decrease in efficiency creating from processes affecting the cell voltage. Losses related to current generation are described by the Faradaic efficiency $\eta_{Faradaic}$.

$$\eta_{Faradaic} = \frac{j}{zFv} \qquad \{2.10\}$$

(where j is the practical current density and v is the number of moles reacting per unit time); as well as the overvoltage losses described in Equations {2.8} and {2.9} and the unreacted fuel supplied γ_{fuel} must be taken into account. Consequently, the overall fuel cell efficiency can be calculated as

$$\eta_{\text{tot}} = \eta_{\text{th}} \cdot \eta_{\text{volt}} \cdot \eta_{\text{Faradaic}} \cdot \gamma_{fuel} \qquad \{2.11\}$$

Due to the several sources of energy loss, actual fuel cell efficiency is considerably lower than the thermodynamic value of 83%. Application under relevant operating conditions, the efficiency of a single fuel cell can reach values of more than 60%. As a result of the additional power consumption of the auxiliary subsystems, the efficiency of fuel cell systems normally ranges between (40 - 50%) [7, 8].

Figure 2.2 shows the net system efficiency and power output as a function of current for the 1.2kW Nexa^{MT} power module PEM FC that will be used in this work for experimental validation. The plot represents the FC operating in its normal range, as shown by the near linear curves. As can be seen from the figure, the FC efficiency decreases significantly as the output power increases. The efficiency drops from 52% at about 8 Amps to 38% at 46 Amps.

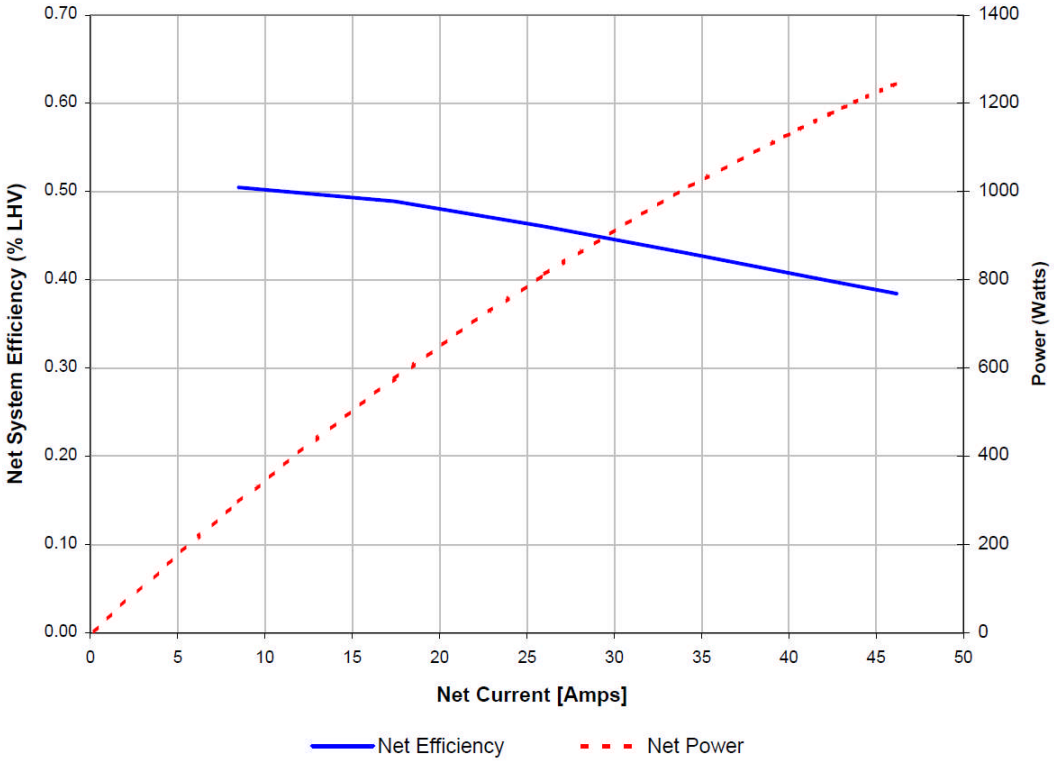

Figure 2.2 Nexa power module efficiency and power as a function of current

2.6 Fuel Cell Types

The FC usually classified by their operating temperature and by the type of electrolyte they use. Fuel cell types and their half-cell reactions are shown in Table 1-1. [9,10]. In this section of this thesis the main types of FC are summarised:

2.6.1 Low Temperature

There are two types of fuel cell classified under low operating temperature:

Proton exchange membrane fuel cell: PEM FCs are believed to be the best type of FC for use as a power source for vehicles to eventually replace the gasoline and diesel internal combustion engines. PEM FC delivers a high power density at low operating temperature (ranging from 60 - 80 C^{o}). As mentioned previously there is no warm up time required and power is generated immediately.

Other advantages are related to the electrolyte being a solid material, compared to a liquid electrolyte. The sealing of the anode and cathode gases is simpler with a solid electrolyte, and therefore, less expensive to manufacture. The solid electrolyte is also more immune to difficulties with orientation and has fewer problems with corrosion, compared to many of the other electrolytes, thus leading to a longer cell and stack life. In addition, has low weight and volume compared with other FCs. One of the disadvantages of the PEM FC for some applications is that the operating temperature is low. Temperatures are not high enough to perform useful cogeneration. Also, since the electrolyte is required to be saturated with water to operate optimally, careful control of the moisture of the anode and cathode streams is important.

FC powered vehicles are the most promising application of PEMFC systems. McNicol, et al.[11] reported that FCV can successfully contend against conventional internal combustion engine vehicles. Yet, the cost for FCV is greater than that for internal combustion engine vehicles as well as the total cost of car using the PEMFC system is about 10 times compared with the conventional internal combustion car engine, which cost around $500–600 \$/kW$. The total cost of the PEMFCs includes the costs of platinum electrode, assembly process, membrane, peripherals and bipolar plate [12].

Table 2-1 Fuel cell types and their half-cell

FC type	**PEMFC**	**AFC**	**PAFC**	**MCFC**	**SOFC**
Electrolyte	Proton exchange membrane	KOH	Phosphoric acid		Solid oxide
Operating temperature	50-100 C^{o}	120-250 C^{o}	≈ 220 C^{o}	≈ 650 C^{o}	≈ 1000 C^{o}
Fuel	H_2	pure H2	H_2	H_2, CO, CH_4	H_2, CO, CH_4
Catalyst	Pt	Pt, Ag	Pt	Ni	Perovskite
Electric efficiency	35-45 %	35-55 %	40 %	>50 %	>50 %
Power range	5-250 kW	<5 kW	≈ 200 kW	200 kW-MW	2 kW-MW
Application	Automotive and portable	Military, space		Combined heat and power generation	
Anode reaction	H_2 ↓ $2\,H^+ + 2\,e^-$	$H_2 + 2\,OH^-$ ↓ $2\,H_2O + 2e^-$	H_2 ↓ $2\,H^+ + 2\,e^-$	$H_2 + CO_3^{2-}$ ↓ $H_2O + CO_2 + 2e^-$	$H_2 + O^{2-}$ ↓ $H_2O + 2e^-$
Ionic charge carrier	H^+	OH^-	H^+	CO_3^{2-}	O^{2-}
Cathode reaction	$\frac{1}{2}\,O_2 + 2\,H^+ + 2\,e^-$ ↓ H_2O	$\frac{1}{2}\,O_2 + 2\,H_2O + 2e^-$ ↓ $2\,OH^-$	$\frac{1}{2}\,O_2 + 2\,H^+ + 2\,e^-$ ↓ H_2O	$\frac{1}{2}\,O_2 + CO_2 + 2\,e^-$ ↓ CO_3^{2-}	$\frac{1}{2}\,O_2 + 2\,e^-$ ↓ O^{2-}

Direct methanol fuel cell (**DMFC**)**:** DMFC is another category of PEMFCs. It is a suitable source of power for portable applications due to long lifetime, low temperature operation, and they do not need to be recharged. In addition, they are fast refuelling system characteristics. Energy source of the DMFC systems is methanol, at anode, methanol is reformed into carbon dioxide (CO_2); while at cathode water or steam is formed using oxygen existing in the air. Their reactions shown in equations {2.12} and {2.13}:

$$Anode \qquad CH_3OH + H_2O \rightarrow CO_2 + 6H^+ + +6e^- \qquad \{2.12\}$$

$$Cathode \qquad (3/2)O_2 + 6e^- + 6H^+ \rightarrow 3H_2O \qquad \{2.13\}$$

Methanol is utilized in DMFCs in form of liquid or vapour. Vapour feed is more required than liquid feed in term of power density and cell voltage. Methanol requires high localised cooling at anode. In addition, the extent of methanol crossover from anode to cathode and gas release at the electro catalyst surface significantly influences the performance of liquid feed cells [13]. From the other point of view, vapour feed cells also have some disadvantages such as high temperature required for fuel vaporisation, less lifetime. Hence, more costly and complex reformer is needed. PEM is considered as the main part in DMFCs to provide high proton conductivity. Furthermore, it offers chemical stability for suitable high performance of DMFC.

2.6.2 Medium/High Temperature

Alkaline (**AFC**)**:** The AFC is very susceptible to contamination, so it requires pure hydrogen and oxygen. It is also very expensive, so this type of FC is unlikely to be commercialized in the near future. However, AFC has a good history in the space program. It is still utilised in the space shuttle in an expensive guise, providing electricity for the on-board systems by combining the pure hydrogen and oxygen stored in the rocket-fuelling system. NASA has first used AFCs to power the shuttle missions and supply drinking water for space applications. Nowadays, they are employed in trucks, forklift, boats, submarines and niche transportation applications [13]. Several catalysts can be used in this fuel cell, e.g. one whose electrolyte is concentrated ($35 - 50\ wt\%$) potassium hydroxide (KOH), operated at less than 120^0C and the other whose electrolyte is more concentrated ($85\ wt\%$) KOH, operated at temperature of around 250^0C. Thus, the AFC operating temperature depends on make of the catalysts, which range ($120 - 250^0C$).

The electrolyte is kept in a porous matrix, and electrocatalysts consist of noble metals and nickel. There are some difficulties with this type of fuel cell and summarised as below:

- Carbon monoxide continuously found in hydrogen produced by reforming hydrocarbon or alcohol fuels, is a poison to the costly metal electrocatalysts
- Carbon dioxide in both air and fuel will react with the KOH electrolyte to produce potassium carbonate. Consequently, the AFC is limited on applications where both pure hydrogen and oxygen can be used.

2.6.3 Very High Temperature

There are three types of FC operating at very high temperature, namely Solid Oxide FC (SOFC), Molten-Carbonate FC (MCFC) and Phosphoric-Acid FC (PAFC), These FCs are best suited for large-scale stationary power generators that could provide electricity for factories or towns. These types of FC operate at very high temperatures (between 600 and 1,100 degrees Celsius), so it has a longer warm-up time. As a result they are unsuitable for use in transport applications. Their advantage is that they can generate steam that can be used to generate more power[14].

Solid Oxide Fuel Cell: this type of fuel cell is suitable for large scale distributed power generation systems with capacity of hundreds of MWs. Commonly, SOFCs are used the product heat to generate more electricity by turning gas turbines and hence increasing the combined heat and power efficiency between (70-80%). They are classified as low harmful gas (NO_X and SO_X) emissions fuel cell. SOFCs can be used as local power generation systems for country side, where there is no access to public grids. In addition, they have low maintenance costs and noise free operation. However, one of the disadvantages is that it takes long $start\text{-}up$ and $cooling\text{-}down$ times along with various chemical and mechanical compatibility issues.

Molten-Carbonate Fuel Cell: currently, MCFC systems are used for natural gas, military and industrial applications. One of most advantage is that they do not require noble metal catalysts for electrochemical reduction. Further, no infrastructure development for the installation is required. In addition, MCFC could be directly fuelled with hydrogen, carbon monoxide, natural gas and propane; on the other hand, long time is needed to generate power which is mostly related to its high operating temperature [15].

Phosphoric-Acid Fuel Cell: PAFCs does not require pure oxygen for its operation as CO_2 does not affect the cell performance or electrolyte. The initial cost of this type of fuel cells is high as it uses air with approximately 21% rather than using pure oxygen which causes three times reduction in the current density. Hence, PAFC is designed in stack bipolar plate to increase the electrode area for higher energy production, but this comes with additional cost. Recently, PAFCs are in the commercial stage with the power capacity of (200 kW-11 MW) already being tested. The PAFCs are expensive to manufacture as a result of the cost of platinum catalyst that covers the electrodes. Electrical efficiency of this type is between 40 and 50% and the combined heat and power efficiency is about 85%.

2.7 Comparison of Fuel Cell Cost with other Power Generating Systems

Currently, several different types and sizes of FCs are in operation around the world providing electricity and heat which are safe and reliable. Since 2002, the total cost of these systems has been reduced, due to fact that the demands for fuel cells are being placed by customers without the need for any financial support. In the last few years, the U.S. Department of Energy has decreased the cost of automotive fuel cells by more than 80% since 2002 from $275/kW in 2002 to $49/kW in 2011 and more than 30% since 2008. Figure 2.3 and Figure 2.4 show the fuel cell system cost and commercially available products which have been developed with fuel cell technology program funding, respectively. Based on the current projections, it is predicted that high-volume manufacturing is targeting a cost of $30/kW by 2017 [16]. Comparison of fuel cell with other power generating systems is presented in Table 2-2.

Table 2-2 Comparison of fuel cell with other power generating systems [13]

	Reciprocating engine: diesel	Turbine generator	Photovoltaic	Wind turbine	Fuel cells
Capacity range	500kW-50MW	500 kW-5 MW	1 kW-1 MW	10 kW-1 MW	200 kW-2 MW
Efficiency	35%	29-42%	6-19%	25%	40-85%
Capital cost ($/kW)	200-350	450–870	6600	1000	1500-3000
O & M* cost ($/kW)	0.005-0.015	0.005-0.0065	0.001-0.004	0.01	0.0019-0.0153

* Operations & Maintenance

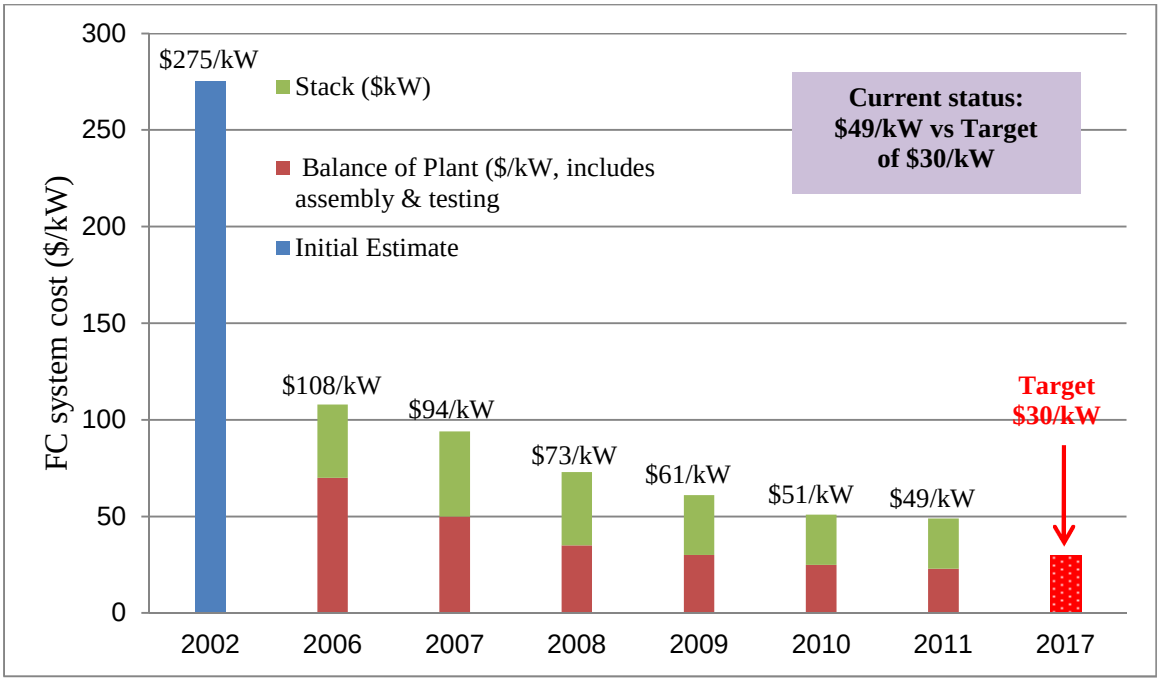

Figure 2.3 Projected transportation fuel cell system cost

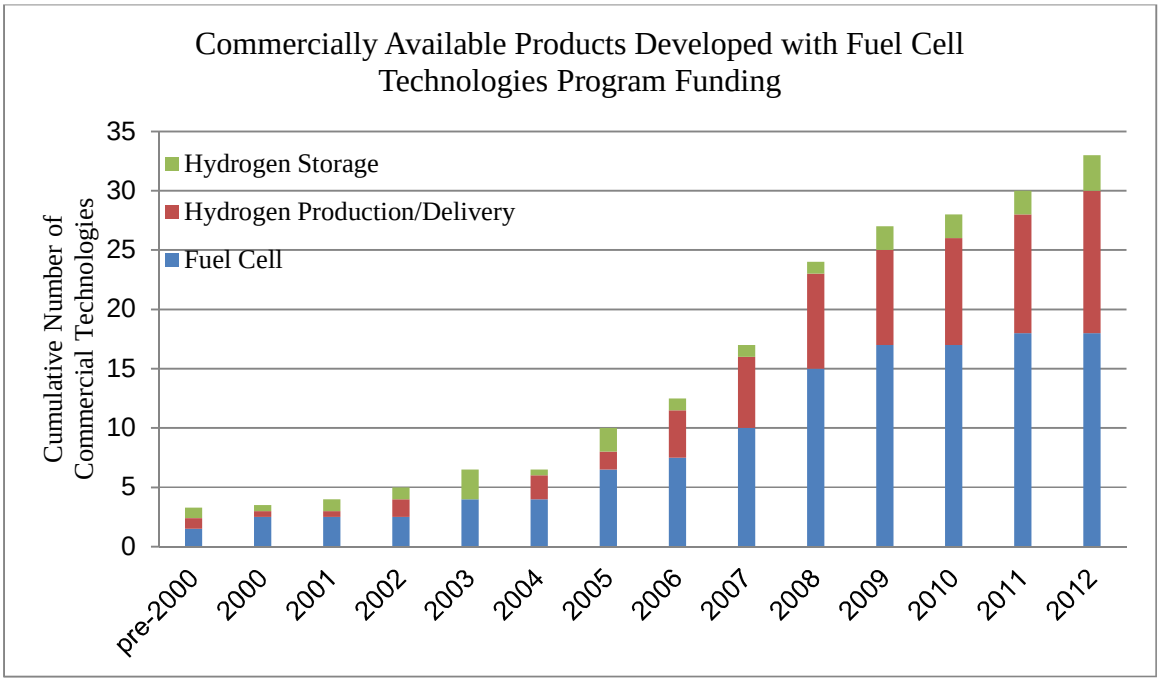

Figure 2.4 Accelerating Commercialization

2.8 Fuel Cell Applications

Earlier, the existing FC types such as SOFCs were only applied in extreme situations; since such a type of FCs required very expensive materials and due to their size could only be used for stationary applications. These problems were addressed when the PEM FC was

invented in the early 1960s by $Willard\ Thomas\ Grubb\ and\ Leonard\ Niedrach$ at General Electric. The first membrane used for electrolytes is the sulfonated polystyrene membrane which was replaced in 1966 by Nafion ionomer, that proved to be better in terms of performance and durability [17].

Generally, FC could power any device that requires electrical energy to function. This could range from a mobile phone up to a factory. In the recent years, the PEM FC is the most developed FC system due to its advantages. In this thesis a few main applications will be included. However, other applications can be found in the literature [2, 4, 7, 9] and [14] . This work will focus on the following main applications:

2.8.1 Transportation Applications

Fuel cell could be applied in large aircraft to power the auxiliary power units APU. FC based auxiliary power units are a promising alternative to conventional motor/generator based technologies. $FC\ APUs$ promise slightly higher efficiencies with significantly reduced emissions and lower noise generation. The system efficiency remains almost constant even at operation down to less than 50% of full capacity.

Another interesting feature of $FC\ APUs$ is that the water produced in the FC can be used in other parts of the system, e.g. Airbus for the first time on a civil aircraft has successfully tested a FCs in flight. $PEM\ FCs$ powered the aircraft's back-up hydraulic and electric power systems (shown in Figure 2.5) The test conducted in February 2008 is part of Airbus' overall plans for an eco-efficient aviation industry. It supports the on-going research to evaluate the potential use and environmental benefits of FC technology and zero emissions power generation in civil aviation.

During the test, the $H_2\ and\ O_2$ based FC system generated up to 20kW of electrical power. The emission free FC system generates water as a "waste" product. The FC system powered the aircraft's electric motor pump and the back-up hydraulic circuit and also operated the aircraft's ailerons.

The system's robustness was confirmed at high gravity loads ($"g"\ loads$) during turns and zero gravity aircraft manoeuvres. During the flight test, the FCs produced around 10 litters of pure water that could be used for the aircraft water and waste systems, making the aircraft lighter and thus increasing the aircraft’s fuel efficiency.

This achievement will enable Airbus and its partners to further develop ways to implement FC technology for replacing other aircraft systems such as the emergency power systems and the APU. Reducing significantly the noise and emission levels in and around airports [18].

Figure 2.5 Airbus powered the back-up hydraulic & electric power systems by PEMFC[18]

Fuel cell could be also used to power aircraft as main power source. FC could power an unmanned and a manned aircraft by using FC hybrid system to power an electric motor. On 28 March, 2007 a manned airplane powered only by a FC and lightweight batteries is shown in Figure 2.6. The systems integration phase of the Boeing Research and Technology Europe ($BR\&TE$) FC Demonstrator Airplane research project was completed including systems integration.

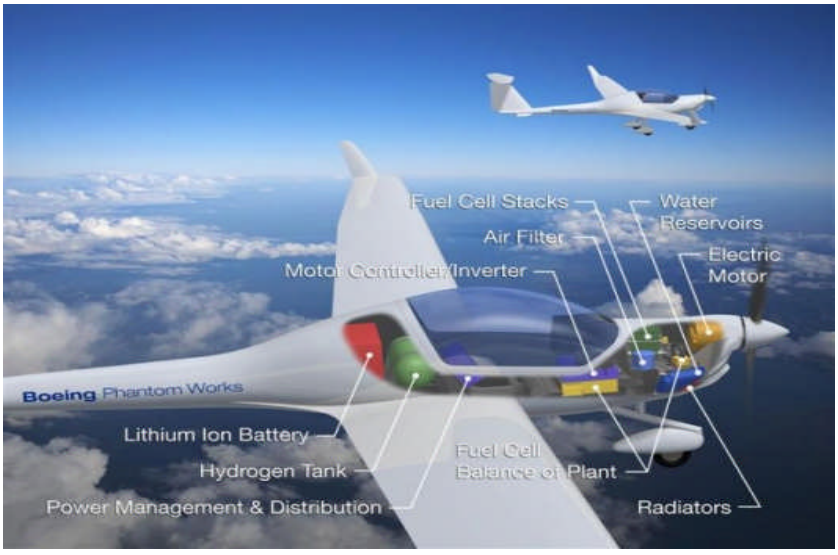

Figure 2.6 Boeing Madrid, Spain, April 03, 2008[19]

Boeing successfully for the first time in aviation history flown a manned airplane powered by $PEM\ FCs$ on 3rd April 2008 over Madrid, Spain. A two-seat Dimona motor-glider with a 16.3 meter (53.5 foot) wingspan was used as the airframe. Built by Diamond Aircraft Industries of Austria, it was modified by BR&TE to include a $PEMFC$ /$lithium\text{-}ion$ battery hybrid system to power an electric motor coupled to a conventional propeller. During the flights, the pilot of the experimental airplane climbed to an altitude of 1,000m above sea level using a combination of battery power and power generated by hydrogen FCs. Then, after reaching the cruise altitude and disconnecting the batteries, the pilot flew straight and level at a cruising speed of 100 km/h for approximately 20 minutes on power only generated by the FCs [19].

2.8.2 Ground Vehicles

FC can be also used in transportation sector as main power source to power electrical motor rather than internal combustion engines; FCs can be 2 to 3 times more efficient than diesel or gasoline internal combustion engines. Those FCvs can be powered by PEM FCs that range in power ≈ 70 - 200kW. Another reason to attract the world to FC is the fact that transportation sector is responsible for over 30% of global NO_x emissions, 23% CO_2 emissions and 18% of CO emissions.

Currently, most of the car manufacturers have made at least one vehicle using fuel cells. Many of the car manufacturers have selected to feed the FC with methanol, some have chosen to use pure hydrogen.

Since 1994, Daimler-Benz working in collaboration with Ballard, built a series of PEMFC powered cars. The first one was fuelled with hydrogen, and in 1997 Daimler-Benz produced a methanol fuelled car range of a 640 km [20].

In 1996, Toyota released a fuel cell/battery hybrid passenger car fed with hydrogen, later on in 1997 followed by a methanol-fuelled car. Toyota announced that the plan to sell a FCVs in 2015, which would make it a leader in a technology that most other automakers regard as at about 10 years ago from being marketable [21]

Some other car manufacturers BMW, Citroën, Peugeot, Renault, General Motors, Volvo, Volkswagen Honda, Chrysler, Ford, and Nissan have also built PEM FC cars operating on hydrogen or methanol. In 1993, Ballard Power Systems demonstrated a 10 m bus with a 120

kW FCs, then in 1995 it was followed by another 200 kW, 12 m heavy-duty transit. These buses operate on compressed hydrogen as fuel [20].

Currently hydrogen FCVs are more expensive than the traditional internal combustion engine vehicles. Many car manufacturers suggested that they are confident that their current R&D programs should be able to bring the cost of production down to few hundred dollars per kW in few years [22].

2.8.3 Stationary Application

FC can be used as a stationary backup power supply, to generate power for remote location or even as a primary power station. There is a high worldwide trend to use variety of renewable power generation and limit the impact on worldwide carbon emissions globally. Stationary FCs such as $PEMFC$, $MCFC$ and $SOFC$ can be used to generate electricity and can range in size from 1 kW to 10 MW [17]. In general, system efficiency can be improved from 40-50% to reach up to 90% when cogeneration or waste heat generation is used in a combined heat and power system.

Residential combined heat and power units have been deployed widely around the world. The Octagon building on Roosevelt Island in New York become the first residential building in the State of New York to be powered and heated by a PAFC 400 kW fuel cell from A United Technologies Company Power. Japan also in 2010 deployed more than $10,000$ units providing home power and heating. South Korea has also deployed combined heat and power units for residential use. These units can be used to provide grid expansion and also for areas where there is no infrastructure or low grid [16].

2.9 Summary of Chapter 1

This chapter presented a review of different fuel cell technologies and their working principle covering low temperature FC such as PEM and methanol; medium/high temperature such as Alkaline and the very high temperature FC such as Solid Oxide, Molten-Carbonate and Phosphoric-Acid. Examples of fuel cell application for transportation (including aerospace), stationary application were also covered. Finally, some examples of recent development and large scale demonstrations were also discussed.

The main findings of this chapter can be summarised as follows:

At present the cost of FCs is higher than that of similar, already existing products, mostly because of small scale production and the hydrogen issue.

In the transportation sector one approach would be to obtain the on-board hydrogen by reforming an alternative fuel. However, this will limit the flexibility of the fuel source. Hence a better method would be the direct storage of hydrogen on-board.

The costs related to FCs could drop significantly in the future if there is an increase in applications that uses FC and the development of better hydrogen fuel storage approach coupled with handling technologies.

The main points from this chapter can be summarised as follows:

- A review covering fuel cell technologies, their advantage and disadvantage and examples of varies applications and their suitability

- A summary of the basics of Proton Exchange Membrane Fuel Cells PEM FCs technology was given, including the explanation of the working principle and the main construction elements.

- A review of the loss mechanisms which determine the maximal cell performance was also presented and will be explained in more details in chapter 5

- A summary of the different types of fuel cell, fuel cell advantages and disadvantages when compared to other power techniques and their application was also covered.

Chapter 3

Hardware Description and Set-Up

3. HARDWARE DESCRIPTION AND SET-UP

This chapter will introduce the different hybrid system types/configuration for fuel cell and auxiliary storage system. Then will cover the experimental set-up configuration developed in this project and the integration challenges that arose during the construction of the hybrid system. In addition, details of the system components will also be covered in this chapter.

3.1 Hybrid System

As stated earlier, this thesis will focus on electric hybrid systems in which all the power sources have an electrochemical basis and no conventional energy sources are involved. Generally any electrical or mechanical system driveline that includes other sources, energy storage and energy converters is called a hybrid system. Combining the FC with an Energy Storage Systems (ESS) in a hybrid system allows for much higher peak power while preserving the high energy density to meet the requirements of these applications. There are also many other benefits of hybridising:

- ESS can be used to supply high transient energy and thus greatly improve system dynamics
- Components can be made to operate in region of higher efficiency since neither one would have to provide the full load and capacity
- ESS can provide power to the FC's auxiliary equipment for start-up and also supply load demand while the FC is warming up
- Components can be of smaller dimensions, particularly the FC, which is the most expensive component
- ESS can condition power output from FC to provide acceptable voltage, improved reliability and extending lifetime of the components

Indeed, repetitive stepped loads lead to lifetime degradation of the FC if not supplemented by an ESS. The ESS may now supply the transient power and enable the FC to more slowly

adjust to the new power levels or operate under nearly steady state conditions. The first benefit also leads to improved power quality of the system, since a rapid increase in load demand could not be handled by the FC or would result in a significant drop in its output voltage, which may even cause shutdown of the system. Thus, it is clear that the hybrid system brings about 'synergistic' benefits where the whole is greater than the sum of its parts [23].

Generally, there are two configurations of the hybrid systems:

3.1.1 Passive Hybrid System

When the hybrid configuration is simply formed by connecting the FC and ESS straight to the load, then we refer to that system as a passive hybrid system, as shown in Figure 3.1. In contrast to simply having a single power source by itself, for instance either the FC or ESS, such a 'passive' hybrid demonstrates a longer run-time and higher power capability. It also decreases the stress on the FC and accordingly conditions the hybrid source terminal voltage. However, there are also a number of disadvantages associated with such a hybrid configuration:

- The ESS terminal voltage must match the nominal voltage of the FC in order not to overcharge the battery, therefore greatly limiting much of the system's design flexibility.

- Since the power distribution between the FC and ESS is passively determined by the impedance characteristics of each source and is thus determined in a rather fixed way, the hybrid system performance may be unnecessarily limited by one of those two components. For example, the peak power capability of the hybrid may be restricted by the FC when the FC first reaches its safe power limit even while the output power of the battery is still well below its maximum.

These disadvantages can be eliminated by introducing a DC/DC converter between the FC and ESS, creating an 'actively' controlled hybrid system. In active hybrids, the power converter is controlled to regulate the power sharing between the FC and ESS in order to maximize the advantages of each component. For example, the FC and ESS can be controlled to generate the maximum power from each simultaneously, thereby greatly increasing the peak power capability beyond that achievable by a passive hybrid, without much increase to

the system weight and volume [24, 25]. Similarly, the active hybrid can be controlled such that the sources operate in their most efficient region, thereby also increasing the system's efficiency. Furthermore, the presence of a power converter at the FC output is essential to obtain bus regulation due to the FC's wide output variation, and more importantly to provide the necessary protection to the FC as discussed. It also allows more flexibility in the system design, as the ESS terminal voltage no longer must match the FC's nominal voltage.

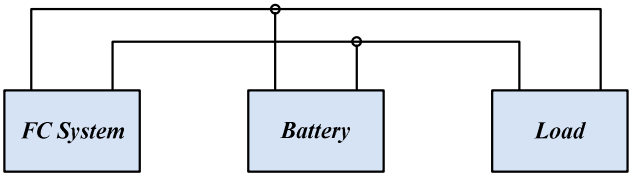

Figure 3.1 Passive hybrid systems

3.1.2 Active Hybrid System

As an alternative to the passive hybrid system, a DC/DC bidirectional converter could be placed between the battery and the fuel cell [26]. In this active hybrid system the load is connected to the battery as an auxiliary source to supply the high transient energy through a DC/DC bidirectional converter while the FC is connected to both the load and the battery through the DC/DC step down converter, as shown in Figure 3.2. The battery provides additional power when a higher power is requested by the load or during a step load change while the FC rises up to the required level. The power flows unidirectional through the converter stage from the FC to the battery and load. Controlling the DC/DC bidirectional converter can change the output current of the FC, as well as the current supplied by the battery.

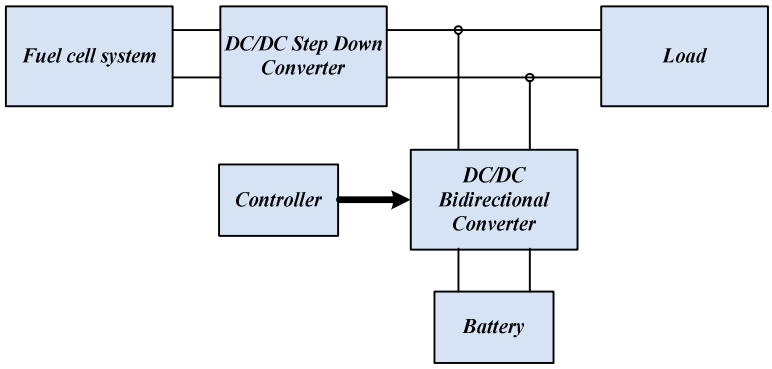

Figure 3.2 Active hybrid configuration

The active hybrid system could be configured in two possible ways, depending on the location of the separate components. In both configurations, the power shared by each source could then be actively controlled. Yet, in one configuration, control of the power converter in

such systems becomes a very complicated; while in the other, the control is being only a problem of the current or voltage regulator, which is less complicated[27; 28]. The active hybrid configuration shown in Figure 3.2 was chosen for this research project due to the fact that this configuration simplifies the hybrid system design and control.

3.1.3 Energy Storage Systems

An auxiliary source to supply or absorb the high transient energy is required to complement the slower output power of the FC. There are many possible power sources to back-up the FC for the transient loads, for instance the super-capacitor, the battery and flywheel. In this thesis, the battery was chosen.

The pros and cons of each are listed in Table 3-1, below;

Table 3-1 Pros and cons of Energy Storage Systems

No	*ESS*	*Pros*	*Cons*
1	*Flywheel*	*Very fast response*	*Little modularity*
		Reduced system complexity	*Low specific energy*
		Minimal maintenance	*Less technologically mature*
		High efficiency	
		High specific power	
2	*Super Capacitor*	*Very fast response*	*Low specific energy*
		High life cycles	
		Low maintenance	
		High specific power	
3	*Battery*	*Modular*	*Reduced life cycles*
		Fast time response	*High maintenance*
		High specific energy	

Hybrids containing both super capacitors/ultra-capacitors (UC) and batteries are common, and the former's fast response and high number of charge-discharge cycles versus the latter's high specific energy is typically the determining factor for the feasibility of their use in a

particular application [25]. In this project WP18-12 lead acid battery was selected to act as the additional source.

3.2 Hybrid System Experimental Set-up

This sub-section will briefly describe each individual component of the hybrid system. Besides the 1.2kW PEM fuel cell Nexa^{MT} power module, there are other main components that form the Fuel cell hybrid system. The FC Nexa module is considered as the main power source, then two WP18-12 (12 VDC) batteries for starting up the system, DC/DC step-down converter to keep the output voltage constant and control unit. These form only the Nexa module as highlighted in Figure 3.3. This was the initial set-up which was used to validate the fuel cell stack model. The system was connected to an electronic load to simulate the various load demands.

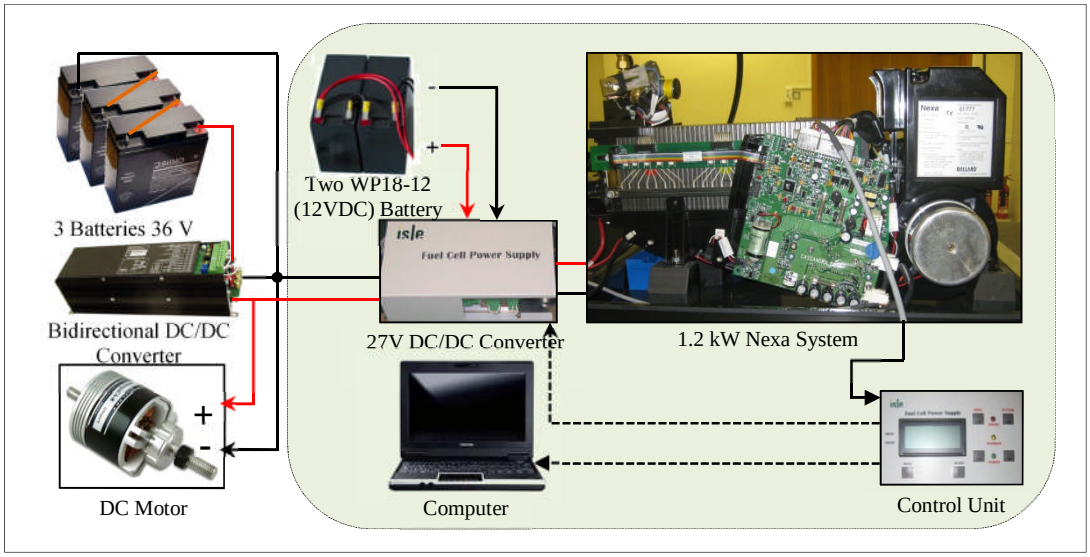

Figure 3.3 Hybrid system experiment set up

This original configuration was then extended by adding another 3 WP18-12 (12 VDC) batteries connected in series as the input to the high voltage terminal of the bidirectional DC/DC converter. The use of the bidirectional converter gives the possibility of charge/discharge the batteries. The extended part is connected in parallel with the main power source to the load as shown in Figure 3.3. The purpose of using a 36 V lead-acid battery is to provide additional power during high power demands. Otherwise the battery pack is either charged by the fuel cell or goes into standby stage when there is a minimum power demand. The complete system was simulated under various operating conditions. Modeling of the

battery, electrical engine and Piper Cub J3 is presented in this chapter and the simulation results are presented in chapter 6.

Two control loops included in the system are governing the delivered power of each source and ensure all the components work within their bounds. The control strategy will be discussed in more details in chapter 6.

3.2.1 Nexa Fuel Cell Power Module Set-up

Nexa (1.2kW) $PEM\ FC$ module consist of a Ballard stack with 46 cells set in series and other auxiliary subsystems including hydrogen system, oxidant air system, cooling system, electronic control system and safety system with sensors and microprocessors integrated on board. The schematic diagram of this FC system is shown in Figure 3.4.

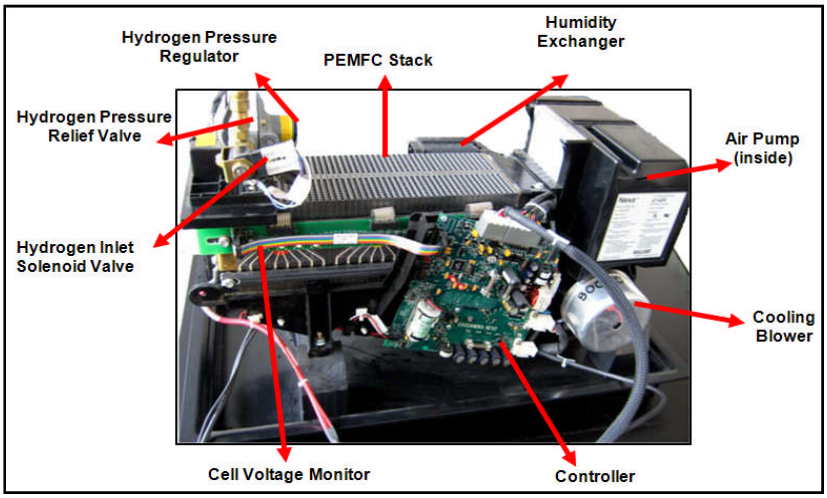

Figure 3.4 Nexa™ system schematic

The dry hydrogen is supplied by high-pressure hydrogen cylinder, while the oxidant air is supplied by an air pump and humidified in a humidity exchanger before entering the FC stack so as to maintain water saturation of the membrane. A cooling fan at the base of the unit is utilised to blow air through vertical cooling channels. A multi-functional data acquisition (DAQ) unit is supplied facilitating status monitoring and data recording. Feedback signals as well as operating parameters (e.g. temperature, pressure, flow rate, gas concentration, current, and voltage) can be measured through the serial port communication. All the information is displayed in real-time using a Lab-View GUI software interface. Lastly, the system is connected to an electronic load to simulate a variable power demand. The Nexa power module specifications are included in Appendix 9.1.

For safety considerations, the Nexa power module FC system was installed in a well-ventilated lab area equipped with an extractor fan located on top of the system for air circulation. The extractor fan is fitted with a hydrogen alarm sensor for health and safety reasons. In addition, the hydrogen cylinder was located outside the lab in a specifically designated storage area. FC operating parameters are continuously monitored to ensure they stay within desired limits (FC stack operating temperature, FC stack current, output voltage and fuel supply pressure). Warnings and shut down alarms are implemented on each of these parameters. Figure 3.5 shows a general view of the setup used in the experimentation of the fuel cell hybrid system at Cranfield University (different angle of view).

The basic installation of a $Nexa^{TM}$ *power module* in the lab and the electrical, mechanical and software interfaces necessary for operation can be found in Appendix 9.5. The system sub-components and the hardware implementation will be presented in the following subsections.

Figure 3.5 Experimental setup general view at Cranfield University

3.2.2 Battery Model

Conveniently, the batteries sit between fuel cells and load, with intermediate specific energy and specific power values. Batteries store the electrical energy as chemical energy and convert it back when needed. Depending on the chemistry used, battery pack is capable of discharging between 45 minutes to 18 hours.

In the simulation model of the hybrid system, the battery pack consisting three batteries was modelled as back up. The specifications of the WP18-12 lead acid battery were programmed into the battery block in SimPowerSystems toolbox. Specifications of the battery can be found in Appendix 9.6.

3.2.3 Electrical Engine Model

The electrical engine specification for "Dualsky XM5050CA DC" was selected to drive the small aircraft (the Piper Cub J3). The selected engine as shown in Figure 3.6 was tested at different throttle command inputs. In the hybrid system, this engine is represented by electronic load; hence, the electrical motor of the Dualsky XM5050CA DC was tested practically in order to obtain the current, voltage and RPM data for various power demands from the Nexa FC system. This test was carried-out as shown schematically again in Figure 3.6. Engine test experimental results and specification can be found in Appendix 9.8 and 9.10, respectively.

Figure 3.6 Dualsky XM5050CA DC Engine

3.2.4 Current Sensor Technology

The current sensor technology works on the principle of Hall Effect which is an application of electromagnetic induction. Consider a simple rectangular plate of conducting material carrying a steady current from left to right as shown in Figure 3.7 (a). There is no measurable voltage in either direction perpendicular to the flow. Now apply a magnetic field

perpendicular to the flow. It is found that a voltage will be generated perpendicular to both the direction of the current and the magnetic field. The presence of the magnetic field distorts the electron flow which becomes uneven and creates a potential difference across the plate's faces as shown in Figure 3.7 (b) [29].

Figure 3.8 shows a typical voltage biased Hall Effect current sensor. The Hall voltage is a low level signal typically of about 30 *microvolt* in a magnetic field of *one gauss*. This low magnitude signal requires a low noise, high impedance and moderate gain amplifier. Because DC currents can flow in either direction, the amplifier output can be driven either positively or negatively. If power supply gives single 5V then the signal output range will be limited between 0V and 5V. The maximum and minimum limits between which the output signal can vary are known as saturation points. Negative saturation is specified relating to ground, while positive saturation is specified as how close the output can go to the positive supply rail [29]. These conditions are illustrated in Figure 3.9.

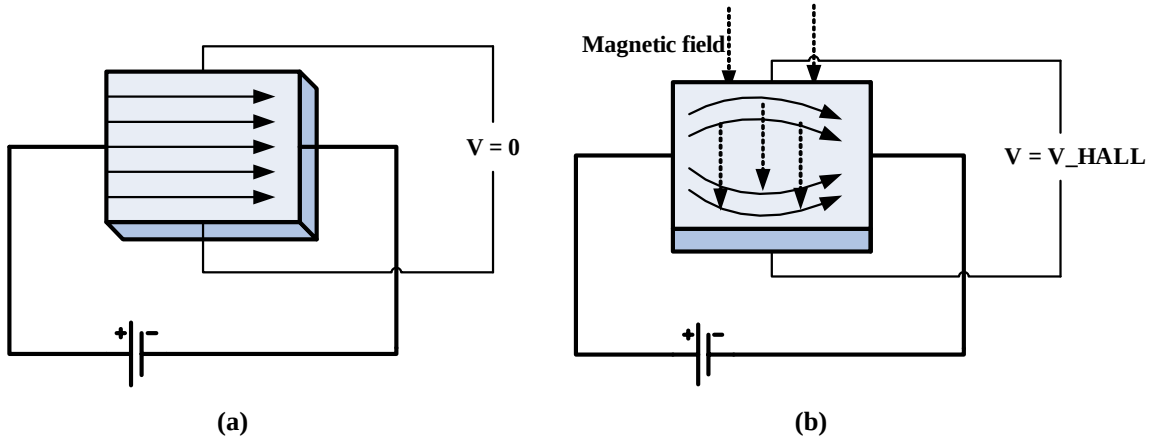

Figure 3.7 The Hall Effect in a conductive plate

(a) without applying magnetic field, (b) applying magnetic field

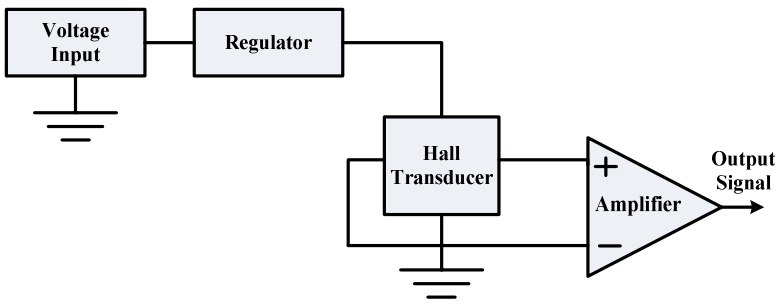

Figure 3.8 A typical voltage mode Hall Effect current sensor

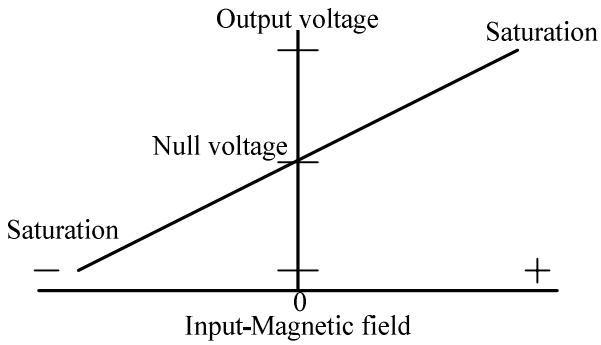

Figure 3.9 Hall Effect sensor transfer curve

In order to sense the current between the battery and the load, numerous AMP25 Linear-to-60A hall sensors from Amploc were used. Amploc current sensors provide galvanic isolation and are capable to measure dc, ac and complex waveforms. Their operating temperatures range from $-55\ C^o$ to $+\ 125\ C^o$. They are light weight, water resistant, window 0.29 inches and the terminals are gold plate (supply voltage, ground and output signal) [30], as shown in Figure 3.10. Sensors specification and electrical characteristics are listed in Table 3-2.

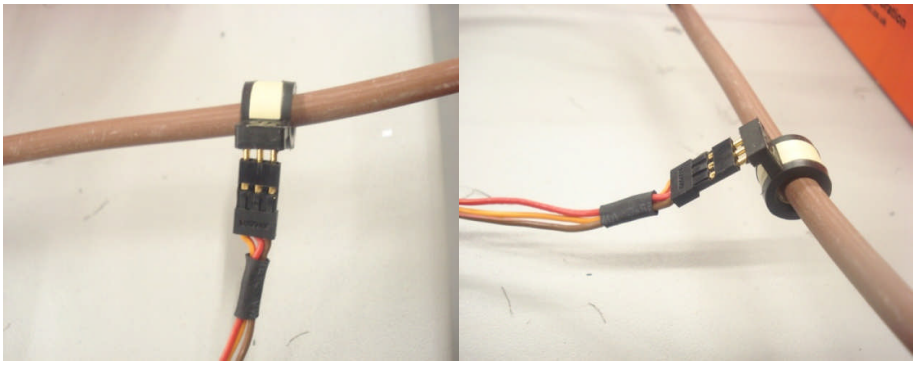

Figure 3.10 AMP25 linear-to-60A current sensor

Table 3-2 Electrical characteristics of AMP25 linear current sensor

$\boldsymbol{Supply\ voltage, V_s}$	$+4.5$ to $+$ 10VDC
$\boldsymbol{Supply\ current}$	10 mA max
$\boldsymbol{Output\ current}$	2 mA max
$\boldsymbol{Offset\ voltage, V_O\ (sensed\ I\ =\ 0A)}$	VS /2 $\pm$ 2%
$\boldsymbol{Output\ voltage, V_O\ is\ proportional\ to\ V_s}$	
$\boldsymbol{Temperature\ error\ Null\ or\ gain}$	0.3%/ 0C
$\boldsymbol{Response\ time}$	3 µ Sec
$\boldsymbol{Linearity\ (Full\ scale)}$	1 %
$\boldsymbol{Accuracy\ (Full\ scale)}$	$\pm$ 2 %
$\boldsymbol{A.C.Hysteresis\ error}$	0.5 %

3.2.5 Electronic Load

An electronic load type EL-1500 produced by Zentro Elektrik is recommended to be used for generating characteristic curves for the fuel cell systems. To add more simplicity to the hardware, this electronic load has been used as load. The characteristics of the electronic load were similar to those of the electrical engine. Specifications of the electronic load can be found in Appendix 9.8. EL-1500 has three modes of operation: constant current, constant resistance and constant power mode. It also has an $IEEE488.2/RS232/USB$ interface integrated with Lab-View driver for external programming. The current, power or resistance of the load were programmed using an external control voltage where a change in voltage from (0 - 10V) changed the set value from (0 – 100%).

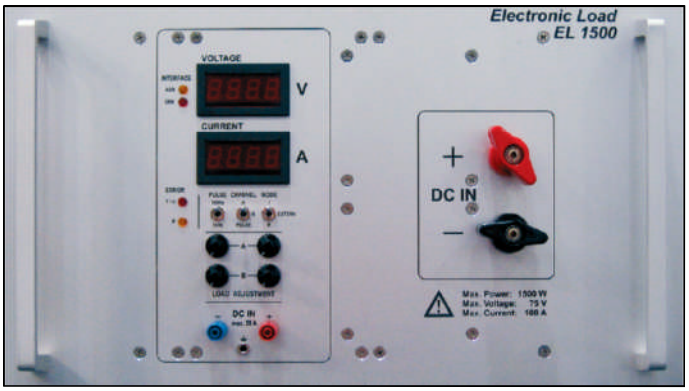

Figure 3.11 Electronic load EL- 1500

3.2.6 Data Acquisition System

The data acquisition system (DAQ) manufactured by National Instruments, high speed PCI-6259 with M-Series multifunction board has been selected and used to send/receive data between the hardware and Matlab/Simulink. Specifications of the DAQ card can be found in Appendix 9.11.

External connections were made using the National Instruments SCB-68 connector block and plug-in data acquisition device card using 68-pin connector, see Figure 3.12 (a). The SCB-68 delivers a robust and very low noise signal termination and is compatible with other National Instruments single and dual-connectors [31]. Single core wire was deemed adequate for connections between the rack and the sensors. The sampling time rate was 3.3Hz.

However, the $SCB-68$ rack can accept only voltage levels below 10V, so a step down voltage divider was used for voltages above 10V, these included the FC voltage, battery

voltage and bus voltage. The software was then used to scale the readings back. Figure 3.12 (b) shows the voltage divider circuit, its reference to ground is formed by connecting two resistors R_1 and R_2 in series ($R_1 = 100K\Omega$ *and* $R_2 = 27\ K\Omega$). By applying Ohm's law: $V_{in} = \ I * (R_1 + R_2), V_{out} = \ I * R_2$ and $I = \frac{V_{in}}{R_1 + R_2}$, so the output voltage can be found by using following equation:

$$V_{out} = \frac{R_2}{R_1 + R_2} * V_{in} \qquad \{3.1\}$$

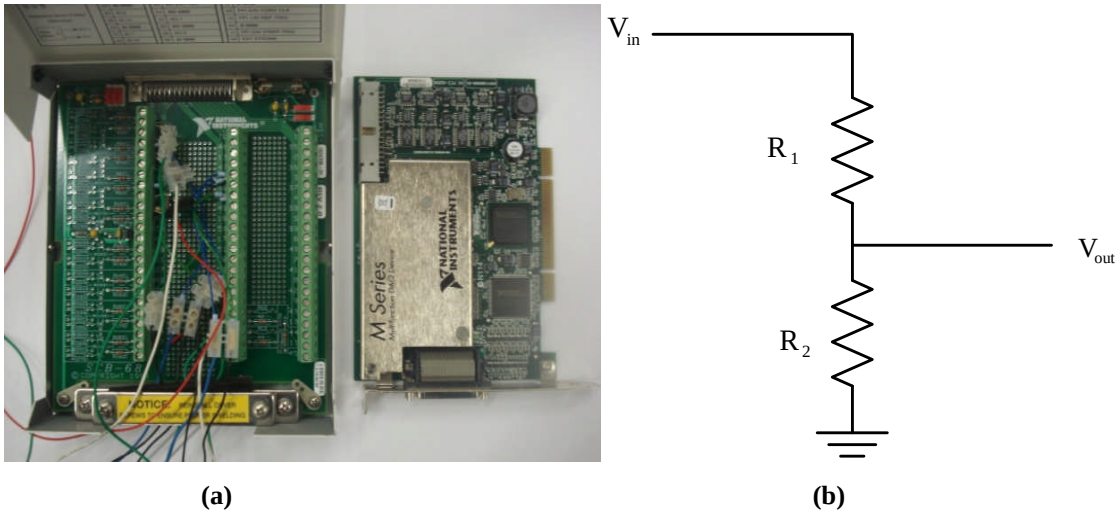

(a) **(b)**

Figure 3.12 (a) DAQ card in the right side of the picture and NI SCB-68 connector block in the left side of picture, (b) Voltage divider circuit

3.2.7 DC/DC Unidirectional Converter

DC/DC converter BSZ PG 1200 model produced by Isle® especially for Nexa FCs is used as a unidirectional converter with control unit which consists of Nexa On/Off buttons, DC/DC and Nexa parameter buttons, a 4-line LCD and 3 LED display as shown in Figure 3.13. The DC/DC converter generates a PWM signal that controls a MOSFET half-bridge. This half-bridge acts as a synchronous step down converter. This topology guarantees the high efficiency of the converter. DC power input is heavily filtered so that electromagnetic interference EMI does not affect the FC. The output voltage is filtered before going out to the load terminals. In order to avoid back flow of current from battery to fuel cell, a return protection is provided, controlled by an integrated micro controller. The converter's specifications are listed in Table 3-3.

Table 3-3 DC/DC converter specification

Output voltage range	11V-15V / 22V-30V
Output voltage range	11V-15V / 22V-30V
Accuracy of output voltage	2%
Nominal output current	100A/50A
Maximum output current	110A/55A
Maximum output power	1200W
Maximum output current ripple	2%
Operating input voltage range	26VDC-48VDC
Maximum input voltage	50V
Minimum voltage drop input to output	2V
Power consumption standby	2W
Ambient temperature	0°C-40°C
Efficiency	96% (24V)
Short-circuit proof	Yes
Thermal protection	Internal 80°C
Mechanical dimensions (***HxBxT***)	(320 x 14 x 80) mm

3.2.8 DC/DC Bidirectional Converter

Figure 3.14 shows the high performance step down DC6350F-S converter from Zahn Electronics. This is a two quadrant (sourcing and sinking current), crystal controlled, dual Half H Bridge, configured in a buck topology programmed for Voltage Loop (VLP). It is a compact, self-contained unit with its own power supply, input and output power filter. Power to the unit is from a DC supply, fuel cell or battery. Each half bridge has 10 transistors in parallel on the top and 10 transistors in parallel on the bottom. Faster response can be achieved because the switching frequency is 31,250Hz. The temperature of the unit is monitored and in the event of an excessively high ambient temperature, then the current to the load is reduced automatically to hold the transistor temperatures to a safe level [36].

DC/DC converters modelling and simulation with an introduction and a brief description of power converters based on switched-mode operation were reviewed and can be found in Appendix 9.14.

Figure 3.13 Unidirectional DC/DC converter BSZ PG 1200 with control unit

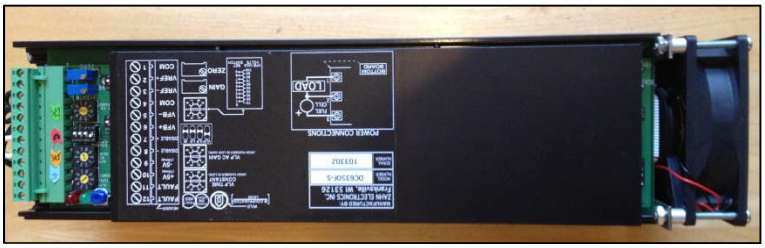

Figure 3.14 Bidirectional DC/DC converter DC6350F-S

3.2.9 Piper Cub J3 aircraft Model

A non-linear dynamic model of the Piper Cub J-3 aircraft (see Figure 3.15) was originally developed by P. R. Thomas [32], updated by De. Lomas [33] as well as Leonardo Lopez and Shahin Moghimi [34]. Since both the physical and 6DoF model were previously researched by the group, it was selected for the project with the intention to emulate accurately the motion and flying characteristics of the aircraft. Table 3-4 shows the main geometry and mass properties of the Piper Cub J-3 aircraft. The simulation model has been modified to replace the piston engine with an electric engine. In order to be able to extrapolate the power requirements with respect to the generated RPM, the experimental test results obtained for the motor were derived and integrated into the nonlinear model. In addition, the simulation model was modified to include a wind model black that takes the external factors into account. In particular, the wind speed and direction.

Table 3-4 Piper Cub J3 geometry and mass properties

Wing span	*2.040 m*
Aerodynamic chord	*0.3070 m*
Wing reference area	*0.6290 m^2*
Aspect ratio	*6.68*
Engine power	*1.29 KW*
Aircraft weight	*5.65 kg*
Centre of gravity position (CG)	*[0.371606,0,0] m*
Centre of pressure position (CP)	*[0.3850.0.0] m*

Figure 3.15 Piper Cub J-3

The block diagram simulation model of the aircraft is shown in Figure 3.16.

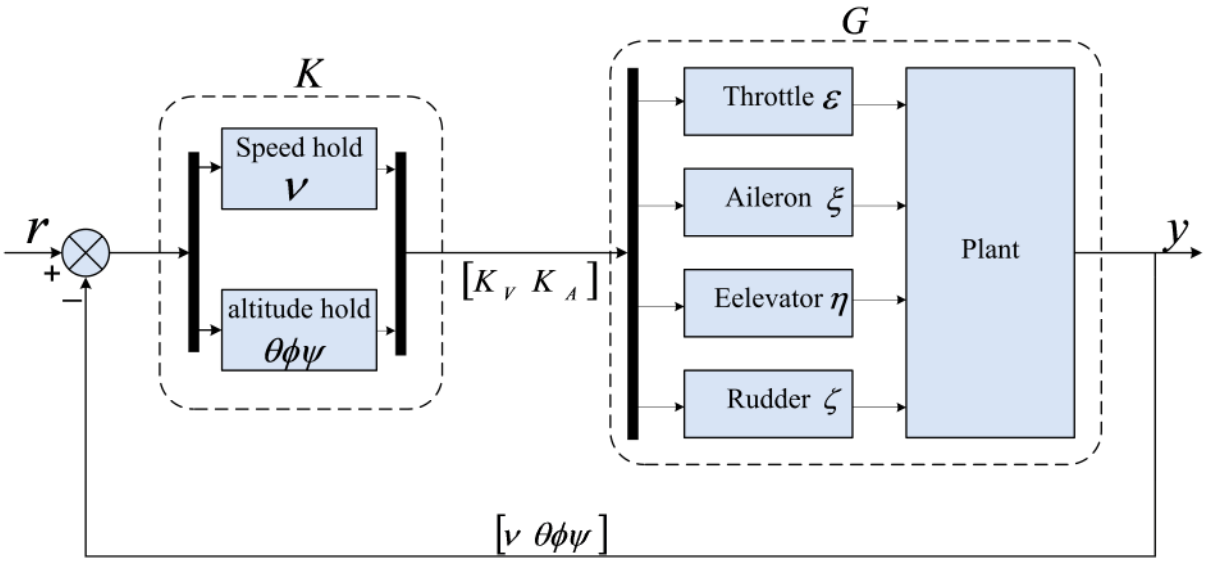

Figure 3.16 Block diagram of Piper J-3 Cub 40 simulation model

$K_A \in \mathbb{R}^3$

where K is the PID controller

G is plant

y is output of the plant

The dynamic model of the aircraft is based on the linearised equations of motion described in Appendix 0. The aerodynamic derivatives of these formulae are estimated from lookup-tables as a function of altitude and airspeed. The flowchart of the model can be found in Appendix 9.7. This includes the following:

- **Aerodynamic Forces and Moments:** the angle of incidence, dynamic pressure, airspeed, aerodynamic coefficients and sideslip are obtained from control surfaces atmospheric parameters, wind impacts, deflections and previous states like angular rates and translational velocities in relation to body axes.
- **Electrical Engine Model:** which is fed by throttle command, velocities in the wind axes, and air density generates the propeller forces and moments.
- **Total Forces and Moments:** takes as inputs the outputs from previous blocks and centers of pressure and gravity, and produces the total forces and moments acting on the aircraft.
- **Equations of Motion Block:** contains full six-degrees of freedom (6DoF) EoM (Body Axis) block from Aerospace Blockset library. Gravity forces in the body frame are added to the forces output from previous block. The unnecessary outputs from the generic block are terminated and masked. The equations of motion of an aeroplane can be found in Appendix 00
- **Mass and Inertia:** In this simple subsystem the center of pressure, mass, inertia, and center of gravity are taken from the Matlab workspace to the simulation.

Additional blocks that are included in the aerodynamic model are basic Simulink blocks; their description can be found in Simulink help. The brief description of the aerodynamic model made above was made in order to present the model only. Autopilot Stability Augmentation System (SAS) was developed by Shahin Moghimi [34]. This part of the model is based on classical PID control and hold autopilots. Further details of the model can be found in previously mentioned authors publications regarding its development [32, 33] and [34].

3.3 Summary of Chapter 3

In this chapter, fuel cell hybrid system and their types/configurations were explained. The different types of energy storage systems used to complement the slower output power of the fuel cell were highlighted. The battery model, electrical engine model and Piper Cub J3 model were also discussed.

Details of how the experiment was set-up in the lab were discussed and each component of the hybrid system individually covered (for the specification of each component see Appendices). The fuel cell hybrid system in the lab consisted of the 1.2kW Nexa PEM FC, as the main power source, 36 V lead-acid batteries WP18-12 (12 VDC), DC/DC step-down converter (to keep the output voltage constant) and DC/DC bidirectional converter (to charge/discharge the batteries). These were discussed alongside with their theoretical foundations, types and connection to the electronic load.

Overall, the integration challenges that arise during the construction of the hybrid system were identified. In addition, advanced solutions were developed to overcome several integration issues faced. Ideally, system modules should be selected so that they can meet the power requirements and operating voltages. The relatively slower output power of the fuel cell and also the challenge of how to control the battery charge/discharge exacerbate the difficulty of system integration.

Chapter 4

Experimental Dynamic Performance Tests

4. EXPERIMENTAL DYNAMIC PREFOMANCE TESTS

In this chapter, before starting the modeling stage, detailed experimental analysis has been carried-out based on a set of experimental tests on Ballard Nexa power module. In particular the emphasis in this chapter was to identify the dynamic performance of the Nexa module of each state and characterise relevant transient response to variable load. Furthermore, to determine some experimental parameters such as experimental temperature and OCV value which will be used in the fuel cell modelling and simulation. The remaining part of this chapter is organized as follows: The dynamic behaviour is checked during different operating conditions such as start-up, shut-down, step-up load and irregular load variations. The dynamic tests that were carried-out are explained with their results and discussion in details in section 4.2. Followed by the performance of the module is tested for both steady state and transient state.

4.1 Experimental Operating Conditions

In order to investigate the dynamic performance and the transient responses of the $PEM\ FC$ under various loads, the experiments have been carried-out under different stages to identify the dynamic characteristics at each stage.

4.1.1 Start-up State

Before starting up the FC system was in OFF state. As a back-up 24 V battery power was applied to the control board, the system transited to STANDBY state. In this state, sensors and actuators were energized and the on-board microprocessor began to continually deliver system data and status signals. A 5V start signal to the Nexa system control board will begin the STARTING sequence. The hydrogen solenoid valve opens and the purge valve periodically cycled to fill the FC stack with hydrogen and the air pump turned on to provide air to the FCs. After that, the cooling fan ran for thermal regulation as well as dilution of purged hydrogen. Once the external load increased from zero to the first step value, the current would accordingly begin to rise until the system reached a normal operating state.

4.1.2 Shut-down State

Once the 5V start signal is removed from the FC system, it transitions to the normal shut down state, and the external load relay was initiated to isolate the FC stack from the load.

Then a shut-down sequence continued to remove residual product water from the anode and cathode flow channels using the air pump and hydrogen purge valve. After the start line was totally turned off and the battery power was disconnected, the system returned to OFF-state.

4.1.3 Step-up Load State

In this state, four load steps were taken for step-up load investigation. The current increased from 0 to 40 Amp with break value of 10 Amp. As the external load changed, the stack voltage and current responded dynamically to new operating conditions until reaching next steady state. In the meantime, other operating parameters changed as a result during each step state, and then adapted themselves to the new state. Among the whole process, the dynamic cell performance under constant load at around 32 Amp was carefully monitored for investigation of purge effects.

4.1.4 Irregular Load Variation State

In this state, The FC system had to go through extreme load changing since the external load did not follow step-by-step regulations. In order to get deeper insight of effects of air flow rate and operating temperature on the FCs dynamic performance, a longer test was carried-out for the dynamic evaluation.

4.2 Results and Discussion

4.2.1 Transient Response in the Start-up Sequences

The Nexa power module FC provides fully automated operation and load response. The 24V batteries must be connected to support start-up and shutdown load and the system must be provided with an adequate hydrogen fuel supply. The transient responses of transmitted status, current and voltage during the start-up states for 35 second are shown in Figure 4.1 and Figure 4.2. Before applying the battery power, the FC system remains in the OFF state. The starting-up process began by applying 24V battery power to the control board, the system transited to stand-by state in 2 seconds. In this state, sensors and actuators were energized and the on-board microprocessor began to continually deliver system data and status signals. Subsequently a 5V start signal initiates the starting sequence. The hydrogen solenoid valve opened and the purge valve periodically cycled to fill the FC stack with

hydrogen. The air pump is turned on to provide air to the FC. Finally, the cooling fan turned on for temperature regulation as well as dilution of purged hydrogen.

The stack voltage began to increase at 13 seconds and reached about 46V. During this state, no current is delivered to the external load. After 21 seconds, the current gradually increased to 1.2A and voltage decreased to 42V, which presents starting-up operation in this time. At 28 second, when normal operation was achieved, the Nexa control board internally transferred parasitic load from the external battery to the FC stack. An external load relay control signal was sent to connect the FC to the external load. Due to this transmission the FC current increase with overshoot due to air pump fast demand, and the voltage decrease with undershoot as shown in Figure 4.2.

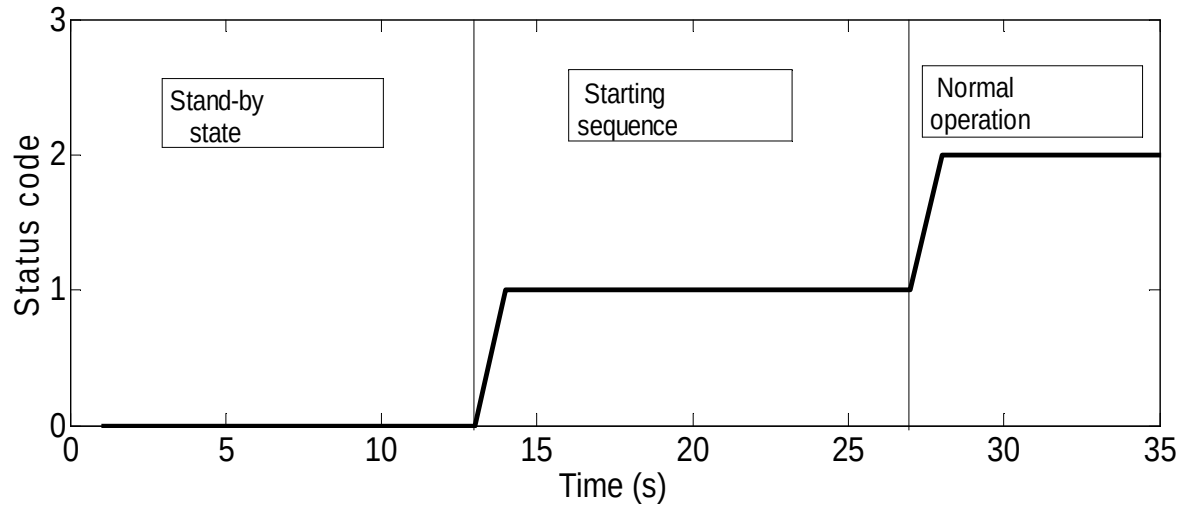

Figure 4.1 Nexa transmitted status in starting-up state

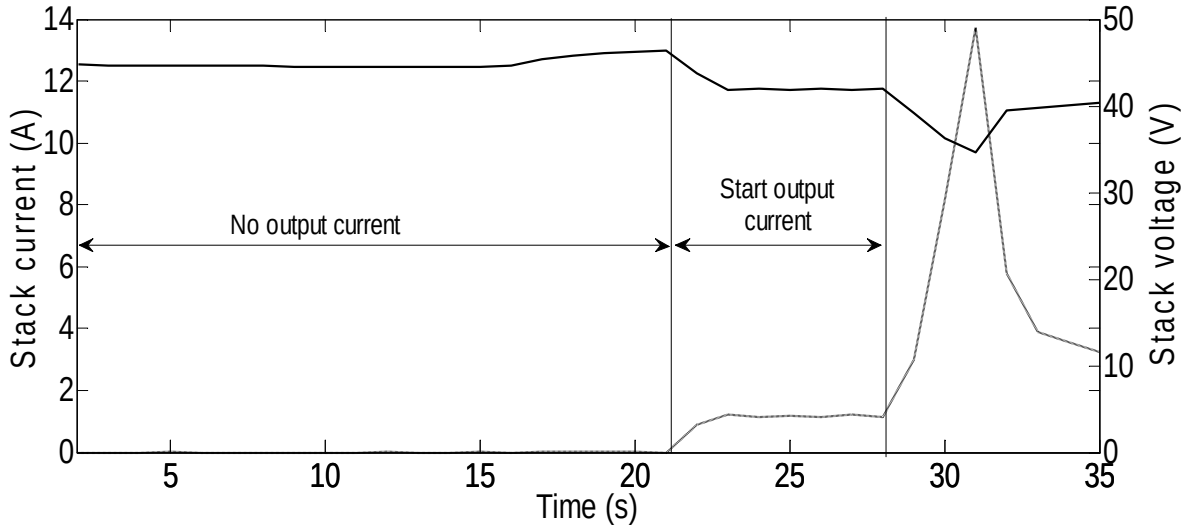

Figure 4.2 Transient responses of the stack output I (A) & V (V) in start-up state

After the STAND-BY sequence, the air pump and cooling fan voltages jump from 0 to 43% and 50%, respectively as shown in Figure 4.3. The air flow rate fluctuate around 20 slpm, its response has overshoot at the beginning of starting-up and normal operation states as illustrated in Figure 4.4. When the external load was connected to the FC at 28 second, the voltage of the air pump increased with an overshoot in order to supply enough oxidant air and flush the stack of residual water.

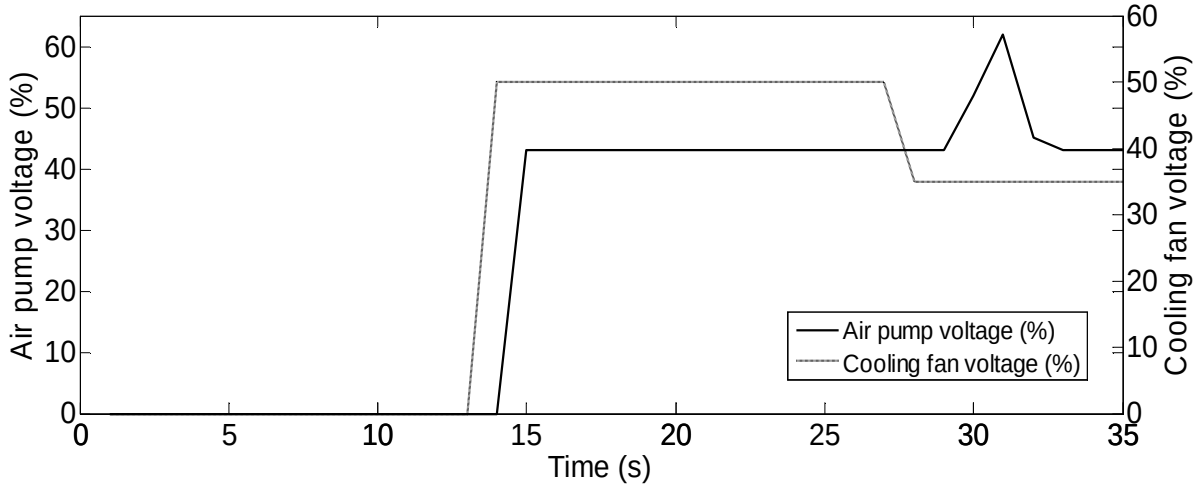

Figure 4.3 The air pump and cooling fan voltage in the Start-up state

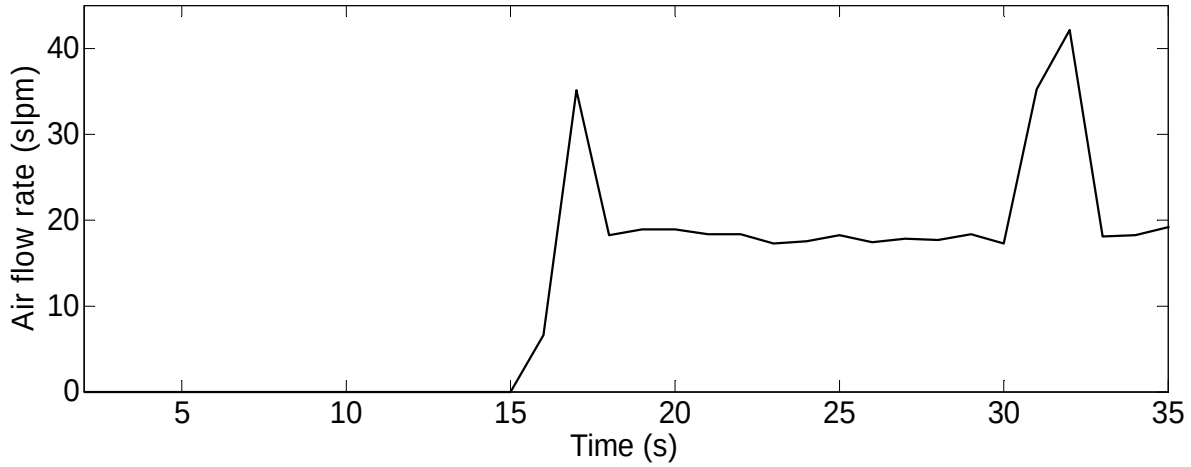

Figure 4.4 Air flow rate in starting-up state (slpm)

The air flow rate goes up proportionally to satisfy the FC consumption. On the other hand, the membranes are still dry without enough water content at the beginning of a low load operation. An appropriate flow rate benefits water uptake and transport in the membrane FCs[42]. On the contrary, the cooling fan voltage drops to 35% so as to regulate the FC stack temperature. In reality, as shown in Figure 4.5. that the stack temperature does not change immediately. Hence, even for a higher current level in the following running of the system, the cooling fan voltage is still kept constantly at 35%.

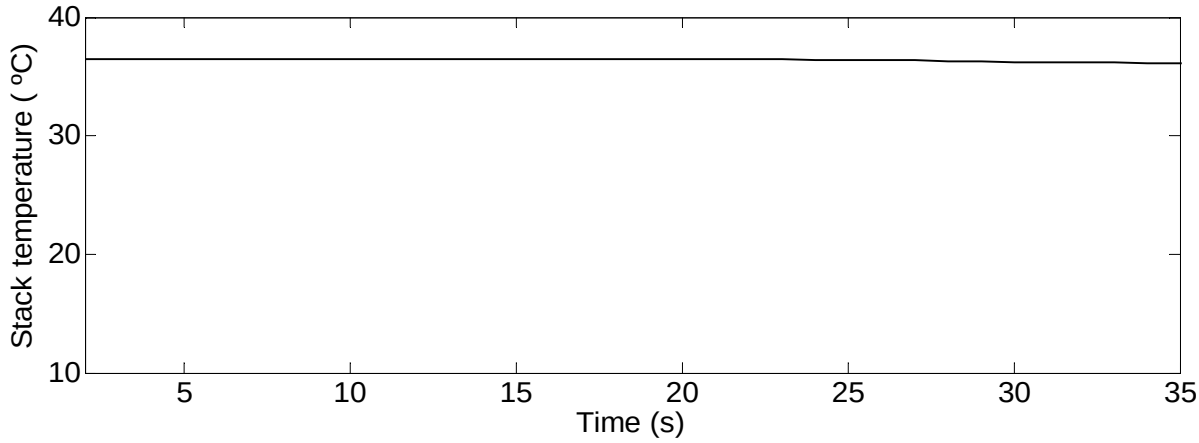

Figure 4.5 Stack temperature in the starting-up state

4.2.2 Transient Response in the Shut-down Sequence

In shut-down mode, the 5V start signal removed from the FC stack and the external load relay was open to isolate the FC stack from the load. Since the FC was in operation for longer than 5 minutes, the shut-down sequence continued to remove residual product water from the anode and cathode channels using the air pump and hydrogen purge valve. The transient responses during the shut-down states are illustrated in Figure 4.6, Figure 4.7, Figure 4.8 and Figure 4.9. The shut-down begins at 419 second, the current drops to 1.58A within 1 second, while the stack voltage increases to 42 V. In this period, the control board internally transferred parasitic load from the FC stack back the external battery, which cause a small undershoot and overshoot in current and voltage, respectively. From 447 seconds, the current drops almost to zero while the stack voltage increase gradually until it reaches the OCV value of 46 V in idle state.

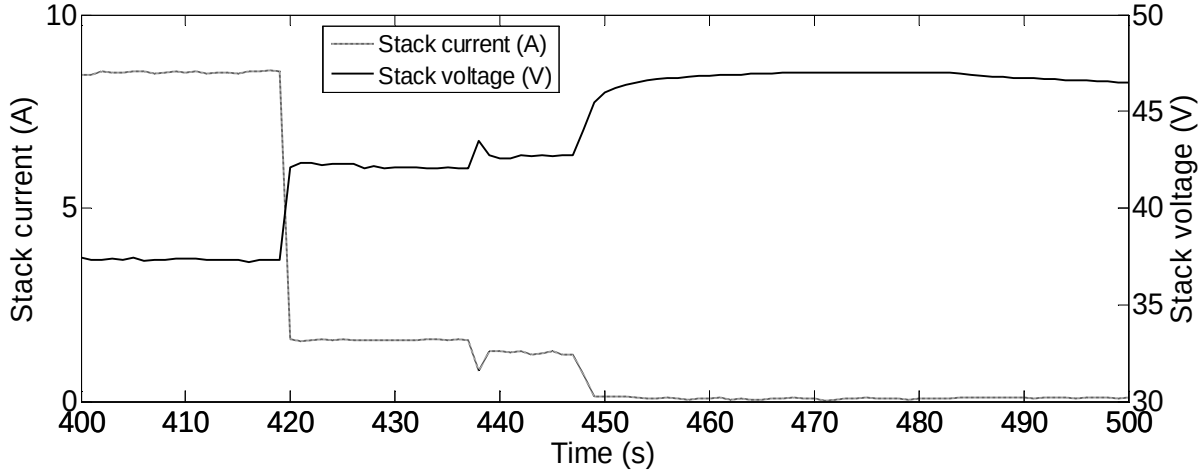

Figure 4.6 Transient responses of the stack output I (A) and V (V) in shut-down state

The air flow rate increase from 20 slpm to 59 slpm in the period from 438 to 482 second then drops to zero as shown in Figure 4.8. At 452 second, the voltage of the cooling fan falls from 35% to zero. Later on at 482 seconds, the air pump drops sharply to zero as shown in Figure 4.9. Upon shut-down sequence, the stack temperature enters a decline phase but drops quite gently as illustrates in Figure 4.7.

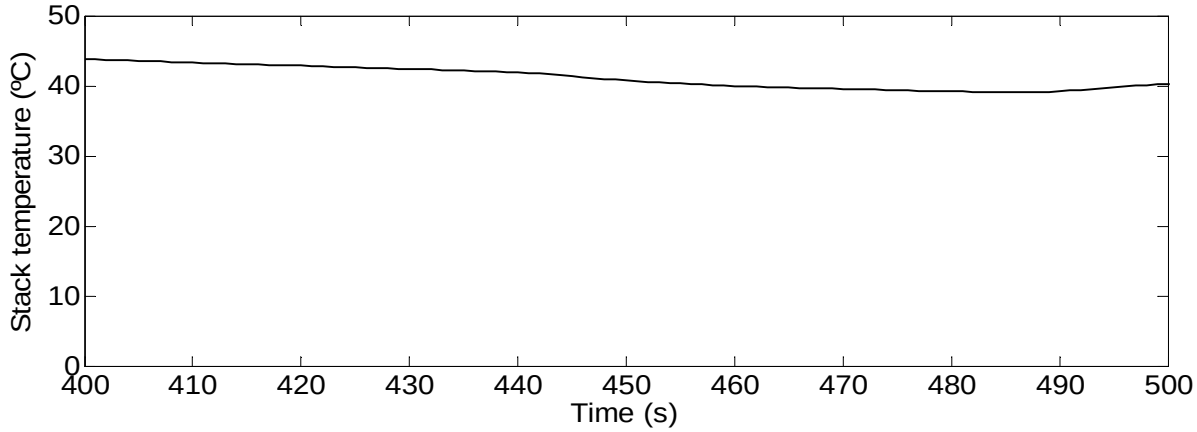

Figure 4.7 Stack temperature in the shut-down state

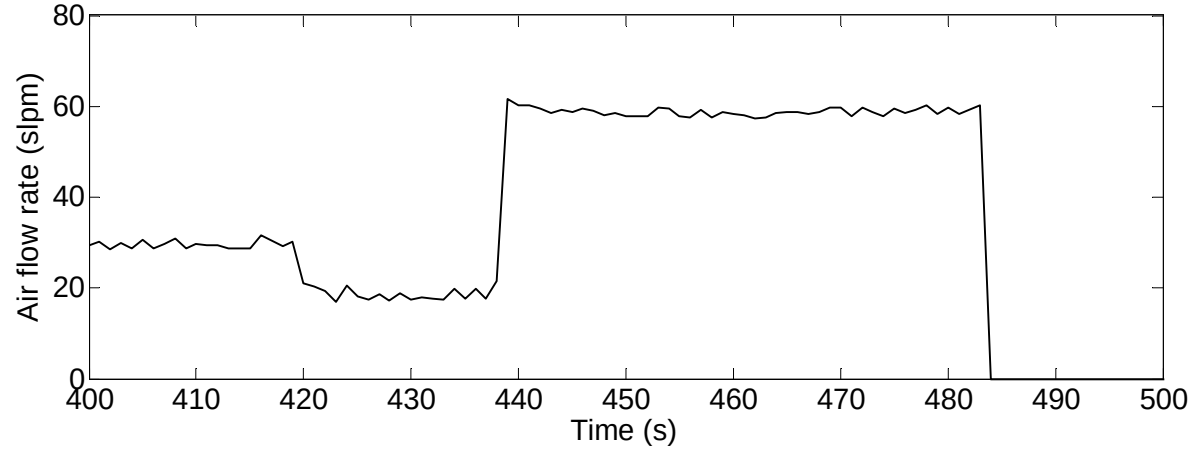

Figure 4.8 Air flow rate in shut-down state (Slpm)

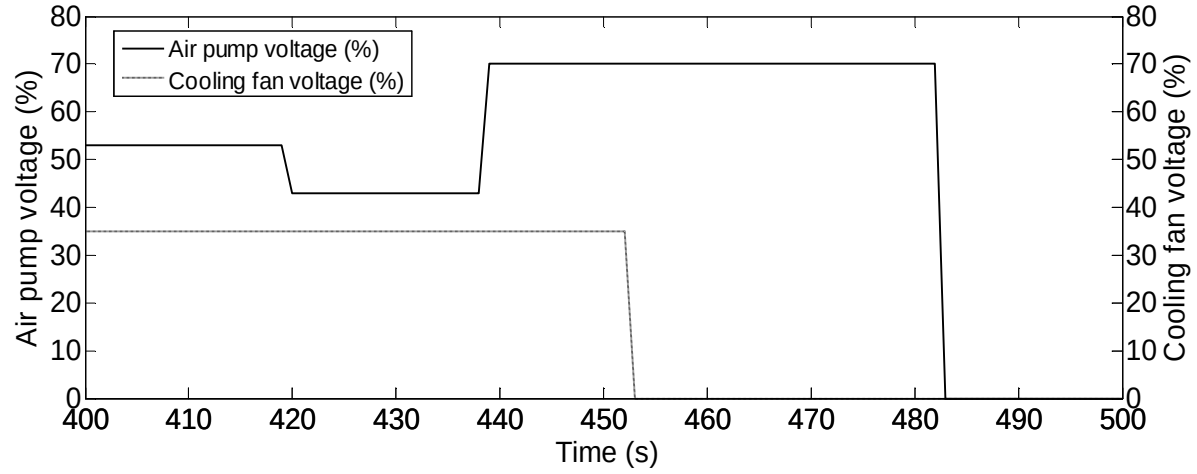

Figure 4.9 The air pump and cooling fan voltage in the shut-down state

4.2.3 Transient Response in the Step-up Load States

The results of this test describe the transient responses of FC parameters (stack current, stack voltage, air pump voltage etc.) during step-up load variation. In this phase the current increases from 10 to 40 A, the stack voltage declines from 35 to 30V and the interval value was 10A. The maximum power of 1.2 kW occurs after 919 seconds as the current remains stable at 40A. As the current increases, the frequency of purge valve operation also increases in order to prevent water flooding in the anode channel and anode gas diffusion layer. The interval between purge valve opening and closing is about 96 seconds in the low-current region of around 10A, but becomes 30 seconds in the high-current region at 40A. This demonstrates that the purging mechanism depends on the feedback of the FC dynamic behavior as shown in Figure 4.13 and Figure 4.14.

The 'red' circle in Figure 4.10. draws attention to the stack voltage undershoot and current overshoot phenomena that occurs when the current transiently increases from 20A to 30A. The current overshoot possibility is elevated for two reasons:

- The different operating conditions lead to disparate water saturation level particularly after a long course of operations.
- Both the humidified water and product water alter the membrane wettability. The voltage undershoots because of an unexpected load action causes temporary dehydration due to electro-osmotic drag on the anode side, and air feeding starvation on the cathode side. The membrane resistance jumps which inevitably leads to a sharp drop in cell voltage [43].

The stack temperature changes almost proportionally with the current without any significant delay as illustrated in Figure 4.12. The air pump voltage was also found to follow the same step-up rhythm to the current increasing trend. The cooling fan voltage at the beginning is constant at 35%, after 700 seconds, it started to step up following the current increase as shown in Figure 4.12. A detailed schematic plot of the FC stack voltage between 650 and 900 seconds under constant load is shown in Figure 4.13. The current is around 30A during this period, while the FC stack runs without any load variation, the stack voltage actually experiences periodic degradation with purge valve operation that helps to remove water from the anode channel. During normal FC operation, liquid water condenses and accumulates due to the dead-end configuration of the FC anode side. Before the purge valve opens, the stack

voltage experiences a slight decline process from 32.2 to approximately 31.76V due to water flooding. An immediate performance enhancement after the purge valve open can be seen at the sharp voltage increase. The purge valve status values are '2' when the valve is open and '0' when the valve is closed (shown in Figure 4.14).

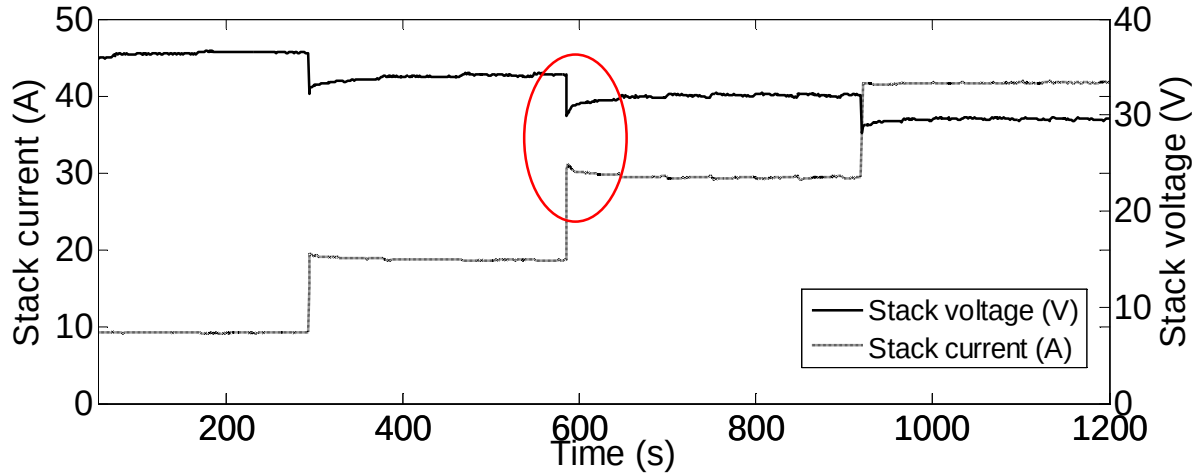

Figure 4.10 Transient responses of the stack output I(A) and V(V) in step-up load states

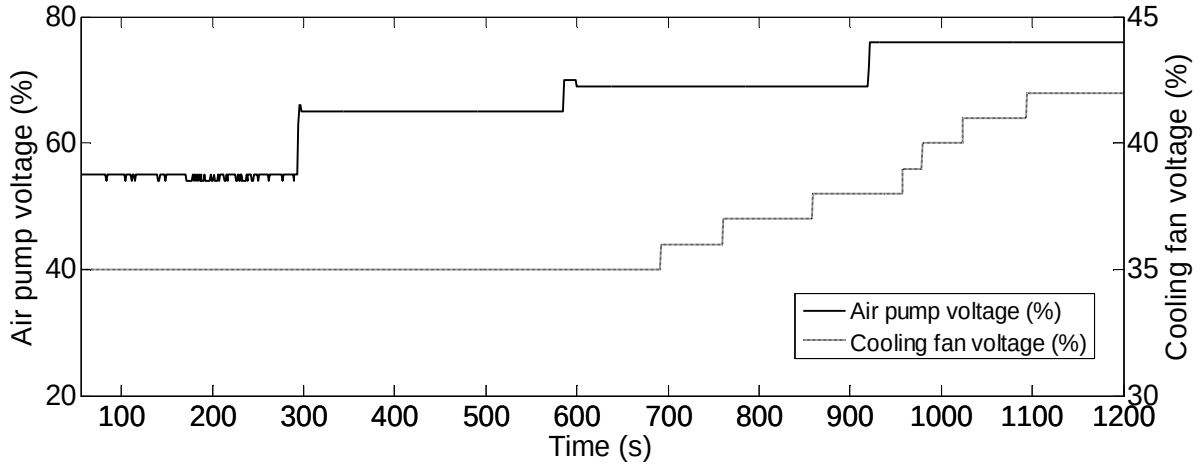

Figure 4.11 The air pump and cooling fan voltage in step-up states

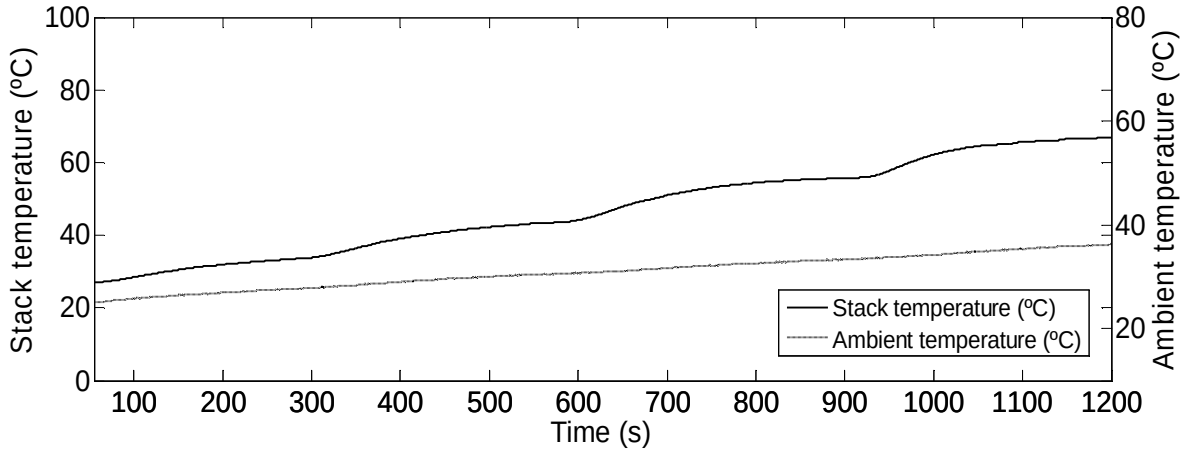

Figure 4.12 Stack and ambient temperatures during step-up states

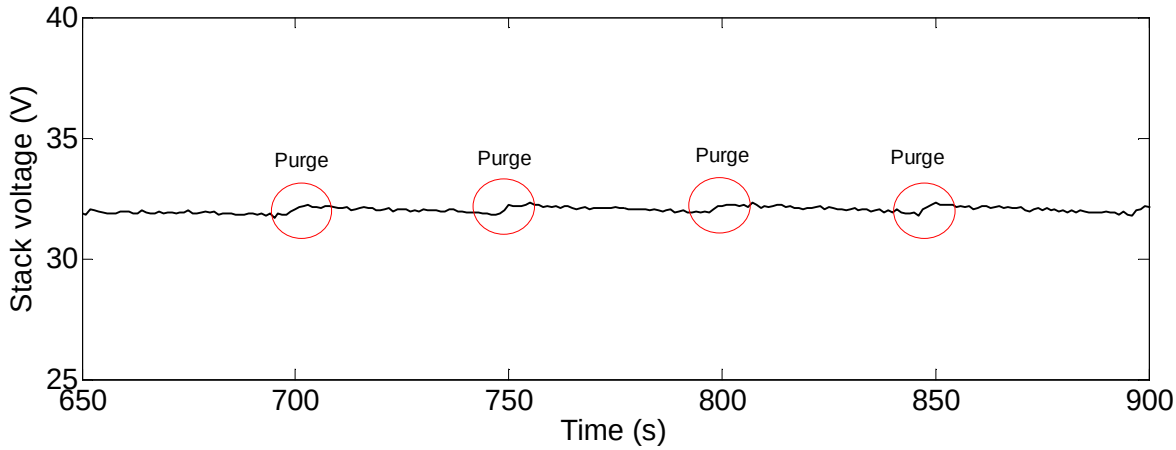

Figure 4.13 Effect of purge valve operation on PEM FC stack voltage in constant load

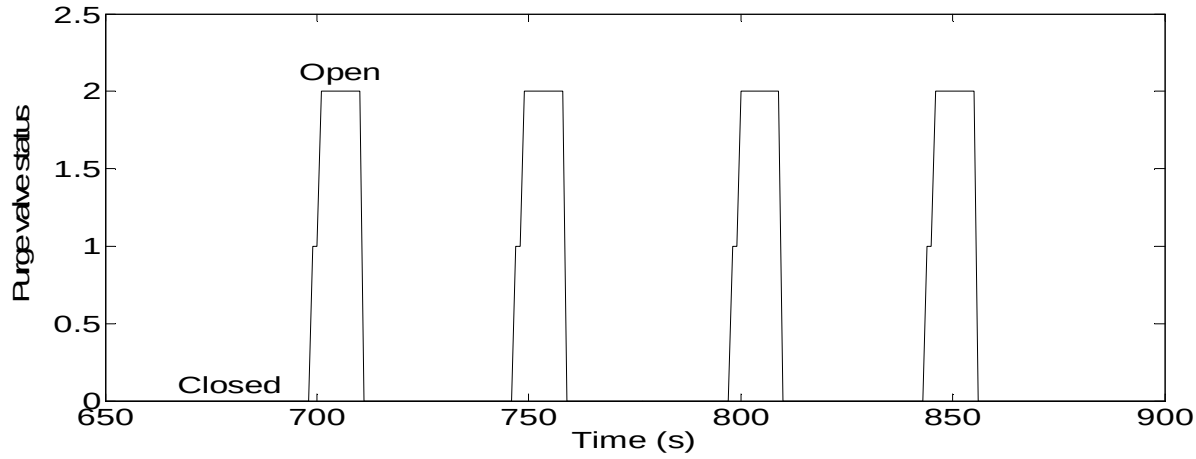

Figure 4.14 Purge valve status during constant load

4.2.4 Transient Response Under Irregular Load Variation

The main objective of this test is to study the effects of temperature and air flow rate supplied by the air pump on the FC stack dynamic performance. In the test the FC supply power to irregular load variation over a longer course. Experimental results are presented in Figure 4.15, Figure 4.16 and Figure 4.17. Heat commonly exists during the FC operation in the forms of exothermic reaction energy and internal energy dissipation. PEM FC stack temperature continuously changes with the load current. However, the temperature directly affects the rate of chemical reactions and the transport of water and reactants. Thus, operations under too-low or too-high temperatures in reality is never recommended except for extreme circumstances such as sub-zero application [42], where it can be regulated by proper thermal control. The stack temperature response followed the load changes in a similar way to that of the current increase or decrease. However, changing slowly without overshoot or undershoot as illustrated in Figure 4.16.

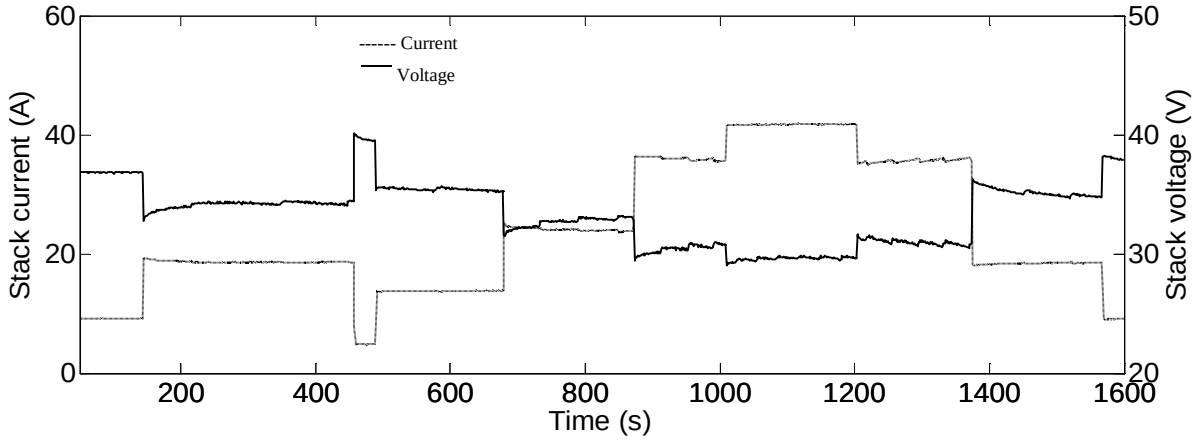

Figure 4.15 Transient responses of the stack output I(A) and V(V) irregular load variation

Figure 4.17. presents the dynamic profile of air pump of the Nexa FC. It can be seen that the air pump voltage changes directly tracking the dynamic trend of current fluctuation without delay with a similar corresponding change in air flow rate. However, the decrease in the amount of air flow rate results in oxygen depletion from the FC cathode channel during power generation. Furthermore, the Nexa FC operation shows that the air flow does not significantly affect the FC stack dynamic performance.

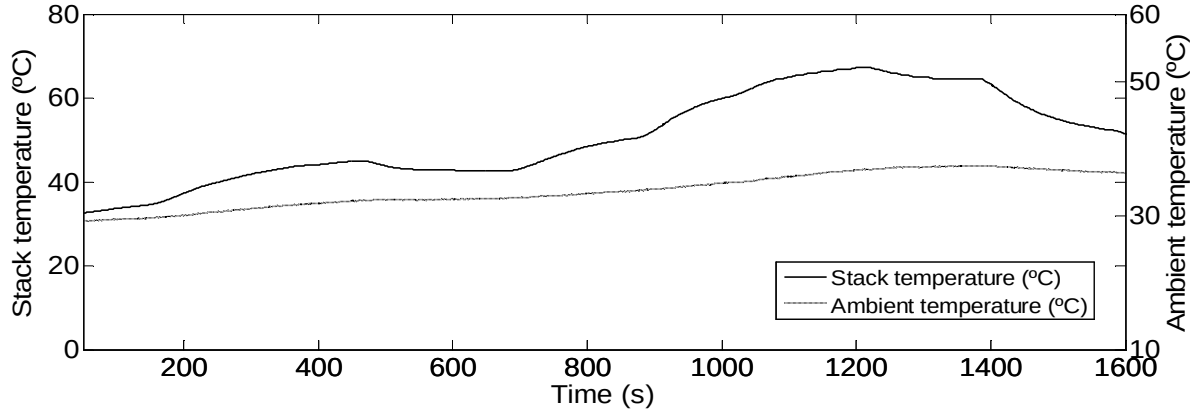

Figure 4.16 Stack and ambient temperatures in irregular load variation

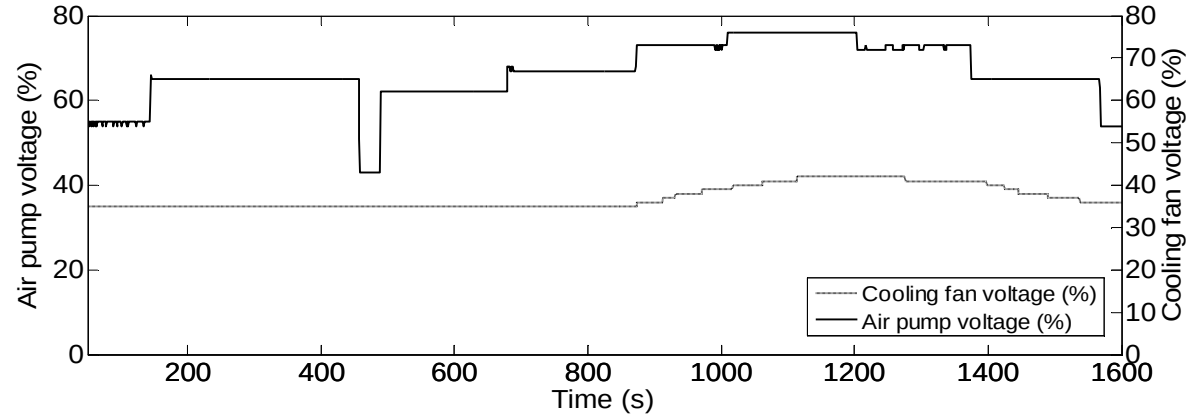

Figure 4.17 The air pump and cooling fan voltage in irregular load variation

4.3 Summary of chapter 4

A set of experimental tests on Ballard Nexa power module were presented. In particular the emphases in this chapter were on the Nexa^{TM} module to identify the dynamic performance of each state and characterize relevant transient response to variable load. The remaining part of this chapter is organized as follows:

The dynamic behaviour was checked during different operating conditions such as start-up, shut-down, step-up load and irregular load variations. In addition, the dynamic tests that were carried-out are explained with their results and in detail discussion. Followed by the performance of the module tested for both steady state and transient state (transient response of the stack during load changes).

The aim of this chapter was to investigate the dynamic performance of a PEM FC stack. This goal has been reached and conclusions can be made as follows:

The control board internally transferred parasitic load from the external battery to the FC stack at start-up. Due to this transmission the FC current increase with overshoot due to air pump fast demand, and the voltage decrease with undershoot. In shut-down sequences control board internally transferred parasitic load from the FC stack back the external battery, which cause current small undershoot and voltage small overshoot.

When the current transiently increases from 20A to 30A, a current overshoot can be observed in the system responses due to two factors. The first factor is that different operating condition results in disparate water saturation level particularly after a long course of running. The second factor is that both the humidified water and product water alter the membrane wettability. Since temporary dehydration due to electro-osmotic drag on the anode side and air feeding starvation on the cathode side, a voltage undershoot was observed at the same time.

Based on the investigation that was curried-out in this chapter some parameters were determined experimentally such as experimental temperature and OCV value and also the effect of start-up sequence, shutdown and transient state on the module. These data/parameters will be used in the fuel cell modelling and simulation.

Chapter 5

Dynamic PEM Fc Stack Modeling

5. FUEL CELL MODELING AND SIMULATION

This chapter presents a dynamic electrochemical simulation model of PEM FC, its parameters were specifically tuned for a $1.2kW\ Nexa\ stack$*. In addition, the simulation model has been improved by taking the equivalent internal resisters into account to be as representative as possible of the* $Nexa\ power\ module$ *system. Moreover, the simulation model was validated using the experimental data from the Nexa fuel-cell stack. The performance of the model was studied and validated for both steady state and transient state (transient response of the stack during load changes). The model assumptions are discussed with the theoretical equations. Simulation results of the proposed model are compared with the experimental data and also verified using MRE calculations. The results show that the percentage error of the simulated model when compared with the experimental results does not exceed 4.1% for the full working process, including the start-up sequence and the transient phase. The validated model can provide the basis for deriving flexible design options and the real-time control for FC hybrid system.*

5.1 Introduction

This chapters starts with a literature review focusing on three objectives: The first is to introduce some of the fuel cell models that were developed in this field and gather the sources of information and data required to develop a PEM fuel cell simulation model based on $Nexa\ Power\ Fuel\ Cell\ Module$ 1.2 kW. The second is to gain an understanding of the fuel cell performance, characteristic, losses mechanism and its phenomena and provide a context for this current study in relation to the state of the art. The third objective is mainly focusing on the fuel cell model validation.

Investigation and development of FC systems for a variety of applications have significantly increased in the last two decades. There are several types of fuel cells, usually classified by their operating temperature and the type of electrolyte they use. Researchers and companies are working on several of those systems to develop the technology further and have commercially available solutions that are economically viable as an alternative to fossil fuelled power systems [44]. The development of the technology requires multidisciplinary effort (e.g. materials, manufacturing process, control systems, power electronics ...etc.)

In this project the work is based on $PEM\ FC$. Due to the high electrical efficiency and lower operating temperature, the $PEM\ FC$ is one of the most promising systems to employ in aerospace, automotive and stationary applications as a replacement for the traditional systems [43; 45-47]. It offers high power density, zero emission, fast start-up and reliable source of power at a relatively low cost [48]. There are number of $PEM\ FC$ models that have been developed in the past. The earlier models on PEM FC presented by Farhat [49] and Yan, et al. [50] offered an empirical polarization curve based on the calculated coefficients. These polarization curves consider only the steady state conditions. For the fuel cell performance description, the polarization curve is an important parameters to measure since the FC performance is characterised by its polarization curve [51].

Although several studies on fuel cell modelling are based on the transient-state phenomena [52-54], it still lacks the optimization of the fuel cell stack performance and a specific transient behaviour when the transient state phenomena are included [55]. Wang, et al. [56] and Zhang, et al. [57] have taken these transient state conditions into consideration and focused on the fluid dynamics inside the fuel cell stack. In the same way, some other $PEM\ FC$ models were also proposed in [58-60], which are focused on a multi-dimensional study. In all these models the effects of gas diffusion layer on $PEM\ FC$ performance is studied and evaluated.

Alotto, et al. [61] developed a complex three dimensional dynamics model, which uses a highly nonlinear fully coupled dynamic numerical model of the membrane. This model includes proton conduction, water flow, heat generation and transport and hydration conductivity. Their model is used also for detecting hot spots related to fluctuations of the PEM thickness. They noted that it is extremely difficult to quantitatively compare experimental data with simulation results, due to the nature of the physical systems. The aforementioned studies on $PEM\ FC$ design are very helpful. However, it still requires an optimal design of the FC model for a better stack performance. There are also several other approaches that were used, Wang, et al. they used the equivalent electrical circuits to model the FC and thermodynamic model as well using a simple current feedback to control the air flow [62].

In literature there are different controls techniques which can be applied to the Fuel cell system to control different variables. For instant, to operation the FC, the requested pressure

and exceed ratio have to be guaranteed in the stack. Therefore, the hydrogen and the mass flow of the oxygen (air) have to be controlled otherwise the electrochemical reactions will not take place. The objective of the controller is to keep the requested O_2 excess ratio to avoid starvation and to reach the desired FC net power [63].

A classical PID control can applied to the fuel cell system. On the other hand, these control acts are not enough for optimal operation. A well feedback approach can be the state feedback regulation, but then again the weakness of the state feedback controller is not adaptive to parameter variation [64]. The feedback control performance can be improved with a feed-forward regulator that takes the disturbances into account into the control signal [65]. Though it desires a bit further effort compared to a simple Singe Input-Single Output (SISO) PID controller, yet it can provide better outputs. Pukrushpan [63] combined a feedback and feed forward controller in his model which has improved the system performance and got a robustness regulator.

Another feed-forward controller is the Model Predictive Controller (MPC). It has a basic model of the real system that makes prediction for the future conditions of the process variables. Gruber, et al. [66] they combined a basic PI regulator with non-linear MPC for PEMFC; The master controller calculates the necessary air flow to stabilize the oxygen excess ratio at a fixed set point. A non-linear model based predictive controller (NMPC) using a Volterra series model is used as a master controller. The slave controller, a non-linear PI, uses the reference of the air flow calculated by the master controller to stabilize the air flow in the compressor and allows reference tracking. Also Golbert and Lewin [67] used a non-linear MPC to achieve optimal efficiency for the PEM FC. They realised that as the efficiency increased, the response of the FC decreased.

Bordons, et al. [36] presented an advanced control of PEM fuel cells based on Generalized Predictive Control (GPC). Their strategies attempted to achieve three different operational objectives. (I) avoidance of starvation, (II) tracking of a desired output voltage and (III) maximization of efficiency. In addition, the model also considered the effect of two different constrains, one operational limit to avoid starvation of the oxygen excess ratio and the others, compressor voltage [68].

Some researchers also made efforts to control the FC using Fuzzy Logic controller: The Fuzzy Logic is a simple control approach which is approximate rather being fixed and exact

and it does not require large computational time. Tekin, et al. [69] proposed an energy management strategy for embedded FC system based on Fuzzy Logic controller. Two different Fuzzy controllers were applied in their model: the first one was for airflow control loop, the second controller was to regulate the airflow set points. Artificial neural networks can also be used to regulate the air flow of the FC.

Hatti [70] developed a neural networks based on a PI controller which was then used to train the neural networks system. In [71], investigated the performance and prediction of PEMFC system using Back-Propagation (BP). The simulation results have shown that the BP based NN can successfully predict the stack voltage and current of PEMFC system by using simply two input variables which are stack current and hydrogen pressure. In a similar way, Ghaderi, et al. [72] proposed a NN model to control the stack terminal voltage and improve the system performance using the input air pressure control signal. The proposed ANN is built based on BP network. Their simulation results show that, applying NN feed forward control can track the output voltage and improve the overall system performance. In addition, it consumes less energy.

There are other control techniques as well used to control other variables that have effect on the efficiency of the FC, such as temperature and humidity. However, are not objectives of this thesis, since the temperature parameter will be empirically used. This will be explained in the next section.

5.2 Modelling of Nexa PEM Fuel Cell Stack

In this section a dynamic electrochemical simulation model of PEM FC is proposed and validated using experimental data from a 1.2kW Nexa power module FC. The aim is to obtain an accurate model based on a 1.2kW Nexa FC that could be used for the development and design of controllers in hybrid fuel cell electrical systems.

In the literature aforementioned, several models were proposed to model the FC stack. Colleen [52] introduced the electrochemical simulation model of $PEM\ FC$, the book is the most recommend for development of PEM FC model. El-Sharkh, et al. [53] introduced a dynamic model for a stand-alone $PEM\ FC$ power plant for residential applications. These models were used as the basis and were modified to model and simulate the Nexa $PEM\ FC$

stack. It also based on a set of experimental investigation, analysis of the dynamic performance and the transient responses of the $PEM\ FC$ under various load that was carried-out as explained in the previous chapter.

The goal in this chapter is to model only the FC stack (Figure 3.4). The auxiliary equipment's are not included. However, the equivalent internal resistance is taking into account and this will be explained in more details in section 5.2.3. The structure of the fuel cell simulation model is divided into two parts as defined in the following sections

5.2.1 Fluid-Dynamics Equations and Modelling Assumptions

A few reduction assumptions were made and discussed broadly along with their theoretical derivations. In order to simplify the model, the humidified air is assumed as an oxidant and the dry air will be equalled to that of the atmospheric air and the dry hydrogen is fed into the anode channel. The nitrogen exchange is neglected since it does not contribute significantly to the reaction.

The proportional relationship of the flow of gas through a valve with its partial pressure can be expressed as [53]:

$$k_{H_2} = \frac{q_{H_2}}{P_{H_2}} \qquad \{5.1\}$$

$$k_{H_{2o}} = \frac{q_{H_{2O}}}{P_{H_{2O}}} \qquad \{5.2\}$$

$$k_{o_2} = \frac{q_{O_2}}{P_{O_2}} \qquad \{5.3\}$$

For the hydrogen, the derivative of the partial pressure can be calculated using the perfect gas equation as follows:

$$\frac{d}{dt} P_{H_2} = \frac{RT}{V_{an}} \left(q_{H_2}^{in} - q_{H_2}^{out} - q_{H_2}^{r} \right) \qquad \{5.4\}$$

The relationship between the reactive gas flows in the gas diffusion layer (GDL) and the load current at the steady state can also be computed [61].

Hydrogen consumption in the anode side is given by:

$$q_{H_2}^r = \frac{N_o i}{2F} = 2kr\,i \qquad \{5.5\}$$

Oxygen consumption in the cathode side is given by:

$$q_{O_2}^r = \frac{N_o i}{4F} = 4kr\,i \qquad \{5.6\}$$

The amount of water produced in the electrochemical reaction is calculated using stoichiometric ratio:

$$q_{H_2O} = \frac{N_o\, i}{2F} \qquad \{5.7\}$$

In transient state, there is a delay between the change in the flow of fuel and oxidant. The following relationships are used to represent the delay [61]:

$$\tau_a \frac{dM_{H_2,net}}{dt} = \frac{i}{2F} - M_{H_2,net} \qquad \{5.8\}$$

$$\tau_c \frac{dM_{O_2,net}}{dt} = \frac{i}{4F} - M_{O_2,net}\tau_c \qquad \{5.9\}$$

Equations {5.4} and {5.5} can be combined and rewritten in the (s) domain, and replacing the output flow by Equation {5.1}, taking the Laplace transform of both sides and separating the hydrogen partial pressure as:

$$P_{H_2} = \frac{1/k_{H_2}}{1+\tau_{H_2}s}\left(q_{H_2}^{in} - 2kr\,i\right) \qquad \{5.10\}$$

Where:

$$\tau_{H_2} = \frac{V_{an}}{k_{H_2}RT}\, s \qquad \{5.11\}$$

The partial pressures of water P_{H_2O}, and oxygen P_{O_2} can be derived using equation{5.10}. The water and oxygen time constants τ_{H_2O} and τ_{O_2} can be calculated using equation{5.11}. The assumption is that no liquid water is carried by the inlet air that enters the cathode channel (the membrane does not allow liquid water transport; rather it allows only gaseous transport).

5.2.2 Electrochemical Equations and Voltage Calculation

The polarization curves for the PEM FC are described in [52; 53]. Due to the convention for voltage losses the actual FC voltage is the addition of the following four terms: the Nernst voltage in terms of gas molarities, the voltage losses in activation overvoltage, ohmic overvoltage and Mass Transport Losses. Therefore, the polarization curves can be expressed in the following equation:

$$\mathcal{V}_{\text{out}} = \text{E} + \text{V}_{act} + \mathcal{V}_{\text{ohmic}} + \text{V}_{\text{conc}} \qquad \{5.12\}$$

The above equation assumes that: oxygen concentration, and the inlet air flow is humidified and there is regularly enough liquid water as described in [73, 52]. The following equations are hence derived to calculate each of the terms in equation{5.12}.

The Nernst voltage is calculated as follows:

$$E = -\frac{Gf_{liq}}{2.F} - \frac{RTk}{2F}(RTk)\log\left(\frac{\left(P_{H_2}O\right)}{P_{H_2}{P_{H_2}}^{0.5}}\right) \qquad \{5.13\}$$

The equivalent temperature was obtained experimentally. The voltage and the ohmic losses are estimated using Ohm's law:

$$\mathcal{V}_{ohmic} = -(i\,r) \qquad \{5.14\}$$

Tafel equation is used to calculate activation losses:

$$V_{act} = -b\log_{10}\left(\frac{i}{io}\right) \qquad \{5.15\}$$

Where the constant

$$b = \frac{RTk}{2\,\alpha F}$$

A concentration loss is obtained as follows:

$$\mathcal{V}conc = \begin{cases} \alpha 1\; i^k\; Ln\left(1 - \dfrac{i}{i_L}\right) & ,1 - \dfrac{i}{i_L} > 0 \\ 0 & ,otherwise \end{cases} \qquad \{5.16\}$$

5.2.3 The Equivalent Internal Resistance

As mentioned in previous chapter section 4.2.1, following the start-up phase, the 1.2kW Nexa™ power module will supply the necessary internal power to operate all the auxiliary subsystems, such as the air compressor, cooling fan, and the control circuit board. Since the module cannot be separated from the auxiliary subsystems, outputs from these subsystems are measured as part of the whole module. Typically in the literature, the internal resistance of the FC stacks which is not the internal resistance of the module is measured. Therefore, the assumption of a constant stack internal resistance and stack temperature will not provide accurate results in the case of a Nexa™ module.

It is more accurate to use the equivalent internal resistance and the stack temperature to measure the internal resistance. To investigate the characteristics of this equivalent internal resistance, an experiment was carried-out under steady-state by adjusting the load to obtain different output voltages of the module by increasing the load current from 1 to 46 A in steps of 0.1A. In this test, the open-circuit voltage of the power module, the output voltage of the power module and the stack current were measured directly. The measured data were used to obtain the equivalent internal resistance which can be determined by:

$$r = \frac{V_o - V_{out}}{i} \qquad \{5.17\}$$

Where (V_o) is the open-circuit voltage of the power module. (i) is the output current of the module; (V_{out}) is the output voltage of the power module. The relationship between the equivalent internal resistance r and the module output current was recorded which represented by the current density $j = \frac{i}{A}$ ($A\,cm^{-1}$) as shown in Figure 5.1. As can be seen, the internal resistance varies with the variation in the load current. This is also due to the conductivity of the membrane is highly affected by the temperate and the water content [74]. The results from the experiments have indicated that both the stack temperature and the equivalent internal resistance are not constant and change as a function of the load current.

Initially using constant values in the simulation for EIR and temperature resulted in an error (simulation versus experimental results) of about 12.1% for the full working process (i.e. including both the start-up and steady state). However, if we use instead the experimental values obtained from the Nexa system in the lab as shown in Figure 5.2., it reduces this error

to about 4.1% i.e. an improvement of around 8%. This will also help in obtaining more accurate results for the other parameters (e.g. the stack current and the corresponding hydrogen and oxygen flow that react).

The electric power delivered by the stack is the product of the stack voltage $\mathcal{V}_{\text{out}}$ and the current drawn i is:

$$P_{out} = \mathcal{V}_{out}\ i \qquad \{5.18\}$$

$$i = IA \qquad \{5.19\}$$

Where I is the cell current density and A is the cell area

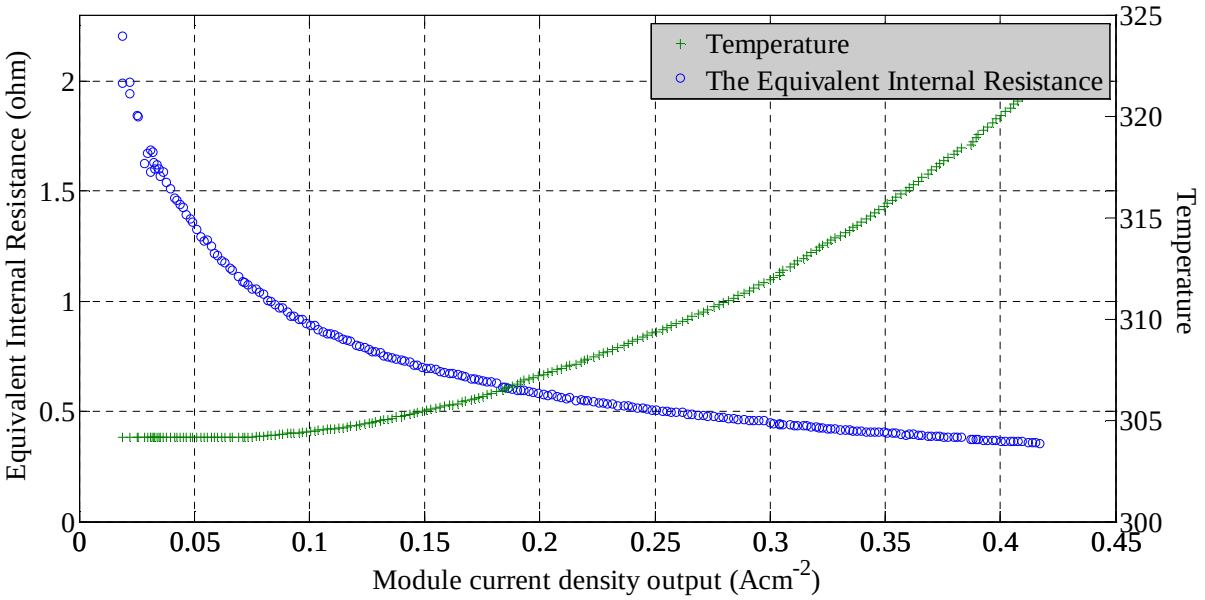

Figure 5.1 The relationship between r (Ω) and module i (Acm^{-2})

The curve fitting equation for EIR is given by:

$$EIR = (194.48 * i^4) + (-214.19 * i^3) + (85.909 * i^2) + (-15.941 * i) + 1.6723$$

The temperature (in Kelvin) is given by: $T = (127.69 * i^2) + (-12.478 * i) + 304.42$

Where "i" is the current density (Acm^{-2})

Based on our observations a new parameter extraction method is given in Table 5-1. Some parameters were determined experimentally.

Table 5-1 PEMFC model parameters

Par	Representation	Units	Value
R	*Ideal gas constant*	$[J/mol\ K]$	*8.314*
F	*Faraday's constant*	$[Coulombs]$	*96487*
Tc	*Temperature **	$[C^o]$	*25*
Tk	*Temperature*	$[k]$	*273.15*
P_{H2}	*Hydrogen pressure*	$[atm]$	*1.273*
P_{H2O}	*water pressure*	$[atm]$	*1*
P_{O2}	*Oxygen pressure*	$[atm]$	*0.16*
A	*Area of cell*	$[cm^2]$	*110*
No	*Number of Cells*	$[No.]$	*46*
r	*Internal Resistance **	$[\Omega/cm^2]$	*0.50*
q_{H2}	*Molar flow of hydrogen*	$[kmol\ s^{-1}]$	*1.5186*
q_{O2}	*Molar flow of oxygen*	$[kmol\ s^{-1}]$	*0.8930*
α	*Transfer coefficient*		*0.5*
$\alpha 1$	*Amplification constant*		*0.095*
io	*Exchange Current Density*	$[A/cm^2]$	$6^{6.912}$
iL	*Limiting current density*	$[A/cm^2]$	*0.418*
Gf	*Gibbs function in liquid form*	$[J/mol]$	*-228170*
k	*Constant k used in mass transport*		*10*
k_{H2}	*Hydrogen valve molar constant*	$[kmol\ s^{-1}\ atm]$	*1.0124*
k_{O2}	*Oxygen valve molar constant*	$[kmol\ s^{-1}\ atm]$	*0.893*
k_{H2O}	*Water valve molar constant*	$[kmol\ s^{-1}\ atm]$	*0.00057*
Vca	*Volume of the anode channel*	$[m^3]$	7.59×10^{-4}
Van	*Volume of the cathode channel*	$[m^3]$	7.59×10^{-4}
kr	*Modelling constant*	$[kmol\ s^{-1}\ A]$	1.192×10^{-6}

* *Experimentally determined parameters*

5.3 Results and Discussion

As discussed earlier, the Nexa FC stack was also modelled mathematically. The inputs to the model are the fuel (oxygen, and hydrogen) and the operating environment (ambient temperature and relative humidity). The stack outputs are the FC stack voltage, current delivered by the stack and the water produced by the chemical reaction.

The validation process consists of simulating the model by applying the real system inputs and comparing those with the experimental results. In order to accomplish this, the following two tests were conducted: (i) constant load (to investigate the equivalent internal resistance and to analyse the steady-state effects), (ii) variable load (to analyse the transient effects). To analyse the track changes in the output parameters and other factors, the output values are treated as a function of time so as to capture any changes in these parameters while plotting.

5.3.1 Steady-State

The steady-state characteristics of the FC were obtained by increasing the load current from 1 to 46 A in steps of 0.1A. In this test, the stack current was measured directly and the measured data were used to validate the model. A comparative graph of this experimental voltage and simulated voltage (constant/vary stack temperature and internal resistance) as a function of time is shown in Figure 5.2.The voltage delivered by the stack is validated by plotting the curves between the present voltage of the cell and the current density, $j = \frac{i}{A} (A\ cm^{-1})$. The voltage values corresponding to the current density taken from the Ballard stack are shown in Figure 5.3.

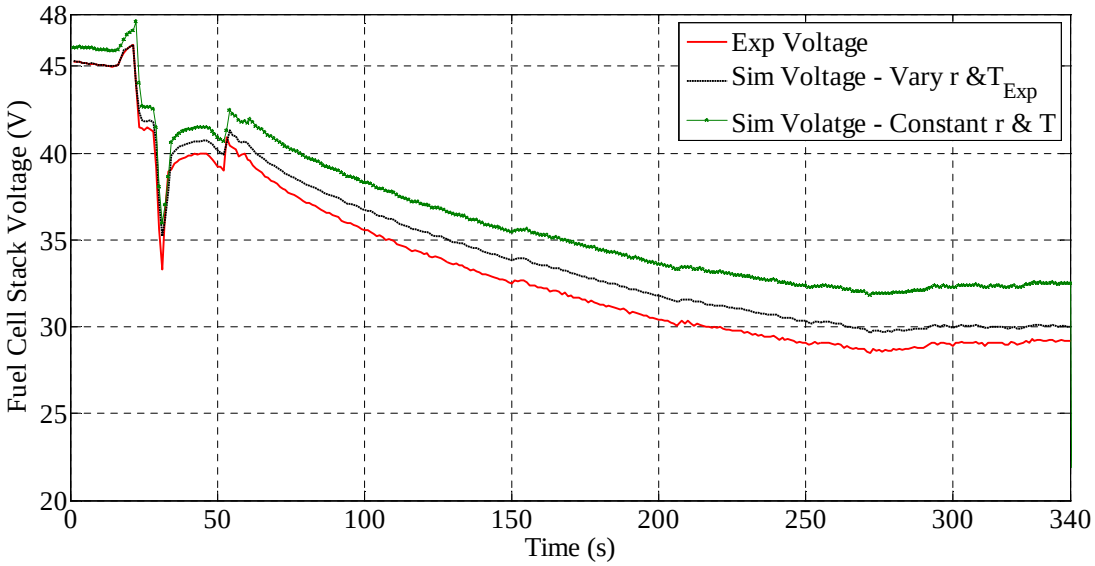

Figure 5.2 Stack voltage (V) during steady-state test

A FC polarization curve that corresponds to the 1.2kW stack is shown in Figure 5.4.

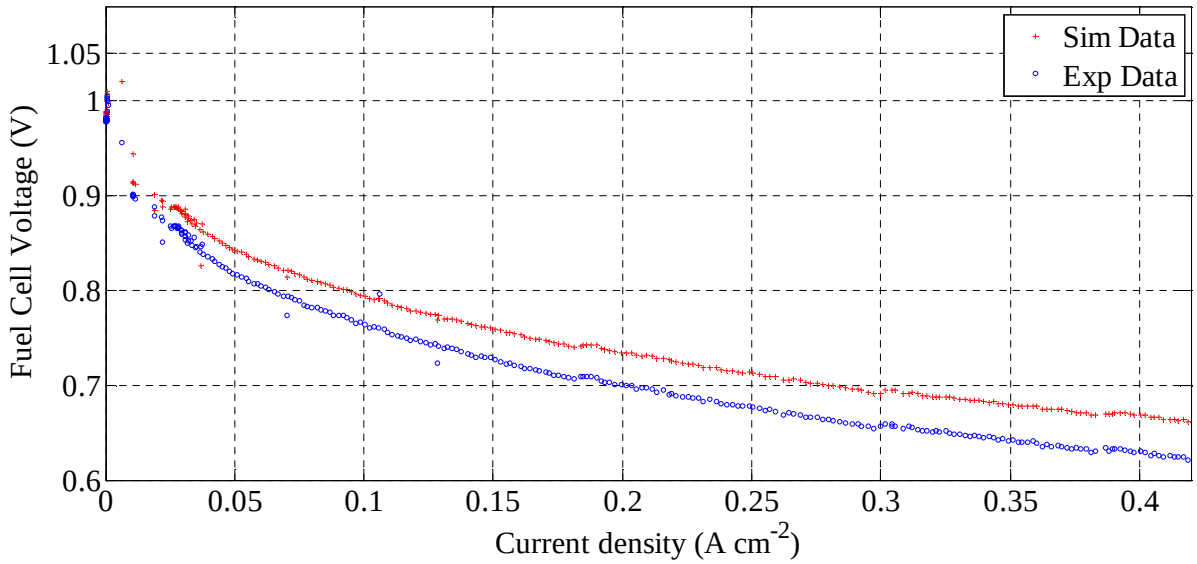

Figure 5.3 Stack current (A cm-2) versus stack voltage (V) in steady-state test

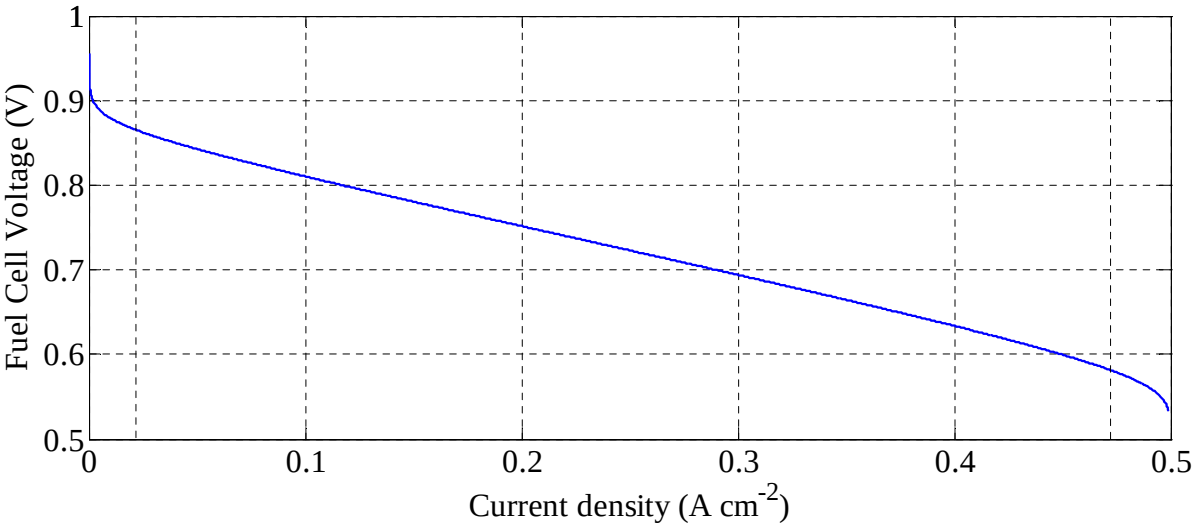

Figure 5.4 Fuel cell polarization curve

Figure 5.5 describes the drop of FC voltage as a function of current density. Due to the open circuit voltage, the activation overvoltage will decrease as the current delivered by the stack increases. As the current density gets higher at a later step, the ohmic losses will also increase. This is derived from the resistance to the proton/electron conduction through the membrane/electrode.

The last type of losses is the mass transport or concentration losses. This loss takes place in both low and high temperature fuel cells, but it is only prevalent at high current densities [54]. Usually in the case of the Nexa system, this occurs when we reach or slightly exceed the

maximum rated output power. This is due to the effect of losing a high concentration of either oxygen or hydrogen at the cathode or anode sides, respectively. In other words this occurs when the FC is using oxygen or hydrogen at a rate quicker than it can be supplied. Despite the fact that the last drop has been modelled based on equation {5.16}, such high current values are not usual because they can cause quick degradation of the cells membranes. The summation of all the above losses forms the output voltage, producing the polarization curve as shown previously in Figure 5.4.

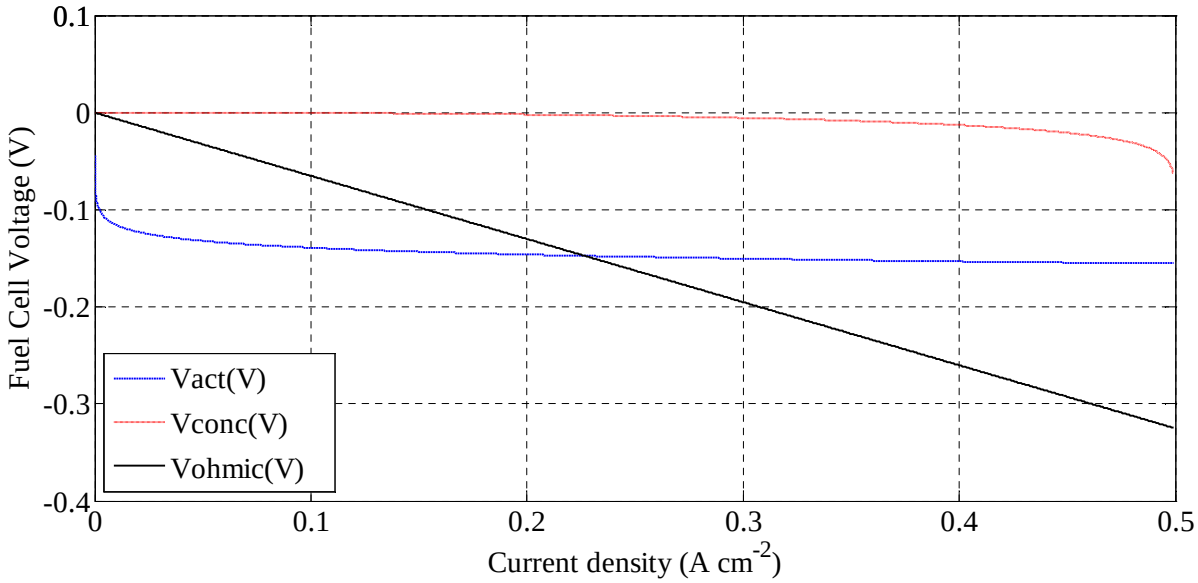

Figure 5.5 FC voltage drops contributions as a function of current density

Figure 5.6 shows the flow rate of hydrogen and Oxygen from the simulation model during the system start up and normal operation stages. It can be seen that by increasing the load current from 1 to 46 A in steps of 0.1A it takes around 275 seconds for the system to reach the steady state and for the flow rate reaction to become steady.

Figure 5.7 illustrates the stack output power as a function of current density. The electric power delivered by the stack is equals to the product of the stack voltage and the current drawn as given in equations {5.18} and {5.19}. The current input is taken from the experimental measurements. As shown, the response of the model matches well with the experimental data. Note that there is no peak output power, because the FC does not go into the concentration loss region.

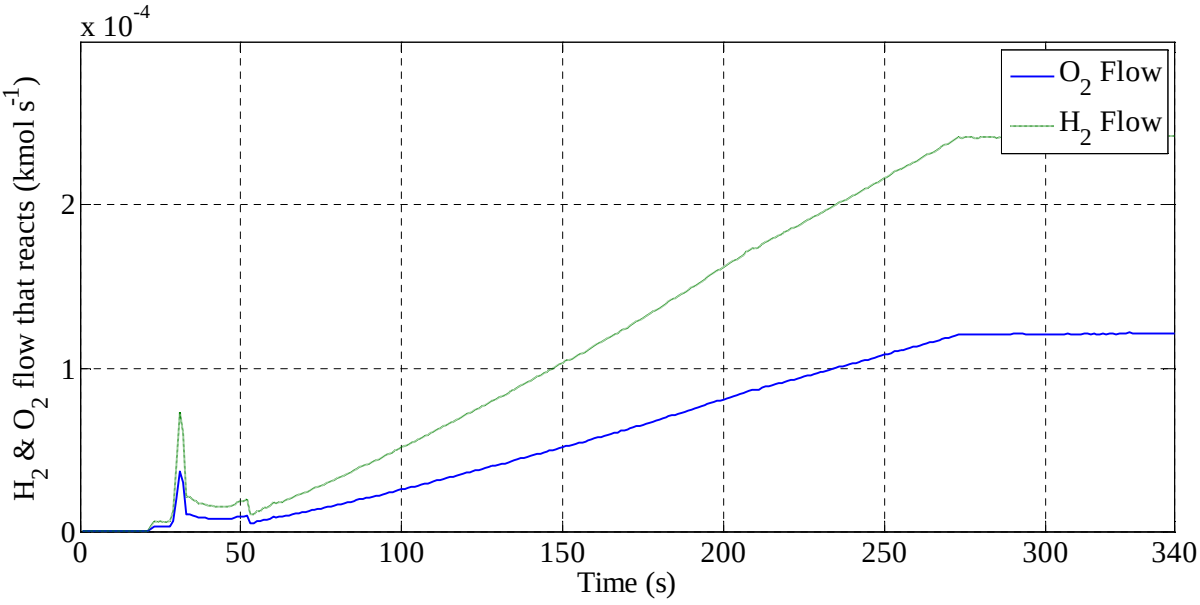

Figure 5.6 Hydrogen and oxygen flow that react during steady-state test

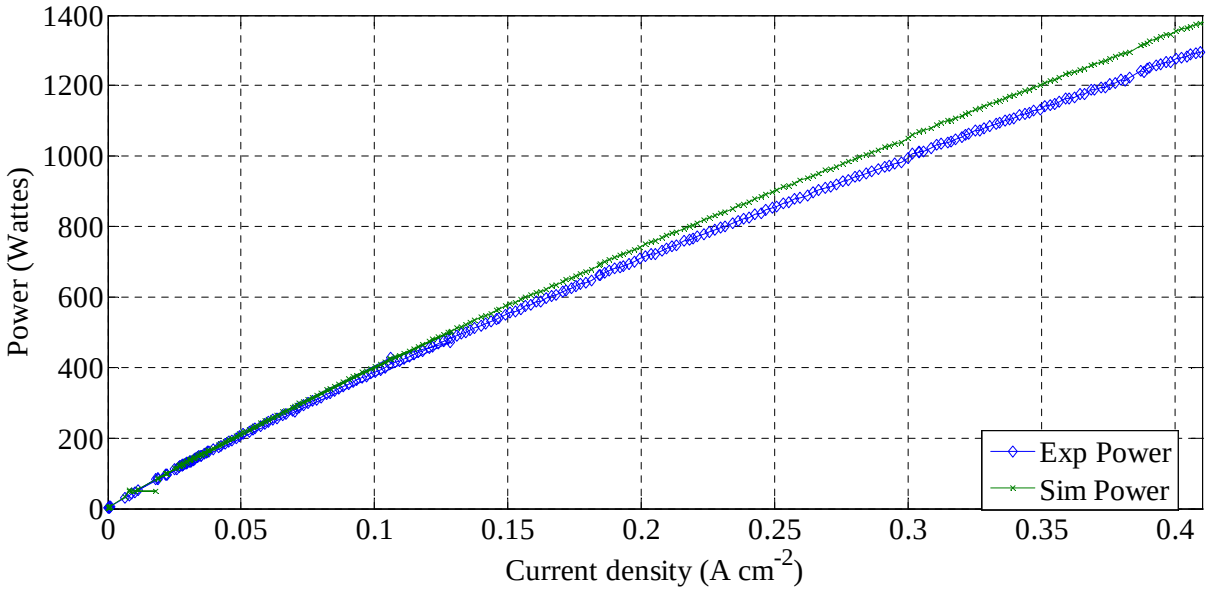

Figure 5.7 Power curve (Gross Power) during steady-state test

5.3.2 Transient Response

The results shown in Figure 5.8 describe the transient responses of the FC parameters (stack current and stack voltage) during step-up and step-down load variation including the experimental data to show the accuracy of the proposed theoretical model.

It is worth mentioning that the first transient response (at around t = 28 seconds) is due to the system start-up. At t = 305 seconds, the current decreases from 34 Amps to 1 Amps, the

simulated stack voltage increase from 34V to 43V, respectively. The improved model gives a very good response and closely follows that obtained from the experimental data. Finally, the corresponding hydrogen and oxygen flow that react during this transient-state test were calculated using equations {5.5} & {5.6} and plotted in Figure 5.9.

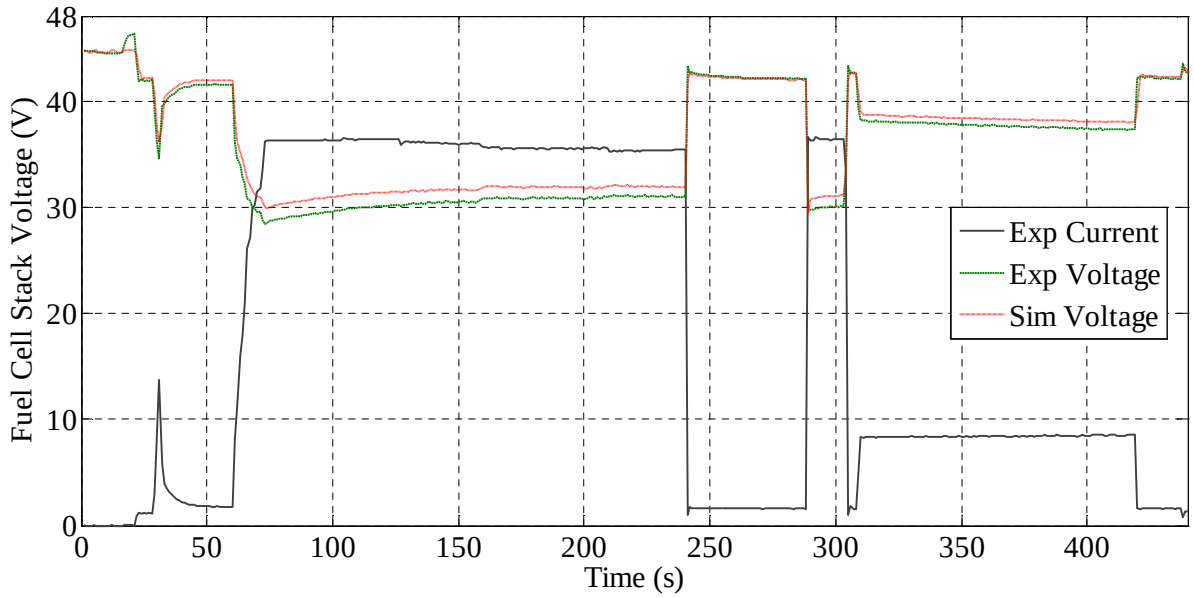

Figure 5.8 Output Voltage during transient -state test

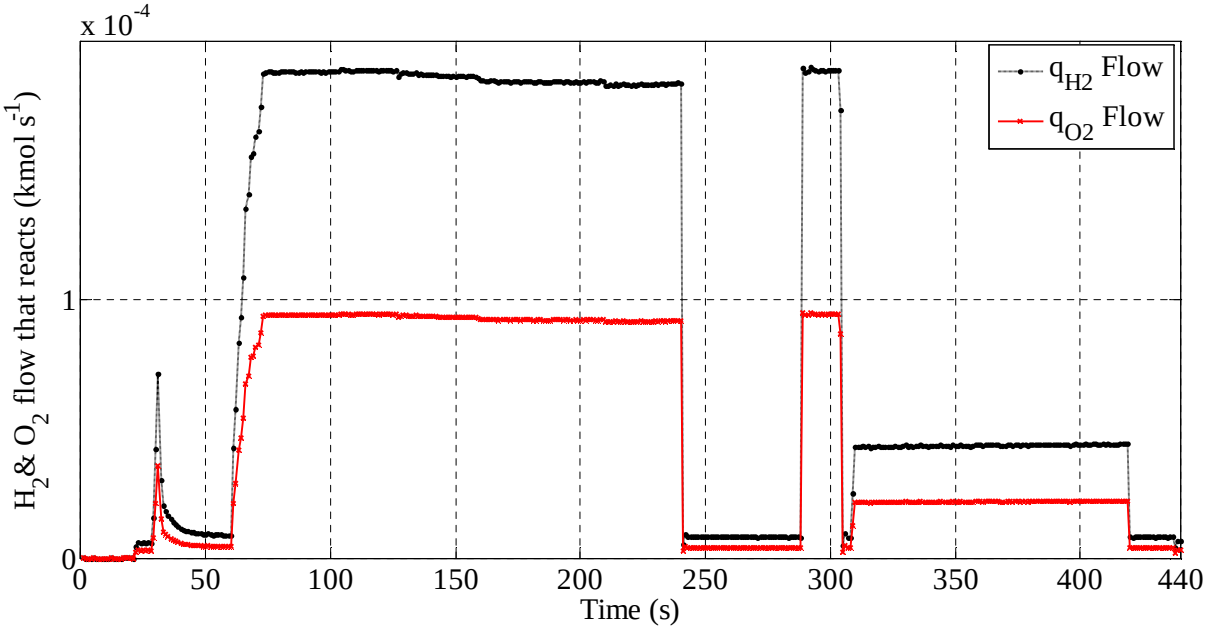

Figure 5.9 Hydrogen and oxygen flow that react during transient -state test

5.4 Model Validation

To check the validity of the model, simulations were carried-out to compare the results with those obtained from the experimental system. Furthermore, the simulation of a1.2kW stack model for both study state and transit state were also covered by considering the effect of the internal resistance under a variety of load variations. Taking the equivalent internal resisters into account has significantly improved the model results and demonstrated around 8% improvement over the constant internal resisters.

Simulation results show that the models can predict the electrical response of the PEM fuel-cell stack under steady-state as well as transient conditions. Based on the obtained simulation results, it is observed that the relative error is less than 4.1% for the full working process including the start-up sequence and the transient phase of this proposed model.

This could be explained by the following two points:

- **Amount of condensed water:** the liquid water, decreases the gas diffusion layer surface, as a result there will be a drops in voltage and FC efficiency, thus increasing the current density [42].
- **Variation of partial pressures**: Variations of the hydrogen partial pressure inside the anode and oxygen partial pressure inside the cathode mainly influence the voltage obtained by the fuel cells. As the pressure of any of these gases increases, the voltage raises for every current stage. Due to the dead-end design of the FC stack system, hydrogen partial pressure inside the anode remains almost constant. Hence, the oxygen partial pressure is more variable during the power demand changes, since it depends on auxiliary equipment dynamics [75]. For more details of the validation of the model accuracy, another error analysis has been performed here using the mean relative error (MRE) as follows:

$$MRE(\%) \;=\; 100 \times \frac{1}{N} \sum_{i=0}^{n} \left| \frac{D_i^e - D_i^s}{D_i^e} \right| \qquad \{5.20\}$$

where (N) is the number of samples, and (D_i^e) and (D_i^s) represent the experimental and simulated data sets, respectively. Employing equation {5.20}, the MRE criterion is applied to the dynamic responses of the stack voltage during both steady state and transient state. Consequently, the relative mean errors of the parameters obtained are 4.1% and 3.3%, respectively.

5.5 Summary of Chapter 5

The above chapter can be summarized by the following points

- A summary of the main FC models developed the over the last decade and published in the open
- A dynamic electrochemical simulation model of PEM FC is proposed and its parameters were adjusted specifically for a $1.2kW\ Nexa\ stack$.
- In addition, instead of assuming a constant temperature in the simulation model, the equivalent internal resisters and temperature experimentally obtained from the $Nexa^{TM}\ module$ system in the lap were used. Comparing the results obtained from the improved simulation model with those from the experimental for the same conditions shows about 8% reduction in error
- The model assumptions are discussed with the theoretical equations. Furthermore, the performance of the model is studied and validated for both steady state and transient state. The results show that the percentage error of the simulated model when compared with calculated using MRE does not exceed 4.1% for the full working process, including the start-up sequence and the transient phase.
- The validated model can provide the basis for deriving flexible design options and the real-time control for FC hybrid system.

In conclusion, one important consideration that should be taken into account when developing FCs systems, is that the equivalent internal resisters of the fuel cell stack is different from the internal resistance of fuel cell. Moreover, the assumption of a constant stack temperature will not provide accurate results in the case of a $Nexa^{TM}\ module$. Thus, the stack temperature should also be considered.

It is valued to design new strategies for controlling the oxygen excess ratio. One starting point could be applied is that; the real-time processing and the advantage of real time neural network estimator can be used.

Chapter 6

Control Strategy

6. CONTROL STRATEGY

In this Chapter, details are given regarding the control strategies that were followed to manage the power in flexible way between each source in this work. An overview of the most common control algorithm- PID controller is briefly discussed along with each term-action; in addition to Integrator Windup and the control objectives. The implementation and the methodologies followed to design and train the controller namely PI, PI controller with anti-windup and ANNC are explained in detail along with the generated references that were used in this design. Finally, the fuel cell optimal operating points are studied followed by discussion of the performance of each controller and the validation.

Several studies on control strategy for FC hybrid electric systems have been carried-out for different applications, based on different control methodologies. Primarily used hybrid FC control strategy is either the load following, where the FC power is set to meet the driver request, or the SOC based control approach. Sometimes a combination of both is also used [76]. The simplest method of the SOC based control turns $On\ or\ oFF$ the FC at given accumulator SOC thresholds. This is commonly used with small APU FC; while in case of larger FC, the FC operation is approximated in many power levels. Those approaches do not take the energy minimization into account. Thus, they do not achieve the optimal fuel range. The following approach offers to bridge this gap.

The main problem arising in the design of the FC hybrid power source is the algorithms for control of the power sharing. The study described in [77] deals with control methods based on two different and conflicting objectives: either maximizing the efficiency of the FC source or maximizing the FC output power. With the previous strategy, the FC would reach the maximum efficiency. However, the battery would eventually run down to depletion; while, with the second strategy, the battery would ultimately become fully charged. Yet, the efficiency would not be maximized

HE Hong-wen, et al. [78] have applied a control strategy for a 5-ton PEM fuel cell and high-power NiMH battery pack hybrid electric bus based on the basic control logic. The results obtained from their experiment point out that the power output of the fuel cell engine follows the driver pedal and drives the motor with better power. However, the battery pack provides

only peak power passively and the average hydrogen economy of the hybrid fuel cell bus is 2.464kg/100km.

Phatiphat, et al. [79] presented a control strategy for a small-scale test bench of 42V, 500Wdc bus having a PEM fuel cell as the main source and super-capacitors as the auxiliary power source for electric vehicle applications. Their main objective is to regulate dc bus voltage based on PI controller using a link voltage regulation; while the fuel cell is operated in almost steady state conditions. Their experimental results with $a\ 500W\ PEM\ FC$ show the FC starvation problem when operating with a dynamic load. The results also confirm that the super-capacitor can improve the system performance for hybrid power sources.

Another approach is found in the work of Masoud and Amin [80], wherein they presented a control strategy of a hybrid fuel cell/battery distributed generation system. The base of the method is to control the power flow from the hybrid power plant to the utility grid and to distribute the power between the fuel cell power plant and the battery energy storage, using $a\ neuro\text{-}fuzzy\ controller$. In addition, for controlling the active and reactive power independently in distribution systems, the current control strategy was based on two Fuzzy Logic controllers. Their simulation results show that the overall system performance including load-following and power management of the hybrid fuel cell distributed generation system is efficient. Also the results point out that the real and reactive power delivered from the FC system to the utility grid can be controlled as desired.

In [82], proposed a control strategy with two objectives: maintaining the state of charge in the batteries above a minimum value and obtaining high efficiency in the hybrid system. If both objectives cannot be satisfied simultaneously, the priority is given to the battery state of charge. Schiffer at el. [83], investigated three control strategies and compared them using a FC hybrid vehicle model. Its objective for energy management is to assure power availability at any time and minimize the hydrogen consumption that leads to an efficient operation of the FC. Their results show that the strategy of utilizing the super-caps with their maximum power in both acceleration and deceleration stages is the best strategy. This resulted in more than 20% hydrogen fuel saving; whereas, controlling their voltage in constant speed and stoppage stages to reach an optimum voltage that depends on the vehicle speed.

One of the proposed control strategies is the hybrid FC/battery to power the train based on optimization techniques presented in [76]. This method is based on a control strategy called

$Equivalent\ Consumption\ Minimization\ Strategy$ $(ECMS)$ and the strategy is to convert all the power flows in equivalent hydrogen consumptions. Yet, the performance of the $ECMS$ is very sensitive to other parameters. i.e. small nonlinear penalty will affect the performance of the $ECMS$. Using the same concept, in [84], an $ECMS$ applied to a real FC/super-capacitor powered vehicle to achieve the real-time optimal power distribution was developed. Experimental results show no significant fuel efficiency improvement with the $ECMS$ approach compared to the original map-based control strategy, which is initially implemented in the vehicle.

One of the most recent and relevant method is presented in [85], wherein a methodology based $Multi\text{-}objective\ genetic\ algorithms$ is applied to achieve parameter optimization for powering the train components and control system simultaneously. Their simulation results show that this method can provide several Pareto-optimal solutions and an acceptable solution can be chosen by decision-makers based on their requirements. Other strategies based on optimization techniques are presented in [86; 87]

Control of the system is required to ensure efficient and robust power transfer from the separate sources without risk or damage of the components. In order to achieve continuous power flow to the load, the controller must control the power converter to regulate the dc bus and balance the power flow from both sources to satisfy the load requirements and their various constraints.

Several control strategies might be applied to meet a set of desired goals; some of them may conflict with other as would be expected, and therefore balances and compromises are necessary. For instance, one may attempt to maximize the $FC's$ efficiency, therefore causing the ESS to run down to depletion. Also, one may choose to charge the ESS only at certain suitable times that would give the maximum efficiency. Moreover, there is yet another balance between efficiency and reliability, when it is desirable to run the FC low power demand to avoid operation in the low efficiency region. As a result, the control strategy can be more complicated by implementing optimization algorithms which would result in best balance between several design objectives and limitations.

In order to achieve the best system performance, instead of choosing a single operating region to satisfy a certain performance objective, each source is controlled in a flexible method in response to the load, to achieve the following objectives:

- ESS should deliver the peak power demand wherever the load is higher than the FC's power capacity
- ESS must provide transient power while the FC rises up to the requested load level to avoid fuel starvation
- dc bus voltage must be controlled at constant value
- FC must charge ESS to maintain it at a desired SOC whenever the load demand is less than the FC's peak capacity to insure maximum power availability to meet peak demand

6.1 PID Controller

The PID controller is the most common control algorithm. The majority of feedback loops are controlled using this algorithm. Essentially most of the loops are PI control. Nowadays, PID controllers are implemented in several different areas and forms. There are standalone controller or as a part of direct digital control package or a hierarchical distributed process control system [88].

Moreover, the controllers are driven in several special purpose control systems. The microprocessor has had a sudden effect on the PID controller. Currently, PID controllers can be designed based on microprocessors. This has given chances to deliver more features [89].

6.1.1 The Algorithm

The "textbook" version of the PID algorithm is defined by:

$$u(t) = K\left(e(t) + \frac{1}{T_i}\int_0^t e(\tau)d\tau + T_d\frac{de(t)}{dt}\right) \quad \{6.1\}$$

where u is the control signal, e is the control error ($e = y_{sp} - y$) and y is the measured process variable. The control signal is as a result of a summation of three terms: the P_term (which is proportional to the error), the I_term (which is proportional to the integral of the error) and the D_term (which is proportional to the derivative of the error). The controller parameters are proportional gain K, integral time T_i, and derivative time T_d.

6.1.2 Proportional Action

In the case of pure proportional control law, Equation {6.1} reduces to

$$u(t) = Ke(t) + u_b \qquad \{6.2\}$$

The control action is simply proportional to the control error. The variable u_b is a reset or a bias. Whenever the control error *e* is 0, the control variable takes the value $u(t) = u_b$. Bias u_b is usually fixed to $(u_{max} + u_{min} / 2)$; however, sometimes, can be adjusted manually therefore the stationary control error is zero at a given set point.

6.1.3 Integral Action

The integral action is to make sure that the process output agrees with the set point during steady state. There is usually a control error with the proportional control during steady state and a minor positive error with the integral action will increase control signal, and a negative error will continuously lead to decreasing control signal no matter how minor the error is.

The steady state error will continuously be zero with integral action as shown in the following argument. Assuming the system is in steady state error with a constant control signal (u_0) and constant error (e_0). From Equation {6.1} the control signal is then given by

$$u_0 = K\left(e_0 + \frac{e_0}{T_i}t\right). \qquad \{6.3\}$$

as long as $e_0 \neq 0$, this obviously reverses the assumption that the control signal e_0 is constant. A controller with integral action will continuously provide zero steady state error.

Integral action can also be visualized as a device that automatically resets the bias term $u_b$of a proportional controller.

From the block diagram in Figure 6.1 a simple calculation can be done to obtain the following equation:

$$u = \mathrm{K\,e} + I \qquad \{6.4\}$$

$$\frac{I}{u} = \frac{1}{1 + sT_i} \Rightarrow u = T_i \frac{dI}{dt} + I. \qquad \{6.5\}$$

Comparing {6.4} with {6.5} one can obtain

$$T_i \frac{dI}{dt} = K\, e \qquad \{6.6\}$$

By solving {6.5} and substituting in {6.4}:

$$u = K\left(e + \frac{1}{T_i}\int e(\tau)d\tau\right) \qquad \{6.7\}$$

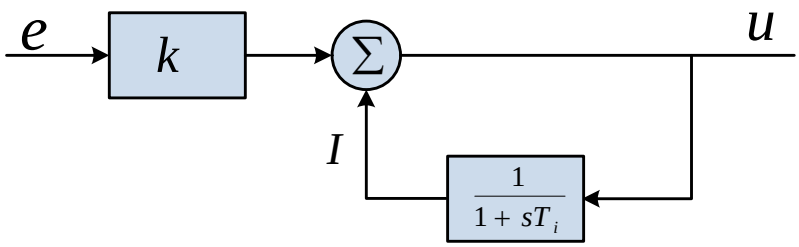

Figure 6.1 Implementation of integral action as positive feedback around a lag

6.1.4 Derivative Action

The derivative action is used to improve the closed loop stability. Derivative control action has no effect on steady-state error, when the rate of change of error is zero. However, in transient state it will tend to speed-up the response time. This control cannot be used on its own but used to complement P-action and I-action to provide the full PID control action [90]. The basic structure of a PD controller is

$$u(t) = K\left(e(t) + t_d \frac{de(t)}{dt}\right). \qquad \{6.8\}$$

In some cases, it is not recommended to use the D-term to control system noise. e.g. switching effect (switching that exist in the converters) because D-term amplify the noise. Hence NS (noise signal) radio will be increased.

To clarify the effect of D-term, we assume the noise signal is sinusoidal

$$N = a \sin wt \qquad \{6.9\}$$

where a is magnitude of the noise signal, w is the frequency of the noise signal

When this signal passes the D-term it will become

$$\dot{N} = a\, w \cos wt \qquad \{6.10\}$$

It is clear that the magnitude of $\dot{N}$ is dependent on frequency of the noise $(a\ w)$ which means the magnitude of the noise signal will be increased with F

$$w = 2\pi F \qquad \{6.11\}$$

The first step was to use PI controller but the performance of the PI controller was not good enough as expected; so the second step in this research is to develop a PI controller with anti-windup. The previous algorithm is modified to design this type of controller in both simulation and the hardware.

6.1.5 Integrator Windup

In the control system with a wide range of operating conditions, some nonlinear effects must be taking into account. Windup is a phenomena caused by the interaction of integral action and saturations. Since all actuators have limitations, there is possibility that the control variable reaches the actuator limits. If this happens, the feedback loop will break and the system goes into an open loop. In this case, if a controller with I-action is used, the error will remain integrated. As a result, the I-term might become very large; hence, it "winds up". Being in this situation, it is necessary that the error has opposite sign for a long time before things return to normal.

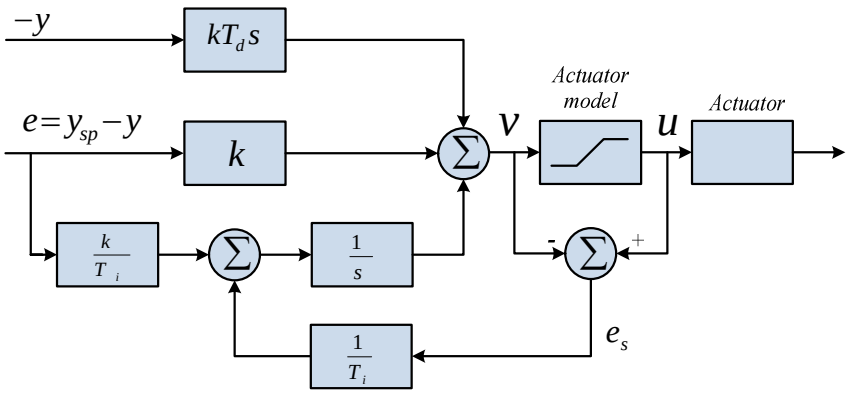

Figure 6.2 Block diagram of a PID controller with anti-windup

There are many methods to avoid windup presented in the literature [90]. Some of those used include Set-point Limitation, Incremental Algorithms and Back-Calculation and Tracking. In this work the Back-Calculation and Tracking have been used as shown in Figure 6.2. This method simply works by taking the difference between the saturation and the controller output, and then the difference serve as feedback to the I-term of the controller. This will guarantee that the difference have opposite sign to the I-term input; thus, the integration will act to reduce its output.

6.2 Design and Implementation of the PI Controller with Anti-Windup

To maximize the PEM FCs efficiency, the optimal operation point of FCs has to be obtained and monitored. The optimal operating point of the Nexa™ power module FC is explained in detail in this section. In order to achieve that goal a PI controller was designed and implemented for the hybrid system in both simulation and the hardware.

As mentioned previously it is not recommended to use the D-term to control such a system, therefore the first step was to use PI controller. However, the performance of the PI controller was not good enough as expected due to the I-term action as explained previously. The second step was to go further to develop PI controller with anti-windup as shown in Figure 6.2.

The implementation of the *PI* controller with anti-windup in hardware is shown in Figure 6.3 The controller parameters are given in Table 6-1.

Table 6-1 PI controller parameters

Parameter	*Value*
Proportional gain (Kp)	*0.1*
Integral gain (Ki)	*0.423*
Saturation	*0.75 -1.2*

The implementation of the PI controller with anti-windup in hardware was based on 1.2kW PEM FC stack (Ballard Nexa1.2 kW), and two batteries in series providing 12V each to the control board, then connected to a 27 V DC/DC step-down converter (BSZ-PG 1200) to keep the output voltage constant. Another 36 V batteries connected to the resistive load through a

DC/DC Bidirectional converter to charge/discharge the battery as shown in Figure 6.3. A multi-functional data acquisition (DAQ) unit is supplied facilitating status monitoring and data recording. In order to measure different operating parameters, current and voltage sensors were used to report feedback signals through the serial port communication. To simulate a variable power demand, the energy produced was delivered to an electronic load. For real-time control and experimental observation, Lab-View based software is used.

The Simulink implementation of the PI controller with anti-windup schematics for this approach is presented in Figure 6.4. The structure of the controller has two loops based on the two variables that have been chosen to be controlled by this control loop. The first loop is a battery state of charge SOC control loop composed of (SOC_{Ref} as a reference of SOC represented by battery voltage and I_{Bat}^{HV} as a battery current feedback). The second loop is the power or current demand composed of (current demand I_D as a reference to meet the power demand requested from the load and I_{Bat}^{LV} as a battery current feedback).

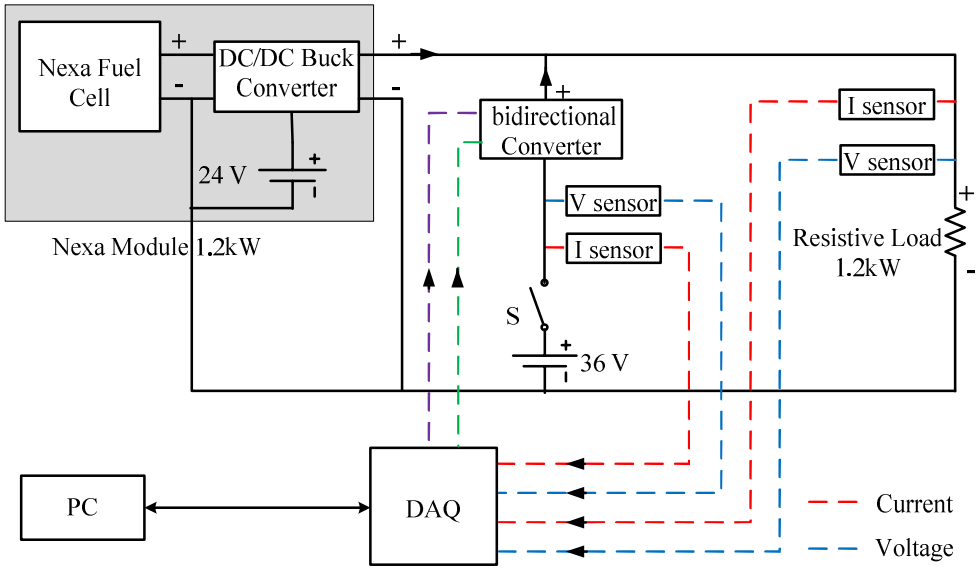

Figure 6.3 Block Diagram of PI controller with anti-windup implementation

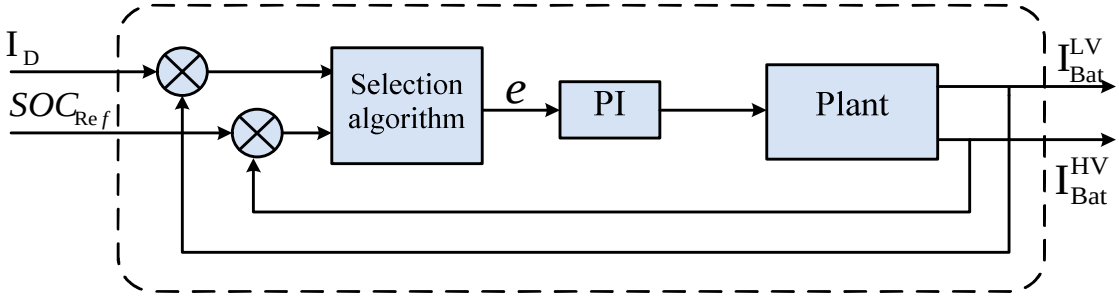

Figure 6.4 PI with anti-windup controller Simulink implemented system

The problem of meeting the power demand is simplified by splitting the problem into two (current problem and voltage problem). Since the FC step down converter maintains the BUS voltage at constant value of 27V, hence, the current problem is solved from the relationship defined as:

$$I_{LV} \text{ or } I_{BUS} = I_{FC}^{LV} + I_{Bat}^{LV} \quad \{6.12\}$$

Which is continuously equal to the total current demand I_D; where I_{FC}^{LV} and I_{Bat}^{LV} are the currents supplied to the bus by the FC and battery respectively. Negative battery current ($I_{Bat}^{LV} < 0$) represents the battery charge and positive ($I_{Bat}^{LV} > 0$) represents the battery discharge. Maintaining the bus voltage constant using the FC dc/dc converter and the bidirectional dc/dc converter gives the possibility of controlling the current problem. The current demand I_D is a measured variable; hence, by controlling I_{LV} , the amount of current drawn from the FC can be determined.

The relationship between the FC output power and efficiency was determined experimentally and results show that the FC efficiency is inversely proportional to the amount of power supplied. However, the dc/dc step-down converter used to keep the FC to a constant bus voltage has a higher input/output efficiency at high power. Combining efficiency with a peak represents the operating point for maximum fuel economy, occurs at I_{FC}^{LV} of ≅ 15 A with 27 V bus. Assuming this current as the FC ideal operating current in the rest of this research project and represent it by I_{FC}^{OP}.

The current that the battery pack is capable of providing depends on its SOC. The SOC is usually defined as the ratio of energy stored in the battery to the rated energy capacity of the battery [91].

$$\overline{SOC} = \frac{V_{Bat}^2}{V_{Bat}^{2Max}} \quad \{6.13\}$$

Where V_{Bat} is the battery instantaneous voltage and V_{Bat}^{Max} is the maximum rated voltage of the battery.

As a result, the SOC can be defined as

$$SOC = \frac{V_{Bat}}{V_{Bat}^{Max}} \quad \{6.14\}$$

Which ranges from “0” at no charge to “1” at full charge.

The key parameter when determining the current shared between the two power sources is the battery SOC. One of the control objectives is to enforce upper and lower limits on the battery SOC at all times. Here we refer to these bounds of the battery SOC between (0.7 - 1).

In this proposed architecture, the charge/discharge of the battery is achieved by controlling the PWM duty cycle applied to the bidirectional DC/DC converter. The relationship between the battery currents before and after the converter I_{Bat}^{HV} and I_{Bat}^{LV} respectively, is determined by the power conservation:

$$\beta \,.\, I_{Bat} \,.\, V_{Bat} = V_{BUS} \,.\, I_{Bat}^{LV} \qquad \{6.15\}$$

$$\beta = \begin{cases} \eta_{discharge}, & while\ discharging \\ 1/\eta_{charge}, & while\ charged \end{cases} \qquad \{6.16\}$$

where β is conservation of power, V_{Bat} is the voltage of the battery, V_{BUS} is the bus voltage, and $\eta_{discharge}$ / η_{charge} are the discharge/charge efficiencies respectively.

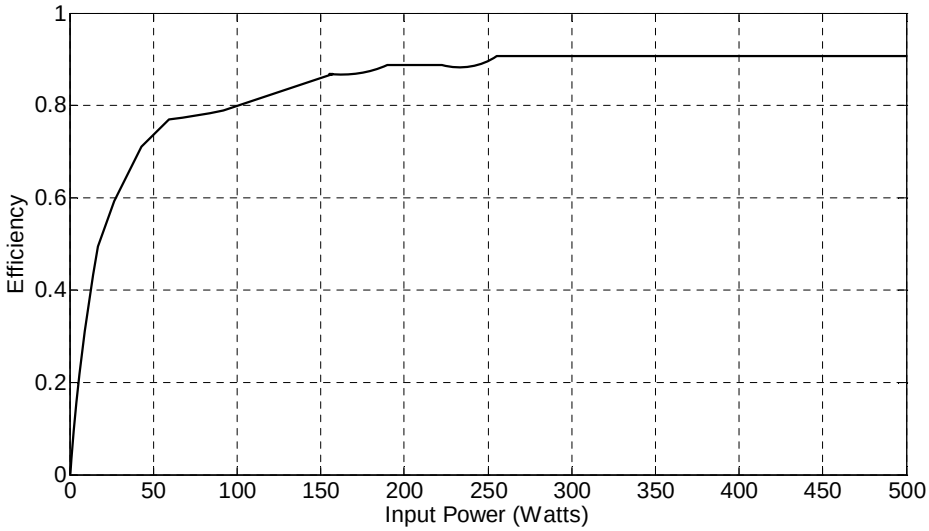

Figure 6.5 Bidirectional dc/dc converter efficiency map

When given the current demand I_D and the battery SOC, a bidirectional dc/dc converter efficiency map as shown in Figure 6.5 can be used to determine the current which is needed from the battery (I_{Bat}^{OP}) in order for the FC to deliver its ideal operating current (I_{FC}^{OP}). Thus, once I_{FC}^{OP} is specified, and I_D and SOC are measured, I_{Bat}^{OP} can be determined from equation{6.17}.

$$I_{Bat}^{OP} = \frac{V_{BUS}\left(I_D - I_{FC}^{OP}\right)}{\beta \cdot V_{Max} \cdot SOC} \quad \{6.17\}$$

where V_{Max} is the battery voltage at full charge.

The electric power delivered by each source (FC & battery) and the total power demand is simply calculated as follows:

$$\begin{aligned} P_{FC} &= \mathcal{V}_{FC}\ I_{FC} \\ P_{Bat} &= \mathcal{V}_{Bat}\ I_{Bat} \\ P_D &= \mathcal{V}_{LV}\ I_{LV} = P_{FC} + P_{Bat} \end{aligned} \quad \{6.18\}$$

A selection algorithm was developed to determine the battery current, based on the battery SOC and the current demand. The FC delivers the difference between the current demand and the current delivered by the battery pack. The FC operating current, current demand and the battery SOC are used along with {6.17} to determine I_{Bat}^{OP} required by the battery in order for the FC to provide its operating current.

6.3 Battery Current Control Charge/Discharge

The major challenge in the presented hybrid system is how to control the battery current charge/discharge. For example, if the battery is fully charged and the converter continues charging the battery, this situation may damage or even lead to the battery exploding during the process. In this proposed hybrid system, two steps are followed to manage the charging/discharging process; firstly, optimizing the charging rate by monitoring the battery voltage to determine the optimum current at that time and secondly, identify when to stop/start the charging/discharging process.

Charging up the battery is adjusted by its SOC, whenever the load current is equal or less than the optimal FC current:

- If battery SOC is less than SOC_{Ref}, the battery charging current reference is positive and a FC current is needed to charge up the battery until it reaches its limits
- If battery SOC is higher than SOC_{Ref}, the battery charging current reference is equal to zero.

As a result, by applying these states or conditions, battery pack will be kept at a desired SOC. So whatever the load demand is, the battery discharging current reference is positive and a battery current is necessary, unless battery SOC is less than SOC_{Ref}. In case of transit state, even if the battery SOC is still below its maximum, a battery current is necessary to supply the remaining power.

6.4 Experimental Results

In this subsection, three tests are carried-out to assess the performance of the PI controller, PI with anti-windup controller and a simulation test to compare the response between them.

6.4.1 Performance Test of the PI Controller in the Hardware Loop

In this subsection a test was carried-out in the hardware-in-the-loop to assess the controller performance. The response of the controller was acceptable and no oscillation were observed as can be seen in Figure 6.6. However, using PI controller was marked by small overshoots specifically at switching time with a magnitude of around 1.5 Amp. This overshoots of the fuel cell current amplitude was during the transient state or sudden power demand load changes (faster current changes cause higher load transients). The worst case overshoot occurs at about t = 100 s, when the current demand jump from about 7 Amp to 46 Amp. In this case, about 15.5 Amps will be provided by the battery and the fuel cell will provide the remaining 30.5 Amps. However, as can be seen in Figure 6.6 zoomed area, the fuel cell current has a maximum overshoot of about 1.5 Amps (i.e. 4.6% overshoot) before settling down. After the overshoot, the system was again allowed to reach its steady state behaviour and the fuel cell current returns to its nominal values in approximately 8 seconds. The other two overshoot values and the system behaviour are very similar to the previous case. However, the overshoot values depend on the power demand; in other words these values are proportional to the power demand.

The overshoot could be explained as having occurred due to the fast demand of power by the auxiliary equipment and as mentioned before, the FC stack has a relatively slow response. This overshoot has a major impact on the voltage response, thus, the power fluctuation equally impact negatively on FC durability. When the load current rises up from a lower to a higher value, the output voltage of the step down DC/DC converter drops and then returns

back to its nominal value, which is called voltage undershoot. Similarly, voltage overshoot happens when current goes down from a higher to a lower value, the DC/DC output voltage spikes up and then return back to the nominal value.

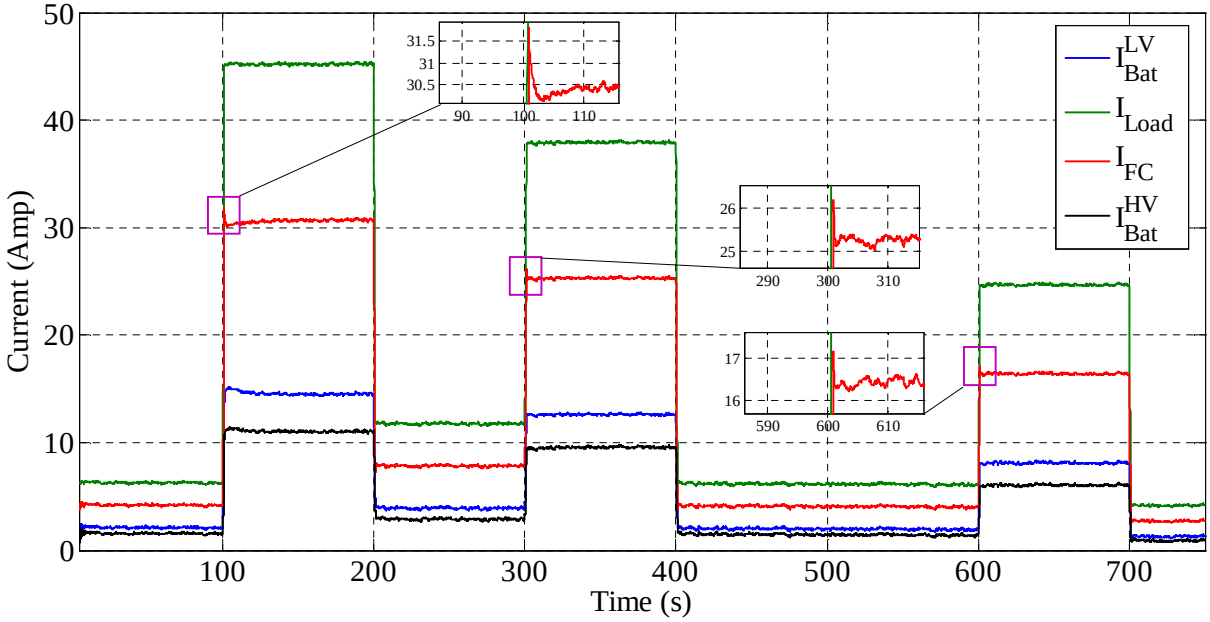

Figure 6.6 PI controller performance test in the hardware loop

6.4.2 Performance Test of the PI Controller with anti-windup in the Hardware Loop

As mentioned previously, in order to prevent integration wind-up problem and improve the PI controller performance, a PI controller with anti-windup was implemented and tested in both simulation and hardware loop. A fully charged battery is used in this test and the load current was set to 30 Amp. 25 Amp was delivered by FC and the remaining current was taken from the battery. At about 70 second the battery discharged to share the load current by 13 Amp as shown in Figure 6.7. The PI controller with anti-windup responded after about 3 seconds and it took 7 seconds to go back to the desired operating point, therefore the anti-windup slows the response of the system. However, there is no overshoot was observed,

While carrying out some experiments in the hardware loop to evaluate the performance of the PI controller and the PI with anti-windup, some issues were identified. These are:

- Since the mathematical model of this system is very difficult to obtain, the suitable method for tuning the controller is manual tuning. This method consumes time and money, and might harm the devices if unstable values are chosen for the controller during the tuning process. However, in the absence of an accurate mathematical

model for the control system, it is difficult to measure the stability margins and optimality of the system.

- Another problem is that oscillations always exist when trying to achieve fast response and vice versa when trying to avoid unnecessary oscillations which are not acceptable in such a system.
- Change in the control settings is needed due to the battery voltage variations.

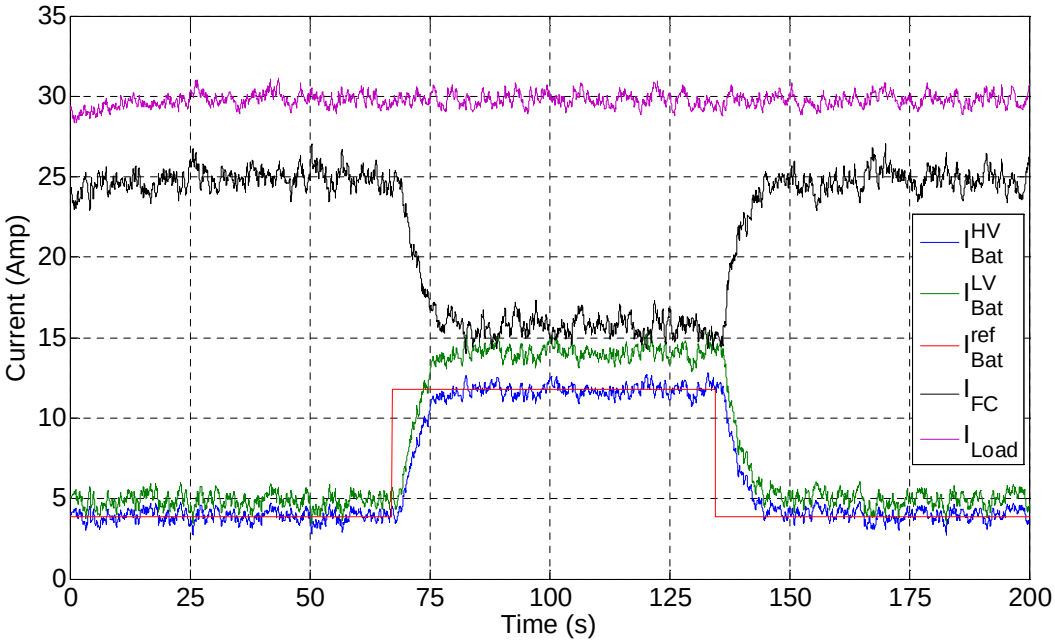

Figure 6.7 PI controller with anti-windup performance test in the hardware loop

6.4.3 Comparison and Evaluation of PI and PI with Anti-windup Controller

The worst case that show the phenomena of overshoot/undershoot occurs when the system switch from one mode to another (different operating conditions). The simulation results of the comparison between PI and PI with anti-wind-up controller are shown in Figure 6.8. The parameters selected for the comparison are the steady-state error, the rise time of the response and the overshoot. This comparison test shows that the battery current output and the controllers (PI and PI with anti-windup) outputs are responding almost immediately to changes in the set-point. However, the response of the PI controller was marked by a large overshoot at around t = 273.8 s when the considered system is changed from charging to discharging mode. The “Proportional” action reduced both the steady-state error and the rise time, decrease the settling time by small amount and increase the overshoot.

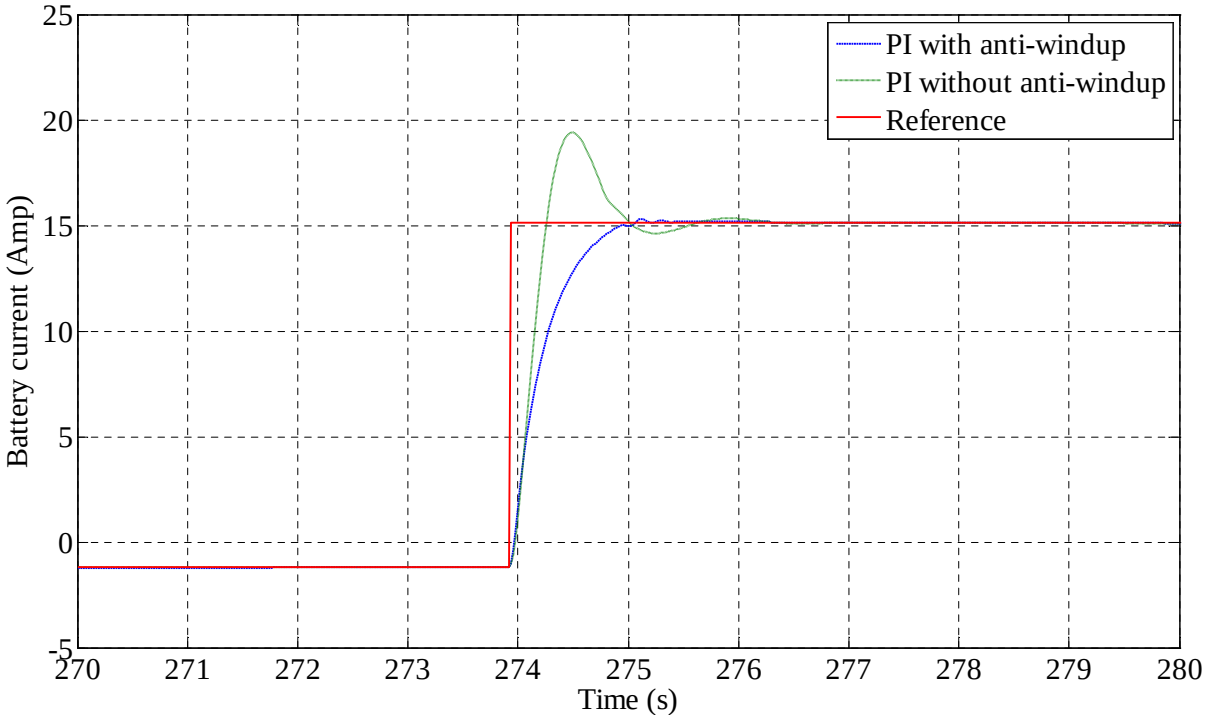

Figure 6.8 Performance comparison of PI and PI with anti-wind-up controller in simulation

In this case, the battery output current reaches almost 19.5 Amp which translates to about 30% overshoot. After the overshoot, the system was allowed to reach its steady state behaviour and the battery current returns to its nominal value in less than 2s. While the simulations result show that the response obtained using PI with anti-windup controller satisfy the load requirements and there is no overshoot observed. It is worth mentioning that for our system the overshoot was the mean concern because the bidirectional DC/DC converter very sensitive and during tests in the lab, 2 converters were damaged due to large spikes in the current. The comparison between the two controllers in terms of overshoot and settling time is given in Table 6-2. This shows that the settling time and overshoots phenomena are improved significantly by using PI with anti-wind-up controller.

Table 6-2 Comparison of PI and PI with anti-windup controller response

	PI controller	*PI with anti-windup*
Settling time (sec)	≈ 1.5	1
Overshoot (%)	≅ 30	0
Rise-time (sec)	0.4	0.7
steady-state error	≅ 0	≅ 0

Though, the PI with anti-wind-up controller satisfies the load requirements and improves the performance of the system. Yet, the controllers need to be re-tuned from time to time due to the dynamics of the system. For example, the internal resistance of the battery is a dynamic nonlinear parameter that varies always with the temperature and discharge state. Moreover, there are some factors that influence the dynamics of the battery which is mainly related to the battery's operational environment, such as ambient temperature, ambient humidity and the battery life [92]. Therefore, the battery voltage will fluctuate under different operating temperatures; as such it is continuously important to regulate the ambient temperature which is very difficult to control in such application.

Consequently, this controller works only under certain conditions. To overcome the above mentioned issue, more advanced controllers such as Fuzzy Logic controllers (FLC), or Artificial Neural Networks (ANN) will be tested. Since ANN uses the relationship between input and output which can be measured from the system rather than using the mathematical model of the system to obtain solutions; ANN is well suited to nonlinear systems and can provide a more responsive, stable and reliable control system [93, 94].

6.5 Basic Principles of Artificial Neural Networks (ANN)

In this project an ANN control strategy will be implemented, with the aim of achieving all the desired properties while trying to maintain an ideal compromise between complexity and performance.

ANN is inspired from the human brain and an attempt to mimic the functionality using a mathematical formulation. This complex system consists of different interconnected processing elements that aim to solve a specific problem; for instance pattern recognition, classification, or wherever a learning process is necessary.

In 1943 McCulloch and Pitts [95] introduced the first fundamental modelling of NN in terms of a computational model of "nervous activity". The neuron espoused is a binary device and each neuron has fixed threshold logic. This model leads the work of Jhon von Neumann, Marvin Minsky, Frank Rosenblatt, and many others. Hebb postulated, in his classical book "The Organization of Behavior" [96], that "the neurons were appropriately interconnected by self-organization and existing pathway strengthens the connections

between the neurons". He proposed that the connectivity of the brain is always changing and learning different functional tasks, and that cell assemblies are created by such changes. By inserting a massive number of simple neurons in an interactive nervous system, it is possible to provide computational power for every element.

As shown in Figure 6.9 the majority of the ANNs use a Multilayer Perceptron (MLP) structure using an input layer, hidden layer, and the output layer.

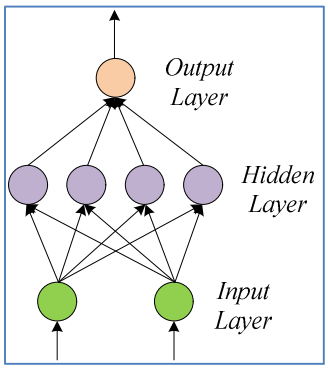

Figure 6.9 ANN basic structure

It has the same general structure as the human brain; the processes are dependent on the structural organisation, whenever the tasks became complicated the neurons are joined together by using layers connected to each other.

The main advantages of ANN are:

- The ability to solve any nonlinear problem, if the system has the right number of neurons.
- ANN can provide satisfactory responses by using sets of inputs even never seen before.
- When an element of the neural network fails, it can continue approximating by their parallel nature.
- After completing the neural network learning process, it does not need to be reprogrammed.

The main disadvantages of ANN are:

- In fact the accuracy of the system is dependents on the quality of the data, if a wide variety of data is not provided, then the ANN might fail in a certain scenarios.
- ANN can only solve the problem for which have been designed.

- The training process requires a set of experimental tests of suitable behavior and in some types is computationally expensive

There are several successful applications where ANNs have been successfully confirmed and reported; see for example the review in [97; 98].

The methods include a set of inputs; these signals are in order relayed from the input layer to the hidden layer which links the signals to the transfer function in charge of the associative memory. The output layer sends the result to the environment resolving the design problem in a majority of cases. Typically, the output will be the initial data for the next layer.

It is worth to mention that artificial neural networks are very similar to biologic systems. However, it is less complicated than biologic systems. It is clear that both follow the same architecture as shown in Figure 6.10 and the structure is simple and extremely connected.

Both configurations have multiple inputs. However, only one output, the ability of the signal is determined by the size of the inputs and weights. The activation function which is sometimes called (transfer function) corresponds to the product between the signals and the respective weights.

$$w_1 I_1 + w_2 I_2 + w_3 I_3 \ldots + w_n I_n + w_b I_b \geq \theta \qquad \{6.19\}$$

This could also be written as:

$$n = wp + b$$

Also, in some literature the inputs $I_1, I_{2,} I_3 \ldots I_n$ written as $x_1, x_2, x_3 \ldots x_n$ are continuous signals which can change in magnitude. Each signal passes through a synaptic weight $w_1, w_2, w_3 \ldots w_n$; these weights can be negative or positive. The sum function accumulates the inputs multiplied by the weights and the transfer function θ produces the output signal when the threshold has been exceeded.

Typically the input to each neuron is written as following:

$$\mathrm{net_i} = \sum_{i=1}^{n} w_i x_i = \vec{x}\vec{y} \qquad \{6.20\}$$

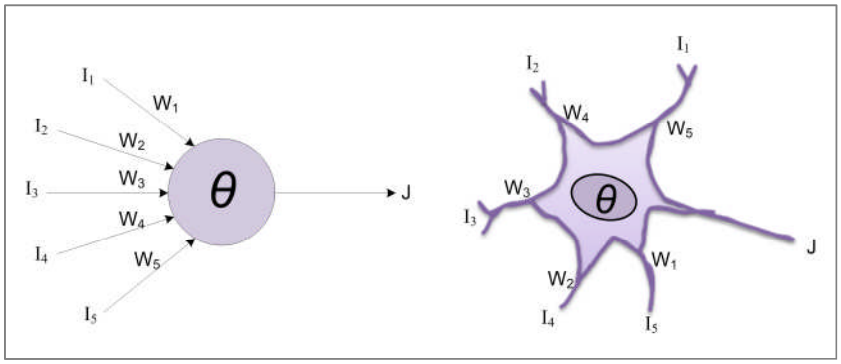

Figure 6.10 Artificial Network and Biologic

The process for the following set of signals is shown in Figure **6.11**.

As soon as the θ value is reached the output corresponds to:

$$x_i = f_i(net_i) \qquad \{6.21\}$$

Where f_i is the transfer function for a specific element responsible to convert the input, net_i, in the output, x_i.

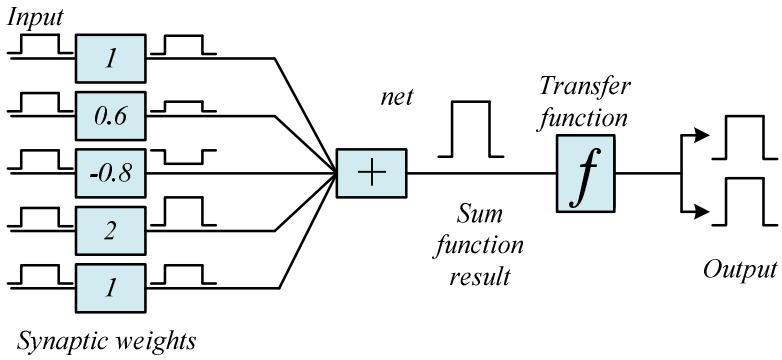

Figure 6.11 ANN Net sum and outputs

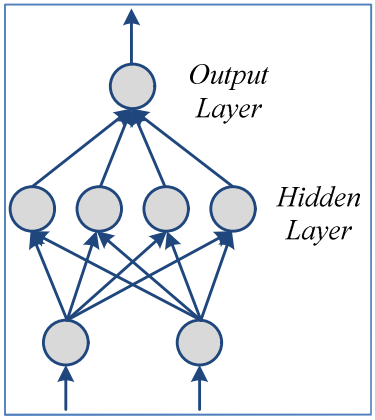

Figure 6.12 MLP with a single hidden layer

The neurons are bunched together making layers that are named depending on the position. As earlier highlighted, an ANN is composed of input layers, hidden layers and output layers. The input layer receives the signals from the environment; the hidden layer defines the ANN topology, which does not have direct contact with the environment and lastly the output layer gives the outcome of the process. The most common multi-layer perceptron (MLP) configuration with single hidden layer is shown in Figure 6.12.

6.6 ANNs Classification and Use of Neural Networks

Neural networks can be classified by several features; the training rules, the nature of the signals, the topology, and the association or the relationship between inputs and outputs [99].There are several different types of ANNs and each one has its own algorithms and formulations.

The first ANN known was ‘’The Perceptron‘’ developed by Warren McCulloch and Walter Pitts. Random synaptic weights were used and multiplied by the inputs to estimate the output. If the sum of the input signals is equal or greater than the threshold value, the output is “1” else it is “0”. In 1957, the Perceptron theory was developed by the psychologist Frank Rosenbalt who proposed the probability concept as method of analysis.

The first perceptron was called photoreception and the aim of this experiment was to emulate the eye of the human. The experimentation showed that the artificial neuron was capable to recognize patterns after a training process. In 1960 the Adeline perceptron (adaptive linear elements) was developed by Bernard Windrow and Marcial Hoff and are currently applied to decrease echoes in telephone lines.

In 1986 the Back-Propagation algorithm was discovered by David Rumelhalt and James McClelland and being used nowadays in several areas [100, 101]. Some other ANNs such as the Adaline, Hopfield Network, Multilayer Perceptron (MLP), Competitive Networks can be found in [98]. There are many investigation and applications that prove the success of the different network configurations, the accuracy of the results depend on the selection of the correct structure and the inputs.

6.6.1 Learning

This tuning process is called training or learning the network including in what manner the synaptic weights must be updated based on the set of inputs by employing a learning rule. Learning or training rules are mathematical algorithms which have to be selected to change the magnitude of the synaptic weights to fit the problem requirements to obtain the right outputs, for instance the optimisation of any function or least squares.

There are three different training methods; supervised training, unsupervised training and reinforcement training. However, the purpose of the learning process is continuously the same. Figure 6.13 summarizes the different training methods using different learning algorithms. Supervised training is the method where an external "teacher" introduces the inputs and corresponding output, to tune the synaptic weights. Table 6-3 summarizes the overall procedure to follow during supervised training.

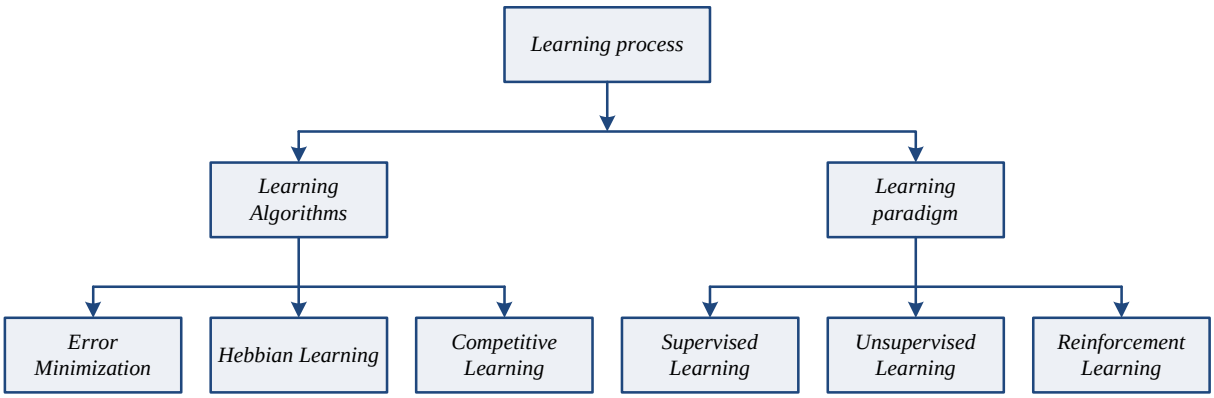

Figure 6.13 Learning classification

Table 6-3 Supervised training

1	Introduce a set of random patterns
2	Get the ANN output matching to the input
3	Error calculation
4	Synaptic weights upgrade via using the training rule
5	If the error is greater than the chosen by the designer, then go back to stage 2, If the classification is acceptable finish

Supervised training is the method that depends only on the process and does not need initial threshold values. The outputs are not restricted by any range allowing the network to find its

own interpretation of the activation function during the process and obtaining the required convergence. There are two common methods for unsupervised training-Principal Components Training and Competitive Training. The third learning method Reinforcement Learning (RL) is characterized by relatively infrequent and general feedback/reinforcement (as compared to the frequent and specific error signals of supervised learning) that must translate into credit assignment to specific system components whose temporal activity histories have varying degrees of overlap with the actual time of the reinforcement [102].

6.6.2 Model Reference Control (MRAC)

This structure was originally developed in 1958 by Whitaker [103]. Neural networks have been applied successfully in the identification and control of dynamic systems. The universal approximation capabilities of the multilayer perceptron makes it a popular choice for modelling nonlinear systems and for implementing general-purpose nonlinear controllers [104]. The neural model reference control architecture shown in Figure 6.14. uses two neural networks; a controller network and a plant model network. When the system is operating, the model outputs and the plant dynamics are continuously compared and the control signal is chosen in order to reduce the error between the closed loop system and the model. The plant model is identified first, and then the controller is trained so that the plant output follows the reference model output.

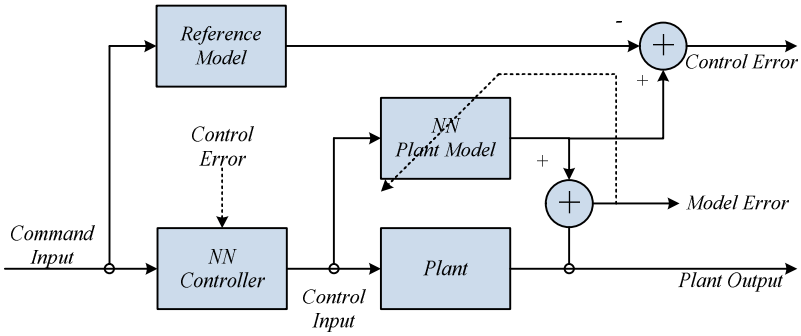

Figure 6.14 Neural Model Reference Control architecture

Most ANNs are adaptive and they change their structure based on the input, output and the feedback, just like the neurons in our brain.

6.6.3 Adaptive Control Systems

Generally, adaptive control is basically a specific type of nonlinear control system that can adjust its parameters to adapt to a changing operating condition. The changes in environment

can represent variations in process dynamics or changes in the characteristics of the disturbances. Research in adaptive control started in the early 50's [105]. Over the past many years, there have been several attempts to define adaptive control; examples of adaptive control are presented in [106].

In the 60's state space and stability theory were presented, offered additional understanding into control theory. Dynamic programming presented by Bellman [107] and [108], improved the understanding and performance of adaptive procedures. There were also extreme developments in parameter estimation and system identification presented in [109].

The theory of Adaptive Model Control was then introduced by Widrow in the 70's, his work summarised in [110]. With the development of microelectronics, a commercial adaptive regulators based on some methods were then launched into the market for several applications in process control, robotics, aerospace and further industrial control ranges were implemented, as a consequence solving several problems.

Many publications describing early and recent work on adaptive control are published by Aseltine, Mancini and Sarture [111], Jacobs, et al. [112]. Currently, adaptive control could be used for different areas, for instance linear systems, non-linear systems, prognosis, stochastic control, control design and optimisation. Adaptive control is typically used to solve two problems. Firstly is the tuning problem, in which the process is constant, on the other hand the parameters related are unknown. Secondly is an adaptation problem, for which the parameters can change during the operation.

Adaptive control is suitable to processes featuring changing dynamics in normal operating conditions subject to stochastic disturbances. The features of adaptive control are:

- Engineering efficiency.
- Changes in the nature of the disturbances.
- Changes in process dynamics, wherever the parameters could change as a result of changes in the operational conditions of the process or nonlinear acts.

The plant's operation might be affected by variations in the operational conditions, non-linear acts. Typically two different solutions are used for industrial processes; adaptive control and robust control. Common adaptation methods are gain scheduling, model reference and self-tuning.

6.7 Design and Implementation of the ANNC

The reason of choosing AMRC was due to its minimal online calculation. However, the architecture requires a separate NNC to be trained offline in addition to the NN system model. The controller training is computationally expensive, as it requires the use of dynamic backpropagation.

The work flow for the NN design process has seven main steps as shown in Table 6-4.

Table 6-4 The work flow for the NN design process

1.	Collect data
2.	Create the network
3.	Configure the network
4.	System identification
5.	Train the network
6.	Validate the network
7.	Use the network

In this research project two AMRC's have been implemented to maximize performance of a FC hybrid power system. As stated in the previous chapter, both controller actions are based on feedback signals from the battery current (I_{Bat}^{HV} and I_{Bat}^{LV}) as the objective is to control the battery charge/discharge and the output power, as shown in Figure 6.15. The inputs are the power demand and the battery SOC while the output of the controller goes into the duty cycle of the bidirectional dc/dc converter.

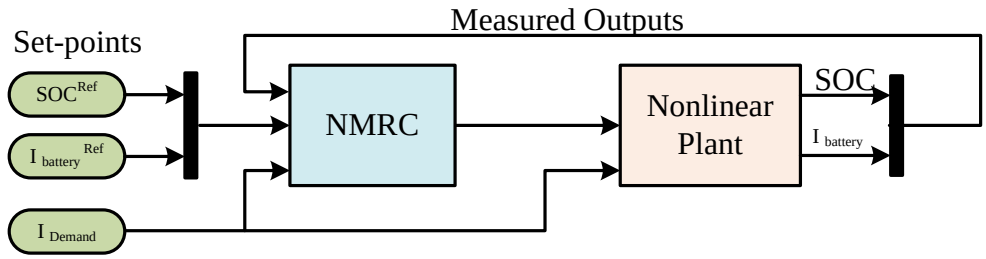

Figure 6.15 Block diagram of ANNC implementation

Control of the FC hybrid system is a challenging task due to nonlinearity behaviour, time variance and delays between inputs and outputs. There are two steps that were followed in using the neural networks for control:

- System identification: develop a NN plant model that you want to control
- Control design: use the NN plant model to assist in the controller training.

Each controller is trained to control the system so that it follows a reference model and the neural network plant model is used to assist in the controller training. Table 6-5 shows the details of the neural network plant model and the neural network controller for both charging/discharging modes as they are implemented in this project.

Table 6-5 Plant identification for charging/discharging modes

Plant identification for charging mode		**Plant identification for discharging mode**	
SOC Network Architecture		**Power demand Network Architecture**	
Size of hidden layer	10	Size of hidden layer	10
Sampling interval (sec)	0.05	Sampling interval (sec)	0.05
No. of delayed plant inputs	2	No. of delayed plant inputs	2
No. of delayed plant outputs	2	No. of delayed plant outputs	2
Training data		**Training data**	
Training samples	10000	Training samples	10000
Maximum plant input	27	Maximum plant input	27.01
Minimum plant input	26.92	Minimum plant input	27.15
Maximum plant output	0	Maximum plant output	0.1
Minimum plant output	-5	Minimum plant output	11.5
Minimum interval value (sec)	0.1	Minimum interval value (sec)	0.1
Training parameters		**Training parameters**	
Training epochs	300	Training epochs	300
Training function	traninlm	Training function	traninlm

6.7.1 Proposed Control Algorithm

To manage energy exchanges between the DC bus, the main source and the battery, one may define two operating modes (or states):

- Charge mode, in which the main source (FC) supplies energy to the battery and/or to the load.
- Discharge mode, in which both FC and battery supply energy to the load.

6.7.2 Training and Validating the Network

It is worth to mention that during the training procedure, the controller training was considerably more time consuming than the plant model training. This is because ‘‘*the controller must be trained using dynamic backpropagation and in dynamic networks, the output depends not only on the current input to the network, but also on the current or previous inputs, outputs, or states of the network*’’ [113].

The training process requires a set of experimental tests of suitable behaviours network inputs and target outputs. The process of training a neural network involves tuning the values of the weights and biases of the network to optimize network performance. In order to improve the results of the controller, different methods were used: one of the options is to initialise the network and then train it again; the second option is to increase the number of hidden neurons, since more neurons in the hidden layer provide the network extra flexibility and lastly, by trying different training functions. The second option has been selected in this thesis, because the network has additional parameters it can enhance.

Figure 6.16 and Figure 6.17 present the random plant input-output and the validation performance, respectively that was used for training the Model Reference Control. In addition, the error that shows the difference between the target output and the network output is depicted. Results do not indicate any major problem with the training. The reference model output and neural network output curves are very similar. The response of the plant for NN Model Reference Control that was used for training the Model Reference Control was identical to the random reference model output.

In Figure 6.18, the network plot shows exact relationship between the outputs of the network and the targets. The training of the network outputs and the targets were almost equal. Validation and testing data indicates that there is an exact relationship between outputs and targets.

The ANN controller improves overall system response and stability. Results of ANN controller and analysis will be explained in more detail along with experimental verification in chapter 7 of this thesis on page 102.

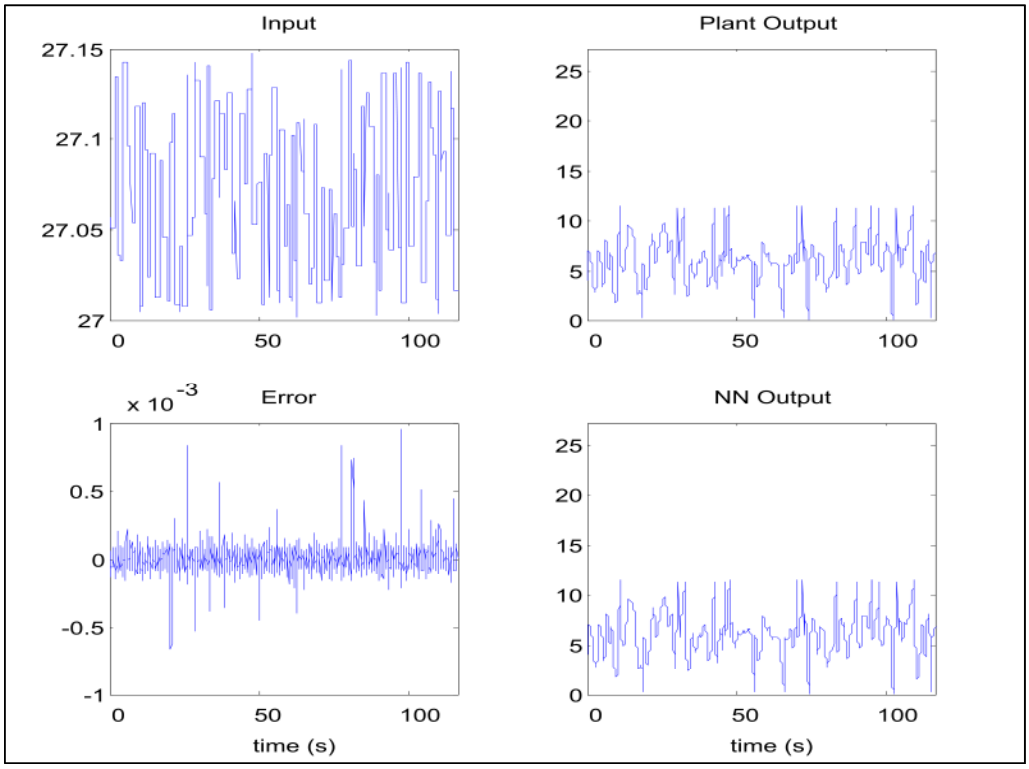

Figure 6.16 Testing data for NN Model Reference Control

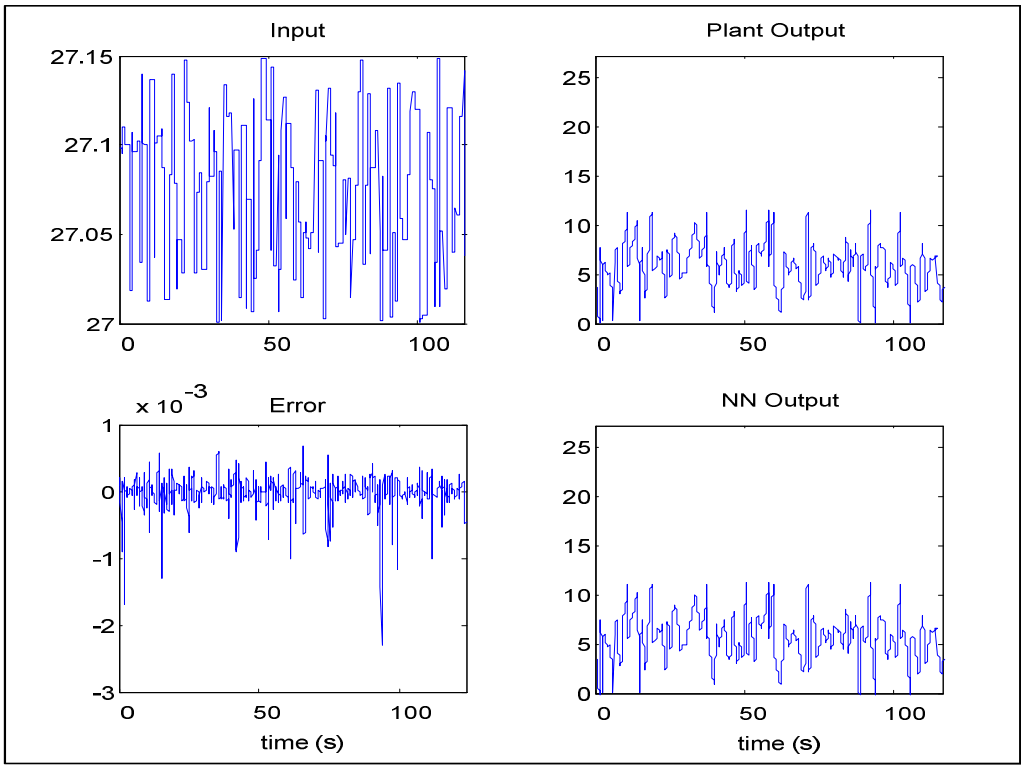

Figure 6.17 Validation data for NN Model Reference Control

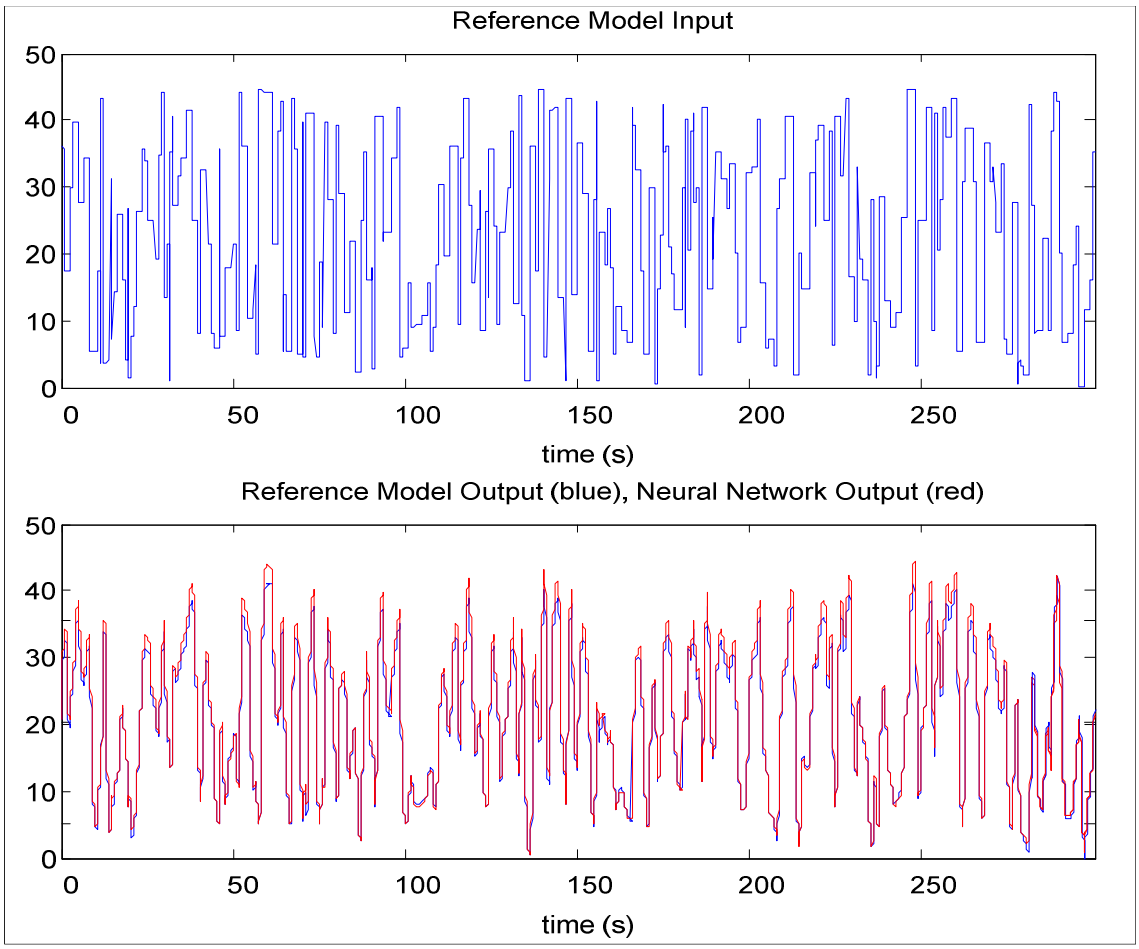

Figure 6.18 Input-Output data and the response of the plant for NN MRC

6.7.3 Experimental Comparison between ANN and PI Controller

In this sub-section an experimental test was carried-out, in order to assess the performance of the ANN controller and compare it with PI controller. An output battery current is chosen as the measured output; the experimental result shown in Figure 6.19. It can be seen that the response obtained using ANN controller satisfy the load requirements and there is no overshoot was observed; while in the case of the PI controller, there was a significant overshoot observed, when the battery current reference rises up from a lower to a higher value and vice versa.

The overshoots that were observed could be translated to about 14 % and 23%, respectively. After the overshoot, the system was allowed to reach its steady state behaviour and the battery current returns to its desired value in about 3.36s. This overshoot has a major impact on the system, thus, the power will be fluctuated. In addition, the setting time is not acceptable in such a system. As the target here for this application is less than 2s.

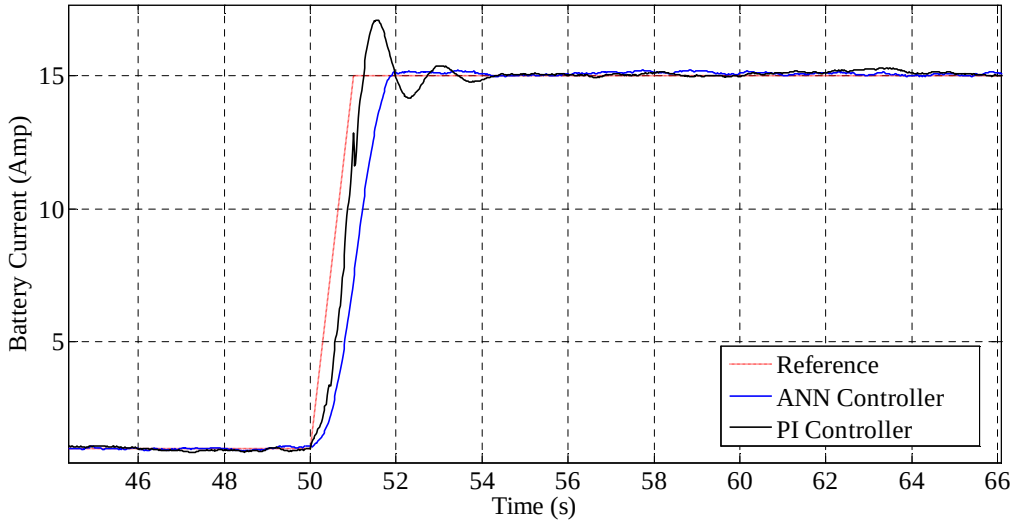

Figure 6.19 Performance comparison between ANN and PI controller

In actual fact, the PI controller responses is depending on the tuning of the controller which influence by dynamics of the system and that make it very difficult to measure the stability of the controller. (The dynamics of the system effect were covered in the previous section). Table 6-6 gives approximated values of time response characteristics for ANN and PI controller.

Table 6-6 Comparison of ANN and PI controller response

	ANN controller	*PI controller*
Settling time (sec)	≈ 1	3.36
Overshoot (%)	0	14
Rise-time (sec)	0.04	0.01
steady-state error	≅ 0	≅ 0

Generally, the ANN controller shows a good performance with regard to settling time and overshoot while the PI controller exhibits a shorter rise time but its settling time is longer than that of ANN. However, it is important to note that there is a significant overshoot in the PI response.

6.8 Summary of Chapter 6

The main points of this work carried-out in this chapter regarding the development of classical and advanced controllers can be summarized as follows:

- The control objectives for the hybrid fuel cell based power system were defined. In order to achieve the best system performance by managing the power in a flexible manner between each source, a control strategy is explained in detail.

- Details of the design and implementation of the *PI* controller, including the integrator windup were presented in this chapter. The results and the controller performance from the simulation were then compared with those obtained from hardware-in-the-loop tests.

- The PI controller with anti-windup had acceptable performance. However, due to the nonlinearities in the system a more advanced controller (ANN) was developed to provide more stable performance.

In conclusion, the controlled system has a range of operating conditions; therefore some nonlinear effects must be taken into account. When a PI controller is used to control such a system, an anti-windup loop has to be added to this controller to ensure the system will not go into an open loop.

As will be seen in the next chapter, when the mission requirements are coupled with external factors (i.e. wind speed and wind direction) maintaining optimal power balance is more challenging. The battery act as a power assist source; the fuel cell efficiency decreases if the fuel cell has to provide more power. Hence the control scheme leverages the hybrid fuel cell/battery architecture to regulate the fuel cell operation within a region of high efficiency.

Chapter 7

Case Studies Results and Discussion

7. CASES STUDY RESULTS AND DISCUSSION

In this chapter three case studies were used to validate and assess the performance of the hybrid system; including battery full charge SOC 100%, worst case scenario and taking into account the external factors such as wind speeds and wind direction. In addition, a comparison between Fuzzy Logic based controller and artificial neural networks based controller performance is also presented. In all cases the FC act as the main power source for the PiperCub J3 aircraft. The tests were carried-out in both simulation and hardware-in-the-loop.

7.1 Case Study I: Battery Fully Charged (high SOC)

As mentioned before, the aim of this project is to investigate the feasibility of using an electric hybrid system consisting of a FC and battery pack to power a small aircraft (PiperCub J3) and then implement an ANN controller for the system. In order to achieve this, a flight scenario based on UAV's flight scenario shown in Figure 7.1. covering take off, climb, cruise, descent and landing was performed and tested in both simulation and hardware-in-the-loop to investigate the system performance at different phases of flight.

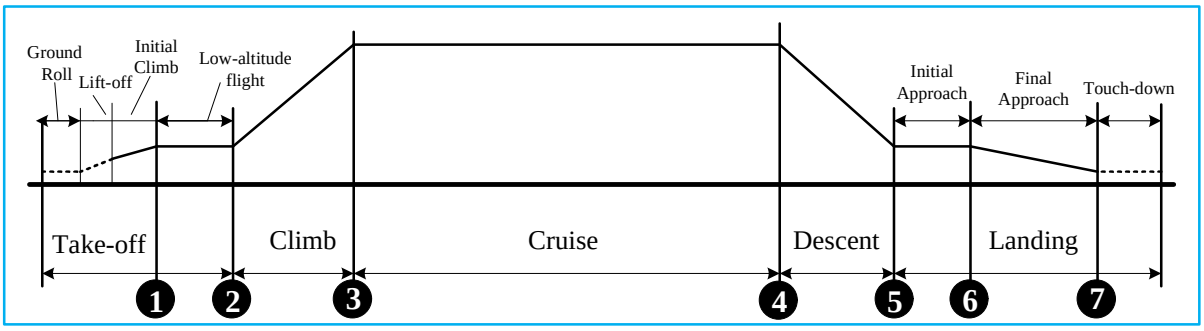

Figure 7.1 Basic UAV's flight scenario

The aircraft model was linked to Flight-Gear, the aircraft climbs to an altitude between 30-60 meter and cruise for a distance of 18km before returning back to land. The flight simulated path is shown in Figure 7.2.

In this case, a fully charged battery is used, SOC almost 100%. The maximum power demands for each phase of flight are given in

Table 7-1. A minimum power demand is considered when the electrical motor is at idle operation with 29% throttle command; for both take off and climb phases maximum power demands occur while the other phases (cruising decent and landing) the aircraft required power from 78.77 to 441.5 watt.

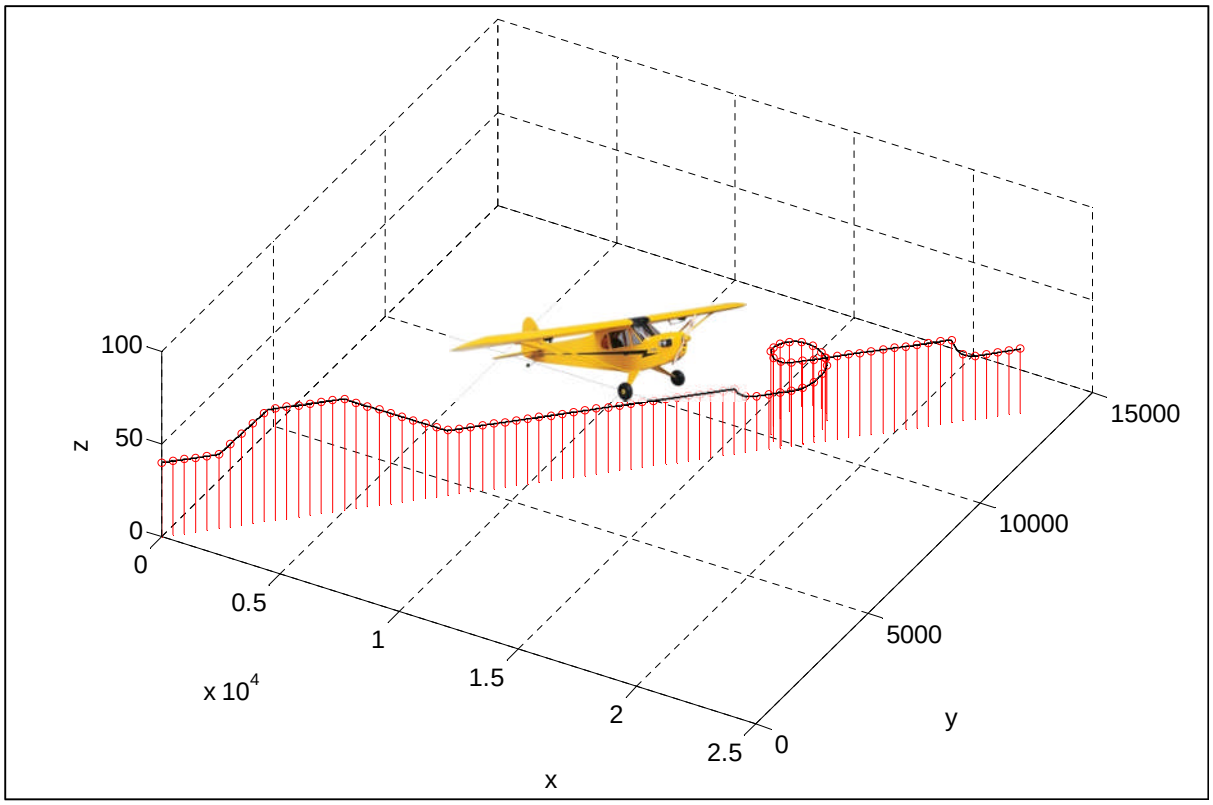

Figure 7.2 Simulation flight path caverning the different phase of flight

Table 7-1 Power demanded for flight scenarios

Throttle command (%)	*Phases of flight*	*Require power (W)*
29	*Idle*	*91.87*
100	*Take off*	*1254*
76.5	*Cruising*	*441.5*
67.2	*Decent*	*276.8*
100	*Climb*	*1254*
49	*Landing*	*78.77*

The throttle commands plot is in Figure 7.3 a, the corresponding current demand of the engine, FC current and battery current are shown in Figure 7.3 b, c, d respectively. The battery SOC and FC efficiency as a function of time are shown in Figure 7.3 e and f

respectively. The FC system efficiency during take-off and climbing is approximately 42% which occurs at full power (1254W) while the maximum FC system efficiency is about 50% occurring at about 440W during cruise stage. It is observed that the system efficiency quickly decline during part loads less than 300W, and this could be explained according to the manufacturer's data sheet as due to dominance of the auxiliary loads requirement for hydrogen consumption. Overall, Net FC system efficiency for the whole scenario is about 49(%).

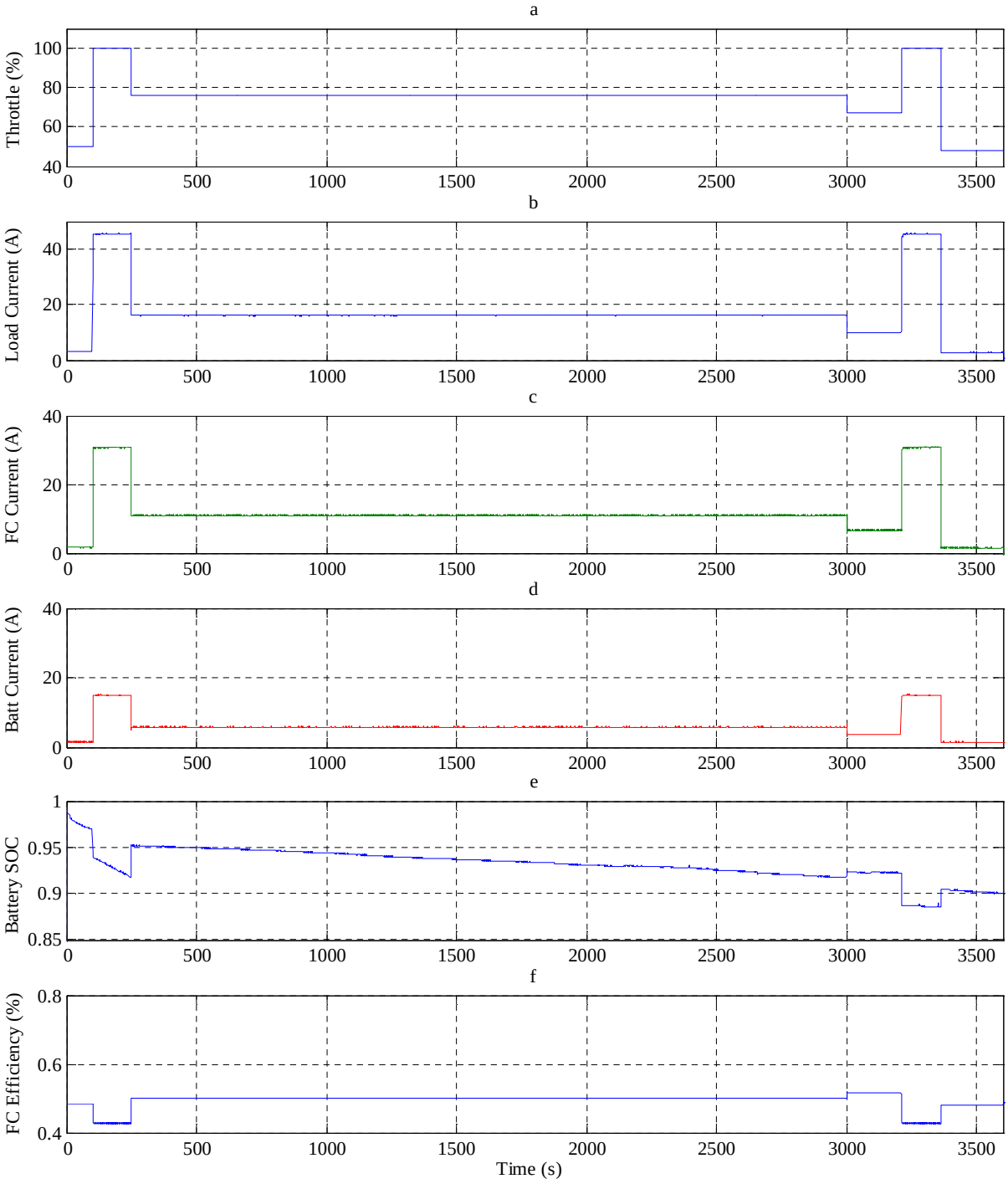

Figure 7.3 Results of case I study part 1

It is worth mentioning that the power requirement for the engine is a function of throttle commands for different flight stages as shown in Figure 7.4. For a sudden change in power requirement, battery responds immediately based on the controller decision and battery SOC to supply the power required. For taxiing and landing stages, because there is no landing-gear the engine is assumed idle with a little thrust.

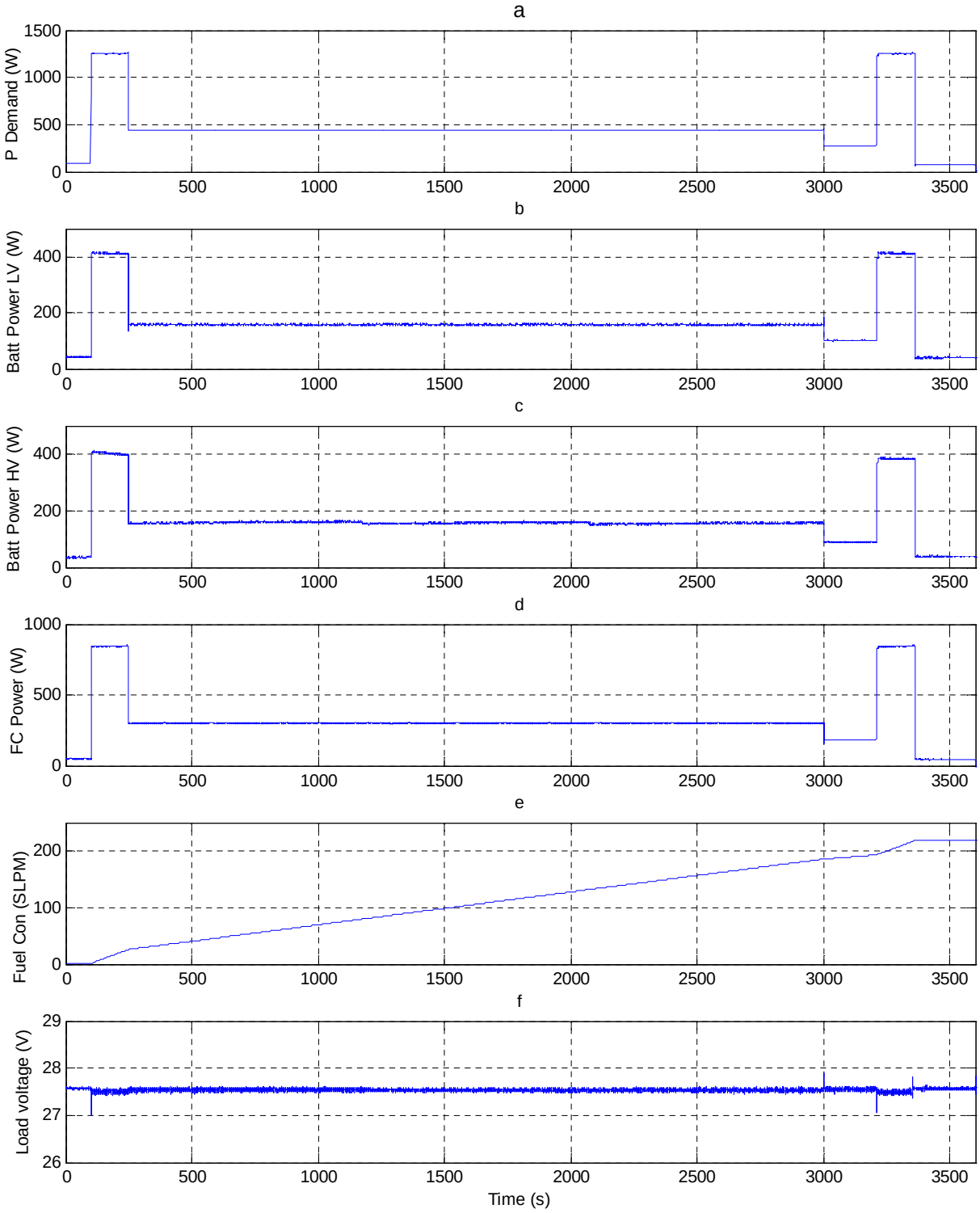

Figure 7.4 Results of case study I part 2

Figure 7.4 a represents the power demand by the engine, b, c and d represent the power delivered by battery from both sides (LV & HV) and fuel cell power respectively. The fuel consumption and behaviour of the load voltage shape during the test are shown in Figure 7.4 e and f respectively.

As can be observed, there are no important overshoots/undershoots on the load voltage amplitude during the different phases of flight with various load conditions. The worst case undershoot occurred at take-off where the maximum power is needed at about 100s. In this case, the load voltage amplitude reaches about 27 V which can be translated into a 1.5 % undershoot below the steady-state value of the load voltage which has an average of 27.5 V. After this small undershoot, the system returned to its nominal value in less than 1s.

In order to know the amount of hydrogen consumed during these flight stages in the simulation, the experimental data obtained during test-run have been utilized to develop a simple linear equation for the relationship between the current delivered by the FC stack and the hydrogen consumed. Using the basic fitting tool in MATLAB, the weights values were determined.

$$H_2 = (p1 \ . \ i) + p2 \qquad \{7.1\}$$

$p1 = 0.0054344$

$p2 = 0.0011355$

Where H_2 (SL/time) is the instantaneous hydrogen amount that was consumed, i (A) is the experimental current. Finally, taken the cumulative summation "cumsum" of H_2 gives the total fuel consumed for the duration of the test.

Figure 7.4 e. shows the hydrogen consumed as function of time at the end of flight scenario which is around 220 litres. For the load voltage, due to the parallel connection, the same voltage is present across each source with a very small variation which is inversely proportional to the current demand as seen in Figure 7.4 f. Little spikes were also observed during transit state which had no effect on the system performance.

The flight was successfully completed on time. $ANNC$ kept FC working at very high efficiency during the whole phases of the scenario apart from take-off and climb where maximum power demands occurred.

7.2 Case Study II: Worst Case Scenario (Battery low SOC)

This case has been carried-out under the same mission time and throttle command as the previous case. However, the battery SOC is different; which was intentionally set to 70% to see the controller performance and investigate if the system can cope with the worst case scenario. One of the ANN control strategies is that if the battery SOC is less than 0.7 which is assumed as 50% of battery SOC in this thesis, then the battery must be charged by the fuel cell.

It can be easily seen in Figure 7.5.C during the taxi stage, almost all the power was delivered by the FC, while in the take-off stage the battery was utilized by the controller to provide the remaining power. However, due to its low SOC, the battery current started to decline slightly and kept declining even through the cruising stage. The controller started forcing the system to rely mainly on the FC to supply the power demand which resulted in very little use of the battery until the decent stage where the controller decided to charge up the battery. Because of the FC running at optimal operation points it can be very easy to generate more power than required by the load to charge up the battery pack through a bi-directional converter. The negative values in Figure 7.5.d correspond to the battery being charged up.

In the go around stage, the aircraft was climbing at the same time as seen in the flight path (see Figure 7.2). This require maximum power, therefore the controller decided again to force the battery to support the FC in this stage despite the battery not reaching its ideal SOC. Finally, in the landing stage, power demand was supplied entirely from the FC.

Having successfully completed the flight, it is clear that during the cruise stage the FC was running below the optimal operation point which resulted in consumption of more fuel compared to the previous case. At the end of the flight, the fuel (hydrogen) needed to satisfy the power requirements of the aircraft was 327.9 litters.

The results confirmed that ANN controller performance can cope with the worst case scenario when the battery cannot continuously handle power to support the FC.

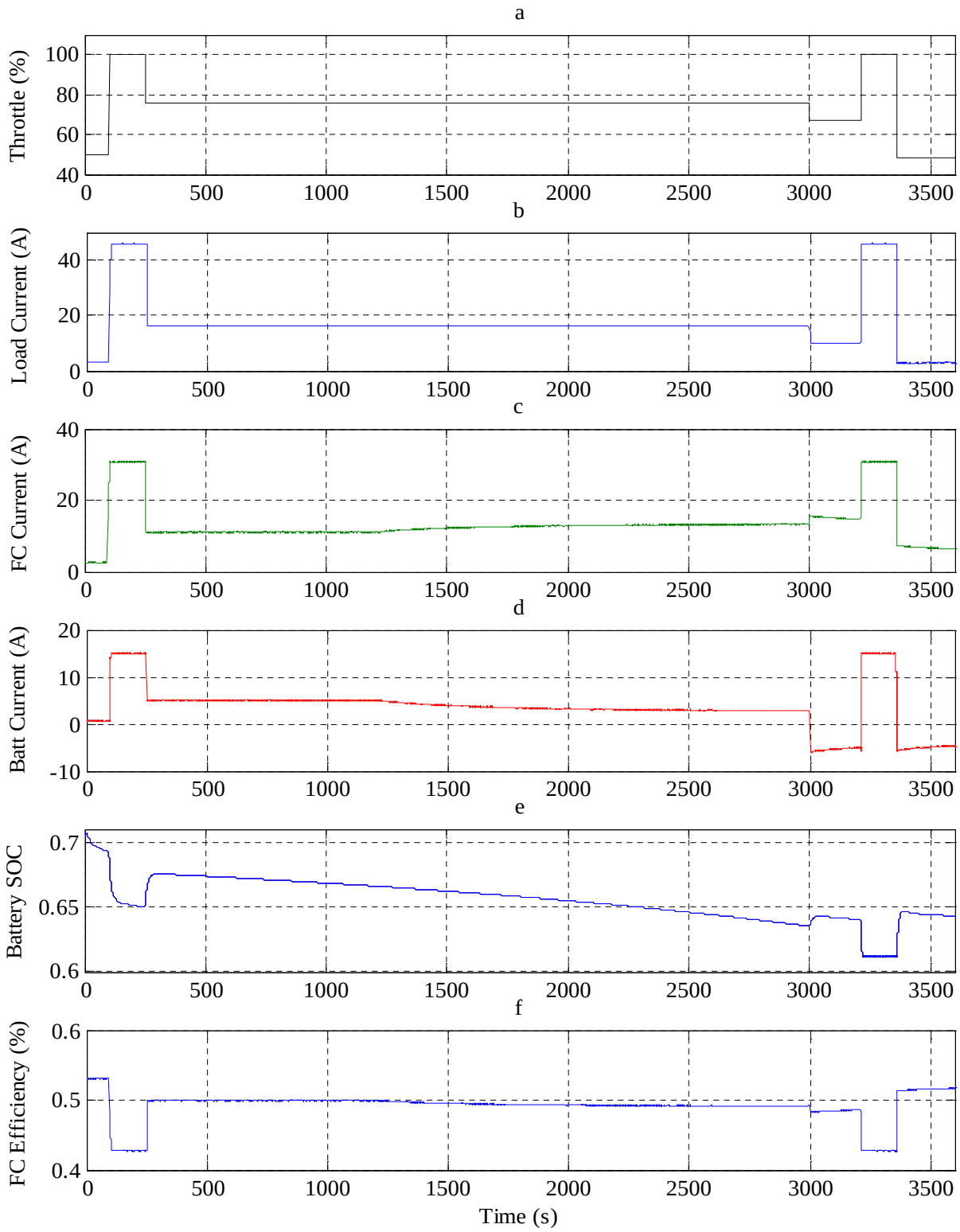

Figure 7.5 Results of case study II part 1: Worst Case Scenario

The throttle commands plot is in Figure 7.5 a, the corresponding current demand of the engine, FC current and battery current are shown in Figure 7.3 b, c and d respectively. The battery SOC and FC efficiency as a function of time are shown in Figure 7.5 e and f, respectively.

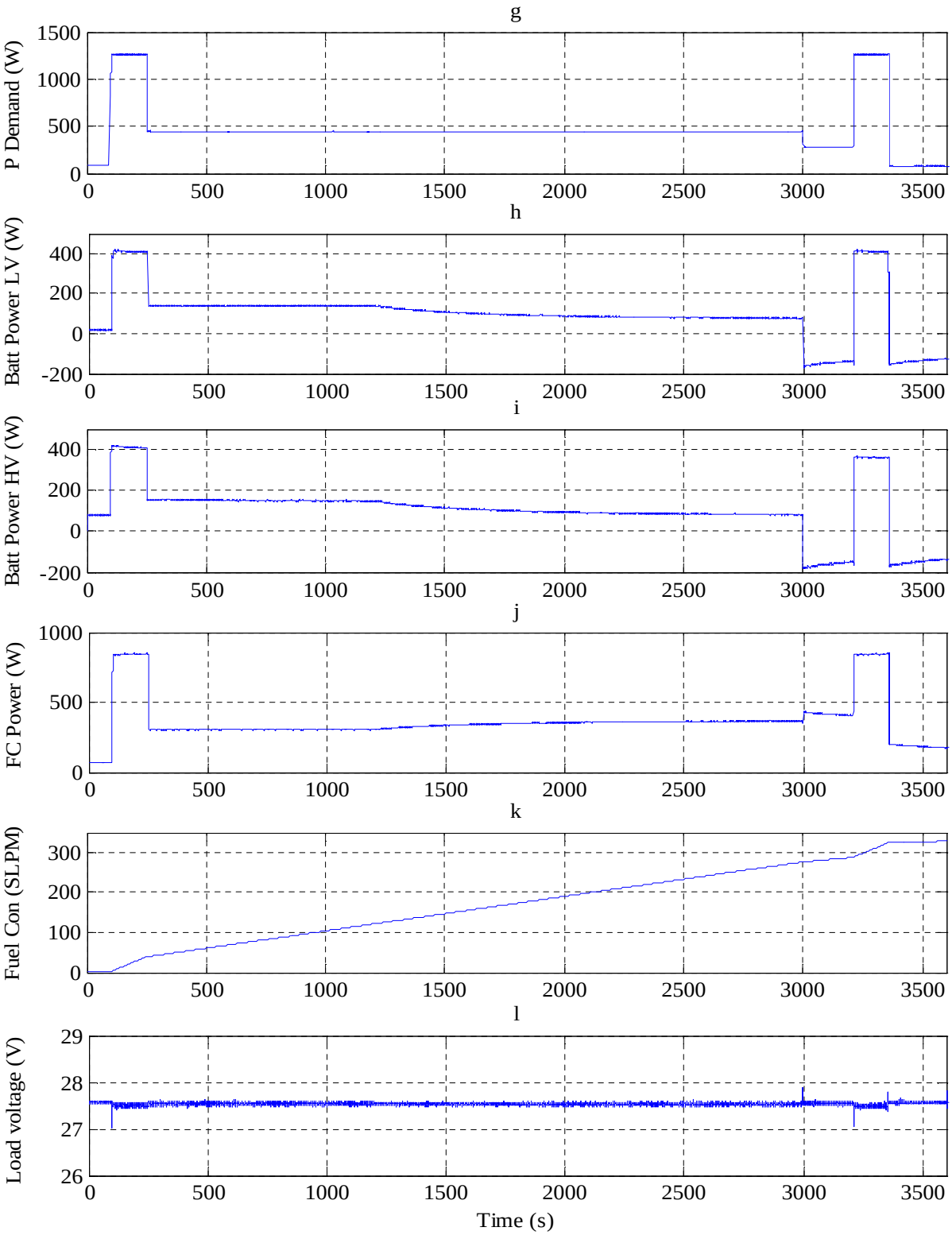

Figure 7.6 Results of case study II part 2: Worst Case Scenario

Figure 7.6 g represents the power demand by the engine, h, i and j represent the power delivered by battery from both sides (*LV* & *HV*) and fuel cell power, respectively. The fuel consumption and behaviour of the load voltage shape during the test are shown in Figure 7.4 k and l, respectively.

7.3 Case Study III: Real Time Implantation with the External Factors

UAVs have been extensively developed for use in both civilian and military applications. Yet, one of the main issues facing small $UAVs$ is their flight durability which relates to the limitations of the possible on-board fuel/battery that can be carried [114]. Wind-energy could be used to extend the flight duration of UAVs. It is also one of the possible ways used to reduce fuel consumption for a planned path [114]. In this sub-section, the real time implementation of the system with external factor (wind speed and wind direction) has been tested. The non-linear dynamic simulation model of the Piper Cub J-3 includes the electrical hybrid system (fuel cell and battery), controller and electrical engine as shown in Figure 7.7. The hybrid system simulation model can be found in the Appendix 9.8. As mentioned previously, the simulation model was modified to include also the wind model block that takes the external factors into account. To run the system in real time, a joystick was used to generate the speed command. As a result, the power requirement for the engine is a function of throttle commands and the controller generates the suitable inputs that respond to the commands. This gives the ability to emulate the motion and flying characteristics of the aircraft, as well as to extrapolate the power requirements with respect to the generated RPM.

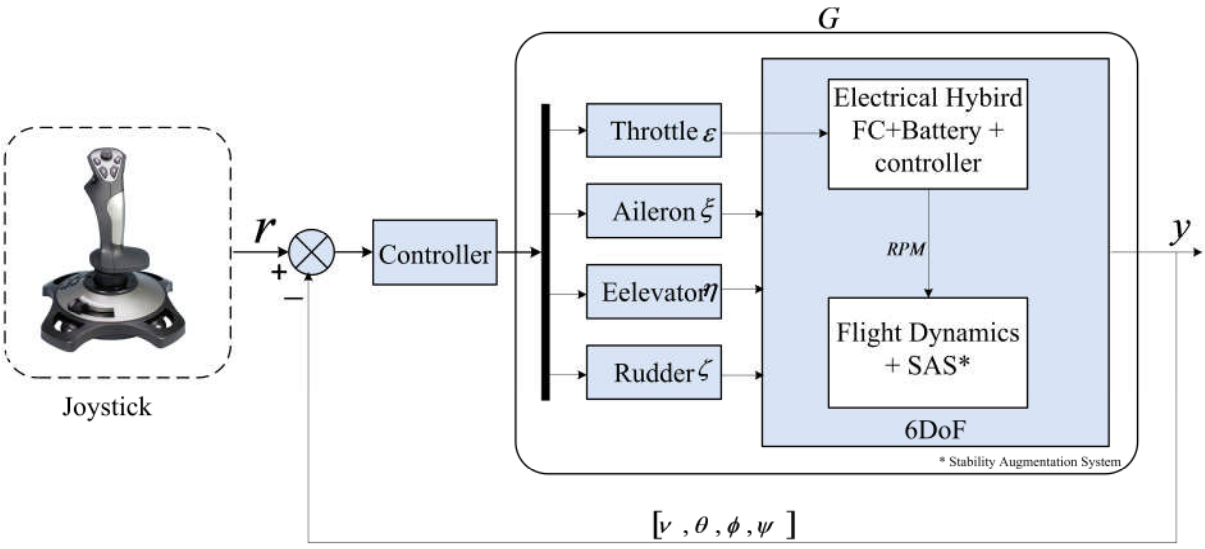

Figure 7.7 Block diagram of the hybrid system simulation model

Currently in the field of autonomous vehicles make, it is recommend that the $UAVs$ will be further deployed in the future to achieve several missions for instance intelligence, observation or rescue and search. Furthermore, as $UAVs$ are commonly very small compared to other commercial aircrafts, the effect of winds is very large, therefore cannot be ignored.

There are some path planning methods that have been developed to handle winds, based on evolutionary computation. Alvarez, Caiti, & Onken [115] have used this method in controlling the path by taking advantage of winds, for instance, maximizing the segment of the path wherever the wind and vehicle are in same direction. Another optimization technique for path planning ‘’wavefront expansion’’ introduced by Zhang, et al. [116]. One of the disadvantages of these methods is that the departure time has to be fixed in advance in order to know the state of the winds, which is required to calculate the travel cost of the $UAVs$. On the other hand, the departure time in several applications, can vary in a given time window. Thus, the choice of a suitable departure time becomes a critical matter. In such conditions where the departure time is wrongly chosen, winds possibly will be against the UAV [117]. introduced a new approach, named ‘’*symbolic wavefront expansion*’’, determining the path and the departure time while reducing the travel time of the UAV in existence of dynamic wind fields. Their approach is manipulating functions rather than numerical values.

In order to take into account the effects of the external factors an UAV wind model developed by [118] has been integrated into 6DOF Simulink model. This consists of three wind models (Horizontal wind model, Wind Shear Model and Dryden Wind Turbulence Model) as shown in Figure 7.8. The inputs to the models are the altitude, direction cosine matrix and ground speed while the output is summation of ground speed of the three models and attitude rates $(p\ q\ r)$.

A headwind is a wind that blows against the direction of travel of an object, while a tailwind wind blows in the direction of travel. In aeronautics, a headwind is useful in take-offs and landing since an airfoil moving into a headwind is capable of making larger lift than the same airfoil moving through tranquil air or a tailwind at equal ground speed. Therefore, pilots and air traffic controller usually choose to take-off or land in the direction of a runway which will supply a headwind. Usually headwinds and tailwinds are measured in relation to the vehicles speed. In order to determine the ground speed of an aircraft either the tail or head wind need to be measured.

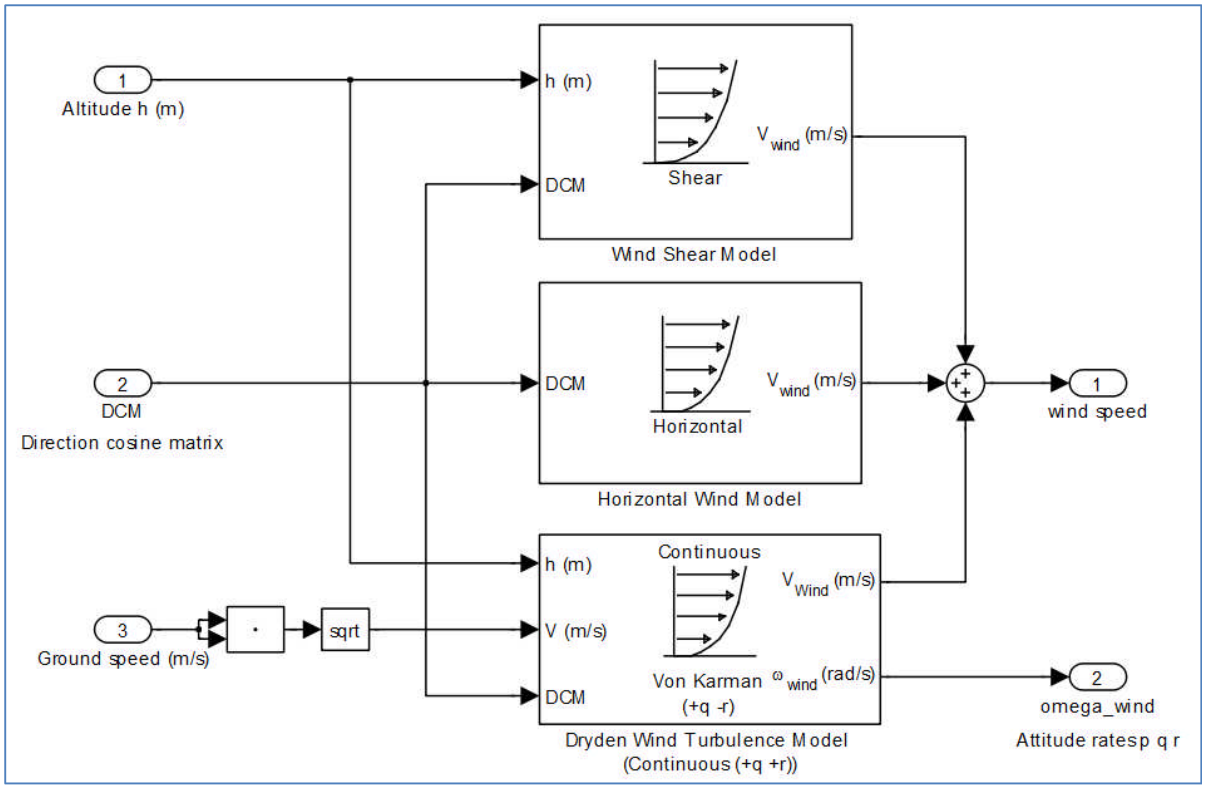

Figure 7.8 wind models block diagram

Assume:

$A = \ Angle\ of\ the\ wind\ from\ the\ direction\ of\ travel$

$WS \ = \ the\ measured\ total\ wind\ speed$

$CW = \ Crosswind$

$HW = \ Headwind$

$Then$

$CW \ = \ sin\,(A)\,.WS$

$HW = \ cos(A)\,.WS$

In this case, three tests have been carried-out in real time (headwind, tailwind, and no wind) and then compared to each other. Since headwind and tailwind do not occur together in normal conditions, the wind speed that was considered at varying altitudes was $(-3, 3$ and $0\ \mathrm{m/s})$. However, the wind direction in all cases was 30 degrees clockwise from north. To clarify the preformed scenario, the flight path and the some other aircraft states such as the aircraft position (x, y, z), heading angle (ψ), patch angle (θ) and roll angle $(\emptyset)$ are shown in Figure 7.10 and Figure 7.9, respectively.

In the first test, the effect of the headwind reduces the UAV speed and increases the time to reach its destination as a result more fuel was consumed (around 151.3 SLPM), while in the second test the tailwind has the opposite effect; increases the UAV speed and reduces the time required to reach its endpoint, thus reduces the fuel consumption (111.1 SLPM). In the last test, it is assumed that the UAV is flying in steady state condition and there is no wind applied; fuel consumption was 124.7 SLPM. Fuel consumption during each test shown in Figure 7.11.

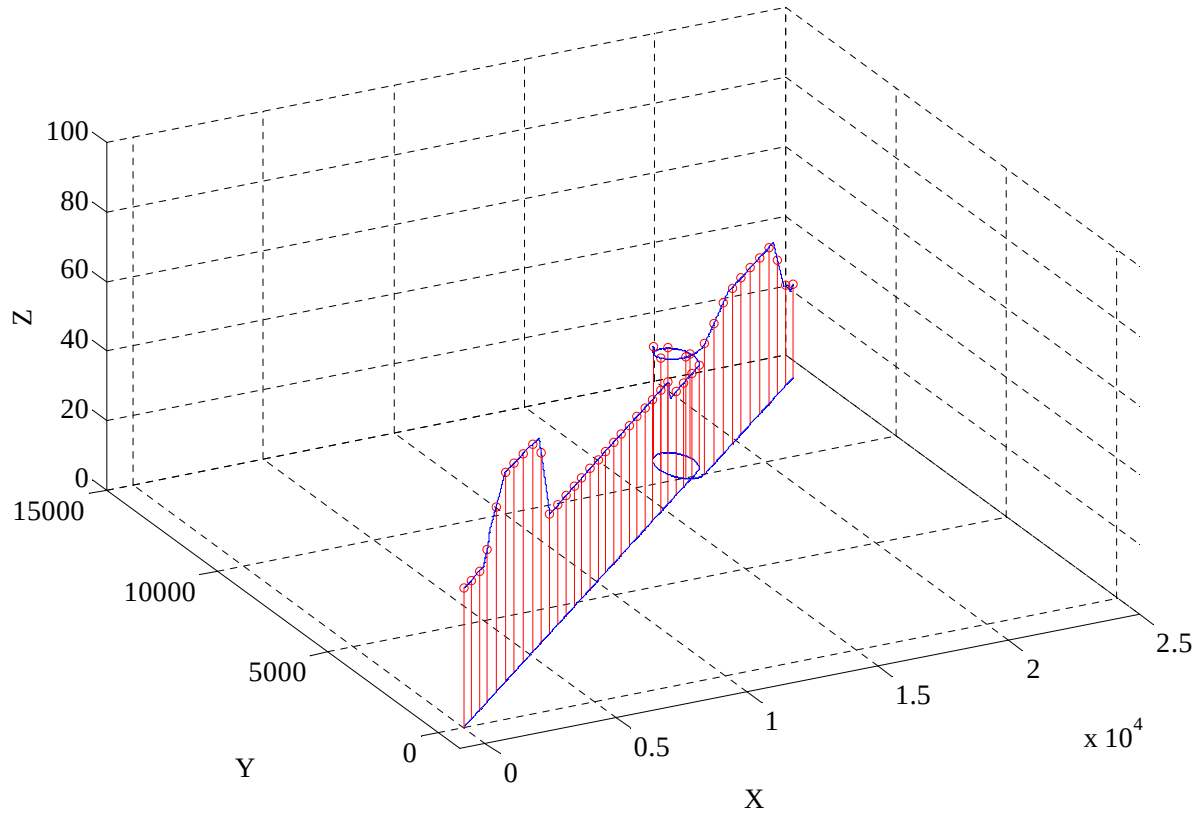

Figure 7.9 Real time flight path caverning the different phase of flight

As seen in the three tests, the flight successfully reached the end point under different wind conditions. However, regarding the fuel consumption of the UAV, it is depending on selecting optimal path which will result in a minimise fuel consumption of the UAVs and minimise time-to-goal.

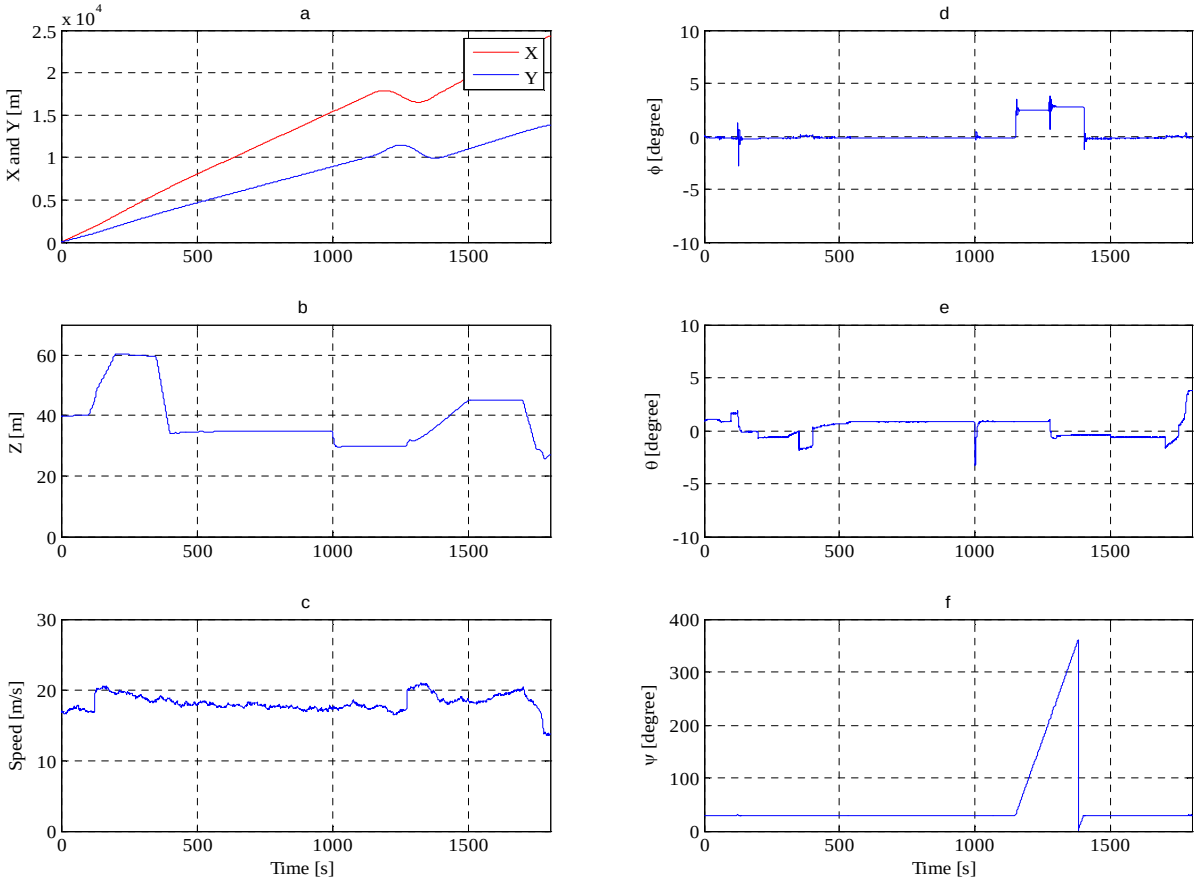

Figure 7.10 UAV's states

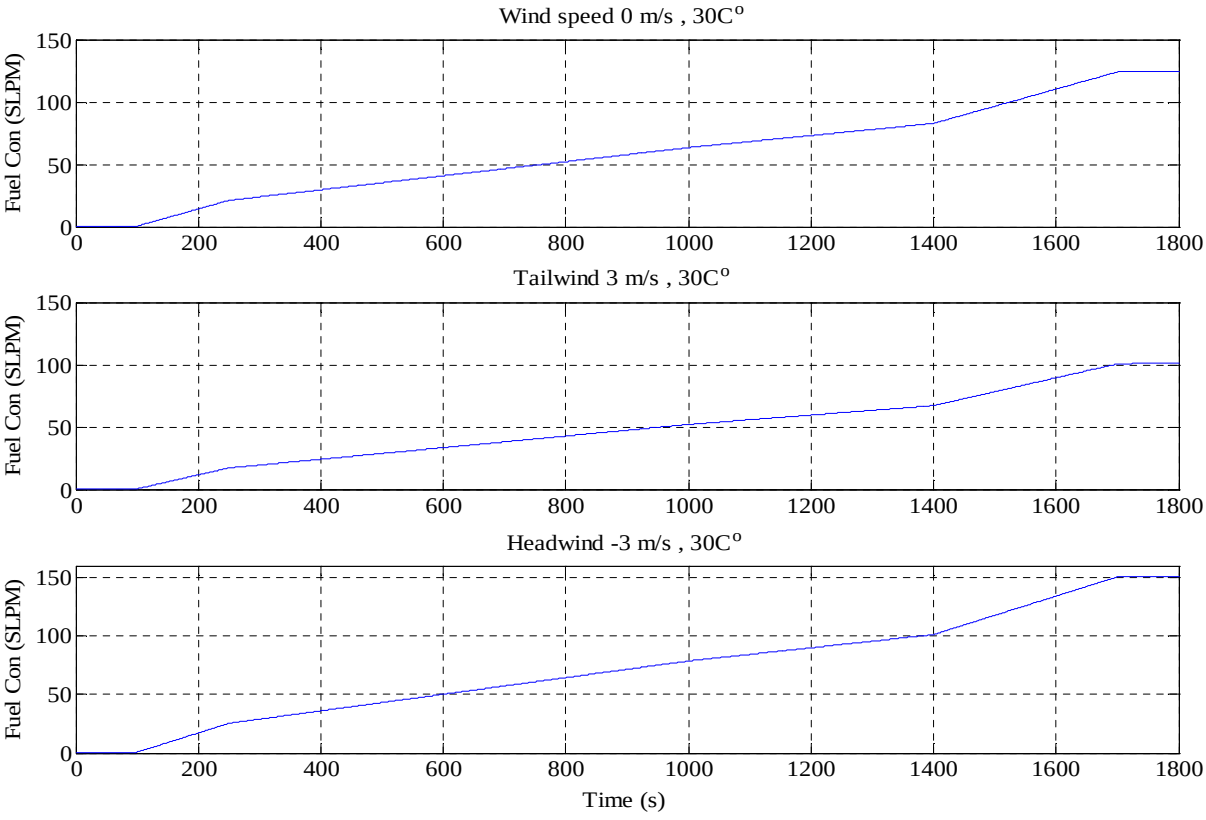

Figure 7.11 Results of case study III

7.4 Comparison between Fuzzy Logic and Neural Networks Performance

In this section, computational method based on Fuzzy Logic controller was developed and compared with ANNC. The study was carried-out in order to assess and compare the performance of two controllers, a quick study using Fuzzy Logic was carried-out to assess the performance of the controller. Please note that the objective was to compare the performance and not detailed development of another controller.

The Fuzzy controller is usually inexpensive to develop than the model-based or conventional controller which does the same task. In addition to this, Fuzzy controllers are relative easy to understand and modify their rules and has simple means of operation. Fuzzy Logic is a form of probabilistic logic or several-values; it deals with reasoning that is approximate instead of exact and fixed [119].

The outputs of the Fuzzy Logic controller are usually related to the inputs by a set of rules. For example, IF X AND Y THEN Z. The IF part (antecedent) defines the state of the input variables and the THEN (consequent) gives the value of the output variable [120]. The Fuzzy Logic is suitable for processes with complex non-linear models, empirically-based, relying on the experience of the operator rather than their technical understanding of the system.

7.4.1 Design of the Fuzzy Logic Controller

Figure 7.12 shows a simple structure of Mamdani type Fuzzy Logic controller which contains four main blocks:

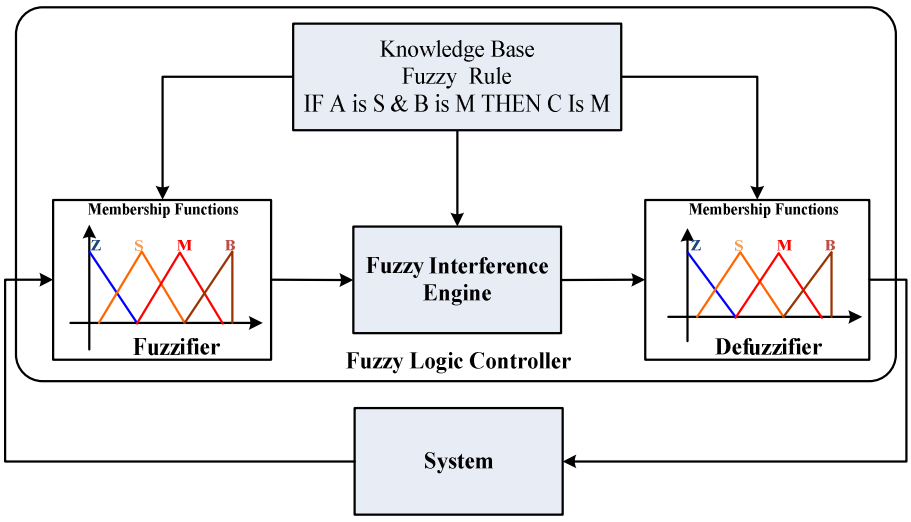

Figure 7.12 Block diagram of a control system containing a Mamdani type of FLC [119]

1- **Fuzzifier**: This transforms the numerical value of the measured input signals into fuzzy quantities (linguistic variables) by using membership functions. This transformation is called the fuzzification. A membership function has a value between 0 and 1, and it indicates the degree of belongingness of a quantity to a fuzzy set.

2- **The knowledge base**: This consists of the linguistic-control rule base and the data base. The rule base (expert rules) specify the control goal actions by means of a set of linguistic control rules. In other words, the rule base contains rules which are provided by an expert. The data base provides information which is used to define the linguistic control rules and the fuzzy data manipulation in the fuzzy-logic controller. The FLC, based on the input signals and by using the expert rules, determines the appropriate output signals (control actions). The rule base contains a set of if-then rules. There are many methods for developing the rule base, such as [121].

- Using the knowledge of a person who is an expert in the application,
- Modeling the process,
- Modeling the control action of the operator.
- Using artificial neural network,
- Using self-organized fuzzy controllers.

3- **The inference engine:** The role of the inference engine starts when the inputs signals are transformed into their linguistic variables. At this point, the inference engine evaluates the if-then rules and gives the results as a fuzzy value for a linguistic variable. In other words, the inference engine simulates human decision making by using Fuzzy Logic rules and fuzzy implication [121]. The output of inference engine, which is a fuzzy value has to be then transformed into a real output value by the FLC and this is the functionality of the defuzzifier.

4- **Defuzzifier:** This transforms the fuzzy values into real quantities and this action is called defuzzification. In order to perform its action, defuzzifier uses the membership functions in reverse way as the fuzzifier does.

7.4.2 Implementation of Fuzzy Logic Controller

The implemented Fuzzy Logic controller input variables are the same as input of the ANN controllers developed in this work (the input variables are the current demand and the battery

state of charge represented by the battery voltage). Figure 7.13 shows the block diagram of the Fuzzy Logic controller developed in this thesis.

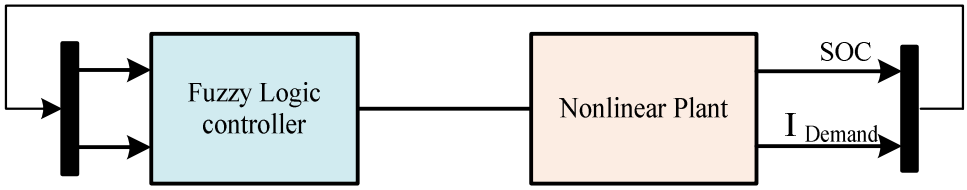

Figure 7.13 Fuzzy Logic controller block diagram

The logic that was followed as a rule for the development of the Fuzzy Logic controller is that, if the total battery SOC is less than 70%, then the battery needs to be charged. The controller output signal goes to the duty cycle of the bidirectional DC/DC converter; based on that a decision regarding how much current to be supplied to or from the batteries. For instance, IF the current demand is high AND battery SOC is high THEN the battery will supply power to assist the FC to operate with high efficiency. IF the current demand is low AND the battery's SOC is low THEN the FC supply power for the engine and charging up the battery through the bidirectional DC/DC converter.

The method that was used to develop the rule base is based on intuitive knowledge and experience gained from carrying-out several experimental and simulation runs. The rule-base developed in this thesis is given in Table 2-1, which contains 40 rules and the same can be found in Appendix 9.15. The abbreviations that are used in the rule table are as follows:

LBC: low battery charge; MBC: medium battery charge; HBC: high battery charge; ZB: zero battery charge; (LBC) low battery discharge; (MBD, MBD1 and MBD2): medium battery discharge; (HBD, HBD1 and HBD2): high battery discharge.

Figure 7.14 shows the triangular membership function for inputs signals current demand and battery SOC and the controller output signal and the surface for the designed FL controller is shown in Figure 7.15.

This comparison of the two controllers was carried-out in simulation only; the battery capacity was reduced to 6Ah to assess the controllers performance. The two controllers (Neural network and Fuzzy Logic) when tested for the same mission duration and applying the same throttle commands, they both successfully satisfied the desired performance for the different phases of flight; while the Fuzzy Logic controller satisfied and show the stability of the control system, it can be seen in Figure 7.16 that there were some oscillation.

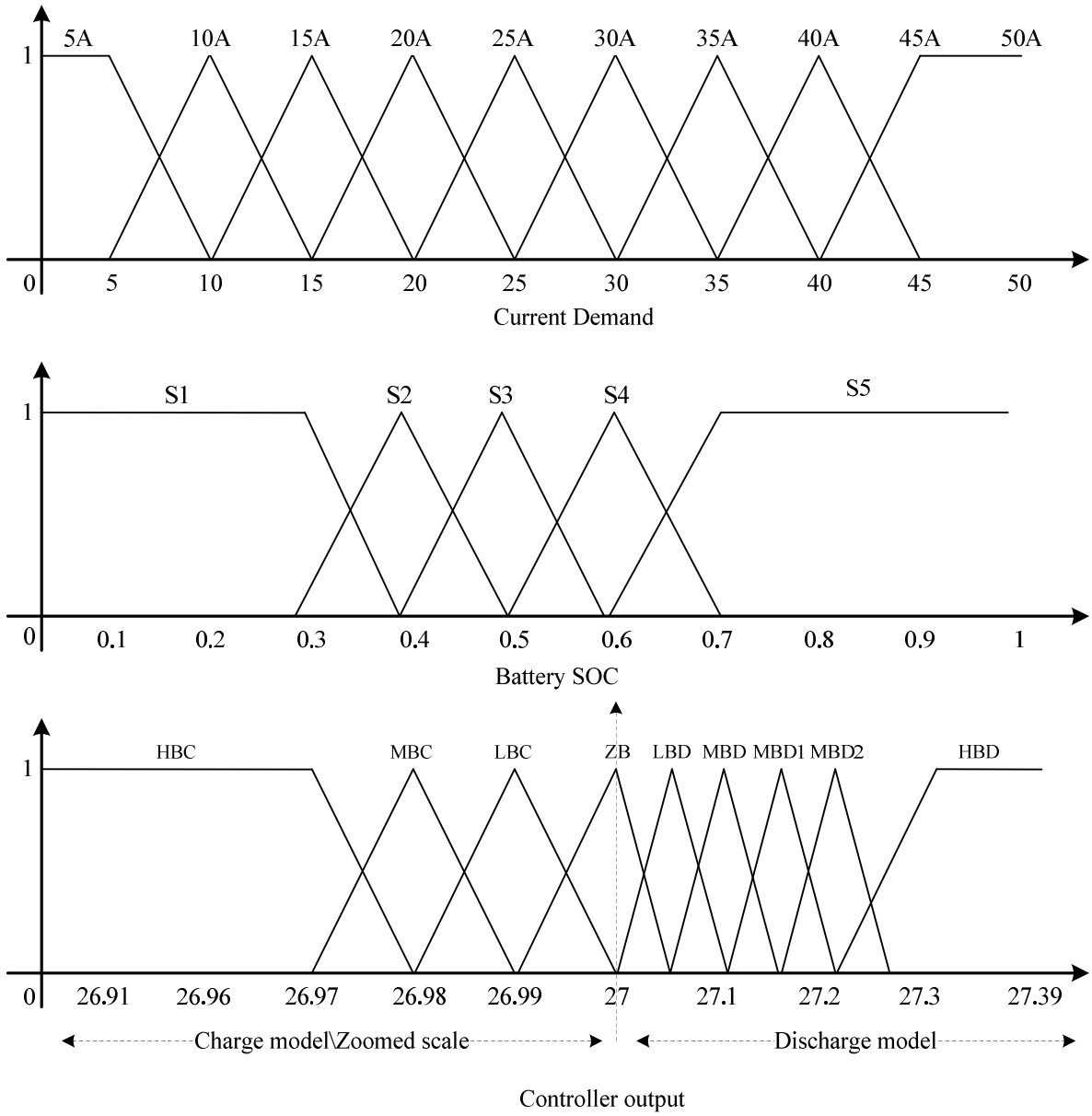

Figure 7.14 Triangular membership for current demand, SOC and FLC output

Table 7-2 Linguistic rules table for FLC

	Current demand								
SOC		5A	10A	15A	20A	25A	30A	35A	40A
	S1	HBC	HBC	LBC	ZB	ZB	LBD	MBD	HBD1
	S2	HBC	HBC	LBC	L BD	LBD	M BD	MBD1	HBD2
	S3	HBC	MBC	ZB	MBD	MBD	MBD1	MBD2	HBD
	S4	MBC	MBC	ZB	MBD1	MBD2	MBD2	HBD	HBD
	S5	LBC	LBC	L BC	HBD1	HBD2	H BD	HBD	HBD

The fuel consumption was 178.9 SLPM and 182.7 SLPM for the Artificial Neural network and Fuzzy Logic controller, respectively. The efficiency of the fuel cell system obtained for different phases of flight was varied from 43% during take-off to about 49% during descent. For cruise the average efficiency was about 50% as shown in in Figure 7.17 f.

ANN controller shows the ability to optimize for a given performance. A ANN controller has slightly better control performance than the FL controller and enhances the efficiency when fuel consumption is calculated. This could be explained due to the fact that in the case of FL, the rule based controller is not always optimally using the power available from the battery. Another fact is that the developed FL algorithm is based on static rules and membership functions, which were formulated based on intuitive knowledge and experience gained from carrying-out several experimental and simulation runs; so the controller design process was carried out off-line. In the case of the proposed ANNC, it is designed dynamically off-line. This ANNC has two stages: the first one being the identification of the plant model and in the second stage, using the identified model, the neural network controller is trained. This controller could be developed to be an adaptive controller simply by feeding back the model error (the error between the actual plant output and the NN model output) to the controller.

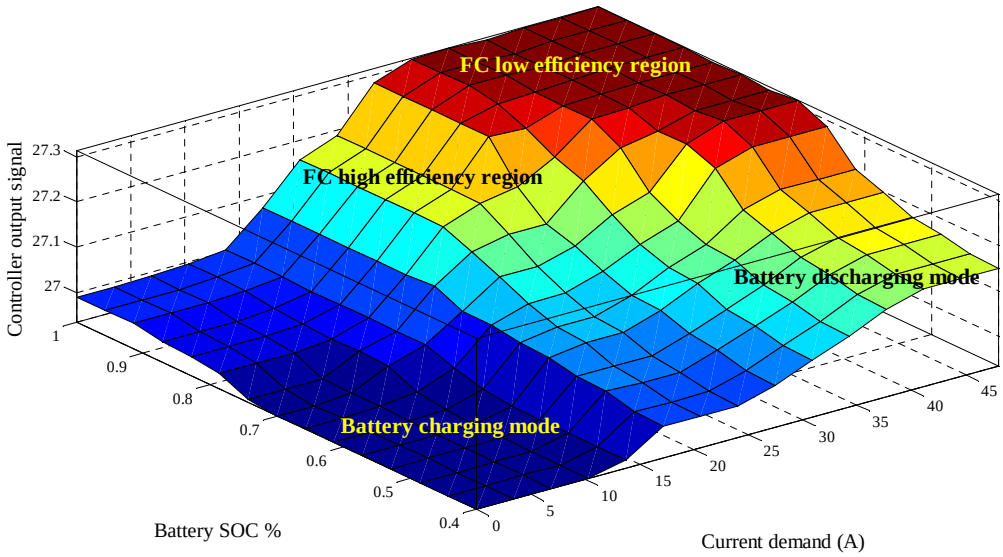

Figure 7.15 Control surface obtained with a Fuzzy controller

Both controller developed gave similar result. However, using artificial neural network controller approach performed slightly better compared to fuzzy logic. From a strictly performance point of view, ANNC controller provided a good performance and demonstrated around 1% improvement over the Fuzzy Logic controller in terms of efficiency and fuel consumption.

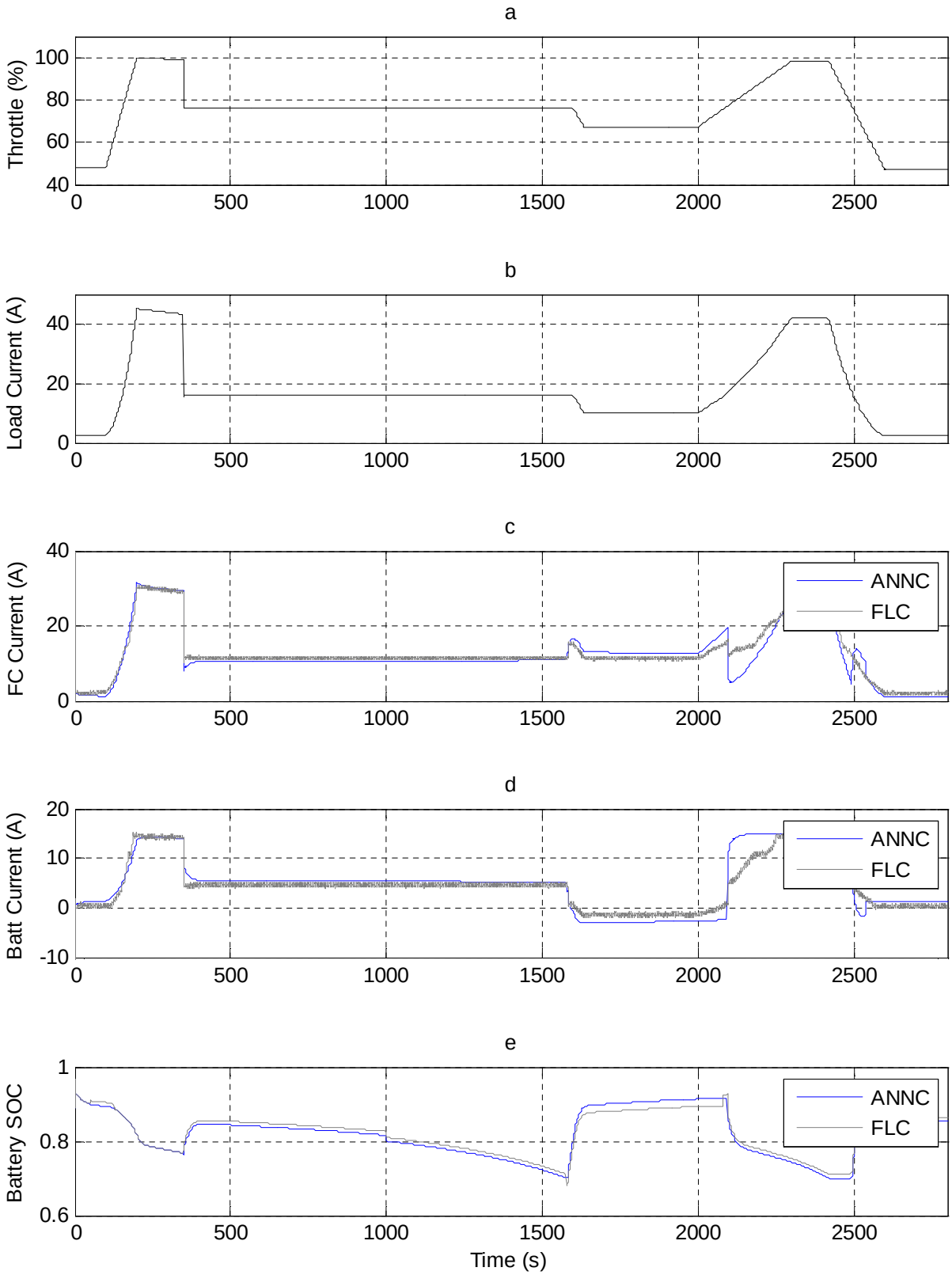

Figure 7.16 Result Part 1 of comparison between F.L and NNC

The throttle commands plot is in Figure 7.16 a, the corresponding current demand of the engine, FC current and battery current are shown in Figure 7.16 b, c and d, respectively. The battery SOC is shown in e.

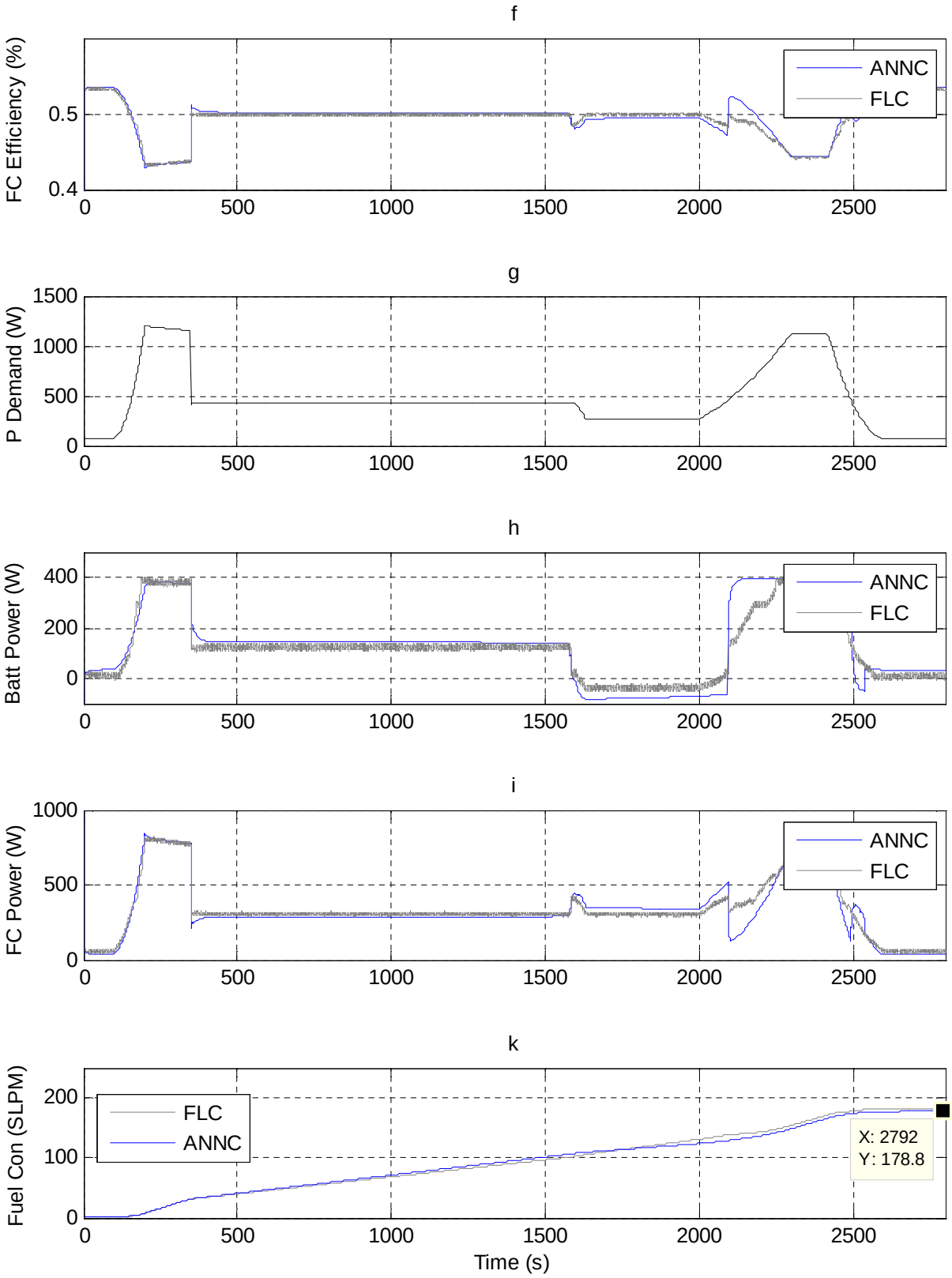

Figure 7.17 Result Part 2 of comparison between F.L and NNC

The FC efficiency as a function of time is shown in Figure 7.17 f; while g, h and i represent the power demand by the engine, power delivered by battery and fuel cell power respectively. The fuel consumption is shown in j.

7.5 Summary of Chapter 7

Three case studies were used to validate and assess the performance of the hybrid system. The three case studies considered were:

- Case study I: Battery fully charged (high SOC)
- Case study II: Worst case scenario i.e. the case of low SOC, where the battery is hardly used as a buffer
- Case study III: Taking into account the external factors such as wind speeds and wind direction

In addition, a comparison between Fuzzy Logic based controller and artificial neural networks based controller performance were also presented.

In all cases the FC act as the main power source for the PiperCub J3 aircraft model. The tests were carried-out in both simulation and hardware-in-the-loop. The desired aircraft power at different phases of flight was calculated including the worst case scenario and the influence of external factors. Furthermore, the quantity of fuel (hydrogen) needed in each case was also calculated.

The performance of the ANN controller in all three case studies was found to be good. The controller kept the response of system within minimum overshoot, minimum rise time and minimum steady state error. In addition, when compared with a Fuzzy Logic controller, the ANN controller demonstrated a slight, around 1% improvement over the Fuzzy Logic controller in terms of efficiency and fuel consumption.

Finally, from a control point of view, the ANN controller in both simulation and hardware-in-the-loop show good enhancement of the performance and improves the overall stability of the hybrid system when compared to a classical controller.

Chapter 8

Conclusions and Further Work

8. CONCLUSIONS AND FURTHER WORK

This chapter summarises the main results of the work carried-out in this project. In addition, it explains in details how the aim was achieved, highlights the contributions to knowledge and recommends areas for further development.

The thesis starts with the aims and objectives of the project and the motivation behind the research. Chapter 2 introduce the reader to the field of fuel cells, their working principles and the main construction elements. Following that a summary of the different types of fuel cells, advantages and disadvantages when compared to other power generating techniques is presented. Examples of application (mainly experimental) where fuel cells were used and some concepts of PEM FCs technology conclude the chapter.

The main findings of this review can be summarised as follows:

- PEM fuel cells are among the most promising systems to employ in aerospace and automotive applications as they offer high power density, low operating temperatures, fast start and are relatively light weight.

- At present the cost of FCs is higher than that of similar, already existing products, mostly because of small scale production and the hydrogen storage and handling issues. The costs related to FCs could drop significantly in the future if there is an increase in applications that uses FC and the development of better hydrogen fuel storage approach coupled with handling technologies.

In the hardware description and setup chapter, the fuel cell hybrid systems and their types/configurations were explained. The different types of energy storage systems used to complement the slower output power of the fuel cell were highlighted. The battery model, electrical engine model and Piper Cub J3 model were also discussed. Each component of the hybrid system is individually covered.

The fuel cell hybrid system in the lab consisted of the 1.2kW Nexa PEM FC as the main power source, 36 V lead-acid WP18-12 (12 VDC) battery as the auxiliary power source, providing the additional power during high/sudden load demands e.g. during take-off. The output from the fuel cell is connected to a DC/DC step-down converter to keep the FC output voltage constant at 27V. A DC/DC bidirectional converter is used to manage and control the

charging/discharging of the battery. The chapter ends with a review of DC/DC converters and mathematical analysis of a simple DC/DC converter topology.

The integration challenges that were encountered and had to be addressed during the construction of the hybrid system were also discussed. The original Nexa system was modified to incorporate programmable bi-directional DC/DC converters and additional 3-batteries. Controlling the charging/discharging of the battery in hardware and interfacing the system with the simulation using the bi-directional DC/DC converter was one of the challenges. The selection and sizing of the components to meet the power requirements and operating voltages also took some time to resolve.

As part of the hardware testing, a set of experimental tests on the 1.2kW Nexa^{TM} power module FC were conducted in different stages for start-up, shut-down, step-up load and irregular load variation. The results of those tests were used to validate the developed fuel cell model. The steady-state and transient-state phenomena were also considered to analyse the system performance at different conditions; such as load current, temperature and stack voltage. The aim of these tests was to investigate the dynamic performance of a PEM FC stack. This goal has been reached and a conclusion has been made herein:

The control board internally transferred the load from the external battery to the FC stack at start-up. As a result of this transmission, the fuel cell current increases with an overshoot due to air pump fast demand, and the voltage decrease with undershoot. In shut-down sequences, control board internally transfer parasitic load from the fuel cell stack back to the external battery, which cause small current undershoot and small voltage overshoot.

When the current transiently increases from 20A to 30A, a current overshoot can be observed in the system responses due to two factors. The first factor is that different operating condition results in disparate water saturation level particularly after a long course of running. The second factor is that both the humidified water and product water alter the membrane wettability. Since there is temporary dehydration due to electro-osmotic drag on the anode side and air feeding starvation on the cathode side, a voltage undershoot was observed at the same time.

Having investigated and analysed the dynamic performance, and obtained satisfactory experimental results, a dynamic electrochemical simulation of Proton Exchange Membrane (PEM) Fuel cell (PEM FC) model was developed and validated using experimental data from

the 1.2kW Nexa power module FC. The performance of the model was studied and validated for both steady state and transient state phenomena (transient response of the stack during load changes). The aim is to obtain an accurate model based on the Nexa FC that could be used for the development and design of controllers in hybrid fuel cell electrical systems.

The model assumptions are discussed extensively as the theoretical equations are presented and the model parameters were adjusted specifically for the 1.2kW Nexa stack. Simulation results of the proposed model are compared with the experimental data and also validated. The results show that the percentage error of the simulated model when calculated using MRE does not exceed 4.1% for the full working process including the start-up sequence and the transient phase.

The dynamic PEM FC Stack Modeling chapter is followed by a conclusion as follows:

One important consideration that should be taken into account when developing FCs systems, is the equivalent internal resistance of the fuel cell stack which is different from the internal resistance of fuel cell. In addition, the assumption of a constant stack temperature will not provide accurate results in the case of a Nexa ™ module power module. Thus, the stack temperature should be also considered.

It is valued to design new strategies for controlling the excess oxygen ratio. One starting point that could be applied is real-time processing and the advantage of real time neural network estimator can be used.

In the control strategy chapter, after a complete system simulation model was developed that consists of a Proton Exchange Membrane hybrid FC system, aircraft model and neural network based controller. The system was integrated in one simulation environment to run in real time and meet the desired power at different phases of flight and optimal level of efficiency.

The control strategy implemented in order to achieve the best system performance by managing the power in a flexible way between each source is described in details. The design and implementation of a classical PI controller, with anti-windup was the first step and was presented in this chapter. When a PI controller is used to control such a system, an anti-windup loop has to be added to this controller to ensure that the system do not go into an open loop. This PI controller was then tested in both simulation and hardware-in-the-loop and

had acceptable performance. However, due to the nonlinearities in the system a more advanced controller Artificial Neural Networks controller (ANN) was developed to provide more responsive and stable performance. Since ANN uses the relationship between input and output which can be measured from the system rather than using the mathematical model of the system to obtain solutions. Similarly the ANN controller was tested in both simulation and hardware-in-the-loop. Results obtained clearly show that the ANN controller provided a more responsive, stable and reliable control system and kept the system's operation at optimal level and efficiency.

In Chapter 7, three case studies were used to validate and assess the performance of the hybrid system: the first case study assumes the battery is at full charge; the second case study takes the other extreme i.e. worst case scenario when the battery is not charged; and the final test scenario takes into account the external factors, in particular, wind speed and direction is applied and consider their impact on different phases of flight.

In all cases the FC act as the main power source for the PiperCub J3 aircraft model. The tests were carried-out in both simulation and hardware-in-the-loop. Result of each case was presented and discussed. The experimental results confirm the validity of the proposed control strategy in the studied topology. The output voltage stays always constant, even when a high power demand is forced on the system. Calculated here is the desired aircraft power at different phases of flight, including worst case scenario as well as the influence of external factors in addition to the fuel (hydrogen) needed for each case.

Finally a comparison between Fuzzy Logic and ANN controller performance was carried out. The purpose of this test is to assess the performance of the NNC controller with another advanced controller. From these analysis and discussions the following conclusion can be made:

From a control point of view, the proposed ANN control strategy allows for managing the energy in the electrical hybrid power system in all cases that were applied. The ANN controller in both simulation and hardware-in-the-loop clearly show significant enhancement of the performance and improves the overall stability of the hybrid system. The ANN controller demonstrated a slight, around 1% improvement over the Fuzzy Logic controller in terms of efficiency and fuel consumption. This gives the fact that the Neural Network controller is more robust than the classical controller in such systems.

The external factors are highly important parameters that should be considered when developing energy management system for UAVs. This is increasing the system's efficiency aimed at maximising the flight duration while minimising power and fuel consumption.

The proposed control strategy can be taken as a good choice for the specific application. Furthermore, it could be applied to other topologies with different types of energy sources such as wind turbine or solar panel in an electrical hybrid power system.

8.1 Future Work

There are a number of issues that were been tackled due to time constraints or were outside the scope of this work. Some of them can improve the overall system fidelity and the Technology Readiness Level (TRL).

The possible future works that may be accomplished are:

The FC hybrid system designed in this thesis is based on existing technology and most of the components have been designed for integration into a wide variety of automotive and stationary power generation applications. In these applications weight is not a big issue, however, in the UAVs design, size and weight are critical parameters. It would be useful to study weight saving methods for designing and manufacturing hybrid system components specifically for aviation application.

In this thesis the matter of hydrogen storage has not been considered. It would be useful for aviation application to consider the issues related to various types of hydrogen storage, temperatures and pressures, and metal hydrides within the limited space available in an airframe.

Although a high fidelity Six Degree of Freedom aircraft model was linked to a higher level energy management system that takes into account external factors such as wind speeds, wind direction. However, optimal path planning has not considered uncertain environmental conditions (turbulence wind, vertical wind) which are highly important for the UAVs to increase their efficiency by minimising power and fuel consumption while maximising flight endurance. It would be more realistic if power requirements from the full flight are studied for manoeuvre and turbulence cases. Optimising trajectory and path planning may help in the design integration and optimisation of FC hybrid power systems on board an aircraft.

REFERENCES

[1] Advisory Council for Aeronautics Research in Europe (November 2009), *European aeronautical research infrastructures*, available at: http://www.acare4europe.com/html/news.asp (accessed 8 May 2012).

[2] O'Hayre, R. P. (2009), *Fuel cell fundamentals*, 2nd ed, John Wiley & Sons, Hoboken, N.J.

[3] B.J. Holland, J.G. Zhu and L. Jamet, *Fuel Cell Technology and Application*, available at: http://services.eng.uts.edu.au/~joe/subjects/eet/AUPEC01_111.pdf (accessed 12 Aug 2012).

[4] Kordesch, K. and Simader, G. (1996), *Fuel cell: and their applications*, Vch, Weinheim.

[5] Lee, J. S., Quan, N. D., Hwang, J. M., Lee, S. D., Kim, H., Lee, H. and Kim, H. S. (2006), "Polymer electrolyte membranes for fuel cells", *Journal of Industrial and Engineering Chemistry*, vol. 12, no. 2, pp. 175-183.

[6] Authors: L. Gubler, N. Prost, S.A. Gürsel, G.G. Scherer (2005), "Proton exchange membranes prepared by radiation grafting of styrene/divinylbenzene onto poly(ethylene-alt-tetrafluoroethylene) for low temperature fuel cells", vol. 2849, no. 176.

[7] Sorensen, B. (2005), *Hydrogen and Fuel Cells: Emerging Technologies and Applications*, Elsevier.

[8] Barbir, F. (2005), *PEM Fuel Cells - Theory and Practice*, Elsevier.

[9] Hoogers, G. (2003), *Fuel Cell Technology Handbook*, 3rd ed, CRC Press LLC, Boca Raton London New York Washington, D.C.

[10] Gubler, L., Prost, N., Gürsel, S. A. and Scherer, G. G. (2005), "Proton exchange membranes prepared by radiation grafting of styrene/divinylbenzene onto poly(ethylene-alt-tetrafluoroethylene) for low temperature fuel cells", *Solid State Ionics*, vol. 176, no. 39–40, pp. 2849-2860.

[11] McNicol, B. D., Rand, D. A. J. and Williams, K. R. (2001), "Fuel cells for road transportation purposes - yes or no?", *Journal of Power Sources*, vol. 100, no. 1–2, pp. 47-59.

[12] Tsuchiya, H. and Kobayashi, O. (2004), "Mass production cost of PEM fuel cell by learning curve", *International Journal of Hydrogen Energy*, vol. 29, no. 10, pp. 985-990.

[13] Mekhilef, S., Saidur, R. and Safari, A. (2012), "Comparative study of different fuel cell technologies", *Renewable and Sustainable Energy Reviews,* vol. 16, no. 1, pp. 981-989.

[14] Larminie, J. and Dicks, A. (2003), *Fuel cell systems explained,* 2nd ed, Wiley, Chichester.

[15] He, W. (1997), "Dynamic performance of a reformer for molten carbonate fuel cell power-generation systems", *Fuel Processing Technology,* vol. 53, no. 1–2, pp. 99-113.

[16] U.S. Department of Energy (April 2012), *Fuel Cell Technologies Program*, available at: www.eere.energy.gov/informationcenter (accessed 12 February 2013).

[17] Research and markets, *Fuel Cells for Residential, Commercial, and Industrial Applications: Market Analysis and Forecasts*, available at: http://www.reportlinker.com/p0170439/Fuel-Cells-for-Residential-Commercial-and-Industrial-Applications-Market-Analysis-and-Forecasts.html (accessed 08 Dec 2012).

[18] Airbus (19 February 2008), *Emission Free Power for Civil Aircraft: Airbus Successfully Demonstrates Fuel Cells in Flight*, available at: http://www.airbus.com/en/presscentre/pressreleases/press-release/?tx_ttnews%5Bswords%5D=emission%20free%20power&tx_ttnews%5Btt_news%5D=1165&tx_ttnews%5BbackPid%5D=1765&cHash=93b9eb25cb (accessed 7 May 2010).

[19] Boeing, *Boeing Successfully Flies Fuel Cell-Powered Airplane*, available at: http://www.boeing.com/news/releases/2008/q2/080403a_nr.html (accessed 8 May 2010).

[20] EG&G Services Parsons, Inc., Science (October 2000), *Fuel Cell Handbook Fifth Edition,* National Energy ed, Science Applications International Corporation, U.S.

[21] Toyota (November, 2012), *Fuel Cell Technology*, available at: http://www.toyota-global.com/innovation/environmental_technology/fuelcell_vehicle/(accessed 19 November 2012).

[22] Ballard (2003), *Nexa™ Power Module User's Manual,* MAN5100078, Ballard Power Systems Inc, Canada.

[23] Chellappan, M. V., Todorovic, M. H. and Enjeti, P. N. (2008), "Fuel Cell Based Battery-Less UPS System", *Industry Applications Society Annual Meeting, 2008. IAS '08. IEEE,* pp. 1.

[24] Moussaoui, Z., Batarseh, I., Lee, H. and Kennedy, C. (1996), "An overview of the control scheme for distributed power systems", *Southcon/96. Conference Record,* pp. 584.

[25] Fadali Hani (2008), *Fuel Cell Distributed Generation: Power Conditioning, Control and Energy Management* (Master thesis), University of Waterloo, Canada.

[26] Jiang, Z. and Dougal, R. A. (2006), "A compact digitally controlled fuel cell/battery hybrid power source", *IEEE Transactions on Industrial Electronics,* vol. 53, no. 4, pp. 1094-1104.

[27] Trentini, M. and Pieper, J. K. (1998), "A case study of multi-objective control: synthesis and analysis", *Control Applications, 1998. Proceedings of the 1998 IEEE International Conference on,* Vol. 2, pp. 1001.

[28] Djekic, O., Brkovic, M. and Roy, A. (1998), "High frequency synchronous buck converter for low voltage applications", *Power Electronics Specialists Conference, 1998. PESC 98 Record. 29th Annual IEEE,* Vol. 2, pp. 1248.

[29] Ramsden, E. (2006), *Hall-Effect Sensors - Theory and Applications,* 2nd Edition ed, Elsevier, USA.

[30] Amploc Current Sensors (2012), *Engineers' Reference Handbook,* available at: http://www.amploc.com/HANDBOOK%20web.pdf (accessed 11 November 2012).

[31] National Instruments (2012), *Shielded I/O Connector Block for DAQ Devices with 68-Pin Connectors,* available at: http://sine.ni.com/nips/cds/view/p/lang/en/nid/1180 (accessed 20 November 2012).

[32] Thomas, P. R. (2009), "Development of an Automated flight test safety system for autonomous system identification of small UAVs ", Bristol, UK.

[33] De Lomas, J. G. D. (2009), *Development of an autonomous fixed-wing UAV platform* (MSc thesis thesis), Department of Aerospace Sciences, Cranfield University.

[34] Moghimi, S. (February 2010), *Navigation and Control Systems Design for Piper UAV Towards Implementation,* Cranfield University, UK.

[35] Cook, M. V. (2007), *Flight Dynamics Principles,* Elsevier/Butterworth-Heinemann.

[36] Zahn Electronics, I. (2012), *Step Down DC/DC Converter*, available at: http://www.zahninc.com/index.html (accessed 20 November 2012).

[37] Aldhaher. (Cranfield University), (2011), *Designing and Inmlementing a Bidirctanal DCDC Converter for Hybird Power Systems* (MSc report), Cranfield University.

[38] KAZIMIERCZUK, M. (2008), *Pulse-width Modulated DC–DCPower Converters,* 1st ed, John Wiley & Sons, Ltd, United Kingdom.

[39] Sander, K. F. (1992), *Electric circuit analysis : principles and applications,* Addison-Wesley, Wokingham, England.

[40] Scherz, P. (2000), *Practical Electronics for inventors,* McGraw-Hills, New Yourk, USA.

[41] Eckardt, B., Hofmann, A., Zeltner, S. and Maerz, M., (2006), *Automotive Powertrain DC/DC Converter with 25kW/dm(exp3) by using SiC Diodes.*

[42] Oheda, A., Omar, B., Chai, S. C., Aseeri, A. and Savvaris, A. (2010), "Experimental analysis of the dynamic performance of PEM fuel cell under various load changes", *Mechanical and Electrical Technology (ICMET), 2010 2nd International Conference on*, pp. 604.

[43] Tang, Y., Yuan, W., Pan, M., Li, Z., Chen, G. and Li, Y. (2010), "Experimental investigation of dynamic performance and transient responses of a kW-class PEM fuel cell stack under various load changes", *Applied Energy,* vol. 87, no. 4, pp. 1410-1417.

[44] Ellis, M. W., Von Spakovsky, M. R. and Nelson, D. J. (2001), "Fuel cell systems: efficient, flexible energy conversion for the 21st century", *Proceedings of the IEEE,* vol. 89, no. 12, pp. 1808-1818.

[45] Wang, Y., Chen, K. S., Mishler, J., Cho, S. C. and Adroher, X. C. (2011), "A review of polymer electrolyte membrane fuel cells: Technology, applications, and needs on fundamental research", *Applied Energy,* vol. 88, no. 4, pp. 981-1007.

[46] Corbo, P., Migliardini, F. and Veneri, O. (2008), "An experimental study of a PEM fuel cell power train for urban bus application", *Journal of Power Sources,* vol. 181, no. 2, pp. 363-370.

[47] Kim, J. Y., Oh, T., Shin, Y., Bonnett, J. and Weil, K. S. (2011), "A novel non-platinum group electrocatalyst for PEM fuel cell application", *International Journal of Hydrogen Energy,* vol. 36, no. 7, pp. 4557-4564.

[48] Bıyıkoğlu, A. (2005), "Review of proton exchange membrane fuel cell models", *International Journal of Hydrogen Energy,* vol. 30, no. 11, pp. 1181-1212.

[49] Farhat, Z. N. (2004), "Modeling of catalyst layer microstructural refinement and catalyst utilization in a PEM fuel cell", *Journal of Power Sources,* vol. 138, no. 1-2, pp. 68-78.

[50] Yan, Q., Toghiani, H. and Causey, H. (2006), "Steady state and dynamic performance of proton exchange membrane fuel cells (PEMFCs) under various operating conditions and load changes", *Journal of Power Sources,* vol. 161, no. 1, pp. 492-502.

[51] Tao, W. Q., Min, C. H., Liu, X. L., He, Y. L., Yin, B. H. and Jiang, W. (2006), "Parameter sensitivity examination and discussion of PEM fuel cell simulation model validation: Part I. Current status of modeling research and model development", *Journal of Power Sources,* vol. 160, no. 1, pp. 359-373.

[52] Colleen, S. (2008), *PEM fuel cell modeling and simulation using Matlab,* Academic Press is an imprint of Elsevier, Amsterdam :Boston.

[53] El-Sharkh, M. Y., Rahman, A., Alam, M. S., Byrne, P. C., Sakla, A. A. and Thomas, T. (2004), "A dynamic model for a stand-alone PEM fuel cell power plant for residential applications", *Journal of Power Sources,* vol. 138, no. 1-2, pp. 199-204.

[54] Del Real, A. J., Arce, A. and Bordons, C. (2007), "Development and experimental validation of a PEM fuel cell dynamic model", *Journal of Power Sources*, vol. 173, no. 1, pp. 310-324.

[55] Pathapati, P. R., Xue, X. and Tang, J. (2005), "A new dynamic model for predicting transient phenomena in a PEM fuel cell system", *Renewable Energy*, vol. 30, no. 1, pp. 1-22.

[56] Wang, X., Xu, J., Yan, W., Lee, D. and Su, A. "Transient response of PEM fuel cells with parallel and interdigitated flow field designs", *International Journal of Heat and Mass Transfer*.

[57] Zhang, Z., Jia, L., Wang, X. and Ba, L. (2011), "Effects of inlet humidification on PEM fuel cell dynamic behaviors", *International Journal of Energy Research*, vol. 35, no. 5, pp. 376-388.

[58] Wu, H., Berg, P. and Li, X. (2010), "Steady and unsteady 3D non-isothermal modeling of PEM fuel cells with the effect of non-equilibrium phase transfer", *Applied Energy*, vol. 87, no. 9, pp. 2778-2784.

[59] Peng, J., Shin, J. Y. and Song, T. W. (2008), "Transient response of high temperature PEM fuel cell", *Journal of Power Sources*, vol. 179, no. 1, pp. 220-231.

[60] Inamuddin, Cheema, T. A., Zaidi, S. M. J. and Rahman, S. U. (2011), "Three dimensional numerical investigations for the effects of gas diffusion layer on PEM fuel cell performance", *Renewable Energy*, vol. 36, no. 2, pp. 529-535.

[61] Alotto, P., Guarnieri, M. and Moro, F. (2010), "A Fully Coupled Three-Dimensional Dynamic Model of Polymeric Membranes for Fuel Cells", *Magnetics, IEEE Transactions on*, vol. 46, no. 8, pp. 3257-3260.

[62] Caisheng Wang, Nehrir, M. H. and Shaw, S. R. (2005), "Dynamic models and model validation for PEM fuel cells using electrical circuits", *Energy Conversion, IEEE Transactions on*, vol. 20, no. 2, pp. 442-451.

[63] Pukrushpan, J. T., Stefanopoulou, A. G. and Huei Peng (2002), "Modeling and control for PEM fuel cell stack system", *American Control Conference, 2002. Proceedings of the 2002*, Vol. 4, pp. 3117.

[64] Giustiniani, A., Petrone, G., Pianese, C., Sorrentino, M., Spagnuolo, G. and Vitelli, M. (2006), "PEM Fuel Cells Control by means of the Perturb and Observe Technique", *IEEE Industrial Electronics, IECON 2006 - 32nd Annual Conference on*, pp. 4349.

[65] Pukrushpan, J. T., Stefanopoulou, A. G. and Huei Peng (2004), "Control of fuel cell breathing", *Control Systems, IEEE*, vol. 24, no. 2, pp. 30-46.

[66] Gruber, J. K., Bordons, C. and Dorado, F. (2008), "Nonlinear control of the air feed of a fuel cell", *American Control Conference, 2008*, pp. 1121.

[67] Golbert, J. and Lewin, D. R. (2007), "Model-based control of fuel cells (2): Optimal efficiency", *Journal of Power Sources,* vol. 173, no. 1, pp. 298-309.

[68] Bordons, C., Arce, A. and del Real, A. J. (2006), "Constrained predictive control strategies for PEM fuel cells", *American Control Conference, 2006,* pp. 6.

[69] Mestan Tekin, Daniel Hissel, Marie-Ccile Pera and Jean Marie Kauffmann (2007), "Energy-Management Strategy for Embedded Fuel-Cell Systems Using Fuzzy Logic", *Industrial Electronics, IEEE Transactions on,* vol. 54, no. 1, pp. 595-603.

[70] Hatti, M. (2007), "Neural Network Controller for P E M Fuel Cells", *Industrial Electronics, 2007. ISIE 2007. IEEE International Symposium on,* pp. 341.

[71] Bhoopal, N., Venu Madhav, G., Pathapati P. R. and Amarnath, Dr. J. (2009), " Modeling of Polymer Electrolyte Membrane Fuel Cell using Artificial Neural Networks", *International Journal of Recent Trends in Engineering,* vol. 2, pp. 75.

[72] Rakhtala, S. M., Ghaderi, R., Ranjbar, A., Fadaeian, T. and Niaki, A. N. (2009), "PEM fuel cell voltage-tracking using artificial neural network", *Electrical Power & Energy Conference (EPEC), 2009 IEEE,* pp. 1.

[73] Spiegel, C. (2008), "Chapter 1 - An Introduction to Fuel Cells", in *PEM Fuel Cell Modeling and Simulation Using Matlab,* Academic Press, Burlington, pp. 1-14.

[74] Barbir, F., Gorgun, H. and Wang, X. (2005), "Relationship between pressure drop and cell resistance as a diagnostic tool for PEM fuel cells", *Journal of Power Sources,* vol. 141, no. 1, pp. 96-101.

[75] Mamlouk, M. and Scott, K. (2011), "A study of oxygen reduction on carbon-supported platinum fuel cell electrocatalysts in polybenzimidazole/phosphoric acid", *Proceedings of the Institution of Mechanical Engineers, Part A: Journal of Power and Energy,* vol. 225, no. 2, pp. 161-174.

[76] Paganelli, G., Guezennec, Y., and Rizzoni, G. (2002), "Optimizing Control Strategy for Hybrid Fuel Cell Vehicle", *Fuel Cell Power for Transportation, SAE 2002 World Congress,* no. 0148-7191, pp. 1691.

[77] Jiang, Z., Gao, L., Blackwelder, M. J. and Dougal, R. A. (2004), "Design and experimental tests of control strategies for active hybrid fuel cell/battery power sources", *Journal of Power Sources,* vol. 130, no. 1–2, pp. 163-171.

[78] He Hong-wen, Zhang Ying-qi and Wan Fan (2008), "Control strategies design for a fuel cell hybrid electric vehicle", *Vehicle Power and Propulsion Conference, 2008. VPPC '08. IEEE,* pp. 1.

[79] Thounthong, P., Raël, S. and Davat, B. (2006), "Control strategy of fuel cell/supercapacitors hybrid power sources for electric vehicle", *Journal of Power Sources,* vol. 158, no. 1, pp. 806-814.

[80] Jung, J. , Loo, J. , Kim, H. (2003), "Power control strategy for fuel cell hybrid electric vehicles", *fuel cell transportation,* vol. 10, no. 4, pp. 201-205.

[81] Jung, J., Lee, Y., Kim H (2003), "Power control strategy for fuel cell hybrid electric vehicles", *Fuel cell transportation,* pp. 201-205.

[82] Schiffer, J., Bohlen, O., De Doncker, R. W., Sauer, D. U. and Kyun Young Ahn (2005), "Optimized energy management for fuelcell-supercap hybrid electric vehicles", *Vehicle Power and Propulsion, 2005 IEEE Conference,* pp. 341.

[83] Rodatz, P., Paganelli, G., Sciarretta, A. and Guzzella, L. (2005), "Optimal power management of an experimental fuel cell/supercapacitor-powered hybrid vehicle", *Control Engineering Practice,* vol. 13, no. 1, pp. 41-53.

[84] Li-Cun Fang and Shi-Yin Qin (2006), "Concurrent Optimization for Parameters of Powertrain and Control System of Hybrid Electric Vehicle Based on Multi-Objective Genetic Algorithms", *SICE-ICASE, 2006. International Joint Conference,* pp. 2424.

[85] Caux, S., Lachaize, J., Fadel, M., Shott, P. and Nicod, L. (2005), "Modelling and control of a Fuel Cell System and Storage Elements in transport applications", *Journal of Process Control,* vol. 15, no. 4, pp. 481-491.

[86] Kim, M. and Peng, H. (2007), "Power management and design optimization of fuel cell/battery hybrid vehicles", *Journal of Power Sources,* vol. 165, no. 2, pp. 819-832.

[87] Åström, Karl J. (Karl Johan), (2006), *advanced pid control (karl johan), 1934-,* Instrumentation, Systems and Automation Society, USA.

[88] Åström, K. J. (2002), "PID control", in *Control System Design,* pp. 216-251.

[89] Dutton, K., Thompson, S., and Barraclough, B. (1997), *The Art of Control Engineering,* Addison Wesley Longman, Pearson Education Limited, Edinburgh Gate, Harlow, Essex, England.

[90] Chen, Q., Gao, L., Dougal, R. A. and Quan, S. (2009), "Multiple model predictive control for a hybrid proton exchange membrane fuel cell system", *Journal of Power Sources,* vol. 191, no. 2, pp. 473-482.

[91] Rakhmatov, D., Vrudhula, S. and Wallach, D. A. (2003), "A model for battery lifetime analysis for organizing applications on a pocket computer", *Very Large Scale Integration (VLSI) Systems, IEEE Transactions on,* vol. 11, no. 6, pp. 1019-1030.

[92] Hunt, K. J., Sbarbaro, D., Żbikowski, R. and Gawthrop, P. J. (1992), "Neural networks for control systems-A survey", *Automatica,* vol. 28, no. 6, pp. 1083-1112.

[93] Kim, D-H Oh, J-W, Lee, I-W, p. 291-298 (2002), "Cerebellar Model Articulation Controller (Cmac) for Suppression of Structural Vibration", pp. p. 291-298.

[94] McCulloch, W. S. and Pitts, W. H. (2007), *A logical calculus of the ideas immanent in nervous activity,* Springer Science, USA.

[95] Hebb, D. O. (2009), *The Organization of Behavior: A Neuropsychological Theory*, John Wiley & Sons Inc, Francis.

[96] Azlan Hussain, M. (1999), "Review of the applications of neural networks in chemical process control - simulation and online implementation", *Artificial Intelligence in Engineering*, vol. 13, no. 1, pp. 55-68.

[97] LOPEZ-MEJIA, L. (2010), *Aircraft Damage Detection and Reconfiguration Using Artificial Neural Networks* (MSc Thesis thesis), Cranfield University, Cranfield, UK.

[98] Slotine, J. J. and Li, W (1991), *Applied Nonlinear Control. Englewood Cliffs*, New Jersey, Prentice-Hall, USA.

[99] Oja, E. and Math, J. (1982), "A simplified neuron model as a principal component analyzer", vol. 15, pp. 267-273.

[100] Narendra, K. S., Lewis, F. L (2001), "Introduction to the special issue on neural network feedback control", vol. 37, no. 8, pp. 11401158.

[101] Bishop, C. M. (1995), *Neural networks for Pattern Recognition*, Oxford University Press, Oxford UK.

[102] Rytter, A. (1993), *Vibration Based Inspection of Civil Engineering Structures* (PhD thesis), University of Aalborg, Denmark.

[103] Peterka, V. (1999), "Adaptive Digital Regulation of Noisy Systems", vol. 13, pp. 537-550.

[104] Åström, K. J. (1983), "Theory and applications of adaptive control - A survey", *Automatica*, vol. 19, no. 5, pp. 471-486.

[105] Bellman, R. (1957), *Dynamic Programming*, Princeton University Press, Princeton, New Jersey.

[106] Bellman, R. (1961), *Adaptive Control Processes. A Guided Tour*, Princeton University Press, Princeton, N. J.

[107] Feldbaum, A., Kraiman, A. (1965), *Optimal control systems*, Academic Press, New York.

[108] Åström, K. J. and Eykhoff, P. (1971), "System identification - A survey", *Automatica*, vol. 7, no. 2, pp. 123-162.

[109] Widrow, B. (1971), *Pattern Recognition and Machine Learning published*, plenum Press, Stanford, California, USA.

[110] Aseltine, J. A. , Mancini, A. R. and Sarture, C. W. (1958), "A. survey of adaptive control systems." IRE. Transaction on Automatic Control", pp. 102-108.

[111] Jacobs, O. (1961), " A Review of Self-Adjusting Systems In Automatic Control", vol. 10, pp. 311.

[112] Martin T. Hagan, O De Jesús, Roger Schultz (1999), "Training Recurrent Networks for Filtering and Control", in L. Medsker and L.C. Jain, Eds., CRC Press, (ed.) *Recurrent Neural Networks: Design and Applications,* pp. 311-340.

[113] Al-Sabban, H., Gonzalez, F., & Smith, N. (2012), "Wind-energy based path planning for electric unmanned aerial vehicles using Markov decision processes", in IEEE (ed.), *International Conference on Robotics and Automation (ICRA),* 26 Sep 2012.

[114] Alvarez, A., Caiti, A. and Onken, R. (2004), "Evolutionary path planning for autonomous underwater vehicles in a variable ocean", *Oceanic Engineering, IEEE Journal of,* vol. 29, no. 2, pp. 418-429.

[115] Weizhong Zhang, Inane, T., Ober-Blobaum, S. and Marsden, J. E. (2008), "Optimal trajectory generation for a glider in time-varying 2D ocean flows B-spline model", *Robotics and Automation, 2008. ICRA 2008. IEEE International Conference on,* pp. 1083.

[116] Soulignac M., Taillibert P., Rueher M. (2008), "Path Planning for UAVs in Time-Varying Winds", in Heriot-Watt University, U. K. (ed.), *The UK Planning Special Interest Group,* December 11-12, 2008.

[117] Deborah, S. (2010), *Wake Vortex Modelling and Simulation for Air Vehicles in Close Formation Flight* (PhD thesis), Aerospace Sciences, Cranfield University.

[118] Novák, V., Perfilieva, I. and Močkoř, J. (1999), *Mathematical Principles of Fuzzy Logic,* Kluwer, Dordrecht Academic.

[119] Lee, C. C. (1990), "Fuzzy logic in control systems: fuzzy logic controller. I", *Systems, Man and Cybernetics, IEEE Transactions on,* vol. 20, no. 2, pp. 404-418.

[120] Adriaenssens, V., Baets, B. D., Goethals, P. L. M. and Pauw, N. D. (2004), "Fuzzy rule-based models for decision support in ecosystem management", *Science of The Total Environment,* vol. 319, no. 1–3, pp. 1-12.

Appendices

9. Appendices

9.1 List of Publication

1- Experimental analysis of the dynamic performance of PEM fuel cell under various load changes, ($ICMET$), 2010 2nd International Conference

2- Experimental Validation of a Dynamics Fuel-Cell Model using a 1.2kW Nexa Power Module, Hydrogen and Fuel Cells Conference 2011

2010 International Conference on Mechanical and Electrical Technology (ICMET 2010)

Experimental Analysis of the Dynamic Performance of PEM Fuel Cell under Various Load Changes

A. Oheda, B. Omar, S. C. Chai, A. Aseeri and A. Savvaris
Department of Aerospace Sciences
School of Engineering, Cranfield University
Cranfield, UK
A.Oheda@cranfield.ac.uk

***Abstract*—The dynamic performance is one of the most important specifications for Fuel Cell system (FCs). In this paper, practical experimental investigation of dynamic performance and transient responses of Proton Exchange Membrane (PEM) FC under various load conditions are presented using Ballard Nexa (1.2kW) PEMFC system. In order to test different characteristics of FCs, the practical tests have been separated into four different categories: for instance start-up, shut-down, step-up load, and irregular load variation. It is observed that the external load changes the current output proportionally and reverses stack voltage consequently. The purge operation benefits performance recovery and improvement during a constant load and its time constant completely depends on the current working point. Overshoot and undershoot behaviours were observed throughout start up and transience. Magnitudes of overshoot/undershoot voltage show a discrepancy under different current intensities conditions.**

The operating temperature of the system reacted quickly to current load without observation of overshoot or undershoot event. At the same time the air flow rate is directly affected by the dynamics load demand. Whereas, the increased amount of air flow rate during different step-changes is not identical, but depends on the requirement of internal reaction and flooding intensity. The results presented in this paper can be extended for validation of dynamic behaviour for different FC models.

Keywords-PEM Fuel Cell; Dynamic performance; Transient response; Undershoot; Overshoot

I. INTRODUCTION

FC play a very importance roles in the new power generation filed due to its inherit virtue such as inherently clean, efficient and reliable source of power. Comparing with the traditional fossil-fuels technologies, FC system has strong robustness over whole load range in the case of little variation. Due to high module structure, FC system can be scaled to variety size to improve the performance and efficiency. However, for further practical deployment, FCs are expected to become more competitive in terms of cost, performance and reliability.

Among the various types of FCs, the Proton Exchange Membrane (PEM) FC has been drawing more attention due to its low operating temperature, ease of start-up and shut-down and compactness [1]. However, it is not able to respond promptly to a load step change due to the delay time for the fuel flow rate to adjust [2].

The majority of recent research focused on steady-state performance of PEM FC by presenting the polarization curves. Since experimental limitations and practical design problems, most of research works are carried out through modeling approaches [3]. However, the dynamic behaviour plays a very important role in evaluation of the whole system performance and obtains stable performance under various operating conditions. Generally, the dynamic performance of PEM FCs is affected by water, heat and gas management. In order to test the several technical problems related with the FC dynamic performance, the practical experiments have been carried out under strong conditions. This review divided into three parts as follows:

A. Temperature operation and gas management

Jong-Woo and Song-Yul [4] proposed a new temperature control strategy based on a thermal circuit. The thermal circuit consists of a bypass valve, a radiator with a fan, a reservoir and a coolant pump. Classic PI controllers and a state feedback control were used for the thermal circuit. In addition, the heat source term, which is dependent upon the load current, was feed-forwarded to the closed loop. The results show that the temperature rise in the catalyst can be kept within an allowable value and duration. The oxygen excess ratio can be maintained at an optimal value by minimizing the influence of temperature variations in the gas flow channel, and the power consumption of the blower reduced by more than 15% by compensation, and 5% by the controlling bypass valve at a multi-step load profile.

Three dimensional simulation of transient response of PEM FCs with consideration of heat balance was carried out by Shimpalee, S. [5] The results showed that the current overshoots the final state value during a change in the electrical load with fixed flow rates of hydrogen and air. Shimpalee, S. et al. [6] they carried out the effects of different operating parameters on the performance of PEM FC by using pure hydrogen on the anode channel and air on the cathode channel. They presented experiments with different FC operating temperatures, different cathode and anode humidification temperatures. Their experimental results are showed the effects of the various operating parameters on the performance of the PEM FC. Ferng, Y. M et. al. [7] they presented a study of the single cell

978-1-4244-8102-6/10$26.00 © 2010 IEEE

Experimental Analysis of the Dynamic Performance of PEM Fuel Cell under Various Load Changes

A. Oheda, B. Omar, S. C. Chai, A. Aseeri and A. Savvaris
Department of Aerospace Sciences
School of Engineering, Cranfield University
Cranfield, UK
A.Oheda@cranfield.ac.uk

***Abstract*—The dynamic performance is one of the most important specifications for Fuel Cell system (FCs). In this paper, practical experimental investigation of dynamic performance and transient responses of Proton Exchange Membrane (PEM) FC under various load conditions are presented using Ballard Nexa (1.2kW) PEMFC system. In order to test different characteristics of FCs, the practical tests have been separated into four different categories: for instance start-up, shut-down, step-up load, and irregular load variation. It is observed that the external load changes the current output proportionally and reverses stack voltage consequently. The purge operation benefits performance recovery and improvement during a constant load and its time constant completely depends on the current working point. Overshoot and undershoot behaviours were observed throughout start up and transience. Magnitudes of overshoot/undershoot voltage show a discrepancy under different current intensities conditions.**

The operating temperature of the system reacted quickly to current load without observation of overshoot or undershoot event. At the same time the air flow rate is directly affected by the dynamics load demand. Whereas, the increased amount of air flow rate during different step-changes is not identical, but depends on the requirement of internal reaction and flooding intensity. The results presented in this paper can be extended for validation of dynamic behaviour for different FC models.

Keywords-PEM Fuel Cell; Dynamic performance; Transient response; Undershoot; Overshoot

I. INTRODUCTION

FC play a very importance roles in the new power generation filed due to its inherit virtue such as inherently clean, efficient and reliable source of power. Comparing with the traditional fossil-fuels technologies, FC system has strong robustness over whole load range in the case of little variation. Due to high module structure, FC system can be scaled to variety size to improve the performance and efficiency. However, for further practical deployment, FCs are expected to become more competitive in terms of cost, performance and reliability.

Among the various types of FCs, the Proton Exchange Membrane (PEM) FC has been drawing more attention due to its low operating temperature, ease of start-up and shut-down and compactness [1]. However, it is not able to respond promptly to a load step change due to the delay time for the fuel flow rate to adjust [2].

The majority of recent research focused on steady-state performance of PEM FC by presenting the polarization curves. Since experimental limitations and practical design problems, most of research works are carried out through modeling approaches [3]. However, the dynamic behaviour plays a very important role in evaluation of the whole system performance and obtains stable performance under various operating conditions. Generally, the dynamic performance of PEM FCs is affected by water, heat and gas management. In order to test the several technical problems related with the FC dynamic performance, the practical experiments have been carried out under strong conditions. This review divided into three parts as follows:

A. Temperature operation and gas management

Jong-Woo and Song-Yul [4] proposed a new temperature control strategy based on a thermal circuit. The thermal circuit consists of a bypass valve, a radiator with a fan, a reservoir and a coolant pump. Classic PI controllers and a state feedback control were used for the thermal circuit. In addition, the heat source term, which is dependent upon the load current, was feed-forwarded to the closed loop. The results show that the temperature rise in the catalyst can be kept within an allowable value and duration. The oxygen excess ratio can be maintained at an optimal value by minimizing the influence of temperature variations in the gas flow channel, and the power consumption of the blower reduced by more than 15% by compensation, and 5% by the controlling bypass valve at a multi-step load profile.

Three dimensional simulation of transient response of PEM FCs with consideration of heat balance was carried out by Shimpalee, S. [5] The results showed that the current overshoots the final state value during a change in the electrical load with fixed flow rates of hydrogen and air. Shimpalee, S. et al. [6] they carried out the effects of different operating parameters on the performance of PEM FC by using pure hydrogen on the anode channel and air on the cathode channel. They presented experiments with different FC operating temperatures, different cathode and anode humidification temperatures. Their experimental results are showed the effects of the various operating parameters on the performance of the PEM FC. Ferng, Y. M et. al. [7] they presented a study of the single cell

978-1-4244-8102-6/10$26.00 © 2010 IEEE

The most important task of this paper was to identify the dynamic performance of each state and characterize relevant transient response to variable load.

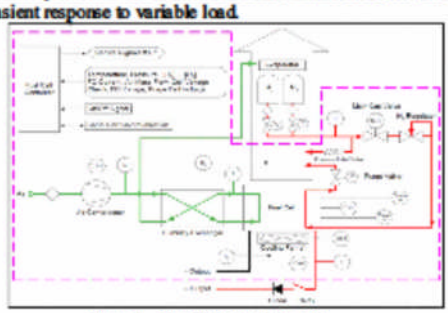

Figure 1. Nexa™ System Schematic

V. Results and Discussion

To track changes in output parameters and other factors these values are treated as a function of time and then plotted. This makes it a lot easier to take notice of any trend changes of these parameters.

A. Transient response in the start-up sequences

The 1.2kW Nexa power module FC provides fully automated operation and load response. Thus 24V batteries must be connected to support start-up and shutdown load; and the system must be provided with an adequate hydrogen fuel supply. The transient responses of transmitted status, current and voltage during the start-up states for 35 second are shown in Fig. 3 and 4. Before applying the battery power, the FC system remains in the OFF state. The starting-up process began by applying 24V battery power to the control board, the system transited to stand-by state in 2 seconds. In this state, sensors and actuators were energized and the onboard microprocessor began to continually deliver system data and status signals. Subsequently a 5V start signal initiates the starting sequence. The hydrogen solenoid valve opened and the purge valve periodically cycled to fill the FC stack with hydrogen. And the air pump turned on to provide air to the FC. Finally, the cooling fan turned on for temperature regulation as well as dilution of purged hydrogen.

The cell voltages began to increase at 13 seconds and reached about 46V. During this state, no current delivers to external load. After 21 seconds, the current gradually increased to 1.2A and voltage decreased to 42V, which presents starting-up operation in this time. At 28 second, when normal operation was achieved, the Nexa control board internally transferred parasitic load from the external battery to the FC stack. As well an external load relay control signal was sent to connect the FC to the external load. Due to this transmission the FC shocked up, it's the current increase with overshoot due to air pump fast demand, and the voltage decrease with undershoot as shown in Fig. 4.

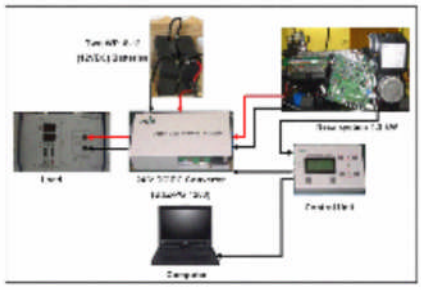

Figure 2. Experiment set up

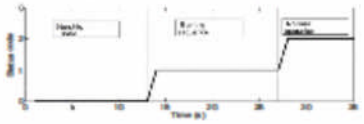

Figure 3. Nexa transmitted status in starting-up state

After the STAND-BY sequence, the air pump and cooling fan voltages jump from 0 to 43% and 50%, respectively as shown in Fig. 6. The air flow rate is fluctuated around 20 slpm, its response has overshoot at the beginning of starting-up and normal operation states as illustrated Fig. 5. When the external load was connected to the FC at 28 second, the voltage of the air pump increased with overshoot in order to supply enough oxidant air and flush the stack of residual water.

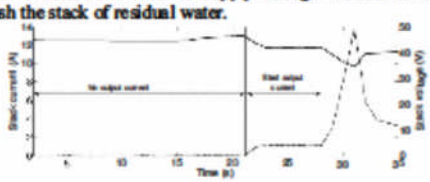

Figure 4. Transient responses of the stack output current (A) & voltage (V) in start-up state

The air flow rate goes up proportionally to satisfy the FC consumption. On the other hand, the membranes are still dry without enough water content at the beginning of a low load operation. An appropriate flow rate benefits water uptake and transport in the membrane FCs [36]. Contrarily, the cooling fan voltage drops to 35% so as to regulate the FC stack temperature. In reality, as shown in Fig. 7 that the stack temperature does not change immediately. Hence, even for a higher current level in the following running of the system, the cooling fan voltage is still kept constantly at 35%.

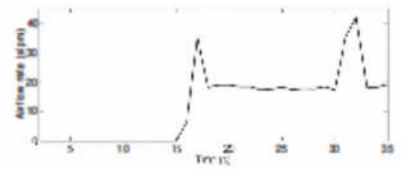

Figure 5. Air flow rate in starting-up state (slpm)

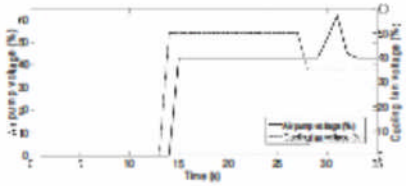

Figure 6. The air pump and cooling fan voltage in the Start-up state

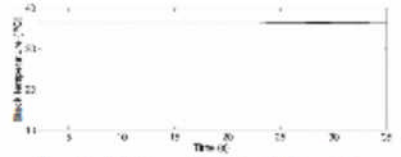

Figure 7. Stack temperature in the starting-up state

B. *Transient response in the shut-down sequence*

In shut-down mode, the 5V start signal removed from the FC stack and the external load relay was open to isolate the FC stack from the load. Since the FC sufficiently operated longer than 5 -minute, then the shut-down sequence continued to remove residual product water from the anode and cathode channels using the air pump and hydrogen purge valve.

The transient responses during the shut-down states are illustrated in Fig. 8, 9, 10 and 11. The shut-down begin from 419 second, the current drops to 1.58A within 1 second, while the stack voltage increases to 42 V. In this period at 438 seconds, the control board internally transferred parasitic load from the FC stack back the external battery, which cause current small undershoot and voltage small overshoot. From 447 seconds, the current drops almost to zero while the stack voltage increase gradually until reaches the OCV value of 46 V in idle state, and continually remove residual product water from the anode and cathode flow channels using the air pump and hydrogen purge valve as shown in Fig. 8.

The air flow rate increase from 20 slpm to 59 slpm in the period from 438 to 482 second than drops to zero as shown in Fig. 10. At 452 second, the voltage of the cooling fan falls from 35 % to zero, later on at 482 seconds, the air pump drops sharply to zero as shown in Fig. 11. Upon shut-down sequence, the stack temperature enters a decline phase but drops quite gently as illustrates in Fig. 9.

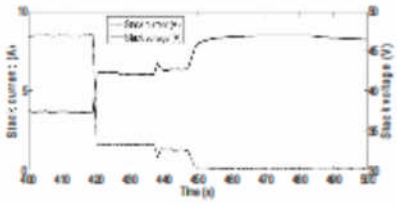

Figure 8. Transient responses of the stack output current (A) and voltage (V) during shut-down state

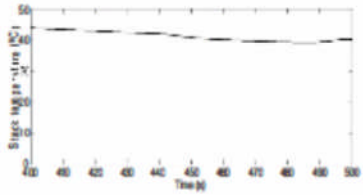

Figure 9. Stack temperature in the shut-down state

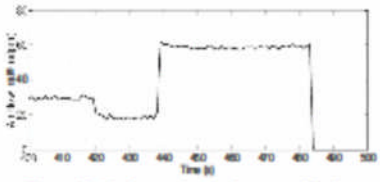

Figure 10. Air flow rate in shut-down state (slpm)

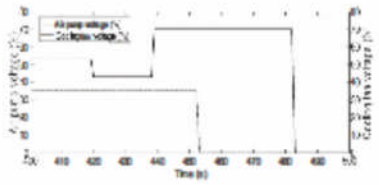

Figure 11. The air pump and cooling fan voltage in the shut-down state

C. *Transient response in the step-up load states*

The results of this test describe the transient responses of FC parameters (stack current, stack voltage, air pump voltage ... etc) during step-up load variation as shown in Fig. 12, 13, 14, 15 and 16. The current increases from 10 to 40 A, the stack voltage decline from 35 to 30V and the interval value was 10A. The maximum power of 1.2 kW occurs after 919 seconds as the current keeps stable at 40A. When the current increase, the frequency of purge valve operation also increases in order to prevent water flooding in the anode channel and anode gas diffusion layer, the interval between

purge valve open and closed is about 96 seconds in the low-current region of around 10A, and become 30 seconds in the high-current region at 40A, which demonstrate the purging mechanism depend on the feedback of the FC dynamic behaviour as shown in Fig. 15 and 16.

The 'red' circle in Fig. 12 is focusing on stack voltage undershoot and current overshoot phenomena that occurs when the current transiently increases from 20A to 30A. The current overshoot possibility is elevated for two reasons: First, is that different operating condition leads to disparate water saturation level particularly after a long course of running. The second, is both the humidified water and product water alter the membrane wettability. The voltage undershoot because of an unexpected load action causes temporary dehydration due to electro-osmotic drag on the anode side, and air feeding starvation on the cathode side. The membrane resistance jumps and inevitably leads to a sharp drop of cell voltage [3].

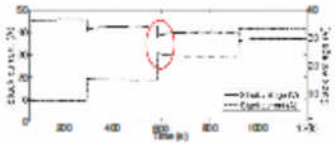

Figure 12. Transient responses of the stack output current (A) and voltage (V) during step-up load states

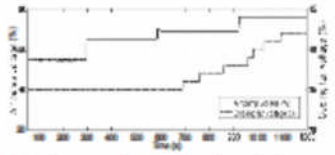

Figure 13. The air pump and cooling fan voltage during step-up states

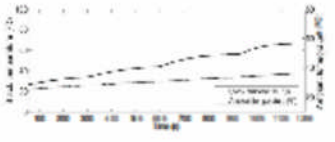

Figure 14. stack and ambient temperatures during step-up states

The stack temperature changes proportionally with the current almost without any delay as illustrated in Fig. 14. The air pump voltage also following the same step-up rhythm to the current increasing trend. The cooling fan voltage at the beginning is constant at 35%, after 700 seconds, it started to step up following the current increase as shown in Fig. 13. Fig. 15 is a detailed schematic plot of the FC stack voltage between 650 and 900 seconds under constant load. The current is around 30A during this period, while the FC stack runs without any load variation, the stack voltage actually experiences periodic degradation with purge valve operation that helps to remove water from the anode channel. During normal FC operation, liquid water condenses and accumulates because of dead-end configuration of the FC anode side. Before the purge valve opens, the stack voltage experiences a slight decline process from 32.2 to approximately 31.76V due to water flooding. An immediate performance enhancement after the purge valve open can be seen at the sharp voltage increase. The purge valve status values are '1' when the valve is open and '0' when the valve is closed as shown in Fig. 16.

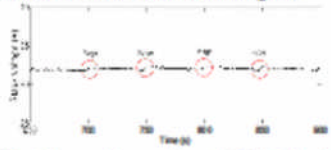

Figure 15. Effect of purge valve operation on PEMFC stack voltage during constant load

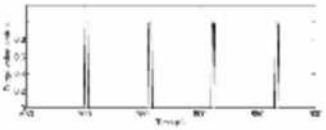

Figure 16. Purge valve status during constant load (0 = valve closed, 1 = valve open)

D. *Transient response under irregular load variation*

The main objective of this test is to study the effects of temperature and air flow rate supplied by the air pump on the FC stack dynamic performance. In the test the FC supply power to irregular load variation over a longer course; experimental results are presented in Fig. 17, 18 and 19. The temperature commonly exists during the FC operation in the forms of exothermic reaction heat transfer and internal heat dissipation. PEM FC stack temperature continuously changes with the load current. However, the temperature directly affects the rate of chemical reactions and the transport of water and reactants. Thus, operations under too-low or too-high temperatures in reality is always not recommended except for extreme circumstance such as sub-zero application [36], where it can be regulated by proper thermal control. The stack temperature response is following the load changes in a similar way to that of the current increase or decrease. However, changing slowly without overshoot or undershoot as illustrated in Fig. 18.

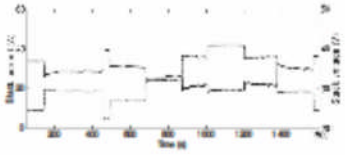

Figure 17. Transient responses of the stack output current (A) and voltage (V) asymmetrical load variation

Fig. 19 presents the air pump and cooling fan voltages of the Nexa FC, it can be seen that the air pump flow rate changes directly tracking the dynamic trend of current fluctuation without any delay. However, the decrease in the amount of air flow rate results in oxygen depletion from the FC cathode channel during power generation. Furthermore, the Nexa FC operation shows that the air flow does not significantly affect the FC stack dynamic performance.

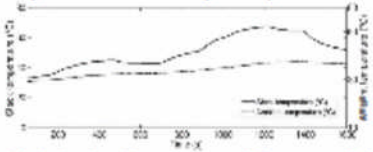

Figure 18. Stack and ambient temperatures during asymmetrical load variation

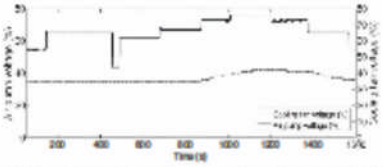

Figure 19. The air pump and cooling fan voltage during asymmetrical load variation

VI. Conclusions

The aim of this study was to investigate the dynamic performance of a PEM FC stack. To reach this goal, a set of experimental tests on Ballard Nexa power module were presented. The dynamic behaviours were checked during different operations conditions such as start-up, shut-down, and step-up and irregular load variation.

The control board internally transferred parasitic load from the external battery to the FC stack at start-up. Due to this transmission the FC shocked up, it's the current increase with overshoot due to air pump fast demand, and the voltage decrease with undershoot. In shut-down sequences control board internally transferred parasitic load from the FC stack back the external battery, which cause current small undershoot and voltage small overshoot.

When the current transiently increases from 20A to 30A, a current overshoot can be observed in the system responses due to two factors. The first factor is that different operating condition results in disparate water saturation level particularly after a long course of running. The second factor is that both the humidified water and product water alter the membrane wettability. Since temporary dehydration due to electro-osmotic drag on the anode side and air feeding starvation on the cathode side, a voltage undershoot was observed at the same time.

With the current increasing, the frequency of purge valve operation also increases in order to prevent water flooding in the anode channel and anode gas diffusion layer. The time interval between purge valve open and closed is about 96 and 30 seconds in the case of the low-current region of around 10A and 40A, respectively.

The stack temperature quickly responses to the load current without observation of overshoot/undershoot. The air flow also follows the same step-up rhythm to the current increasing trend. The cooling fan is constant at 35% at the beginning and steps up when the load current and stack temperature increase.

References

[1] W. Choi, J. W. Howze and P. Enjeti, "Development of an equivalent circuit model of a fuel cell to evaluate the effects of inverter ripple current," J. Power Sources, vol. 158, pp. 1324-1332, 8/25, 2006.

[2] M. Uzunoglu and M. S. Alam, "Dynamic modeling, design and simulation of a PEM fuel cell/ultra-capacitor hybrid system for vehicular applications," Energy Conversion and Management, vol. 48, pp. 1544-1553, 5, 2007.

[3] Y. Tang, W. Yuan, M. Pan, Z. Li, G. Chen and Y. Li, "Experimental investigation of dynamic performance and transient responses of a kW-class PEM fuel cell stack under various load changes," Appl. Energy, vol. 87, pp. 1410-1417, 4, 2010.

[4] J. Ahn and S. Choe, "Coolant controls of a PEM fuel cell system," J. Power Sources, vol. 179, pp. 252-264, 4/15, 2008.

[5] S. Shimpalee, D. Spuckler and J. W. Van Zee, "Prediction of transient response for a 25-cm2 PEM fuel cell," J. Power Sources, vol. 167, pp. 130-138, 5/1, 2007.

[6] L. Wang, A. Husar, T. Zhou and H. Liu, "A parametric study of PEM fuel cell performances," Int J Hydrogen Energy, vol. 28, pp. 1263-1272, 11, 2003.

[7] Y. M. Ferng, Y. C. Tzang, B. S. Pei, C. C. Sun and A. Su, "Analytical and experimental investigations of a proton exchange membrane fuel cell," Int J Hydrogen Energy, vol. 29, pp. 381-391, 3, 2004.

[8] H. Wu, P. Berg and X. Li, "Steady and unsteady 3D non-isothermal modeling of PEM fuel cells with the effect of non-equilibrium phase transfer," Appl. Energy, 2009.

[9] W. Yan, H. Chu, J. Chen, C. Soong and F. Chen, "Transient analysis of water transport in PEM fuel cells," J. Power Sources, vol. 162, pp. 1147-1156, 2006.

[10] W. Yan, C. Soong, F. Chen and H. Chu, "Transient analysis of reactant gas transport and performance of PEM fuel cells," J. Power Sources, vol. 143, pp. 48-56, 2005.

[11] S. Shimpalee, W. Lee, J. W. Van Zee and H. Naseri-Neshat, "Predicting the transient response of a serpentine flow-field PEMFC: II: Normal to minimal fuel and AIR," J. Power Sources, vol. 156, pp. 369-374, 6/1, 2006.

[12] J. Zou, X. Peng and W. Yan, "Dynamic analysis of gas transport in cathode side of PEM fuel cell with interdigitated flow field," J. Power Sources, vol. 159, pp. 514-523, 2006.

[13] W. H. Zhu, R. U. Payne, D. R. Cahela and B. J. Tatarchuk, "Uniformity analysis of MEA and stack Levels for a Nexa PEM fuel cell system," J. Power Sources, vol. 128, pp. 231-238, 4/5, 2004.

[14] A. J. del Real, A. Arce and C. Bordons, "Development and experimental validation of a PEM fuel cell dynamic model," J. Power Sources, vol. 173, pp. 310-324, 2007.

[15] K. P. Adzakpa, J. Ramousse, Y. Dubé, H. Akremi, K. Agbossou, M. Dostie, A. Poulin and M. Fournier, "Transient air cooling thermal modeling of a PEM fuel cell," J. Power Sources, vol. 179, pp. 164-176, 4/15, 2008.

Hydrogen production, storage and utilisation - from nanomaterials to demonstrators

Experimental Validation of a Dynamic Fuel-Cell Model using a 1.2kW Nexa Power Module

A. Oheda,[a] S. Lazarus[b] and A. Savvaris[*]

a, Department of FMCS, Cranfield University, Cranfield, MK43 0AL, UK. a.Oheda@cranfield.ac.uk

b, Department of FMCS, Cranfield University, Cranfield, MK43 0AL, UK.

**,* Department of FMCS, Cranfield University, Cranfield, MK43 0AL, UK.

Abstract

A dynamic electrochemical simulation model of Proton Exchange Membrane (PEM) fuel cell (FC) is proposed in this paper and validated using experimental data from a 1.2kW Nexa power module fuel-cell. Two reduction assumptions were made and discussed broadly along with their theoretical derivations. This work was mainly focused on the validation of the proposed model. The real-time experimental tests were conducted in different stages for start-up, shut-down, step-up load and irregular load variation. The results of those tests are used to validate the physical and numerical characteristics of the proposed model. The steady-state and transient-state phenomena are also considered to analyze the system performance at different conditions; such as load current, pressure of reactant gases, temperature and stack voltage.

Results obtained from the simulation show that the observed relative error is less than 4.1% for the full working process including the start-up sequence and the transient phase, when it was compared with the experimental results. In addition, it could be attained that the proposed model can predict the electrical response of the PEM FC stack under steady-state as well as in the transient state conditions. The aim is to obtain an accurate model based on a 1.2kW Nexa fuel-cell that could be used for the development and design of controllers in hybrid fuel cell electrical systems.

Keywords- PEM FC; Modeling and Simulation; Dynamic; Fuel Cells; Transient response

I. INTRODUCTION

Investigation and development of Fuel Cell (FC) systems for a variety of applications have significantly increased in the last two decades. There are several types of fuel cells, usually classified by their operating temperature and the type of electrolyte they use. Researchers and companies are working on several of those systems to develop the technology further and have commercially available solutions that are economically viable as an alternative to fossil fuelled power systems [1]. The development of the technology requires multidisciplinary effort (e.g. materials, manufacturing process, control systems, power electronics ...etc.)

In this paper work is based on Proton Exchange Membrane fuel cells (PEM FC).Due to the high electrical efficiency and lower operating temperature, the PEM FC is one of the most promising systems to employ in aerospace, automotive and stationary applications as a replacement for the traditional systems [2–5]. It offers high power density, zero emission, fast start-up and reliable source of power at a relatively low cost [6]. There are number of PEM FC models that have been developed in the past. The earlier models on PEM FC presented by Farhat [7] and Yan, et al [8] offered an empirical polarization curve based on the calculated coefficients. These polarization curves consider only the steady state conditions. For the fuel cell performance description, the polarization curve is an important parameters to measure since the FC performance is characterised by its polarization curve [9].

Although several studies on fuel cell modelling are based on the transient-state phenomena [10-12], it still lacks the optimization of the fuel cell stack performance and a specific transient behaviour when the transient state phenomena are included [13]. Wang, et al [14] and Zhang, et al [15] have taken these transient state conditions into consideration and focused on the fluid dynamics inside the stack. In the same way, some other PEM FC models have also proposed in [16-18], which are focused on a multi dimensional study. In all these models the effects of gas diffusion layer on PEM FC performance is studied and evaluated.

Alotto, et al [19] developed a complex three dimensional dynamics model, which uses a highly nonlinear fully coupled dynamic numerical model of the membrane. This model includes proton conduction, water flow, heat generation and transport and hydration conductivity. The aforementioned studies on PEM FC design are very helpful. It still requires an optimal design of the FC model for a better stack performance. In this analysis the simulation results of the improved model are validated using a 1.2kW PEM FC Nexa power module. Results of the steady-state and transient-state phenomena are presented to analyze the system performance at different conditions; such as load current, pressure of reactant gases, temperature, stack voltage ...etc.

The new proposed model is computationally more attractive and offers a real-time control of the PEM FC systems for both steady-state and transient-state phenomena. In this paper the emphasis is on the model validation. The remaining part of this paper is organized as follows: The test tools of the design are presented in section II, The modelling of the PEM FC is detailed with its mathematical equations are derived in section III. The results and discussion are presented in section IV, and the model performance and validation are given in section IIV followed by the Conclusion

II. TEST TOOLS

In this paper the experimental data were obtained from Nexa (1.2kW) PEM FC module. The module consist of a Ballard stack with 46 cells set in series and other auxiliary subsystems including hydrogen system, oxidant air system, cooling system, electronic control system and safety system with sensors and microprocessors integrated on board. The schematic diagram of this FC system is shown in Fig. 1.

The dry hydrogen is supplied by high-pressure hydrogen cylinder, while the oxidant air is supplied by an air pump and humidified in a humidity exchanger before entering the FC stack so as to maintain water saturation of the membrane. A cooling fan at the base of the unit is utilised to blow air through vertical cooling channels. A multi-functional data acquisition (DAQ) unit is supplied facilitating status monitoring and data recording. Feedback signals as well as operating parameters (e.g. temperature, pressure, flow rate, gas concentration, current, and voltage) can be measured through the serial port communication. All the information is displayed in real-time using a LabView GUI software interface. Lastly, the system is connected to an electronic load, to simulate a variable power demand.

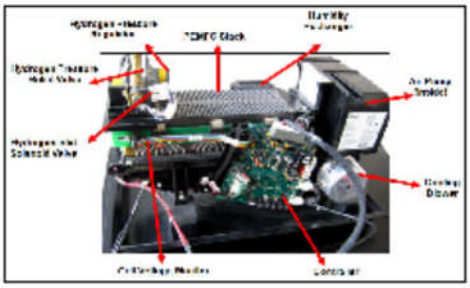

Figure 1. Nexa™ System Schematic

III. PEM FC MODELLING

In the literature as mentioned previously several models have been proposed to model the fuel cell stack. Colleen [10] introduced electrochemical simulation model of PEM FC. El-Sharkh, et al [11] introduced a dynamic model for a stand-alone PEM FC power plant for residential applications. Those models were used as the basis and were modified to model and simulate the Nexa PEM FC stack as follows:

A. Fluid-dynamics equations and modelling assumptions

The fluid-dynamics model used is shown in Fig. 2 and the details of the model derivations are given below. In order to simplify the model, the humidified air is assumed as an oxidant and the dry air will be equalled to that of the atmospheric air and the dry hydrogen is fed into the anode channel. The nitrogen exchange is neglected since it is an inert gas.

The proportional relationship of the flow of gas through a valve with its partial pressure can be expressed as [11]:

$$k_{H2} = \frac{qH_2}{PH_2} \quad \{1\}$$

$$k_{H2O} = \frac{qH_2O}{PH_2O} \quad \{2\}$$

$$k_{O2} = \frac{qO_2}{PO_2} \quad \{3\}$$

For the hydrogen, the derivative of the partial pressure can be calculated using the perfect gas equation as follows:

$$\frac{d}{dt}P_{H2} = \frac{RT}{V_{an}}\left(q_{H_2}^{in} - q_{H_2}^{out} - q_{H_2}^{r}\right) \quad \{4\}$$

The relationship between the reactive gas flows in the gas diffusion layer (GDL) and the load current at the steady state can be computed as follows [20]:

For the hydrogen consumption in the anode side is

$$q_{H_2}^{r} = \frac{N_0 I}{2F} = 2\,kr\,i \quad \{5\}$$

For the oxygen consumption in the cathode side is

$$q_{O_2}^{r} = \frac{N_0 I}{4F} = 4\,kr\,i \quad \{6\}$$

The amount of water produced in the electrochemical reaction is calculated using stoichiometric ratio:

$$qH_2O = \frac{N_0 I}{2F} \quad \{7\}$$

In transient state, there is a delay between the change in the flow of fuel and oxidant. The following relationships are used to represent the delay effects [20]:

$$\tau_a \frac{dM_{H2,net}}{dt} = \frac{I}{2F} - M_{H2,net} \quad \{8\}$$

$$\tau_c \frac{dM_{O2,net}}{dt} = \frac{I}{4F} - M_{O2,net} \quad \{9\}$$

Equations {4} and {5} can be rewritten in the (s) domain as:

$$P_{H2} = \frac{\frac{1}{k_{H2}}}{1+\tau_{H2}\,s}\left(q_{H_2}^{in} - 2\,kr\,i\right) \quad \{10\}$$

Where:

$$\tau_{H2} = \frac{V_{an}}{k_{H2}RT} \quad \{11\}$$

The partial pressures of water P_{H2O}, and oxygen P_{O2} can be derived using equation {10}. For the water and oxygen time constants τ_{H2O} and τ_{O2}, respectively, both can be calculated using the equation {11}.

The assumption is that no liquid water is carried by the inlet air that enters the cathode channel, since the membrane does not allow the liquid water transport; rather it allows only gas transport.

B. Electrochemical equations and voltage calculation

The polarization curves for the PEM FC are described in[10][11]. Since all of the voltage losses had a ($-^{ive}$) sign in front of each of the equations, the actual FC voltage is the addition of the following four terms; the Nernst voltage (E) in terms of gas molarities, the voltage losses in activation overvoltage (V_{act}), ohmic overvoltage (V_{ohmic}) and Mass Transport Losses (V_{conc}).

Fig. 9 describes the drop of fuel cell voltage as a function of current density.

Due to the open circuit voltage, the activation overvoltage (V_{act}) will decrease as the current delivered by the stack increases. As the current density gets higher at a later step, the ohmic losses (V_{ohmic}) will also increase. They are derived from the membrane resistance to move the protons and from the electrical resistance of the electrodes to move the electrons. Thus the need of moving electrons and to split and shape chemical relationships is required when the current density get higher.

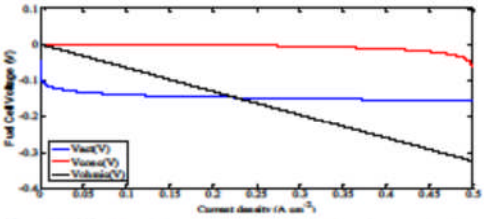

Figure 9. FC voltage drops contributions as a function of current density

The last type of losses is the mass transport or concentration losses (V_{conc}). This loss takes place in both low and high temperature fuel cells, however, it is only prevalent at high current densities [21]. Usually in the case of the Nexa system this occurs when we reach or slightly exceed the maximum rated output power. This is due to the effect of losing a high concentration of either oxygen or hydrogen at the cathode or anode sides, respectively. In other words this occurs when the fuel cell is using oxygen or hydrogen at a rate quicker than it can be supplied. Despite the fact that the last drop has been modelled based on equation {16}, such high current values are not usual as they can cause quick degradation of the cells membranes .

The summation of all the above losses forms the output voltage, producing the polarization curve as shown previously in Fig. 8.

Fig. 10 shows the flow rate of hydrogen and Oxygen from the simulation model during the system start up and normal operation stages. It can be seen that by increasing the load current from 1 to 46 A in steps of 0.1A it takes around 275 seconds for the system to reach the steady state and for the flow rate that react to become steady.

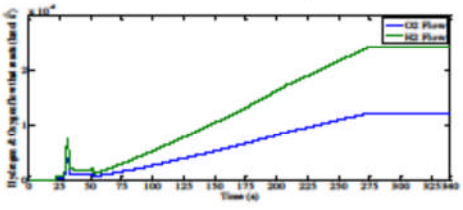

Figure 10. Hydrogen and oxygen flow that react during steady-state test

Fig. 11 illustrates the stack output power as a function of current density. The electric power delivered by the stack is equals to the product of the stack voltage (V_{out}) and the current drawn (i) as given in equations {19} and {20}. Where the current input (i) is taken from the experimental measurements.

As can be observed, the responses of the model match well with the experimental data. Note that there is no peak output power occurs, because the fuel cell does not go into the concentration region.

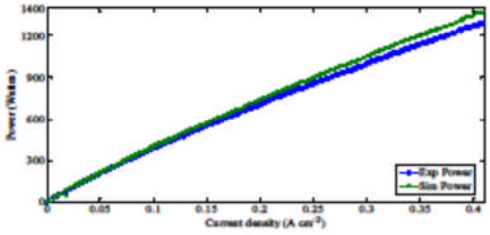

Figure 11. Power curve (Gross Power) during steady-state test

B. *Transient response*

The results shown in Fig. 12 describe the transient responses of the FC parameters (stack current and stack voltage) during step-up and step-down load variation includes the experimental data to show the accuracy of the proposed theoretical model.

It is worth mentioning that the first transient response (at around t = 28 seconds) is due to the system start-up. At t = 305 seconds, the current decreases from 34 Amps to 1 Amps, the simulated stack voltage increase from 34V to 43V, respectively. The experimental analysis and the results of the dynamic performance of this work were already published in[22].

The improved model gives a very good response and closely follows that obtained from the experimental data. Finally, the corresponding hydrogen and oxygen flow that react during this transient-state test are plotted in Fig. 13.

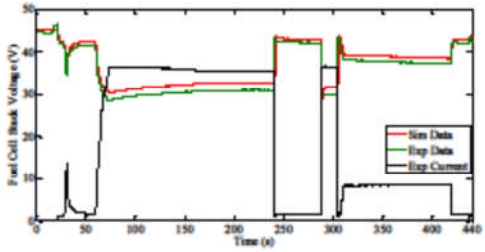

Figure 12. Output Voltage during transient -state test

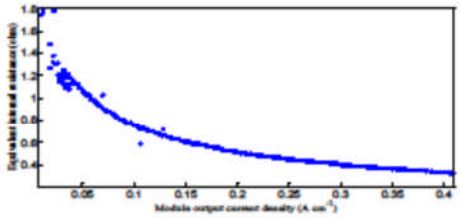

Figure 5. The relationship between (r)(Ω) and module (i) (Acm^{-2})

Based on our observations, a new parameters extraction method is given in Table. 1, some of which are obtained experimentally.

TABLE I. PEMFC MODEL PARAMETERS

Par	Representation	Value
R	Ideal gas constant (J/mol K)	8.314
F	Faraday's constant (Coulombs)	96487
Tc	Temperature in degrees C°	25
Tk	Temperature in k	273.15
P_{H2}	Hydrogen pressure in atm	1.273
P_{H2O}	water pressure in atm	1
P_{O2}	Oxygen pressure in atm	0.16
A	Area of cell (cm^2)	110
No	Number of Cells	46
r	Internal Resistance (Ω/cm^2)	0.50
q_{H2}	Molar flow of hydrogen (kmol s^{-1})	1.5186
q_{O2}	Molar flow of oxygen (kmol s^{-1})	0.8930
α	Transfer coefficient	0.5
$\alpha 1$	Amplification constant	0.095
io	Exchange Current Density (A/cm^2)	$10^{-6.912}$
iL	Limiting current density (A/cm^2)	0.418
Gf	Gibbs function in liquid form (J/mol)	-228170
k	Constant k used in mass transport	10
k_{H2}	Hydrogen valve molar constant (kmol $s^{-1}atm$)	1.0124
k_{O2}	Oxygen valve molar constant (kmol $s^{-1}atm$)	0.893
k_{H2O}	Water valve molar constant (kmol $s^{-1}atm$)	0.00057
Vca	Volume of the anode channel (m^3)	7.59×10^{-4}
Van	Volume of the cathode channel (m^3)	7.59×10^{-4}
kr	Modelling constant kmol $s^{-1}A$	1.192^{-7}

IV. RESULTS AND DISCUSSION

As discussed earlier, the Nexa fuel cell stack has been modelled. The Simulink configuration ode14× (extrapolation) solver method with fixed step size of 0.0002s was used in this model. The inputs to the model are the fuel (oxygen, and hydrogen) and the operating environment (ambient temperature and relative humidity). The stack outputs are the fuel cell stack voltage, current delivered by the stack and the water produced by the chemical reaction.

The whole process is consists of simulating the model by applying the real system inputs and comparing those with the experimental results. In order to accomplish this, the following two tests were conducted: (i) Constant load (to investigate the equivalent internal resistance and to analyze the steady-state effects), (ii) Variable load (to analyze the transitory effects). To analyze the track changes in the output parameters and other factors, the output values are treated as a function of time so as to capture any changes in these parameters while plotting.

A. Steady-State

The steady-state characteristics of FC were obtained by increasing the load current from 1 to 46 A in steps of 0.1A. In this test the stack current was measured directly, the measured data were used to validate the model and a comparison graph of this experimental voltage and simulated voltage as a function of time is shown in Fig. 6. The voltage delivered by the stack is validated by plotting the curves between the present voltage of the cell and the current density, $j = \frac{I}{A}(A\,cm^{-1})$. The voltage values corresponding to the current density taken from the Ballard stack are shown in Fig. 7.

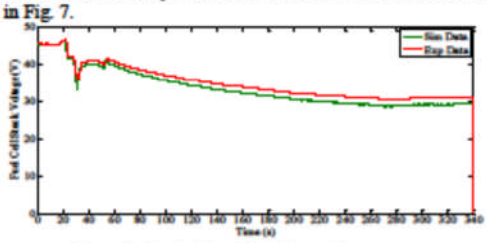

Figure 6. Stack voltage (V) during steady-state test

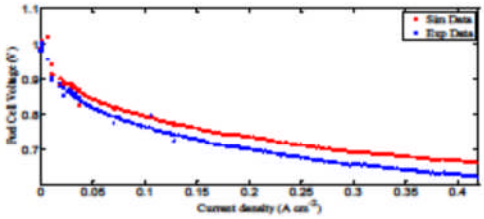

Figure 7. Stack current (A cm^{-2}) versus stack voltage (V) during steady-state test

A FC polarization curve that corresponds to the 1.2kW stack is shown in Fig. 8

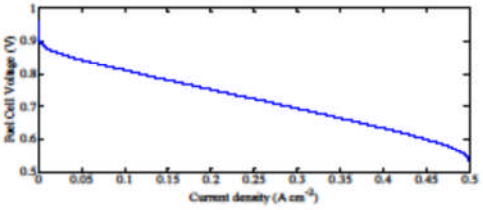

Figure 8. Fuel cell polarization curve

Fig. 9 describes the drop of fuel cell voltage as a function of current density.

Due to the open circuit voltage, the activation overvoltage (V_{act}) will decrease as the current delivered by the stack increases. As the current density gets higher at a later step, the ohmic losses (V_{ohmic}) will also increase. They are derived from the membrane resistance to move the protons and from the electrical resistance of the electrodes to move the electrons. Thus the need of moving electrons and to split and shape chemical relationships is required when the current density get higher.

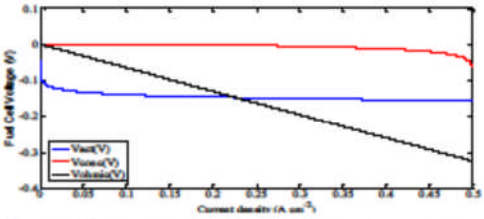

Figure 9. FC voltage drops contributions as a function of current density

The last type of losses is the mass transport or concentration losses (V_{conc}). This loss takes place in both low and high temperature fuel cells, however, it is only prevalent at high current densities [21]. Usually in the case of the Nexa system this occurs when we reach or slightly exceed the maximum rated output power. This is due to the effect of losing a high concentration of either oxygen or hydrogen at the cathode or anode sides, respectively. In other words this occurs when the fuel cell is using oxygen or hydrogen at a rate quicker than it can be supplied. Despite the fact that the last drop has been modelled based on equation {16}, such high current values are not usual as they can cause quick degradation of the cells membranes .

The summation of all the above losses forms the output voltage, producing the polarization curve as shown previously in Fig. 8.

Fig. 10 shows the flow rate of hydrogen and Oxygen from the simulation model during the system start up and normal operation stages. It can be seen that by increasing the load current from 1 to 46 A in steps of 0.1A it takes around 275 seconds for the system to reach the steady state and for the flow rate that react to become steady.

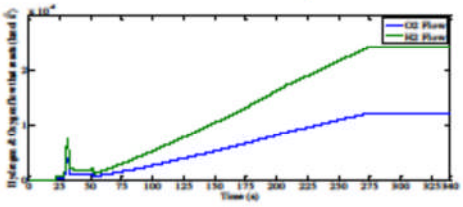

Figure 10. Hydrogen and oxygen flow that react during steady-state test

Fig. 11 illustrates the stack output power as a function of current density. The electric power delivered by the stack is equals to the product of the stack voltage (V_{out}) and the current drawn (i) as given in equations {19} and {20}. Where the current input (i) is taken from the experimental measurements.

As can be observed, the responses of the model match well with the experimental data. Note that there is no peak output power occurs, because the fuel cell does not go into the concentration region.

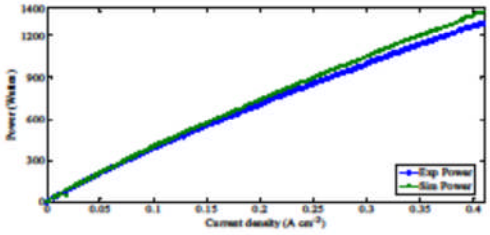

Figure 11. Power curve (Gross Power) during steady-state test

B. *Transient response*

The results shown in Fig. 12 describe the transient responses of the FC parameters (stack current and stack voltage) during step-up and step-down load variation includes the experimental data to show the accuracy of the proposed theoretical model.

It is worth mentioning that the first transient response (at around t = 28 seconds) is due to the system start-up. At t = 305 seconds, the current decreases from 34 Amps to 1 Amps, the simulated stack voltage increase from 34V to 43V, respectively. The experimental analysis and the results of the dynamic performance of this work were already published in[22].

The improved model gives a very good response and closely follows that obtained from the experimental data. Finally, the corresponding hydrogen and oxygen flow that react during this transient-state test are plotted in Fig. 13.

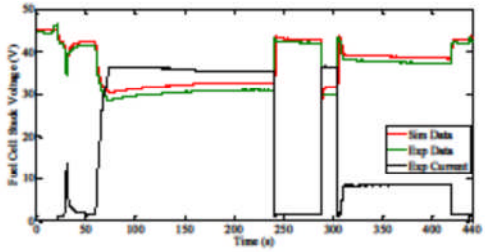

Figure 12. Output Voltage during transient -state test

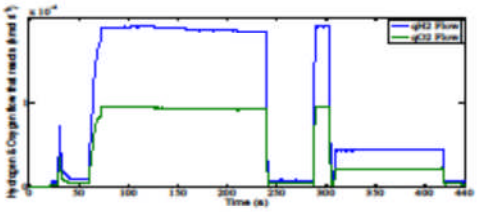

Figure 13. Hydrogen and oxygen flow that react during transient -state test

V. MODEL VALIDATION

To check how large the validity of this model is, simulations have been carried out to compare the response and results with those obtained from the experimental system. Furthermore, the simulation of a1.2kW stack model for both study state and transit state were also covered by considering the effect of the internal resistance under a variety of load variations.

Simulation results show that the models can predict the electrical response of the PEM fuel-cell stack under steady-state as well as transient conditions. Based on the obtained simulation results, it is observed that the relative error is less than 4.5% for the full working process including the start-up sequence and the transient phase of this proposed model.

This could be explained by the following three remarks:

- **Temperature**: fuel cell stack temperature has an effect on fuel cell performance; since temperature changes affect the gas pressure inside both the cathode and anode. As the temperature increase, it increases the voltage at every current stage. Therefore, the assumption of a constant stack temperature would result in introducing some errors in the case of a Nexa power module [23].
- **Amount of condensed water**: the liquid water, decreases the gas diffusion layer surface, as a result there will be a drops in voltage and fuel cell efficiency, thus increasing the current density.
- **Variation of partial pressures**: Variations of the hydrogen partial pressure inside the anode and oxygen partial pressure inside the cathode mainly influence the voltage obtained by the fuel cells. Since the pressure of any of these gases increases, the voltage raises for every current stage. Due to the dead-end design of the fuel cell stack system, hydrogen partial pressure inside the anode remains almost constant. Hence, the oxygen partial pressure is more variable during the power demand changes, since it depends on auxiliary equipment dynamics.

For more details of the validation of the model accuracy, another error study has been presented here using the mean relative error (MRE) as follows:

$$MRE(\%) = 100 \times \frac{1}{N}\sum_{i=0}^{n}\left|\frac{D_i^a - D_i^s}{D_i^a}\right| \qquad \{21\}$$

Where (N) is the number of samples, and (D_i^a) and (D_i^s) represent the experimental and simulated data sets respectively. Employing equation {21}, the MRE calculation is applied to the dynamic responses of the stack voltage during both steady state and transit state. Consequently, the relative mean errors of the parameters obtained are 4.5% and 3.9%, respectively.

VI. CONCLUSIONS

A dynamic electrochemical simulation of Proton Exchange Membrane (PEM) Fuel cell (FC) model is presented in this paper. In order to demonstrate the accuracy of the proposed model, an experimental validation was carried out using the experimental data from a commercial 1.2kW Nexa power module. The performance of the model is studied and validated for both study state and transient state phenomena (transient response of the stack during load changes).

The model assumptions are discussed extensively, as the theoretical equations are presented and the model parameters have been adjusted specifically for a 1.2kW Nexa stack. Simulation results of the proposed model are compared with the experimental data and also verified using MRE calculation. The results show that the percentage error of the simulated model when compared with the experimental results does not exceed 4.5% for the full working process including the start-up sequence and the transient phase.

VII. LIST OF SYMBOLS

PEM	Proton Exchange Membrane
FC	Fuel cell
k_{H2}	Hydrogen valve molar constant (kmol s^{-1} atm)
k_{H2O}	Water valve molar constant (kmol s^{-1} atm)
k_{O2}	Oxygen valve molar constant (kmol s^{-1} atm)
q_{H2}	Molar flow of hydrogen (kmol s^{-1})
q_{H2O}	Molar flow of water (kmol s^{-1})
q_{O2}	Molar flow of oxygen (kmol s^{-1})
q_{H2}^{in}	Hydrogen input flow (kmol s^{-1})
q_{H2}^{out}	Hydrogen output flow (kmol s^{-1})
q_{H2}^{r}	Hydrogen flow that reacts (kmol s^{-1})
P_{H2}	Hydrogen partial pressure (atm)
P_{H2O}	Water partial pressure (atm)
P_{O2}	Oxygen partial pressure (atm)
τ_{H2}	Hydrogen time constant (s)
τ_{H2O}	Water time constant (s)
τ_{O2}	Oxygen time constant (s)
M_{H2}	Molar mass of hydrogen (kg kmol s^{-1})
M_{H2O}	Molar mass of water (kg kmol s^{-1})
τ_a	Fuel flow delay (s)
τ_c	Oxidant flow delay (s)
M_{O2}	Molar mass of oxygen (kg kmol s^{-1})
Van	Volume of the anode channel (m^3)
Vca	Volume of the cathode channel (m^3)
R	Universal gas constant (J $kmol^{-1}$ K)

C_{O2}	Oxygen concentration (0.21%)
Tc	Temperature in degrees C°
Tk	Temperature in k
T	Stack Temperature (k)
No	Number of FCs in the stack
i	Stack current (A/cm^2)
I	Cell current (A/cm^2)
F	Faraday's constant (Coulombs)
kr	Modelling constant = No/4F (kmol s^{-1}A)
V_{out}	DC output voltage of FC stack
P_{out}	power delivered by the stack (w)
E	Nernst voltage (V)
S	s domain
r	Stack internal resistance (Ω/cm^2)
V_{out}	Output voltage of the power module (V)
V_o	Open-circuit voltage of the power module (V)
I_{fc}	Output current of the power module (A)
τ_{H2}	Hydrogen time constant (s)
τ_{O2}	Oxygen time constant (s)
τ_{H2O}	Water time constant (s)
E	Nernst voltage (V)
b	Constant of Tafel
V_{ohmic}	Over potential due to ohmic loss (V)
V_{act}	Activation over potential (V)
V_{conc}	Concentration over potential (V)
A	Area of cell (cm^2)
No	Number of cells
α	Transfer coefficient
α1	Amplification constant
io	Exchange Current Density (A/cm^2)
iL	Limiting current density (A/cm^2)
Gf	Gibbs function in liquid form (J/mol)
k	Constant k used in mass transport
k_{H2}	Hydrogen valve constant (kmol s^{-1}atm)
k_{O2}	Oxygen valve constant (kmol s^{-1}atm)
k_{H2O}	Water valve constant (kmol s^{-1}atm)
GDL	Gas diffusion layer

REFERENCES

[1] M. W. Ellis, Von Spakovsky, M. R., & D. J. Nelson, Fuel cell systems, "Efficient, flexible energy conversion for the 21st century", IEEE,vol. 89, pp.1808-1818, 12, 2001.

[2] Y. Tang, W. Yuan, M. Pan, Z. Li, G. Chen and Y. Li, "Experimental investigation of dynamic performance and transient responses of a kW-class PEM fuel cell stack under various load changes," Appl. Energy, vol. 87, pp. 1410-1417, 4, 2010.

[3] Y. Wang, K. S. Chen, J. Mishler, S. C. Cho and X. C. Adroher, "A review of polymer electrolyte membrane fuel cells: Technology, applications, and needs on fundamental research," Appl. Energy, vol. 88, pp. 981-1007, 4, 2011.

[4] P. Corbo, F. Migliardini and O. Veneri, "An experimental study of a PEM fuel cell power train for urban bus application," J. Power Sources, vol. 181, pp. 363-370, 7/1, 2008.

[5] J. Y. Kim, T. Oh, Y. Shin, J. Bonnett and K. S. Weil, "A novel non-platinum group electrocatalyst for PEM fuel cell application," Int J Hydrogen Energy, vol. 36, pp. 4557-4564, 4, 2011.

[6] A. Bıyıkoğlu, "Review of proton exchange membrane fuel cell models," Int J Hydrogen Energy, vol. 30, pp. 1181-1212, 9, 2005.

[7] Z. N. Farhat, "Modeling of catalyst layer microstructural refinement and catalyst utilization in a PEM fuel cell," J. Power Sources, vol. 138, pp. 68-78, 11/15, 2004.

[8] Q. Yan, H. Toghiani and H. Causey, "Steady state and dynamic performance of proton exchange membrane fuel cells (PEMFCs) under various operating conditions and load changes," J. Power Sources, vol. 161, pp. 492-502, 10/20, 2006.

[9] W. Q. Tao, C. H. Min, X. L. Liu, Y. L. He, B. H. Yin and W. Jiang, "Parameter sensitivity examination and discussion of PEM fuel cell simulation model validation: Part I. Current status of modeling research and model development," J. Power Sources, vol. 160, pp. 359-373, 9/29, 2006.

[10] PEM Fuel Cell Modelling and Simulation Using MATLAB. Colleen Spiegel, 2008, Elsevier Inc

[11] M. Y. El-Sharkh, A. Rahman, M. S. Alam, P. C. Byrne, A. A. Sakla and T. Thomas, "A dynamic model for a stand-alone PEM fuel cell power plant for residential applications," J. Power Sources, vol. 138, pp. 199-204, 11/15, 2004.

[12] A. J. del Real, A. Arce and C. Bordons, "Development and experimental validation of a PEM fuel cell dynamic model," J. Power Sources, vol. 173, pp. 310-324, 11/8, 2007.

[13] P. R. Pathapati, X. Xue and J. Tang, "A new dynamic model for predicting transient phenomena in a PEM fuel cell system," Renewable Energy, vol. 30, pp. 1-22, 1, 2005.

[14] X. Wang, J. Xu, W. Yan, D. Lee and A. Su, "Transient response of PEM fuel cells with parallel and interdigitated flow field designs," Int. J. Heat Mass Transfer.

[15] Z. Zhang, L. Jia, X. Wang and L. Ba, "Effects of inlet humidification on PEM fuel cell dynamic behaviors," Int. J. Energy Res., vol. 35, pp. 376-388, 2011.

[16] H. Wu, P. Berg and X. Li, "Steady and unsteady 3D non-isothermal modeling of PEM fuel cells with the effect of non-equilibrium phase transfer," Appl. Energy, vol. 87, pp. 2778-2784, 9, 2010.

[17] J. Peng, J. Y. Shin and T. W. Song, "Transient response of high temperature PEM fuel cell," J. Power Sources, vol. 179, pp. 220-231, 4/15, 2008.

[18] Inamuddin, T. A. Cheema, S. M. J. Zaidi and S. U. Rahman, "Three dimensional numerical investigations for the effects of gas diffusion layer on PEM fuel cell performance," Renewable Energy, vol. 36, pp. 529-535, 2, 2011.

[19] P. Alotto, M. Guarnieri and F. Moro, "A Fully Coupled Three-Dimensional Dynamic Model of Polymeric Membranes for Fuel Cells," Magnetics, IEEE Transactions on, vol. 46, pp. 3257-3260, 2010.

[20] Caisheng Wang, M. H. Nehrir and S. R. Shaw, "Dynamic models and model validation for PEM fuel cells using electrical circuits," Energy Conversion, IEEE Transactions on, vol. 20, pp. 442-451, 2005.

[21] R. Chris and S. Scott, "Introduction to Fuel Cell Technology", Department of Aerospace and Mechanical Engineering, University of Notre Dame, Notre Dame, U.S.A., May 2003.

[22] A. Obeda, B. Omar, S. C. Chai, A. Asseri and A. Savvaris, "Experimental analysis of the dynamic performance of PEM fuel cell under various load changes," in Mechanical and Electrical Technology (ICMET), 2010 2nd International Conference on, 2010, pp. 604-609.

[23] K. P. Adzakpa, J. Ramousse, Y. Dubé, H. Akremi, K. Agbossou, M. Dostie, A. Poulin and M. Fournier, "Transient air cooling thermal modeling of a PEM fuel cell," J. Power Sources, vol. 179, pp. 164-176, 4/15, 2008.

9.2 Nexa Power System Module Specifications

Outputs

Water	Maximum flow rate of product Ho_2 at rated power as both liquid and vapour < 870 ml/hour
Heat	approximately 1650 watts of waste heat are generated by the fuel cell system

Inputs	
Maximum H_2 fuel consumption at Rated Power	<18.5 SLPM
Maximum air consumption at rated power.	approximately 90 slpm
Hydrogen Inlet	
Pressure PH_2	70 to 1720 kPa(g)
Fuel inlet supply temperature	5 to 80 ºC
Maximum H_2 fuel flow rate at maximum power during anode purging	≤ 20.0 slpm
Pressure Relief Valve Setting	2400 kPa(g)
Connection	45º flared tube fitting (male) for 1/4" OD tubing
Process Air Inlet	
Pressure	Approximately Atmospheric
Maximum air consumption at rated power.	approximately 90 slpm
Process Air Outlet	
Composition	Oxygen-depleted air
Maximum allowable flow restriction on outlet connection, measured as pressure drop to ambient	3.44 kPa (0.5 psi) at 100 SLPM, 55ºC
Temperature	< 55 ºC; depends on the FC stack operating temperature
Flow	≤ 90 slpm
Entrained Product Water	870 mL/hour maximum at rated power
Air Outlet Connection	Outer diameter of oxidant air outlet tube is 16 mm OD
Cooling Air Inlet	
Composition	Ambient air
Pressure	Atmospheric
Flow	3600 slpm maximum
Cooling Air Outlet	
Composition	Ambient air
Coolant Outlet Restriction	Maximum Allowable Pressure Drop or Back-pressure 0.35 kPa (1.4 inches of water) at maximum cooling air flow rate.
Cooling air outlet temperature	~ 17 C°above ambient at rated load and operating temperature
Flow Rate	Maximum required cooling air flow rate 3600 slpm (140 scfm)

9.3 Basic Installation of a Nexa™ Power Module in the Lab

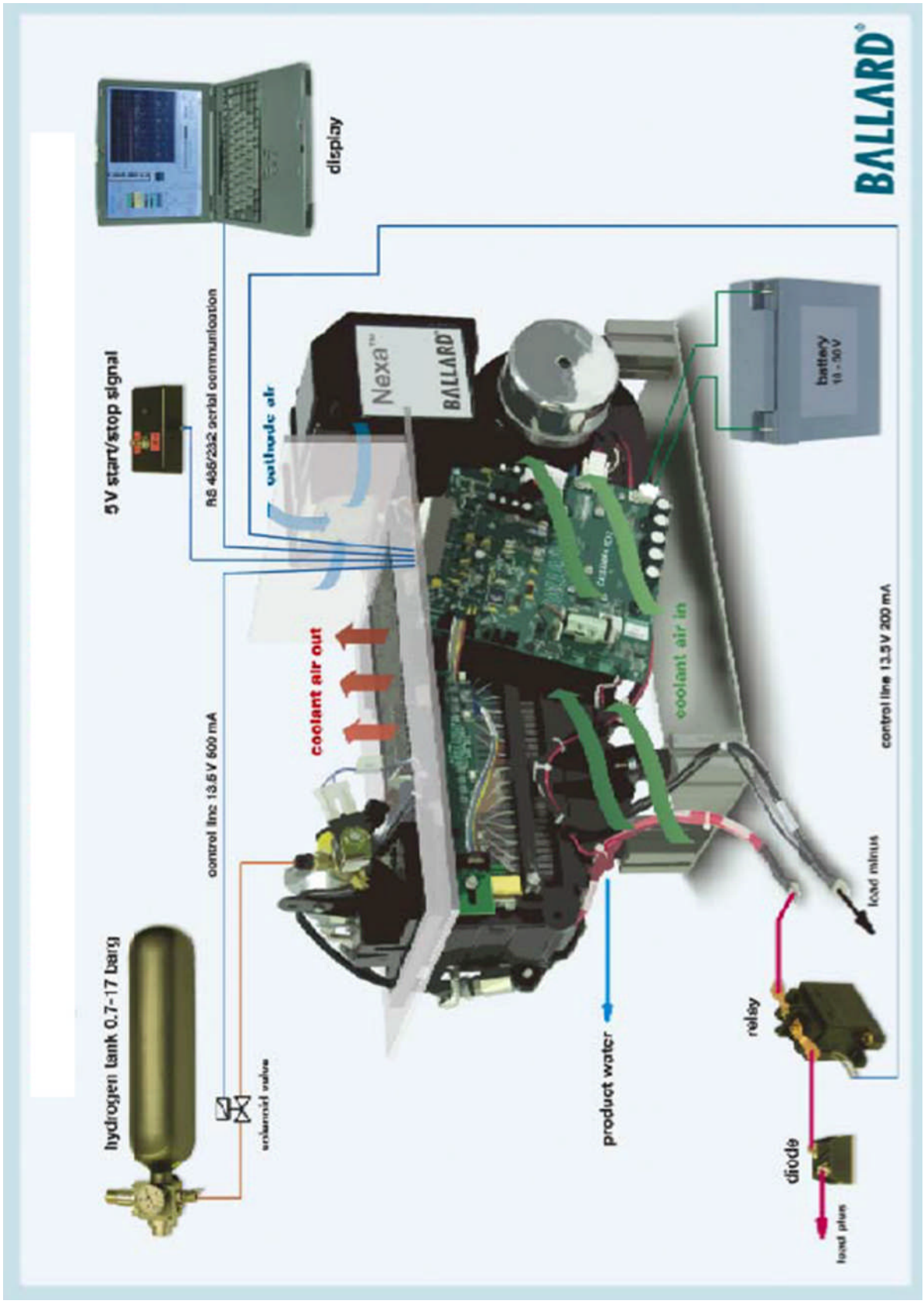

Figure 9.1 Basic installation of a Nexa™ power module in the lab

9.4 The Main Screen of the Nexa Software Lab

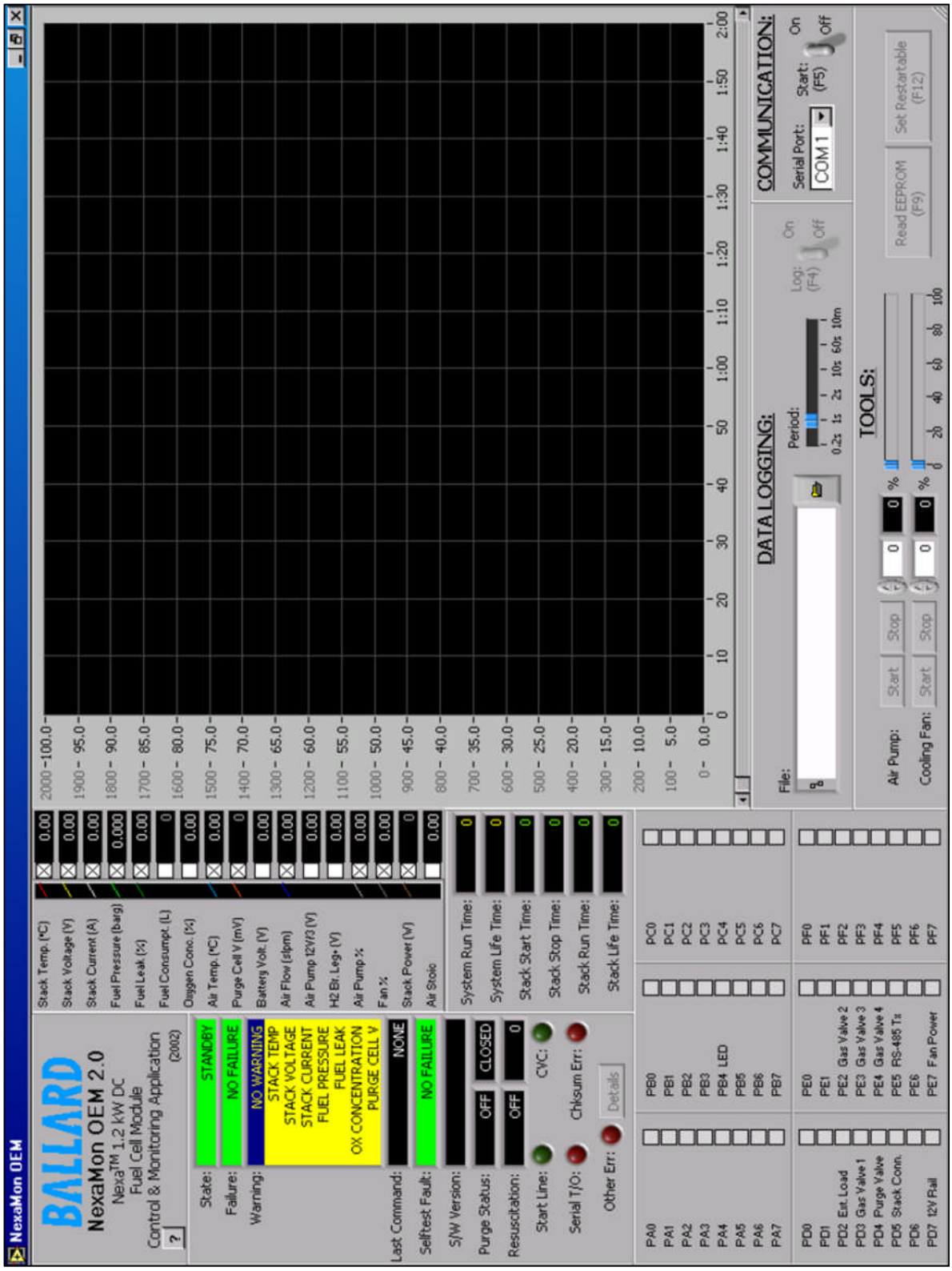

Figure 9.2 The main screen of the Nexa software

9.5 The NexaTM Module Interfaces

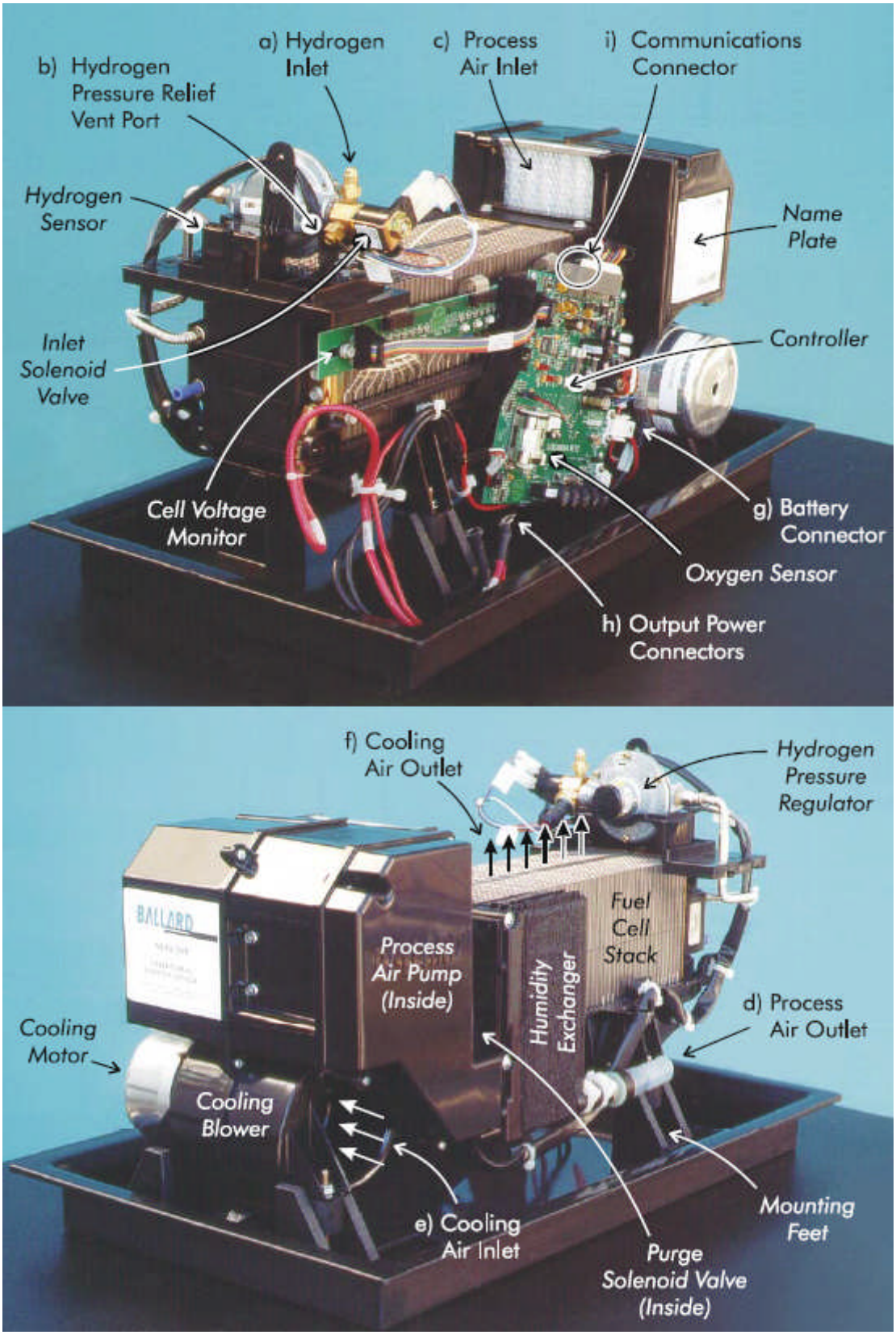

Figure 9.3 The Nexa^{TM} module interfaces

9.6 Specifications of the WP18-12 Lead Acid Battery

	RECHARGEABLE SEALED LEAD ACID BATTERY	Revision 3.3

WP18-12IE

Specifications

Nominal Voltage (V) 12V

Nominal Capacity

20hour rate	(0.9A	to	10.50V)	18Ah
10hour rate	(1.8A	to	10.50V)	17.1Ah
5hour rate	(3.06A	to	10.20V)	15.3Ah
1C	(18A	to	9.60V)	12.6Ah
3C	(54A	to	9.60V)	9.18Ah

Weight 6.283kg(13.82Lbs.)

Internal Resistance (at 1KHz) 10 mΩ

Maximum Discharge Current for 30 seconds : 360A

Maximum Discharge Current for 5 seconds : 720A

Operating Temperature Range

Charge	0℃(32℉)	to	40℃ (104℉)
Discharge	-15℃(5℉)	to	50℃ (122℉)
Storage	-15℃(5℉)	to	40℃ (104℉)

Charge Retention (shelf life) at 20℃ (68℉)

1 month	92%
3 month	90%
6 month	80%

Charging Methods at 25℃(77℉)

Cycle use:
Charging Voltage 14.4 to 15.0V
Maximum Charging Current : 5.4A
Standby use :
Float Charging Voltage 13.50 to 13.80V

Life expectancy :
Cycle Use :
100% depth of discharge 225 cycles
80% depth of discharge 250 cycles
50% depth of discharge 750 cycles
Standby Use : 3~5years

Case Material ABS
(Option : 94-HB & 94V-0 flame retardant case)
Terminal F3

Dimensions

mm(Inch)

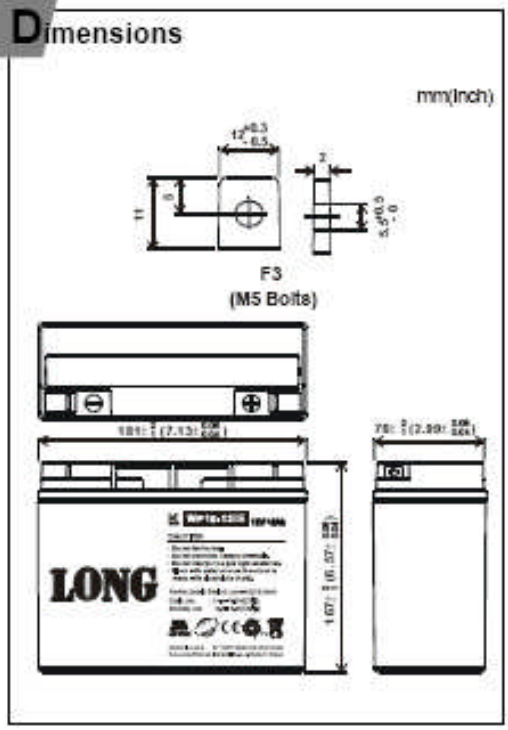

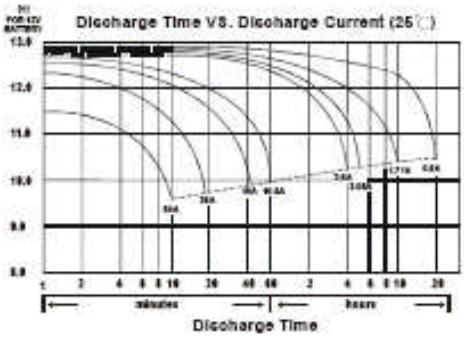

廣隆光電科技股份有限公司 Kung Long Batteries Industrial Co., Ltd.
南投市自立三路 6 號 NO. 6 TZU-LI 3 ROAD NANTOU CITY TAIWAN TEL: +886-49-2254777 ~8 FAX: +886-49-2253607

Table 9-1 Specifications of the WP18-12 lead acid battery

Chemistry	Lead Acid
Voltage	12
Capacity	18000 mAh / 18.00 Ah
Rating	216 Whr
Cell	6 cells
Connector	NB
Length	7.13 inch / 18.11 cm
Width	3.03 inch / 7.70 cm
Height	6.57 inch / 16.69 cm
Color	Gray
Weight	12.6 lb / 5.72 Kg
Warranty	1 Year
UPC Code	880487207785

9.7 The dynamic model of the Piper Cub J3 aircraft

The dynamic model of the aircraft includes the Aerodynamic Forces and Moments, Electrical Engine Model, Total Forces and Moments, Equations of Motion Block and Mass and Inertia.

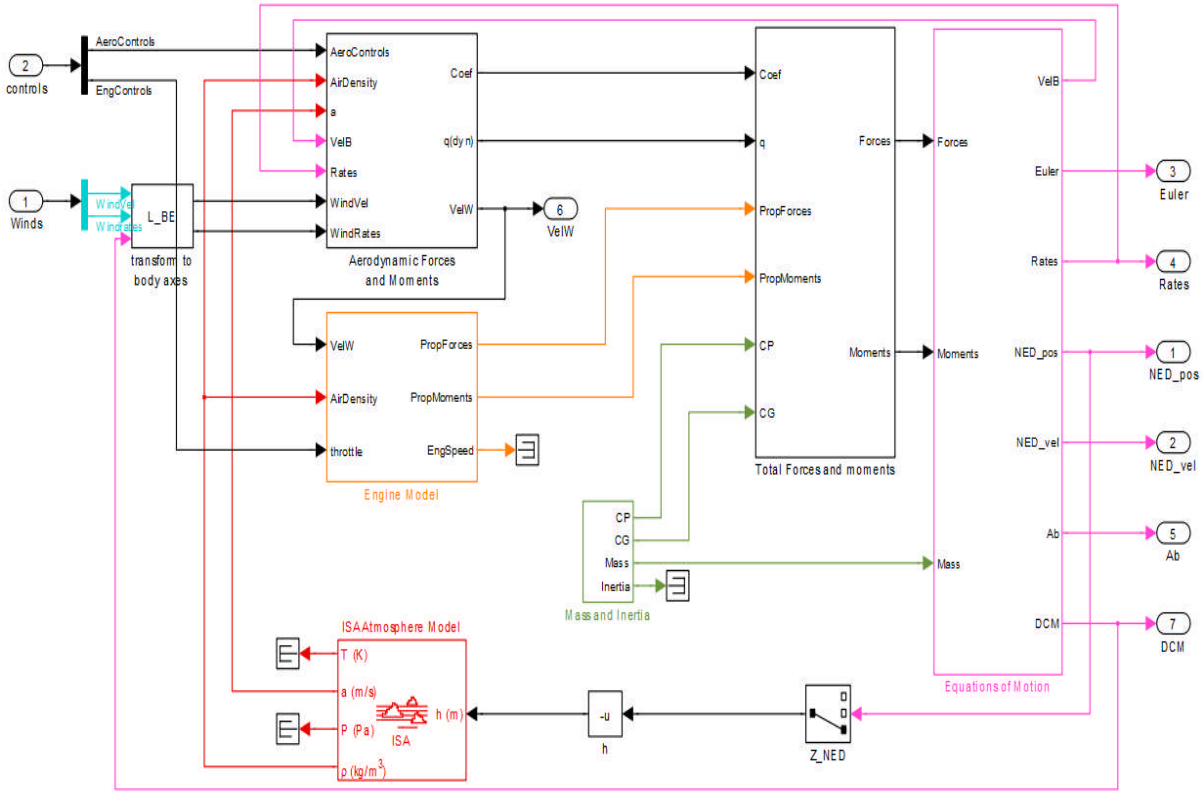

Figure 9.4 Piper J-3 Cub 40 simulation model - aircraft dynamics

9.8 High Level of the Hybrid System Simulation Model

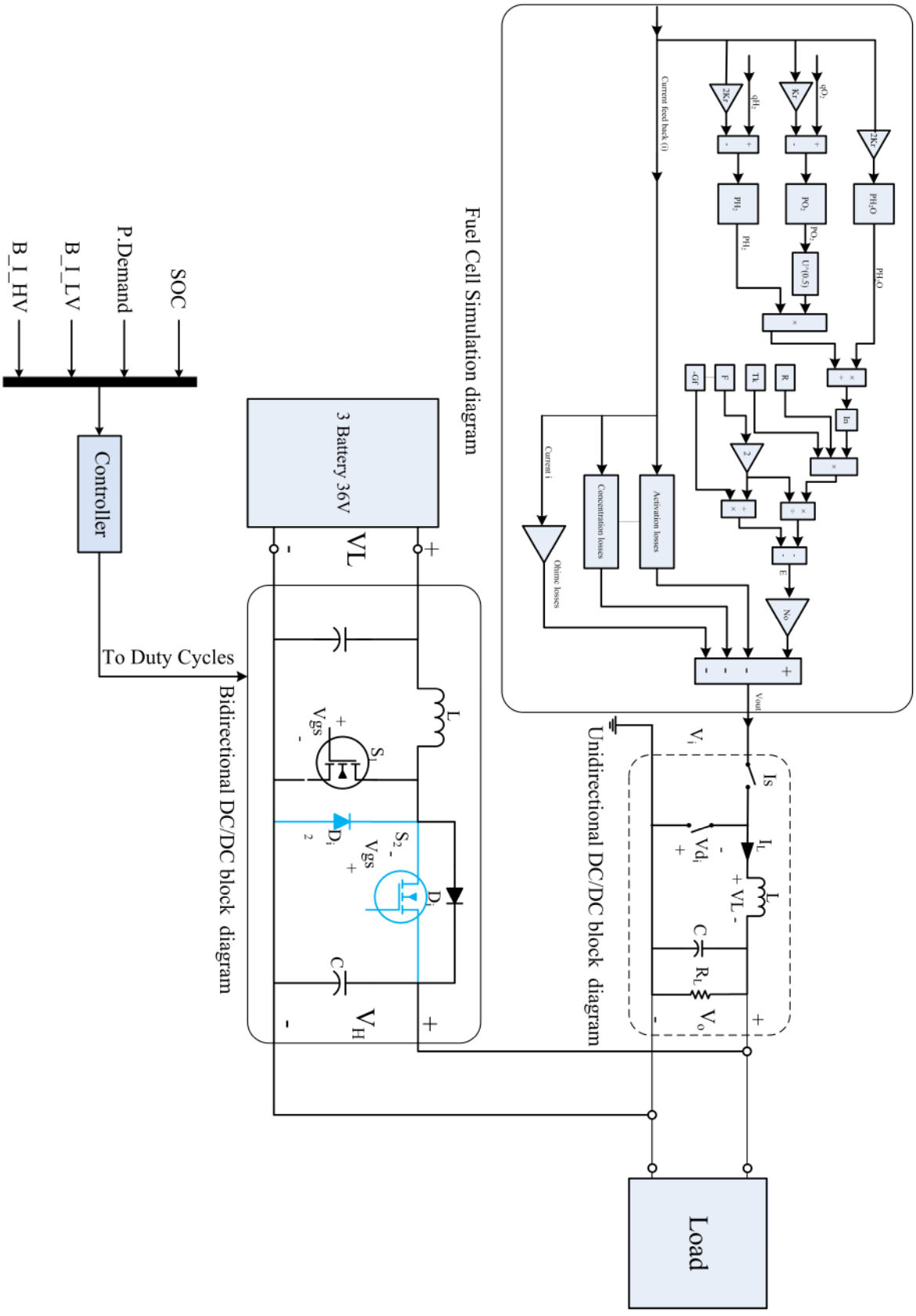

9.9 DC Engine Test

Table 9-2 DC Engine Test

Throttle command (%)	Amps	Voltage	RPM
34.48276	0.42	27	1581.011
37.93103	0.75	27	1647.728
41.37931	1.2	27	1738.704
44.82759	1.69	27	1837.767
48.27586	2.23	27	1946.939
51.72414	2.85	27	2072.285
55.17241	3.6	27	2223.912
58.62069	4.6	27	2426.082
62.06897	5.9	27	2688.903
65.51724	7.3	27	2971.941
68.96552	9.1	27	3335.847
70.68966	10.1	27	3538.017
72.41379	10.9	27	3699.753
74.13793	12.3	27	3982.791
75.86207	13.5	27	4225.395
77.58621	14.3	27	4387.131
79.31034	15.6	27	4649.952
81.03448	17.1	27	4953.207
82.75862	18.8	27	5296.896
84.48276	20.5	27	5640.585
86.2069	22	27	5943.84
87.93103	24	27	6348.18
89.65517	25.3	27	6611.001
91.37931	27.7	27	7096.209
93.10345	29.3	27	7419.681
94.82759	31.5	27	7864.455
96.55172	33.9	27	8349.663
98.27586	36.5	27	8875.305
100	38.6	27	9299.862

9.10 Specifications of the XM5050CA– 8 Brushless Motor

DualSky X-MOTOR XM5050CA-8 1250W X-Motor Brushless Motor - 575Kv is designed specifically for airplanes requiring.

Motor Name	Weight	Efficiency	Power	Amperage	Motor Constant
XM5050CA-8 (brushless)	285g	84%	1250 W	60A for 15s	575 rpm/V

9.11 Electronic Load Specifications

An electronic load type EL-1500 manufactured by Zentro Elektrik is recommended to be used for generating characteristic curves for the fuel cell systems.

Table 9-3 Electronic Load Specifications

Power (W)	**Load voltage (V)**	**Load current (A)**	**Load resistance (w)**	**Weight (Kg)**	**Model number**
1500	1-75	1-100	0.02-10k	12	ELA1500/75/100D

9.12 DAQ Card's Specifications

The data acquisition system (DAQ) manufactured by National Instruments, high speed PCI-6259 with M-Series multifunction board.

Table 9-4 DAQ card's specifications

Family	**Bus**	**Analog Inputs**	**Al Resolution (bits)**	**Analog Outputs**	**AO Resolution**	**Max Update Rate (MS/s)**	**AO Range (V)**	**Digital I/O**	**Correlated (clocked) DIO**
NI 6259	PCI	32	16	4	16	2.8	±10 ±5	48	32, up to 10 MHz

9.13 Electrical Current Sensor Specifications

Sensors specification and electrical characteristics

Table 9-5 Electrical Current Sensor Specifications

Supply voltage, V_S	+4.5 to +10VDC
Supply current	10 mA max
Output current	2 mA max
Offset voltage, V_O (sensed I = 0A)	V_S /2±2%
Output voltage, V_O is proportional to V_S	
Temperature error Null or gain	0.3%/ ^{0}C
Response time	3 µ Sec
Linearity (Full scale)	1 %
Accuracy (Full scale)	± 2 %
A.C. Hysteresis error	0.5 %

9.14 DC/DC Converters Modelling and Simulation

This section will give an overview of the DC/DC converter developed by S. Aldhaher [37] to be used in this work. The converter was used to connect the batteries to the system. An introduction and a brief description of power converters based on switched-mode operation were reviewed and presented here. Mathematical analysis was performed on a simple converter topology to derive the equations that govern the operation of converters.

9.14.1 Principle of Operation

Switched Mode Converters convert one DC voltage level to up or down level by storing energy from the input power source in a temporary storage for instance capacitors or inductors, afterward discharging the stored energy at different level to the output load. Power MOSFETS and power transistors switches are used to achieve the storing and discharging of the energy. The output voltage level is controlled by the duty cycle (switching time) and frequency of the switches. Higher switching frequencies supply steady and low ripple output. It is mostly limited to the highest switching frequency of the switches and components used [38]. Figure 9.5 shows an example of a switching signal.

The duty cycle D is equal to:

$$D = \frac{T_{on}}{T_{on} + T_{off}} = \frac{T_{on}}{T_s} \quad \{9.1\}$$

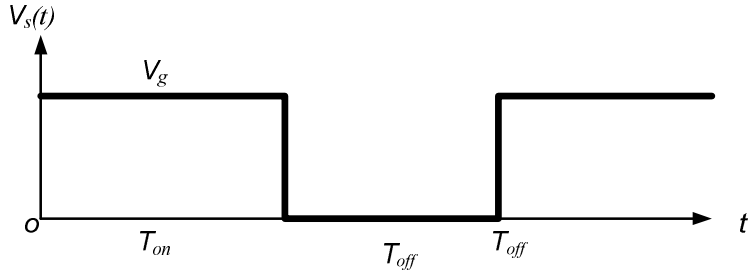

Figure 9.5 Switching Signal

Where T_{off} is the time at which the signal is zero or low, T_{on} is the time at which the signal is high and T_s is the time of the switching signal.

9.14.2 Buck Converters

The basic circuit configuration used in Step-down or Chopper or Buck converter is shown in Figure 9.6. The output voltage of the converter is continuously lower than the input voltage and can never go above it. The circuit consists of the flowing:

- An inductor (L) which is operates as the energy storage element in which energy is stored in the shape of a magnetic field.
- A MOSFET transistor (S) which controls the charging of energy in the inductor.
- A diode (D_i) that controls the energy discharging of the inductor.
- A capacitor (C) that smooth's the output voltage, decreases the voltage ripples and allows the voltage at the load to be regular.
- A load that is represented as a resistor (R_L).
- The input voltage source (V_i).

A switching signal or a square-wave is applied to the gate terminal of the MOSFET switch that controls the (On) and (Off) states of the switch. The output voltage is relative to the duty cycle of the switching signal [39].

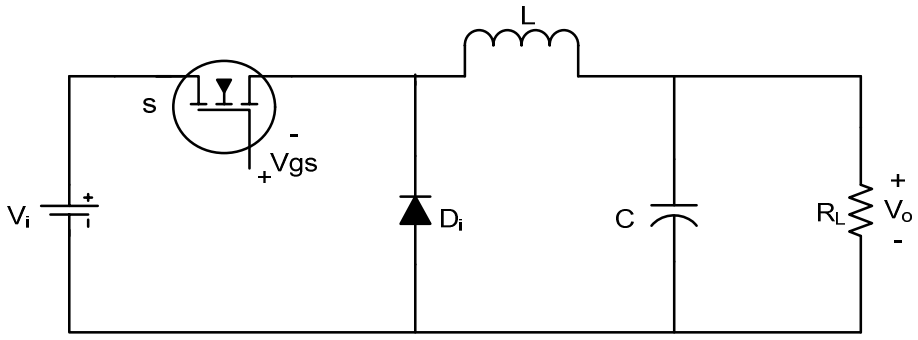

Figure 9.6 Circuit representing a step-down converter

There are two operating modes:

- Continuous Current Mode (CCM): in this mode the inductor current and the energy stored never reaches zero during the whole switching cycle.
- Discontinuous Current Mode (DCM): here in this mode, the current and energy stored will go down to zero at some time in the switching cycle resulting in high current ripple values.

The inductance of the inductor, the values of the switching signal frequency and the value of the load decide the operating mode of the converter.

It is preferred to get the output voltage equation as function of the duty cycle of the switching signal. To simplify the calculation, the circuit below shows the same converter but with the MOSFET and diode substituted by ideal switches. The value of the capacitance is considered big enough to keep the output voltage constant. The analysis of the circuit is based on transient analysis where the current and voltage relation will be derived in one switching cycle as shown in Figure 9.5.

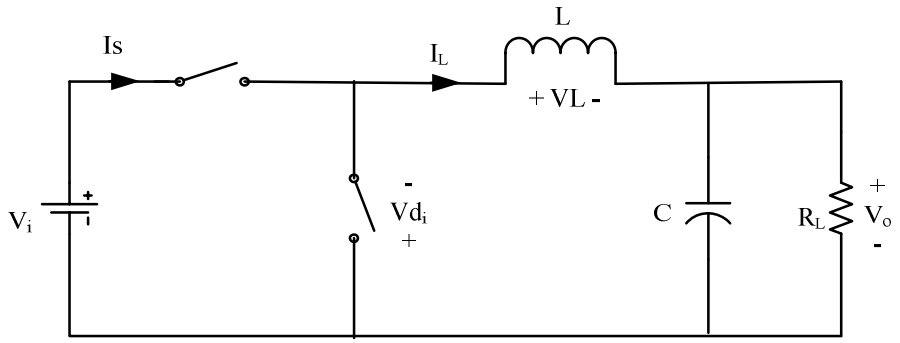

Figure 9.7 Step-down converter circuit substituted with ideal switches

- From $t = 0$ to $t = T_{on}$

In this period the switching signal will cause the switch that represents the MOSFET to be in the On position connecting the circuit to the input voltage as well as allowing it to charge the inductor and store energy in the form of a magnetic field. The current will flow from the voltage source through the inductor to the load and back to the source. The diode must be in the Off position as it is reverse biased.

The voltage across the inductor in this period is equal to [40] .

$$V_L = V_i - V_o = L \frac{dI_L(t)}{dt} \quad \{9.2\}$$

The current through the inductor based on the above equation is equal to:

$$I_L(T_{on}) = \frac{1}{L}\int_0^{T_{on}} V_L \,.dt + I_L(0) = \frac{1}{L}\int_0^{T_{on}} (V_i - V_0).dt + I_L(0) = \frac{(V_i - V_o).T_{on}}{L} + I_L(0) \quad \{9.3\}$$

Where $I_L(0)$ is current through the inductor at the start of the switching cycle.
The entire increase in energy stored in the inductor during this time is set to be equal:

$$\Delta E_{on} = \frac{1}{2}.L.(\Delta I_L)^2 = \frac{1}{2}.L.[I(T_{On})^2 - I_L(0)^2] \quad \{9.4\}$$

- From $t = T_{on}$ to $t = T_s$:

Throughout this time the switching signal is small causing the MOSFET to be in the Off position, separating the circuit from the input voltage source. This will cause the magnetic field stored in the inductor from the previous period to discharge its energy to the load. The diode is forward biased and is represented now as closed switch.

The voltage across the inductor is:

$$V_L = -V_o = L\,\frac{dI_L(t)}{dt} \quad \{9.5\}$$

Based on the above equation the current through the inductor is equal to:

$$I_L(T_s) = \frac{1}{L}\int_{T_{on}}^{T_s} V_L\,.dt + I_L(T_{on}) = \frac{1}{L}\int_{T_{on}}^{T_s} -V_o.dt + I_L\,(T_{on})$$
$$= \frac{-V_o.(T_s - T_{ON})}{L} + I_L(T_{on}) = \frac{-V_o.(T_{Off})}{L} + I_L(T_{on}) \quad \{9.6\}$$

Replacing eqn. {9.3}into eqn. {9.6}

$$I_L(T_s) = \frac{-V_o.\left(T_{Off}\right)}{L} + \frac{(V_i - V_o).T_{on}}{L} + I_L(0) \quad \{9.7\}$$

The reduce in energy stored in the inductor is given by:

$$\Delta E_{Off} = \frac{1}{2}.L.(\Delta I_L)^2 = \frac{1}{2}.I_L.[I(T_{On})^2 - I_L(T_s)^2] \quad \{9.8\}$$

Assume that the converter is operating in steady state condition; the increase in energy in the first time on the switching cycle is equal to the decrease in energy discharged from the inductor [38].

$$\Delta E_{On} = \Delta E_{Off} \quad \{9.9\}$$

Replacing eqn. {9.4} and {9.8} into the above eqn. results in

$$\frac{1}{2}.L.[I_L(T_{On})^2 - I(0)^2] = \frac{1}{2}.L.[I_L(T_{On})^2 - I_L(T_s)^2] \quad \{9.10\}$$

To simplify the above equation. It can now be written as given in {9.11}

$$I_L(T_s) = I_L(0) \qquad \{9.11\}$$

The current at the beginning of the switching cycle is equal to the current at the end of the switching cycle.

Replacing eqn. {9.7} into the above eqn.

$$\frac{-V_o.\left(T_{Off}\right)}{L} + \frac{(V_i - V_o).T_{on}}{L} + I_L(0) = I_L(0) \qquad \{9.12\}$$

The above equation can be simplified to

$$(V_i - V_o).T_{on} = V_o.T_{Off} \qquad \{9.13\}$$

That reduced to

$$\frac{V_o}{V_i} = \frac{T_{On}}{T_{On+}\,T_{Off}} = \frac{T_{On}}{T_s} = D \qquad \{9.14\}$$

Lastly, the output voltage equation for step-down converter is equal to

$$V_o = D.V_i \qquad \{9.15\}$$

Based on the eqn. {9.15} the maximum output voltage of the converter is equal to the input voltage V_i where $D = 1$, and the minimum output is equal to zero voltage when $D = 0$. The above equation shows that the output voltage is only proportional to the duty cycle in spite of the load, although the output will slightly depend on the value of the load as well as other parameters for example the capacitor, the internal resistances of the inductor and the switch, in addition to the voltage drop across MOSFET, the diode and the frequency of the switching signal.

9.14.3 Boost Converters

Another basic circuit configuration used is the Step-up or Chopper or Boost converter shown in Figure 9.8. The output voltage of the converter is continually larger than the input voltage source.

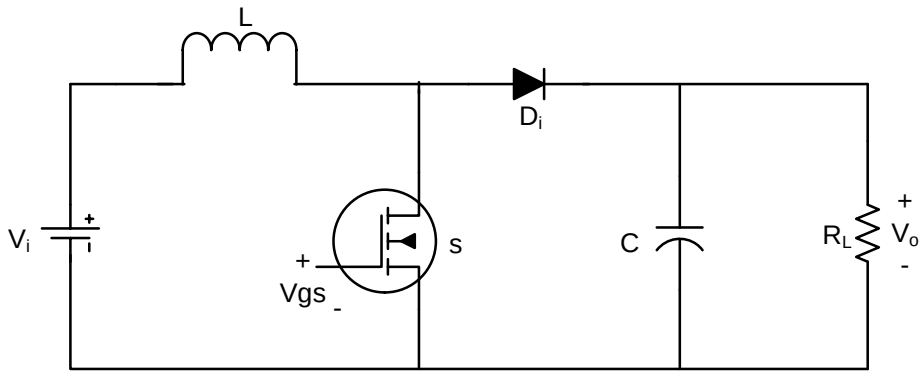

Figure 9.8 Step-up converter

Basically the circuit is very similar to the step-down converter, it consists of the same components, a MOSFET switch, an inductor for energy storage and a diode to control the charging and discharging of the inductor.

It is preferred to get the output voltage equation as function of the duty cycle of the switching frequency. Once more, it is assumed that the converter is operating in CCM. Figure 9.9 shows the same configuration but with the MOSFET and diode substituted by ideal switches. The value of the capacitance is considered big enough to keep the value of the output voltage constant. Similar to the step-down converter, the analysis of this circuit is based on transient analysis, where the current and voltage relation will be derived in one switching cycle.

- From $t = 0$ to $t = T_{on}$

In this period the switching signal is high and will cause the MOSFET to be in the On position, thus the voltage source will charge and store energy in the inductor. The current will flow from the voltage source to the inductor and then through the switch and back to the source; here is no current will flow to the load from the source as the On position of the MOSFET will form a short circuit path for the current. The voltage across the inductor is equal to:

$$V_L = V_i = L \frac{dI_L(t)}{dt} \qquad \{9.16\}$$

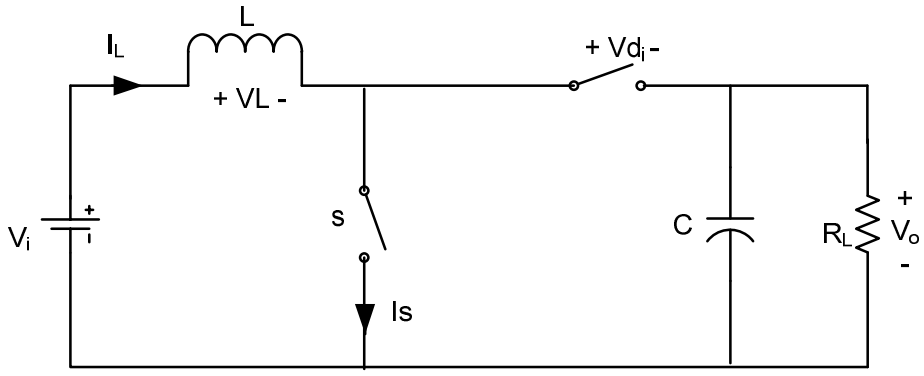

Figure 9.9 Boost converter circuit replaced with ideal switches

Based on the above equation, the current through the inductor is equal to:

$$I_L(T_{on}) = \frac{1}{L}\int_0^{T_{on}} V_L\,.dt + I_L(0) = \frac{1}{L}\int_0^{T_{on}} V_i.dt + L_L\,(0) = \frac{V_i.T_{on}}{L} + I_L(0) \qquad \{9.17\}$$

In this time, the total increase in energy stored in the inductor is:

$$\Delta E_{on} = \frac{1}{2}.L.(\Delta I_L)^2 = \frac{1}{2}.L.[I_L(T_{On})^2 - I_L(0)^2] \qquad \{9.18\}$$

- From $t = T_{on}$ to $t = T_s$:

the switching signal cause the MOSFET to be in the Off position and the inductor will release the energy to the load through the diode. The voltage across the inductor is:

$$V_L = V_i - V_o = L\,\frac{dI_L(t)}{dt} \qquad \{9.19\}$$

The current at the end of the cycle is equal to:

$$\begin{aligned} I_L(T_s) &= \frac{1}{L}\int_{T_{on}}^{T_s} V_L\,.dt + I_L(T_{on}) = \frac{1}{L}\int_{T_{on}}^{T_s} (V_i - V_o).dt + I_L\,(T_{on}) \\ &= \frac{(V_i - V_o).(T_s - T_{ON})}{L} + I_L(T_{on}) = \frac{(V_i - V_o).(T_{Off})}{L} + I_L(T_{on}) \end{aligned} \qquad \{9.20\}$$

Replacing eqn. {9.17} into eqn. {9.20}

$$I_L(T_s) = \frac{(V_i - V_o).(T_{Off})}{L} + \frac{V_i.T_{on}}{L} + I_L(0) \quad \{9.21\}$$

And the reduction in energy stored in the inductor is:

$$\Delta E_{Off} = \frac{1}{2}.L.(\Delta I_L)^2 = \frac{1}{2}.L.[I_L(T_{On})^2 - I_L(T_s)^2] \quad \{9.22\}$$

Assume that the converter is operating in steady state condition; the increase in energy in the first time of the switching cycle is equal to the decrease in energy released from the inductor. Based on eqn. {9.11}, both the inductor current at the beginning and at the end of the switching cycle is equal.

$$I_L(T_s) = I_L(0) \quad \{9.23\}$$

Replacing eqn. {9.21} into the above eqn.

$$\frac{(V_i - V_o).(T_{Off})}{L} + \frac{V_i.T_{on}}{L} + I_L(0) = I_L(0) \quad \{9.24\}$$

Simplifying the above eqn. results in:

$$(V_i - V_o).T_{off} + V_i.T_{On} = 0 \quad \{9.25\}$$

Again this reduces to:

$$\frac{V_o}{V_i} = \frac{T_{On+}T_{Off}}{T_{Off}} = \frac{T_s}{T_{Off}} = \frac{1}{1-D} \quad \{9.26\}$$

Lastly, the output voltage equation for a step-up converter is:

$$V_o = \frac{V_i}{1-D} \quad \{9.27\}$$

From the above equation the output voltage ranges from V_i when $D = 0$, to infinity when $D = 1$. But the maximum output voltage that can be achieved from the converter is limited to

the highest power evaluations of the MOSFET and diode used, with the internal resistances of the switch, the capacitor and the inductor.

9.14.4 Bidirectional Converters

The aim of using a DC/DC bi-directional converter in this project is to be able to control both charging and discharging of the 36 Vbattery pack. The step-down and step-up converters are unidirectional converters; they only allow power to flow in one direction through the converter. In order to get a bidirectional converter, the previous circuits of the step-down and step-up converters are merged into one circuit as shown in [37,41]. Based on step-down and step-up converters circuits shown in Figure 9.6 and Figure 9.8, it can be seen that the two circuits are extremely similar. The diode in the step-down converter is replaced by MOSFET in the step-up converter and, the MOSFET switch in the step-down converter is replaced by a diode in the step-up converter.

After combing the two circuits of both the step-down and the step-up converters, the bidirectional converter is formed as shown in Figure 9.10 consisting of two diodes, two MOSFET switches and a single inductor.

The circuit so obtained has two terminals; low voltage V_L terminal and high voltage V_H terminal. If the converter is to be operated as a step-down converter, then the high voltage terminal must be connected to a voltage source and the low voltage terminal must be connected to the load while applying the PWM switching signal to the MOSFET S_2. If it is to be operated otherwise, then the high voltage terminal must be connected to a voltage source and the low voltage terminal must be connected to the load while applying the PWM switching signal to the MOSFET S_1.

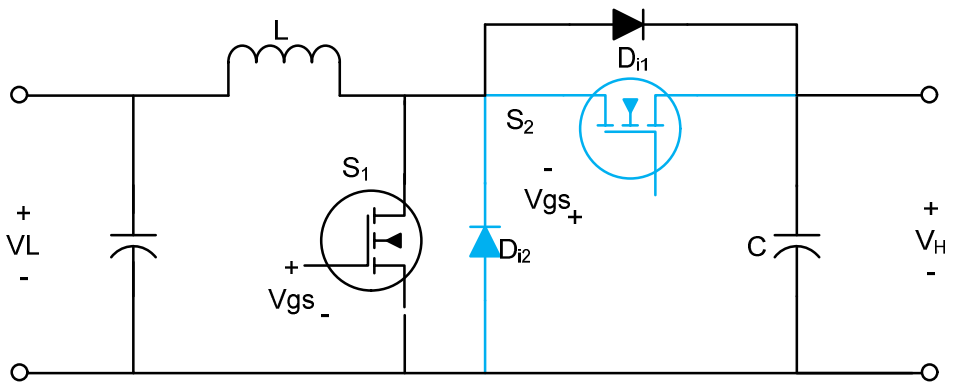

Figure 9.10 Bidirectional DC/DC converter

9.14.5 DC/DC Bidirectional Capability

The power converter must be able to operate either a step-up or a step-down converter. For step-up converter, the converter must be able to convert the input voltage into a higher output voltage; for instance if there is a low power required then the converter can operate as a step up converter allowing batteries to be charged. For step-down converter, the converter must be able to convert the input voltage into a lower output voltage. For instance if more power is demanded, then the converter will operate as step down converter to allow the batteries to deliver more power to the load. In addition the bidirectional converter must have a constant output voltage with minimum overshoots and ripple.

9.14.6 Power Regulation

The power regulation must have the ability to set the amount of current from or to any source that is connected to it. Also it allows several sources to share a load with the capability of controlling the amount of power each source will contribute to the load. For instance the converter can control how much charging current that can flow into the batteries and to control also the amount of current that a battery can provide to a load connected. These setting are determined by the controller.

In this project the requirement is to distribute an electronic load between a PEM FC system and 36 V batteries, the current delivered by each source can be controlled and changed while the load is active. The methods used for the current to share a load between several converters require a controller to regulate the output voltage of each converter to obtain the desired current level to be contributed to the load as explained in [37]. Figure 9.11 shows a similar circuit to the DC-DC converter that act as an independent power regulator module; it is based on PWM and the sharing ratio between the batteries and fuel cell is set and controlled by changing the duty cycle of the PWM signal.

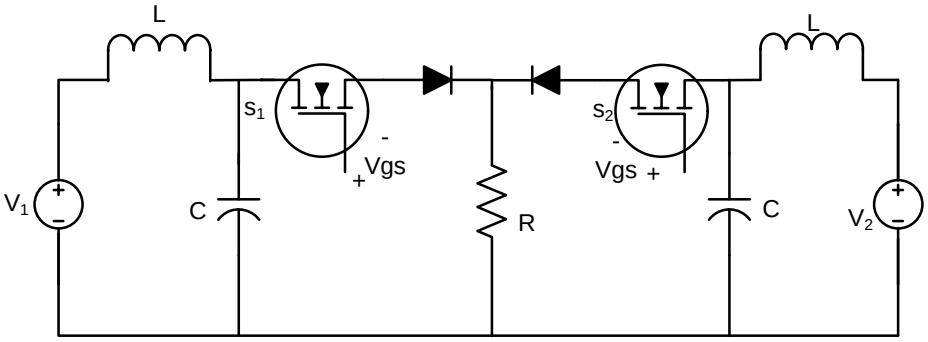

Figure 9.11 Power regulator

The above configuration circuit allows each source to supply power to the load for an exact period of time decided by the switching times of the two MOSFET switches S_1 and S_2, the capacitors and inductors are used as filters to allow steady current to flow from both sources. For instance if the batteries is required to supply 30% of the power and the fuel cell is required to provide 70% of the power then a PWM signal with a 30%, 70% duty cycle must be applied to the switch S_2 and S_1 respectively and must be opposite to each; if the PWM signal to S_2 is low then the PWM signal applied to S_1 must be high and vice versa as given in Figure 9.12. The two diodes are used to protect and to stop current flow from one power source to the other.

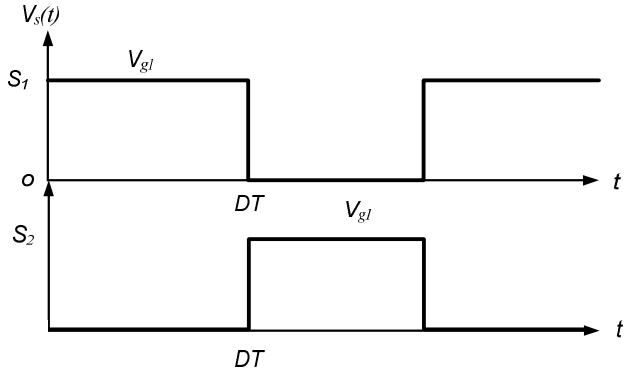

Figure 9.12 Switching signals

To begin with, the analysis of this circuit is based on transient analysis where the relations between the power and current delivered from both sources as a function of the duty cycle will be obtained. Also, assuming that the inductors and the capacitors are to be very large. Figure 9.13 shows the same circuit but with the inductors and capacitors removed and also with the replacement of the MOSFET switches with ideal switches.

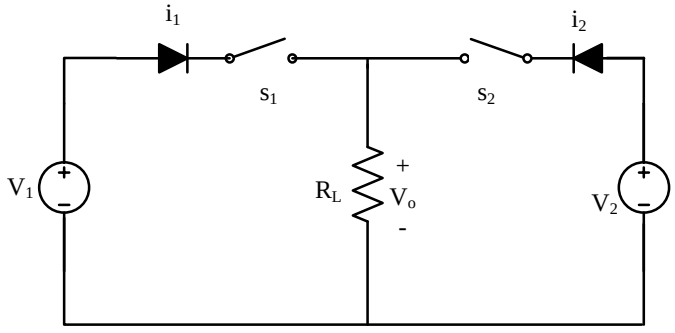

Figure 9.13 Power regulator circuit replaced with ideal switches

Beginning with the first power source V_1 the instantaneous current i_1 can be calculated as flowing:

$$i_1 = \begin{cases} \frac{V_1}{R_L} & ;\ 0 \le t \le D.T \\ 0 & ;\ D.T < t \le T \end{cases} \quad \{9.28\}$$

The average current is equal to:

$$i_{1avg} = \frac{1}{t}\int_0^T i_1 . dt = \frac{1}{T}\int_0^{D.T} \frac{V_1}{R_L} . dt + \frac{1}{T}\int_{D.T}^T 0 . dt = \frac{D.V_1}{R_L} \quad \{9.29\}$$

And the average power delivered from V_1 is equal to:

$$P_{1avg} = V_{1avg} . i_{1avg} = \frac{D.V_1^2}{R_L} \quad \{9.30\}$$

For the second power source V_2 the instantaneous current i_2 is calculated as follows:

$$i_2 = \begin{cases} 0 & ;\ 0 \le t \le D.T \\ \frac{V_2}{R_L} & ;\ D.T < t \le T \end{cases} \quad \{9.31\}$$

The average current is equal to:

$$i_{2avg} = \frac{1}{t}\int_0^T i_2 . dt = \frac{1}{T}\int_0^{D.T} 0 . dt + \frac{1}{T}\int_{D.T}^T \frac{V_2}{R_L} . dt = \frac{(1-D).V_2}{R_L} \quad \{9.32\}$$

And the average power delivered from V_2 is equal to:

$$P_{2avg} = V_{2avg} . i_{2avg} = \frac{(1-D).V_2^2}{R_L} \quad \{9.33\}$$

The full power supplied to the load is:

$$P_L = P_{1avg} + P_{2avg} = \frac{D.V_1^2}{R_L} + \frac{(1-D).V_2^2}{R_L} \quad \{9.34\}$$

If $V_1 \approx V_2 = V$, then eqn. reduces to

$$P_L = \frac{V^2}{R_L} \qquad \{9.35\}$$

Also the average voltage across the load and the voltage V are equal; otherwise the voltage will vary between $V_1 and\ V_2$.

9.14.7 DC/DC Converter Controller

The controller must be able to set the required voltage to be achieved from the converter at both terminals. Normally, a lower voltage is set at one terminal and a high voltage is set at the second terminal. These voltages must be kept constant with minimum fluctuations over the full power variety of the bidirectional converter irrespective of any transients and changes that might occur in the sources.

As discussed in section 9.14.2 from both equations {9.15} and {9.27} for step-down and step-up converter, respectively it can be noticed that the output voltage of the converter is controlled by the duty cycle of the switching frequency; the output voltage will follow the duty cycle in either ways i.e. decrease or increase with respect to the input voltage of the source. For the converter, in order to set the required output voltage and to keep it constant against any rapid changes, load transients and any variations in the input voltage of the source, a controller is necessary.

Based on [38] there are two common ways of controlling systems for switched mode power supplies; current mode control CMC and voltage mode control VMC. In CMC the output current and voltage are sampled and compared to a reference signal and error produced is used to control the duty cycle, while in VMC the output voltage from the converter is sampled and compared to a reference signal where an error signal is produced and is used to control the duty cycle of the switching signal that is applied to the MOSFET switches. In this project VMC will be used for the controller.

Figure 9.14 illustrates the components of a commonly used VCM controller, the converter output voltage V_{out} is measured and compared to the reference voltage V_{ref} and an error signal e is generated. The error signal is amplified and stated as well as is applied to a comparator. Then the error signal is compared by the comparator with a saw tooth signal from a signal generator to generate the PWM signal that will drive the output voltage of the converter to the required value. Figure 9.15 shows the PWM signal obtained.

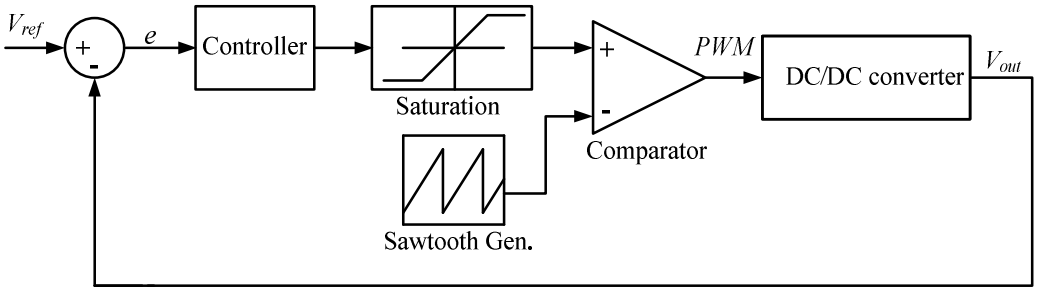

Figure 9.14 VMC controller

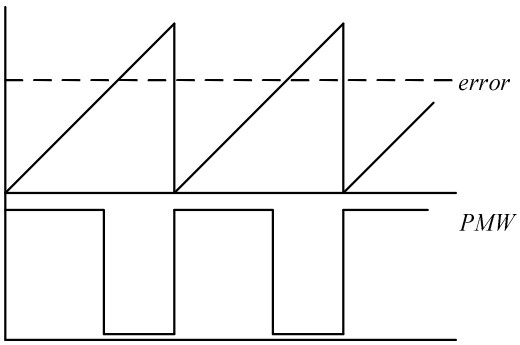

Figure 9.15 PWM signal

Finally, the proposed DC/DC converter was modelled in Matlab/Simulink by using the SimPowerSystems library. After getting initial simulations from each circuit and obtaining satisfactory results, they were integrated together according to the planned system. The output voltage of the fuel cell was regulated by using DC/DC step down converter, which gives a constant output voltage of 27V. A simple PID controller was used to control the output voltage.

9.14.8 The Equations of Motion

‘’The equations of motion of an aeroplane are the foundation on which the whole framework of flight dynamics is built and provide the essential key to a proper understanding of flying and handling qualities’’[35]. At their simplest, the EoM can describe small perturbation motion about trim only. While at their most complex they can be totally descriptive embodying aeroelastic effects, dynamic stability, atmospheric disturbances, control system dynamic and static stability simultaneously for a given aeroplane configuration. The EoM allow the rather intangible description of flying and handling qualities to be related to control parameters and quantifiable stability, which in turn might be related identifiable aerodynamic characteristics of the airframe.

For initial studies the theory of small perturbation is applied to equations to enhance their functional visibility and to see their analytical solation. Yet, for more advanced applications, the fully descriptive non-linear form of the equations may be retained. In this case the equations are very hard to solve analytically and recourse would be made to computer simulation techniques to effect a numerical solution [35].

The fully coupled linearised small equations of motion for an aircraft, referred to *wind axes*, in which all assumed non-negligible derivatives are retained and which include the height perturbation variable h may be written as, [35]. The perturbation variables shown in Figure 9.16 and summarised in Table 9-6.

Table 9-6 Summary of motion variables

	Trimmed equilibrium			*Perturbed*		
Aircraft axis	*ox*	*oy*	*oz*	*ox*	*oy*	*oz*
Force	*0*	*0*	*0*	X	Y	Z
Moment	*0*	*0*	*0*	L	M	N
Linear velocity	U_e	V_e	W_e	U	V	W
Angular velocity	*0*	*0*	*0*	p	q	r
Attitude	*0*	θ_e	*0*	ϕ	θ	ψ

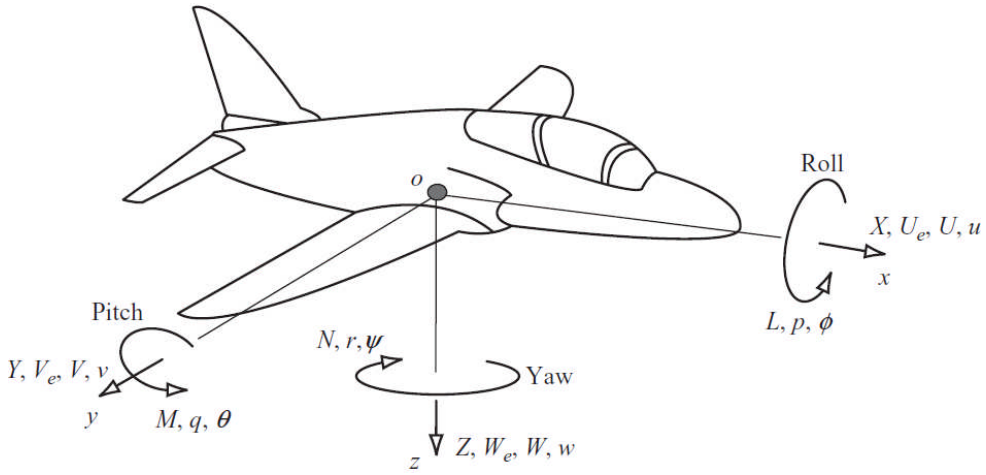

Figure 9.16 motion variables notation

$$\mathbf{M}\dot{\mathbf{x}}(t) = \mathbf{A}'\mathbf{x}(t) + \mathbf{B}'\mathbf{u}\,(t) \qquad \{9.36\}$$

Where, the state vector is given by,

$$\mathbf{x}^{\mathrm{T}}(t) = [u\ \ w\ \ q\ \ \theta\ \ h\ \ v\ \ p\ \ r\ \ \phi\ \ \psi\,] \qquad \{9.37\}$$

and, the *vector is given by*,

$$\mathbf{u}^{\mathrm{T}}(t) = [\,\eta\ \ \tau\ \ \xi\ \ \zeta\,] \qquad \{9.38\}$$

Clearly, since the longitudinal-lateral-directional coupling derivatives are all assumed to be negligibly small, the longitudinal and lateral-directional group of equations of motion my be separated and treated quite independently. Note that this assumption and treatment of the equations may only be applied safely when the perturbation motion referred to is genuinely small.

The matrices in the *state equation* {9.36} are defined below. The *mass matrix* is denoted **M**, the state is denoted $\mathbf{A}'$ and the *input matrix* is denoted $\mathbf{B}'$**.**

$$\mathbf{M} = \begin{bmatrix} \mathrm{M}_1 & 0 \\ 0 & \mathrm{M}_2 \end{bmatrix}$$

$$\mathrm{M}_1 = \begin{bmatrix} m & 0 & 0 & 0 & 0 \\ 0 & \left(m - \overset{\circ}{Z}_{\dot{w}}\right) & -\overset{\circ}{Z}_{\dot{q}} & 0 & 0 \\ 0 & -\overset{o}{M}_{\dot{w}} & \left(I_y - \overset{o}{M}_{\dot{q}}\right) & 0 & 0 \\ 0 & 0 & 0 & 1 & 0 \\ 0 & 0 & 0 & 0 & 1 \end{bmatrix}$$

$$\mathrm{M}_2 = \begin{bmatrix} m & 0 & 0 & 0 & 0 \\ 0 & \left(I_x - \overset{\circ}{L}_{\dot{p}}\right) & I_{xz} + \overset{\circ}{L}_{\dot{r}} & 0 & 0 \\ 0 & -\left(I_{xz} + \overset{o}{N}_{\dot{p}}\right) & \left(\mathrm{I}_z - \overset{o}{N}_{\dot{r}}\right) & 0 & 0 \\ 0 & 0 & 0 & 1 & 0 \\ 0 & 0 & 0 & 0 & 1 \end{bmatrix}$$

$$\mathbf{A}' = \begin{bmatrix} \mathrm{A}_1 & 0 \\ 0 & \mathrm{A}_2 \end{bmatrix}$$

$$\mathrm{A}_1 = \begin{bmatrix} \overset{\circ}{X}_u & \overset{\circ}{X}_w & \overset{\circ}{X}_q & -mg & 0 \\ \overset{\circ}{Z}_u & \overset{\circ}{Z}_w & \left(\overset{o}{Z}_q + mU_e\right) & 0 & 0 \\ \overset{\circ}{M}_u & \overset{\circ}{M}_w & \overset{\circ}{M}_q & 0 & 0 \\ 0 & 0 & 1 & 0 & 0 \\ 0 & -1 & 0 & U_e & 0 \end{bmatrix}$$

$$\mathrm{A}_2 = \begin{bmatrix} \overset{\circ}{Y}_v & \overset{\circ}{Y}_p & \left(\overset{\circ}{Y}_r - mU_e\right) & mg & 0 \\ \overset{\circ}{L}_v & \overset{\circ}{L}_p & \overset{\circ}{L}_r & 0 & 0 \\ \overset{\circ}{N}_v & \overset{\circ}{N}_p & \overset{\circ}{N}_r & 0 & 0 \\ 0 & 1 & 0 & 0 & 0 \\ 0 & 0 & 1 & 0 & 0 \end{bmatrix}$$

$$\mathbf{B}' = \begin{bmatrix} \mathrm{M}_1 & 0 \\ 0 & \mathrm{M}_2 \end{bmatrix}$$

$$B_1 = \begin{bmatrix} \overset{\circ}{X}_\eta & \overset{\circ}{X}_r \\ \overset{\circ}{Z}_\eta & \overset{\circ}{Z}_r \\ \overset{\circ}{M}_\eta & \overset{\circ}{M}_r \\ 0 & 0 \\ 0 & 0 \end{bmatrix} \text{ and } B_2 = \begin{bmatrix} \overset{\circ}{Y}_\xi & \overset{\circ}{Y}_\zeta \\ \overset{\circ}{L}_\xi & \overset{\circ}{L}_\zeta \\ \overset{\circ}{N}_\xi & \overset{\circ}{N}_\zeta \\ 0 & 0 \\ 0 & 0 \end{bmatrix}$$

In the above equation the engine thrust perturbation denoted τ and it is assumed that the resultant vector lies in the aircraft plane of symmetry such that the lateral-directional thrust derivatives are zero i.e.,

$$\overset{\circ}{Y}_\tau = \overset{\circ}{L}_\tau = \overset{\circ}{N}_\tau = 0 \qquad \{9.39\}$$

The use of thrust perturbation variable τ rather than throttle lever angle perturbation variable ε in the above formulation of equations of motion facilitates the introduction of the engine dynamics as shown in thrust and engine dynamics paragraph below. However, it does mean that the derivatives must be appropriately defined in this instance.

- **The height equation**

The height equation is readily obtained by transforming the velocity components referred to aircraft axes through the Euler angles into earth axes. If the velocity components in aircraft axes are $U, V \; and \; W$ and the corsponding velocity components in earth axes are $U_E, V_E \; and \; W_E$ then, resolving through the Euler angles $\psi, \theta \; and \; \phi$ it may be establish that,

$$\begin{bmatrix} U_E \\ V_E \\ W_E \end{bmatrix} = \begin{bmatrix} \sin\psi\cos\theta & \cos\psi\sin\theta\sin\phi - \sin\psi\cos\phi & \cos\psi\sin\theta\cos\phi + \sin\psi\cos\phi \\ \sin\psi\cos\theta & \sin\psi\sin\theta\sin\phi + \cos\psi\cos\phi & \cos\psi\sin\theta\sin\phi - \cos\psi\sin\phi \\ -\sin\theta & \cos\theta\sin\phi & \cos\theta\cos\phi \end{bmatrix} \begin{bmatrix} U \\ V \\ W \end{bmatrix} \qquad \{9.40\}$$

Now initially the aircraft is assumed to be in trimmed flight such that the aircraft such the flight axes and earth are coincident and in these circumstances the steady Euler angles are all zero. In perturbed flight $\psi, \theta \; and \; \phi$ represent the aircraft attitude perturbations and the aircraft velocity components may be written,

$$U = U_e + u$$

$$V = V_e + v$$

$$W = W_e + w$$

Thus, using the small angle approximation the equation {9.40} may be written,

$$\begin{bmatrix} U_E \\ V_E \\ W_E \end{bmatrix} = \begin{bmatrix} 1 & \theta\phi - \psi & \theta\phi - \psi \\ \psi & 1 + \psi\theta\phi & \psi\theta - \phi \\ -\theta & \phi & 1 \end{bmatrix} \begin{bmatrix} U \\ V \\ W \end{bmatrix} \qquad \{9.41\}$$

The small perturbation height equation follows directly since,

$$\dot{h} = -W_E = \theta U_e - w \qquad \{9.42\}$$

when products and squares of small quantities are ignored.

- **Thrust and engine dynamics**

The engine thrust perturbation τ has axial components $\tau_x, \tau_y \; and \; \tau_z$, and if the perpendicular from the engine thrust line to the origin of the aircraft axes has components $(x_e, y_e \; and \; z_e)$ then,

$$\begin{aligned} \overset{\circ}{X}_\tau &= \tau_x & \overset{\circ}{L}_\tau \tau &= y_e\tau_z - z_e\tau_y \\ \overset{\circ}{Y}_\tau &= \tau_y & \overset{\circ}{M}_\tau \tau &= x_e\tau_x - x_e\tau_x \\ \overset{\circ}{Z}_\tau &= \tau_z & \overset{\circ}{N}_\tau \tau &= z_e\tau_y - y_e\tau_x \end{aligned} \qquad \{9.43\}$$

Since $\tau_x, \tau_y \; and \; \tau_z$ are all functions of τ and the engine thrust line geometry, the derivatives all functions of engine installation geometry only.

For the purposes of stability and control analysis is common practice to approximate the dynamics of a turbojet to a simple first order lag with time constant T_τ which is usually of the order of a few seconds. The engine control transfer function, expressed in terms of small perturbation variables, may by written,

$$\frac{\tau(s)}{\varepsilon(s)} = \frac{k_\tau}{(1 + sT_\tau)} \qquad \{9.44\}$$

where ε represents throttle lever angle. The corresponding equation of motion assuming zero initial conditions may be written,

$$T_\tau \dot{\tau}(t) = k_\tau \varepsilon(t) - \tau(t) \qquad \{9.45\}$$

- **Decoupled longitudinal motion**

The upper left hand sub-matrix of the left side of equation {9.36} always has an inverse thus, separating the longitudinal equation from the matrix equation {9.36} and including the engine dynamics equation {9.45} leads to,

$$\mathbf{M}\dot{\mathbf{x}}(t) = \mathbf{A}'\mathbf{x}(t) + \mathbf{B}'\mathbf{u}\,(t) \qquad \{9.46\}$$

where,

$$\mathbf{x}(t)^T = [u \;\; w \;\; q \;\; \theta \;\; h \;\; \tau\,] \qquad \{9.47\}$$

$$\mathbf{u}(t)^T = [\eta \;\; \varepsilon\,]$$

The matrices are defined as follows

$$\mathbf{M} = \begin{bmatrix} m & 0 & 0 & 0 & 0 & 0 \\ 0 & \left(m - \overset{\circ}{Z}_{\dot{w}}\right) & -\overset{\circ}{Z}_{\dot{q}} & 0 & 0 & 0 \\ 0 & -\overset{o}{M}_{\dot{w}} & \left(I_y - \overset{o}{M}_{\dot{q}}\right) & 0 & 0 & 0 \\ 0 & 0 & 0 & 1 & 0 & 0 \\ 0 & 0 & 0 & 0 & 1 & 0 \\ 0 & 0 & 0 & 0 & 0 & T_\tau \end{bmatrix}$$

$$\mathbf{A}' = \begin{bmatrix} \overset{\circ}{X}_u & \overset{\circ}{X}_w & \overset{\circ}{X}_q & -mg & 0 & \overset{\circ}{X}_\tau \\ \overset{\circ}{Z}_u & \overset{\circ}{Z}_w & \left(\overset{o}{Z}_q + mU_e\right) & 0 & 0 & \overset{\circ}{Z}_\tau \\ \overset{\circ}{M}_u & \overset{\circ}{M}_w & \overset{\circ}{M}_q & 0 & 0 & \overset{\circ}{M}_\tau \\ 0 & 0 & 1 & 0 & 0 & 0 \\ 0 & -1 & 0 & U_e & 0 & 0 \\ 0 & 0 & 0 & 0 & 0 & -1 \end{bmatrix} \qquad \mathbf{B}' = \begin{bmatrix} \overset{\circ}{X}_\eta & 0 \\ \overset{\circ}{Z}_\eta & 0 \\ \overset{\circ}{M}_\eta & 0 \\ 0 & 0 \\ 0 & 0 \\ 0 & k_\tau \end{bmatrix}$$

In the above matrices the first three rows represent aircraft dynamics, the next two rows represent aircraft geometry and the last row represents the engine dynamics.

- **The classical longitudinal models**

Since the engine dynamics do not influence the small perturbation stability of the aircraft and observing that height does not influence any other state variable, then equations {9.46} may be simplified by deleting the appropriate rows and columns.

Further, it may be assumed that, in the first instance, the acceleration derivation $\overset{\circ}{Z}_{\dot{w}}, \overset{\circ}{Z}_{\dot{q}}$ *and* $\overset{\circ}{M}_{\dot{q}}$ are negligibly small, and hence may also be omitted from equations {9.46}.

The simplified longitudinal equations may thus be written,

$$\begin{bmatrix} m & 0 & 0 & 0 \\ 0 & m & 0 & 0 \\ 0 & -\overset{o}{M}_{\dot{w}} & I_y & 0 \\ 0 & 0 & 0 & 1 \end{bmatrix} \begin{bmatrix} \dot{u} \\ \dot{w} \\ \dot{q} \\ \dot{\theta} \end{bmatrix} =$$

$$\begin{bmatrix} \overset{\circ}{X}_u & \overset{\circ}{X}_w & 0 & -mg \\ \overset{\circ}{Z}_u & \overset{\circ}{Z}_w & \left(\overset{o}{Z}_q + mU_e\right) & 0 \\ \overset{\circ}{M}_u & \overset{\circ}{M}_w & \overset{\circ}{M}_q & 0 \\ 0 & 0 & 1 & 0 \end{bmatrix} \begin{bmatrix} u \\ w \\ q \\ \theta \end{bmatrix} + \begin{bmatrix} \overset{\circ}{X}_\eta & \overset{\circ}{X}_\tau \\ \overset{\circ}{Z}_\eta & \overset{\circ}{Z}_\tau \\ \overset{\circ}{M}_\eta & \overset{\circ}{M}_\tau \\ 0 & 0 \end{bmatrix} \begin{bmatrix} \eta \\ \tau \end{bmatrix} \qquad \{9.48\}$$

The equation of motion may be obtained in the standard state variable format by multiplying equation {9.48} by the inverse of the *mass* matrix **M.** the equations of motion are then expressed in terms of normalized, or *concise*, dimensional derivatives as follows,

$$\begin{bmatrix} \dot{u} \\ \dot{w} \\ \dot{q} \\ \dot{\theta} \end{bmatrix} = \begin{bmatrix} x_u & x_w & 0 & -g \\ z_u & z_w & (Z_q + U_e) & 0 \\ m_u & m_w & m_q & 0 \\ 0 & 0 & 1 & 0 \end{bmatrix} \begin{bmatrix} u \\ w \\ q \\ \theta \end{bmatrix} + \begin{bmatrix} x_\eta & x_\tau \\ z_\eta & z_\tau \\ m_\eta & m_\tau \\ 0 & 0 \end{bmatrix} \begin{bmatrix} \eta \\ \tau \end{bmatrix} \quad \{9.49\}$$

where, the concise derivative are given by,

$$\begin{array}{lll} x_u = \frac{\overset{\circ}{X}_u}{m} & z_u = \frac{\overset{\circ}{Z}_u}{m} & m_u = \frac{\overset{\circ}{Z}_u \overset{\circ}{M}_{\dot{w}}}{mI_y} + \frac{\overset{\circ}{M}_u}{I_y} \\ x_w = \frac{\overset{\circ}{X}_w}{m} & z_w = \frac{\overset{\circ}{Z}_w}{m} & m_u = \frac{\overset{\circ}{Z}_w \overset{\circ}{M}_{\dot{w}}}{mI_y} + \frac{\overset{\circ}{M}_u}{I_y} \\ x_q = 0 & z_q = \frac{\overset{\circ}{Z}_q}{m} & m_u = \frac{\overset{\circ}{Z}_q \overset{\circ}{M}_{\dot{w}}}{mI_y} + \frac{\overset{\circ}{M}_{\dot{w}} U_e}{I_y} + \frac{\overset{\circ}{M}_q}{I_y} \\ x_w = \frac{\overset{\circ}{X}_\eta}{m} & z_\eta = \frac{\overset{\circ}{Z}_\eta}{m} & m_u = \frac{\overset{\circ}{Z}_\eta \overset{\circ}{M}_{\dot{w}}}{mI_y} + \frac{\overset{\circ}{M}_\eta}{I_y} \\ x_w = \frac{\overset{\circ}{X}_\tau}{m} & z_\tau = \frac{\overset{\circ}{Z}_\tau}{m} & m_u = \frac{\overset{\circ}{Z}_\tau \overset{\circ}{M}_{\dot{w}}}{mI_y} + \frac{\overset{\circ}{M}_\tau}{I_y} \end{array}$$

Note that the derivative $\overset{\circ}{M}_{\dot{w}}$ is usually small enough to be regarded as a correction term in the above expressions for the concise derivatives.

- **Decoupled lateral-directional motion**

The lower right hand sub-matrix of the left hand side of equation {9.36} always has an inverse thus, separation the lateral-directional equations out from the matrix equation {9.36} leads to,

$$\mathbf{M}\dot{\mathbf{x}}(t) = \mathbf{A}'\mathbf{x}(t) + \mathbf{B}'\mathbf{u}\,(t) \quad \{9.50\}$$

where,

$$\begin{aligned} \mathbf{x}(t)^T &= [v \;\; p \;\; r \;\; \phi \;\; \psi] \\ \mathbf{u}(t)^T &= [\xi \;\; \zeta] \end{aligned} \quad \{9.51\}$$

The matrices are defined as follows

$$\mathbf{M} = \begin{bmatrix} m & 0 & 0 & 0 & 0 \\ 0 & \left(I_x - \overset{\circ}{L}_{\dot{p}}\right) & -\left(I_{xz} + \overset{\circ}{L}_{\dot{r}}\right) & 0 & 0 \\ 0 & -\left(I_{xz} + \overset{\circ}{N}_{\dot{p}}\right) & \left(I_z - \overset{\circ}{N}_{\dot{r}}\right) & 0 & 0 \\ 0 & 0 & 0 & 1 & 0 \\ 0 & 0 & 0 & 0 & 1 \end{bmatrix}$$

$$\mathbf{A}' = \begin{bmatrix} \overset{\circ}{Y}_v & \overset{\circ}{Y}_p & \left(\overset{\circ}{Y}_r - mU_e\right) & mg & 0 \\ \overset{\circ}{L}_v & \overset{\circ}{L}_p & \overset{\circ}{L}_r & 0 & 0 \\ \overset{\circ}{N}_v & \overset{\circ}{N}_p & \overset{\circ}{N}_r & 0 & 0 \\ 0 & 1 & 0 & 0 & 0 \\ 0 & 0 & 1 & 0 & 0 \end{bmatrix} \quad \mathbf{B}' = \begin{bmatrix} \overset{\circ}{Y}_\xi & \overset{\circ}{Y}_\zeta \\ \overset{\circ}{L}_\xi & \overset{\circ}{L}_\zeta \\ \overset{\circ}{N}_\xi & \overset{\circ}{N}_\zeta \\ 0 & 0 \\ 0 & 0 \end{bmatrix}$$

In the above matrices the first three rows represent aircraft dynamics; the next two rows represent aircraft geometry.

- **The classical lateral models**

With reference to equations {9.9} observe that yaw attitude ψ does not influence any other state variable then, equations {9.9} may be simplified by deleting the last two rows and column in the **M** and $\mathbf{A}'$ matrices**.** Further, it may be assumed that, in the first instance, the acceleration derivatives $\overset{\circ}{L}_{\dot{p}}, N_{\dot{p}}, \overset{\circ}{L}_{\dot{r}}$ *and* $\overset{\circ}{N}_{\dot{r}}$ and inertia product I_{xz} are negligibly small, and hence may also be omitted from equations {9.9}. As for longitudinal equations, the simplified longitudinal equations {9.9} may be pre-multiplied be the inverse of the mass matrix **M** to obtain the simplified equation of motion in state variable format.

The equations are the expressed in terms of concise dimensional derivatives as follows,

$$\begin{bmatrix} \dot{v} \\ \dot{p} \\ \dot{r} \\ \dot{\phi} \end{bmatrix} = \begin{bmatrix} y_v & y_p & (y_r - U_e) & g \\ I_v & I_p & I_r & 0 \\ n_v & n_p & n_r & 0 \\ 0 & 1 & 1 & 0 \end{bmatrix} \begin{bmatrix} v \\ p \\ r \\ \phi \end{bmatrix} + \begin{bmatrix} y_\xi & y_\zeta \\ I_\xi & I_\zeta \\ n_\xi & n_\zeta \\ 0 & 0 \end{bmatrix} \begin{bmatrix} \xi \\ \zeta \end{bmatrix} \qquad \{9.52\}$$

where, the concise derivative are given by,

$$y_v = \frac{\overset{\circ}{Y}_v}{m} \quad y_p = \frac{\overset{\circ}{X}_P}{m} \quad y_r = \frac{\overset{\circ}{X}_r}{m} \quad y_\xi = \frac{\overset{\circ}{X}_\xi}{m} \quad y_\zeta = \frac{\overset{\circ}{X}_\zeta}{m}$$

$$I_v = \frac{\overset{\circ}{L}_v}{I_x} \quad I_p = \frac{\overset{\circ}{L}_P}{I_x} \quad I_r = \frac{\overset{\circ}{L}_r}{I_x} \quad I_\xi = \frac{\overset{\circ}{L}_\xi}{I_x} \quad I_\zeta = \frac{\overset{\circ}{L}_\zeta}{I_\zeta}$$

$$n_v = \frac{\overset{\circ}{N}_v}{I_z} \quad n_p = \frac{\overset{\circ}{N}_P}{I_z} \quad n_r = \frac{\overset{\circ}{N}_r}{I_z} \quad n_\xi = \frac{\overset{\circ}{N}_\xi}{I_z} \quad n_\zeta = \frac{\overset{\circ}{N}_\zeta}{I_\zeta}$$

Note that if any of the acceleration derivatives and the inertia product are not negligible then the definitions of the concise derivatives must be altered to suit. It is also found that the derivatives $y_p y_\xi$ are negligible and these may be omitted from equations of motion in the interests of simplicity. The lateral-directional state matrix may therefore be written,

$$\mathbf{A}_{lat} \begin{bmatrix} y_v & y_p & (y_r - U_e) & g \\ I_v & I_p & I_r & 0 \\ n_v & n_p & n_r & 0 \\ 0 & 1 & 1 & 0 \end{bmatrix}$$

9.15 Rule base of the Fuzzy Logic controller

1	IF	Current demand is 5A	AND	SOC is S1	THEN	Output is HBC
2	IF	Current demand is 5A	AND	SOC is S2	THEN	Output is HBC
3	IF	Current demand is 5A	AND	SOC is S3	THEN	Output is HBC
4	IF	Current demand is 5A	AND	SOC is S4	THEN	Output is MBC
5	IF	Current demand is 5A	AND	SOC is S5	THEN	Output is LBC
6	IF	Current demand is10A	AND	SOC is S1	THEN	Output is HBC
7	IF	Current demand is 10A	AND	SOC is S2	THEN	Output is HBC
8	IF	Current demand is 10A	AND	SOC is S3	THEN	Output is MBC
9	IF	Current demand is 10A	AND	SOC is S4	THEN	Output is MBC
10	IF	Current demand is 10A	AND	SOC is S5	THEN	Output is LBC
11	IF	Current demand is 15A	AND	SOC is S1	THEN	Output is LBC
12	IF	Current demand is 15A	AND	SOC is S2	THEN	Output is LBC
13	IF	Current demand is 15A	AND	SOC is S3	THEN	Output is ZB
14	IF	Current demand is 15A	AND	SOC is S4	THEN	Output is ZB
15	IF	Current demand is 15A	AND	SOC is S5	THEN	Output is LBC
16	IF	Current demand is 20A	AND	SOC is S1	THEN	Output is ZB
17	IF	Current demand is 20A	AND	SOC is S2	THEN	Output is LBD
18	IF	Current demand is 20A	AND	SOC is S3	THEN	Output is MBD
19	IF	Current demand is 20A	AND	SOC is S4	THEN	Output is MBD1
20	IF	Current demand is 20A	AND	SOC is S5	THEN	Output is MBD1
21	IF	Current demand is 25A	AND	SOC is S1	THEN	Output is ZB
22	IF	Current demand is 25A	AND	SOC is S2	THEN	Output is LBD
23	IF	Current demand is 25A	AND	SOC is S3	THEN	Output is MBD
24	IF	Current demand is 25A	AND	SOC is S4	THEN	Output is MBD2
25	IF	Current demand is 25A	AND	SOC is S5	THEN	Output is MBD2
26	IF	Current demand is 30A	AND	SOC is S1	THEN	Output is LBD
27	IF	Current demand is 30A	AND	SOC is S2	THEN	Output is MBD
28	IF	Current demand is 30A	AND	SOC is S3	THEN	Output is MBD1
29	IF	Current demand is 30A	AND	SOC is S4	THEN	Output is HBD2
30	IF	Current demand is 30A	AND	SOC is S5	THEN	Output is HBD
31	IF	Current demand is 35A	AND	SOC is S1	THEN	Output is MBD

32	IF	Current demand is 35A	AND	SOC is S2	THEN	Output is HBD1
33	IF	Current demand is 35A	AND	SOC is S3	THEN	Output is HBD2
34	IF	Current demand is 35A	AND	SOC is S4	THEN	Output is HBD
35	IF	Current demand is 35A	AND	SOC is S5	THEN	Output is HBD
36	IF	Current demand is 40A	AND	SOC is S1	THEN	Output is HBD1
37	IF	Current demand is 40A	AND	SOC is S2	THEN	Output is HBD2
38	IF	Current demand is 40A	AND	SOC is S3	THEN	Output is HBD
39	IF	Current demand is 40A	AND	SOC is S4	THEN	Output is HBD
40	IF	Current demand is 40A	AND	SOC is S5	THEN	Output is HBD